THÈSE DE DOCTORAT
Université d'Aix-Marseille

École doctorale: *Physique et Sciences de la Matière*

Spécialité : **Energie, Rayonnement et Plasma**

Edge Localized Mode control
by Resonant Magnetic Perturbations
in tokamak plasmas

Presentée par:

François Orain

Thèse soutenue publiquement le 28 novembre 2014 devant le jury composé de :

Pr. Howard WILSON	Rapporteur – Professeur à l'Université de York
Pr. Sibylle GÜNTER	Rapporteur – Directeur scientifique à l'IPP Garching
Pr. Peter BEYER	Examinateur – Professeur à l'Université d'Aix-Marseille
Dr. Guido HUYSMANS	Examinateur – Coordinateur Scientifique à ITER
Dr. Marina BÉCOULET	Directrice de thèse – HDR au CEA

Contents

Abstract

The growth of plasma instabilities called Edge Localized Modes (ELMs) in tokamaks results in the quasiperiodic relaxation of the edge pressure profile. As the large transient heat fluxes due to ELMs are foreseen to strongly reduce the divertor lifetime in ITER, ELM control is mandatory in ITER. One of the promising control methods planned in ITER is the application of external resonant magnetic perturbations (RMPs) which already proved to be efficient for ELM mitigation/suppression in current tokamak experiments. However a significant progress in understanding the interaction between plasma flows, RMPs and ELMs is needed to explain the experimental results and make reliable predictions for ITER.

In this perspective, non-linear modeling of ELMs and RMPs is done with the reduced MHD code JOREK, in toroidal geometry including the X-point and the Scrape-Off Layer. The initial model has been further developped to describe self-consistent plasma flows – with the addition of the bi-fluid diamagnetic drifts, the neoclassical friction and a source of parallel rotation – and to simulate the RMP penetration consistently with the plasma response.

As a first step, the plasma response to RMPs (without ELMs) is studied for JET, MAST and ITER realistic plasma parameters and geometry. For JET parameters, three regimes of plasma response are found depending on the plasma resistivity and the diamagnetic rotation: at high resistivity and slow rotation, the magnetic islands generated by the RMPs on the edge resonant surfaces rotate in the electron diamagnetic direction and their size oscillates. At faster rotation, the generated islands are static and their size is reduced by the plasma screening. An intermediate regime with slightly oscillating quasi-static islands is found at lower resistivity.

The general behaviour of the plasma/RMP interaction, common to the three studied cases, is the following: RMPs are generally screened by the formation of response currents, induced by the plasma rotation on the resonant surfaces. RMPs however penetrate at the very edge ($\psi_{norm} > 0.95$) where an ergodic zone is formed. The amplification of the non-resonant spectrum of the magnetic perturbations is also observed in the core. The edge ergodization induces an enhanced transport at the edge, which slightly degrades the pedestal profiles. RMPs also generate the 3D-deformation of the plasma boundary with a maximum deformation near the X-point where lobe structures are formed.

Then the full dynamics of a multi-ELM cycle (without RMPs) is modeled for the first time in realistic geometry. An ELM is characterized by the growth of precursors, rotating in the electron diamagnetic direction at half the diamagnetic frequency, followed by the non-linear expulsion of plasma filaments through the edge transport barrier. This behaviour found in modeling accurately matches several experimental observations. After an ELM crash, the diamagnetic rotation is found to be instrumental to stabilize the plasma and to model the cyclic reconstruction and collapse of the plasma pressure profile. ELM relaxations are cyclically initiated each time the pedestal gradient crosses a

triggering threshold. After a few transient ELMs, a quasiperiodic ELMy regime is obtained, characterized by a similar coupling between modes, similar maximum pressure gradient reached when the crash occurs and similar power deposition on the divertor plates, cyclically recovered for all the ELMs. Diamagnetic drifts are also found to yield a near-symmetric ELM power deposition on the inner and outer divertor target plates, in closer agreement with experimental measurements as compared to previous simulations where the diamagnetic rotation was neglected.

Last the ELM mitigation and suppression by RMPs is observed for the first time in modeling. The non-linear coupling of the RMPs with unstable modes is found to modify the edge magnetic topology and to induce a continuous MHD activity in place of a large ELM crash, resulting in the mitigation of the ELMs. The ELM footprints follow the RMP footprint, although modulated by other modes. At larger diamagnetic rotation, a bifurcation from unmitigated ELMs (at low RMP current) towards fully suppressed ELMs (at large RMP current) is obtained: the large permanent transport induced by the RMP-driven MHD activity stabilizes the plasma under the stability threshold thus ELMs are fully suppressed.

Résumé

Le développement d'instabilités nommées ELMs (pour "Edge Localized Modes") dans les plasmas de tokamaks génère la relaxation quasi-périodique du profil de pression au bord. Les calculs prédictifs pour le futur tokamak ITER montrent que la forte charge thermique imposée sur le divertor lors des relaxations d'ELMs pourrait réduire drastiquement la durée de vie du divertor : dès lors, il apparait indispensable de mitiger ou supprimer les ELMs dans ITER. Une des méthodes de contrôle des ELMs prévue pour ITER est l'application de Perturbations Magnetiques Résonantes (RMPs en anglais), cette méthode s'étant avérée efficace pour mitiger ou supprimer les ELMs dans les expériences réalisées sur les tokamaks actuels. Néanmoins, une meilleure compréhension de l'interaction entre les ELMs, les RMPs et les écoulements du plasma est nécessaire pour interpréter de façon congrue les résultats expérimentaux et faire des prédictions fiables pour ITER.

Dans ce contexte, la simulation non-linéaires des ELMs et des RMPs est réalisée avec le code de MHD réduite JOREK, en géométrie toroidale incluant le point-X et la "Scrape-Off Layer". Le modèle initial de JOREK a été raffiné afin de décrire de façon cohérente les écoulements du plasma – les effets bi-fluides diamagnétiques, la friction poloidale néoclassique et une source de rotation parallèle ont été ajoutés – et de simuler la pénétration des RMP en prenant en compte la réponse du plasma.

Dans un premier temps, la réponse du plasma aux RMPs (sans ELMs) est étudiée dans le cas des tokamaks JET, MAST et ITER, dans une géométrie réaliste et avec des paramètres expérimentaux typiques. Dans le cas JET, trois régimes de réponse du plasma sont observés dans les simulations, dépendant de la résistivité du plasma et de la rotation diamagnétique : pour une résistivité élevée et une rotation faible, les îlots magnétiques induits par les RMPs sur les surfaces de résonance tournent dans le sens diamagnétique ionique, et la taille des îlots oscille. Mais lorsque la rotation diamagnétique est plus importante, les îlots sont statiques et leur taille est réduite par l'écrantage induit par le plasma. Un régime intermédiaire est également observé à faible résistivité, caractérisé par des îlots quasi-statiques oscillant faiblement.

Le mécanisme global de l'interaction entre le plasma et les RMPs, commun aux trois cas étudié, est le suivant : les RMPs sont globalement écrantées par des courants de réponse induits par la rotation du plasma sur les surfaces de résonance. Les RMPs pénètrent seulement à l'extrême bord (pour $\psi_{norm} > 0.95$) où une zone ergodique se forme. L'amplification du spectre non-résonant de perturbations magnétiques est en revanche observée au centre du plasma. L'ergodisation du bord génère une augmentation du transport au bord, ce qui dégrade légèrement les profils de piédestal. Les RMPs provoquent également la déformation tridimensionnelle des profils de densité et température, ainsi que de la séparatrice. Cette déformation est maximale près du point-X où une structure de lobes se forme.

Ensuite, la modélisation de la dynamique d'un cycle d'ELMs (sans RMPs), obtenue

pour la première fois en géométrie réaliste, est présentée. Un ELM est caractérisé d'abord par la croissance d'un mode dit "précurseur" dans le piédestal, tournant dans la direction diamagnétique électronique, suivie par l'expulsion de filaments de plasma à travers la barrière de transport externe. Cette description théorique d'un ELM correspond relativement bien avec les faits expérimentaux observés dans différents tokamaks. Nos simulations montrent que la rotation diamagnétique est un paramètre clé permettant au plasma de recouvrer un état stable après la relaxation d'un ELM. La compétition entre la stabilisation diamagnétique et la déstabilisation du plasma par l'injection de puissance induit alors une dynamique cyclique de reconstruction et d'effondrement du profil de pression. Le déclenchement d'un ELM a lieu dès lors qu'un seuil relatif au gradient de pression est franchi. Après quelques ELMs transitoires, un régime d'ELMs quasi-périodique est observé dans les simulations, dans lequel le couplage des modes, le maximum de gradient de pression pour lequel la relaxation a lieu ainsi que le dépot de puissance sur le divertor, sont similaires pour chaque ELM. De plus, la prise en compte de la rotation diamagnétique permet d'obtenir un dépot de puissance quasi-symétrique sur les plaques de divertor interne et externe, proche des observations expérimentales.

Enfin la mitigation et la suppression des ELMs sont obtenues pour la première fois dans nos simulations. Le couplage non-linéaire des RMPs avec des modes instables du plasma induit une modification de la topologie magnétique au bord. Ainsi, les relaxations d'ELMs, subites et énergétiques, sont remplacées par une activité MHD continue induisant un transport permanent important, d'où la mitigation de la puissance des ELMs. Les empreintes des ELMs sur le divertor ("footprints") suivent les empreintes générées par les RMPs, mais sont légèrement modulées par la présence des autres modes. Lorsque la vitesse diamagnétique est importante, est observée la bifurcation d'un état où les ELMs ne sont pas mitigés (pour un faible courant circulant dans les bobines RMP) vers un état où les ELMs sont totalement supprimés (pour un courant plus important) : le transport important dû à l'activité MHD induite par les RMPs a pour effet de maintenir le plasma en-dessous du "seuil de stabilité" et donc de supprimer les ELMs.

Introduction

Contents

The increasing scarcity of fossil fuels as well as the impact of the carbon-fuels on the climate change make it necessary to find clean and sustainable sources of energy. In this respect, the achievement of fusion energy would represent a "grail" for mankind, as it would provide a large amount of energy while burning almost inexhaustible and clean resources (the deuterium found in sea water and the lithium found in rocks). Furthermore, compared to fission power plants, the nuclear waste that would be produced by fusion plants – which only consists in materials activated by neutrons – becomes less radioactive than coal within one century, and the difficulty of sustaining fusion reactions make that a Tchernobyl-like explosion would be impossible with a fusion plant.

However, whereas it took only a couple of decades to create fission power plants after the discovery of the neutron in 1932, international collaborations on nuclear fusion have been started since the 1950s without achieving yet to industrially produce energy issued from fusion reactions. This is due to the fact that the physics involved is much more complicated, which motivates worldwide research in this domain. The international collaboration ITER [ITER 1999] (for International Thermonuclear Experimental Reactor, also meaning "the way" in Latin) currently in construction in Cadarache, France, represents a step forward towards the sustained and profitable production of energy from fusion reaction.

ITER will have to face several physical challenges. Among them is the control of plasma instabilities called Edge Localized Modes (ELMs), which should induce large transient heat loads on the machine. This thesis is thus motivated by the need for an improved understanding of the physics underlying the ELMs and their control methods.

1.1 Main principle of nuclear fusion

The cohesion of the nucleus of an atom depends on the mass number of the atom. The binding energy per nucleon as a function of the atomic mass is presented in Fig. 1.1. It shows that the light atoms such as Hydrogen and the heavy atoms such as Uranium are less tightly bound than average mass numbers, Iron being the most tightly bound atom. Thus considering Einstein's formula $\Delta E = \Delta mc^2$, there are two different ways to release energy from nuclear reactions [CEA]. Fission consists in the splitting of a heavy atom such as Uranium when bombarded by a neutron: the fission products being more tightly bound, the reaction releases $200 MeV$ of energy corresponding to the difference of mass. At the opposite, energy can be released by a fusion reaction, where light atoms (isotopes of Hydrogen) fuse to form a more binded atom (Helium).
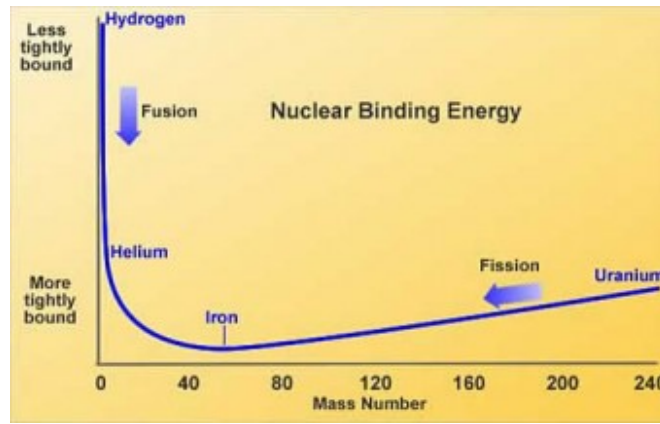
Figure 1.1: Binding energy per nucleon as a function of the atomic mass
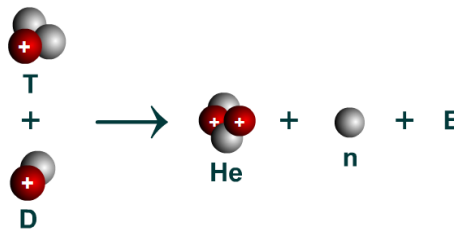
Figure 1.2: Deuterium-Tritium fusion reaction

The most probable fusion reaction is the Deuterium-Tritium (D-T) reaction (Fig. 1.2), which releases an atom of helium $(3, 56 MeV)$ and a neutron $(14, 03 MeV)$. As the D-T reaction rate (Fig. 1.3) is larger than the rate of the other possible fusion reactions, the present research on controlled nuclear fusion aims at producing energy from the D-T reaction [Wesson 2011]. Since the Tritium is very rare in nature – T is radioactive with an half-life of $\sim 12, 3$ years [Lucas 2000] –, Lithium modules will be used in the ITER blanket, such that Lithium bombarded with neutrons (issued from fusion reactions) will breed Tritium [ITER 1999]:

$$^6Li + n \rightarrow {}^4He + T \tag{1.1}$$

Thus the Li-D reaction can be sustained, since the combination of both reactions (Fig. 1.2 and *Eq.* (1.1)) gives:

$$^{6}Li + D \rightarrow 2 \ ^{4}He \qquad (1.2)$$
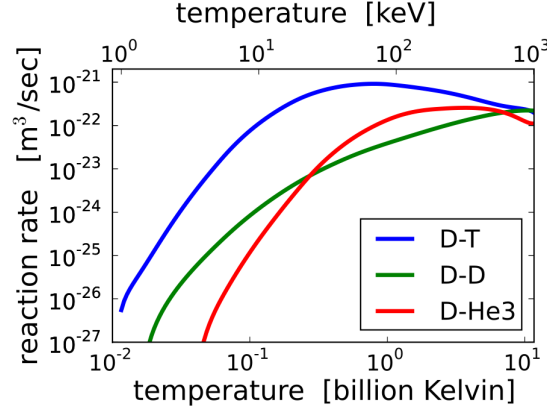
Figure 1.3: Reaction rate of fusion reactions depending on the temperature

However, the diagram presented in Fig. 1.3 shows that the D-T matter has to be heated up to $10keV$ ($\approx$ 100 million degrees) to make this reaction probable. At this extremely high temperature, the D-T mix is in a state called plasma (ionized gas). The two nuclei, positively charged, have to overcome the repulsive barrier between nuclei – called Coulomb barrier – before fusing, which explains why such a high temperature is necessary. An important parameter called the amplification factor Q, quantifies the efficiency of a fusion reactor. Q is the ratio of the power exhausted by fusion reactions against the injected power. The larger Q is, the more "profitable" a reactor is. $Q \approx 0.64$ was obtained in the JET tokamak [Keilhacker 1999]. ITER aims at reaching $Q = 10$ during $100s$ [ITER 1999] and future fusion power plant (DEMO) should reach $Q > 30$. The amplification factor Q is related to the triple factor $Tn_e\tau_e$, where T and n_e are respectively the plasma temperature and electron density and τ_e is the confinement time. The confinement time is the time it takes for the plasma to lose its energy content if the sources sustaining it are abruptly switched off. The ignition (self-sustained fusion reaction), corresponding to $Q = \infty$, is characterized by the Lawson criterion which quantifies this triple product. For the D-T reaction and for the optimum temperature $T \approx 20keV$ given by Fig. 1.3, the Lawson criterion is:

$$n_e\tau_e > 1.5 \times 10^{20} s/m^3 \qquad (1.3)$$

On Earth, there are two main ways to reach the Lawson criterion. First, in the fusion by inertial confinement, lasers are targeting a micro-ball of D-T, resulting in a high density plasma ($\approx 10^{31}m^{-3}$) confined by inertia but a very low confinement time ($\approx 10^{-11}s$). This method has among others military applications. Second, in the fusion by magnetic confinement, the plasma is magnetically confined by magnetic coils in a torus, resulting in a lower density ($\approx 10^{20}m^{-3}$) but a larger confinement time ($\approx 10s$). Two main kinds

of machines allow for the magnetic confinement, called stellerators and tokamaks. As the tokamak is currently the most advanced technique in view of producing energy from fusion reaction, the tokamak configuration was chosen for ITER. An empirical scaling law demonstrated that the energy confinement time – and therefore the amplification factor – increases with the size of the tokamak ($\tau_E \propto R_0^{1.98}$, R_0 being the major radius of the tokamak) [Hawryluk 2009]. So ITER will be larger ($R_0 = 6.2m$) than the existing experimental tokamaks ($R_0 = 3m$ in the case of the largest tokamak, JET (UK)), and future fusion plants should be even larger ($R_0 \approx 9m$).

1.2   Magnetic confinement in tokamaks
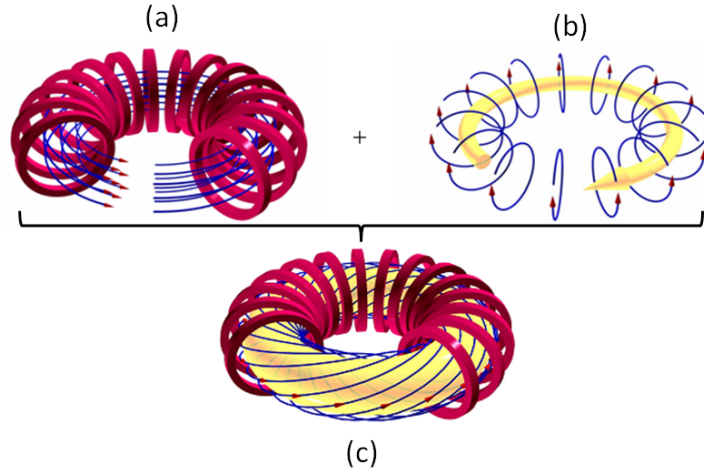
Figure 1.4: Toroidal (a) and poloidal (b) field resulting in a helicoidal (c) field in a tokamak.

The principle of the tokamak is to "trap" the particles in a magnetically confined torus. Since the plasma is electrically charged, the ions and electrons gyrate around the magnetic field lines at the cyclotron frequency $\omega_s = q_s B/m_s$, as presented in Fig. 1.5. q_s and m_s are respectively the charge and mass of the species s (ion or electron) and B is the magnetic field. The gyration radius around a magnetic field line is given by the Larmor radius $\rho_s = v_{th,s}/\omega_s$ ($v_{th,s} = \sqrt{2T/m_s}$ being the thermal velocity of the species). For a hot tokamak plasma ($T \sim 10keV$) with a strong magnetic field $B > 1$ Tesla, the ion Larmor radius is of the order of $1mm$, which is much smaller than the minor radius $a \sim 1m$ of the tokamak, and the electron Larmor radius is even smaller (around $10^{-5}m$). Thus we can consider that the ions and electrons are "stuck" to the magnetic field applied in the toroidal direction. However, the particles also have a slow drift movement (in the poloidal direction), due to the gradient of the magnetic field and the centrifugal force, and depending on the sign of their charge. Thus in addition to the toroidal magnetic field, a poloidal component of the magnetic field is necessary to compensate for this drift velocity. That is why both toroidal and poloidal components of the magnetic field are needed to obtain the confinement of the particles in the tokamak. The toroidal magnetic

field is produced by a set of coils located in the poloidal plane (Fig. 1.4(a)), whereas the poloidal field is induced by the toroidal plasma current (Fig. 1.4(b)), itself induced by transformer effect – due to the discharge of a vertical solenoid placed at the center of the tokamak – and by other current sources [Wesson 2011]. The total resulting magnetic field is therefore helical (Fig. 1.4(c)).
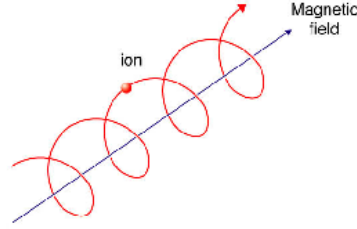
Figure 1.5: Rotation of the particles around the magnetic field lines
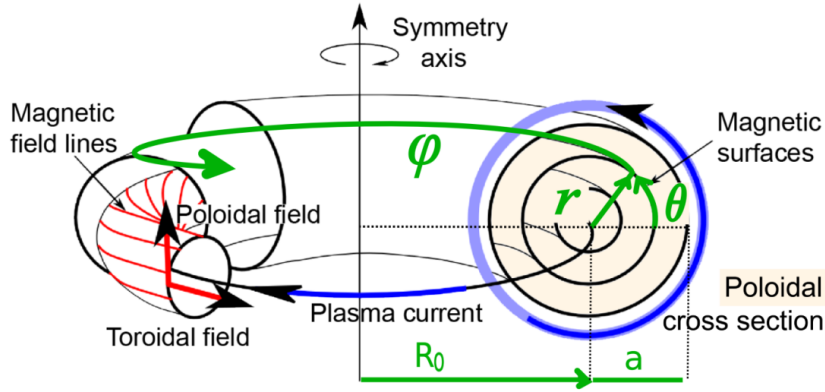
Figure 1.6: Magnetic surfaces in a tokamak

The magnetic surfaces are embedded into each other, as drawn in Fig. 1.6. In this particular case where the poloidal cross-section is circular, a magnetic surface can be characterized by its minor radius r. Yet in the general case, the poloidal magnetic flux, which is the magnetic flux in the poloidal direction averaged over the toroidal angle, is the adequate radial coordinate. As a tokamak is toroidally axisymmetric, the poloidal flux on a point P is given by:

$$\psi(P) = \int \int_{\Sigma_P} \boldsymbol{B} \cdot \boldsymbol{d\Sigma_P} \tag{1.4}$$

where Σ_P is the disk lying on P and whose axis is the axis of symmetry of the tokamak. ψ is constant over a given magnetic surface, thus each magnetic surface can be labeled by the value of ψ. In this thesis, we also use the normalized poloidal flux $\psi_N = \frac{\psi - \psi_{axis}}{\psi_{edge} - \psi_{axis}}$ which varies between 0 at the center and 1 at the plasma edge. In the same manner, the magnetic surfaces can be characterized by their helicity q given by

$$q = \frac{rB_\varphi}{RB_\theta} \tag{1.5}$$

The variables r and R are the radial coordinates along the minor (a) and major (R_0) radii, and B_φ and B_θ represent the toroidal and poloidal field. The surfaces where q can be written as $q = m/n$ with m and n integer correspond to the rational surfaces: a particle which follows (or more exactly gyrates around) a field line belonging to a rational surface will return to the same point after covering n toroidal turns and m poloidal turns. We will see in section 1.4 that these rational surfaces play a major role regarding the magnetic stability.

1.3 H-mode plasmas and Edge Localized Modes

1.3.1 H-mode

A regime of improved confinement was discovered in the ASDEX tokamak [Wagner 1982] in 1982, called H-mode for "high confinement". The H-mode is obtained more easily in an X-point configuration for the magnetic field, presented in Fig. 1.7: additional coils are used such that the poloidal field vanishes at a given position, resulting in an "X-point" magnetic structure. In this configuration, the magnetic surfaces are closed at the center of the plasma, up to the last closed flux surface called "separatrix"; over the separatrix, the field lines are open, in an area called the Scrape-Off Layer (SOL). The open field lines reach the Plasma Facing Components (PFC) called divertor, which is constituted of two actively-cooled target plates (in the inner and outer sides of the tokamak), specially designed in the aim of receiving high heat loads.
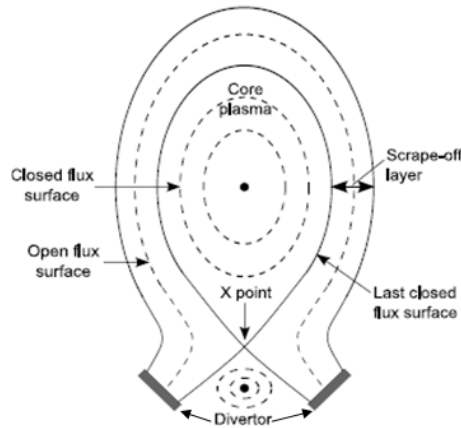
Figure 1.7: Poloidal section of the tomakak in X-point configuration

Contrary to the L-mode (for "low confinement") where the radial pressure profile – along the minor radius – is roughly parabolic (Fig. 1.8), the H-mode is characterized by a very steep pressure profile at the edge of the plasma, as if the pressure was set on a pedestal. This "pedestal" is formed due to the apparition of an external transport barrier (ETB). This induces a significant enhancement of the confinement, *i.e.* a higher density
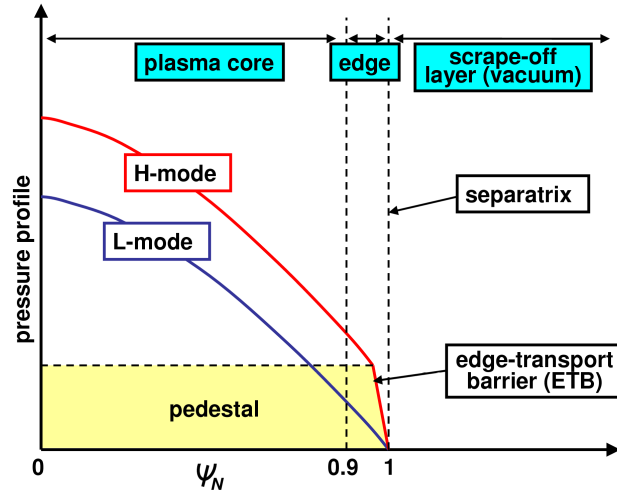
Figure 1.8: Radial pressure profile in L and H modes. The radial coordinate in x-axis is the normalized poloidal flux $\psi_N = \frac{\psi - \psi_{axis}}{\psi_{edge} - \psi_{axis}}$.

and temperature in the core. However the mechanisms governing the formation of the ETB and the L-H transition are not yet well understood.

1.3.2 Edge Localized Modes

1.3.2.1 Experimental observations

Usually in the experiments, after the L-H transition, three consecutive phases appear. First, small and frequent bursts ($\approx 100Hz - 2kHz$) of energy are expelled from the plasma and reach the divertor. These bursts are called "type-III ELMs" (for Edge Localized Modes). Second, as the injected power is increased, a burst-free quiescent period is observed, called "ELM-free period". Third, at further increased injected power, a period when large bursts are observed is reached [Sartori 2004]. These quasi-periodic bursts, called "type-I ELMs" or "giant ELMs", occur at a frequency of about $10 - 100Hz$. The ELM relaxations are best detected by the D_α signal, which is the measurement of the α-ray emissions occurring when the Deuterium is recycled, *i.e.* when it comes back to the plasma after reaching the divertor. Therefore the D_α signal gives a good estimate of the particle flux reaching the divertor and of the ELM duration and frequency. The D_α signal in blue in Fig. 1.9 clearly shows the three consecutive stages after the L-H transition (type-III ELMs, ELM-free H-mode and type-I ELMs) in a typical discharge of the JET tokamak.

A complete phenomenology of the ELMs occuring in the different tokamaks can be found in [Zohm 1996, Connor 1998, Suttrop 2000, Bécoulet 2003, Kamiya 2007]. ELMs are characterized by the quasi-periodic relaxation of the pressure pedestal profile in H-mode, associated with the expelling of energy and particles from the bulk plasma through the Edge Transport Barrier, as sketched in Fig. 1.10. In the case of type-I ELMs, an
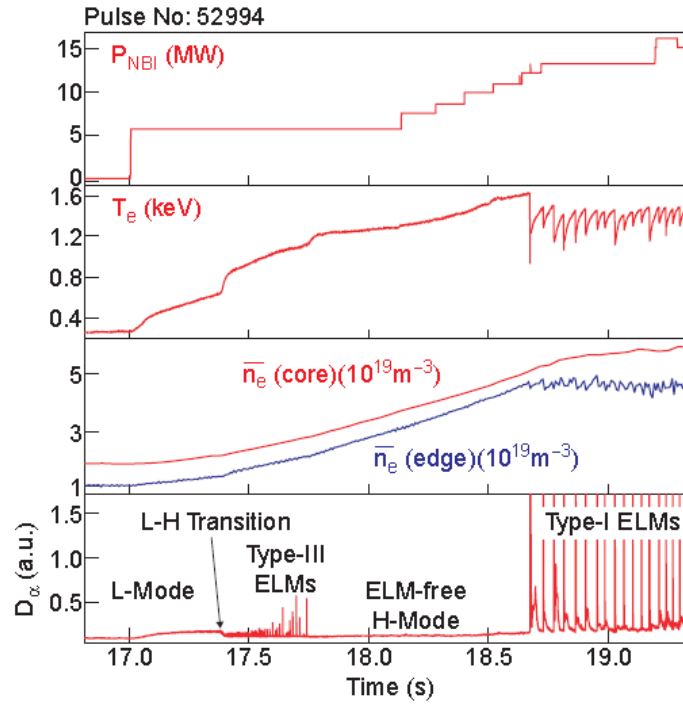
Figure 1.9: Typical L-H transition in the JET tokamak. From [Perez von Thun 2004]

ELM can expulse up to 15% of the pedestal energy from the bulk plasma. After the collapse of the pressure profile, the pedestal builds-up again until another ELM crash occurs, resulting in a cyclical dynamics.
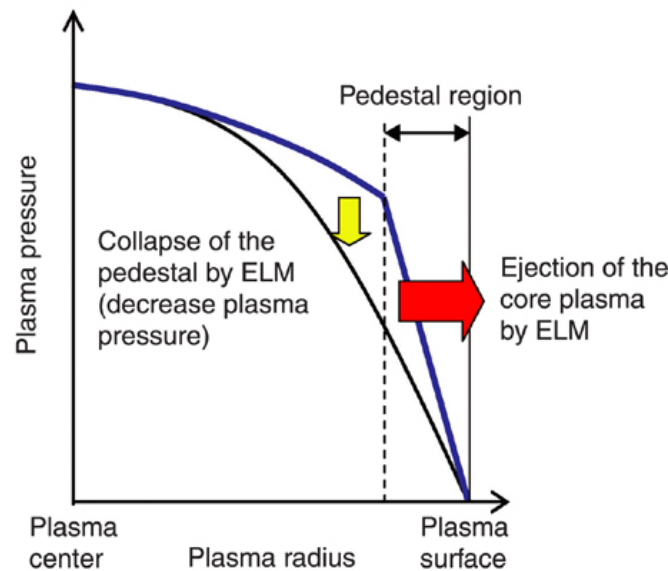
Figure 1.10: Pressure profile relaxation due to an ELM

Even though there is a complex and variable ELM zoology depending on the tokamaks and the plasma configuration, a general behaviour of the ELMs has been evidenced.

During an ELM cycle, the following steps have been identified. First, ELM precursors are growing and rotating, associated with the observation of magnetic precursors and temperature fluctuations observed with the Electron Cyclotron Emission (ECE) imaging [Classen 2013, Yun 2011, Dunai 2014, Kirk 2013b]. Due to the growth of the precursors, plasma filaments are formed first in the pedestal before they are ejected into the SOL. The shear of the plasma filaments was observed with the ECE diagnostic, and the three-dimentional filamentation was also observed in the experiments, e.g. in MAST with the fast camera, as presented in Fig. 1.11. The energy expelled from the pedestal then reaches the divertor target plates, resulting in a high heat load on the divertor, diagnosed among others by the D_α signal. After the ELM, a quiescent period can then be observed before the growing of another ELM precursor, and so on.
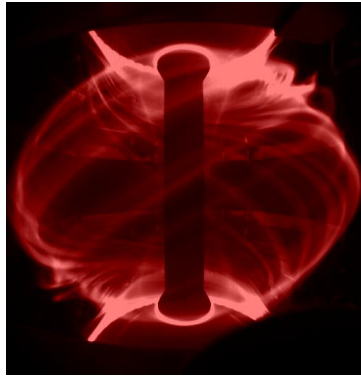
Figure 1.11: Plasma filaments during an ELM in MAST. From [Kirk 2006].

Theoretically, type-I ELMs are believed to be peeling-ballooning instabilities, and type-III ELMs (less clearly understood) are described either as pure peeling instabilities (in low density plasmas) or as resisitive peeling-ballooning instabilities, as detailed further in section 1.3.2.2. Experimentally, the main distinctions between type-I and type-III ELMs are the following: type-III ELMs expel less energy ($1-5\%$ of the plasma energy) through the ETB than type-I ELMs ($\sim 10-15\%$): thus the pedestal more quickly rebuilds after type-III ELM relaxations, which induces more frequent ELMs in the case of type-III (as described above). Moreover, the ELM frequency shows an opposite dependence on the applied heating power: the type-III ELM frequency decreases with the heating power, whereas the type-I ELM frequency increases [Zohm 1996]. As for the so-called "type-II" ELMs, they characterize small instabilities (even smaller than type-III ELMs) associated with small and frequent fluctuations of the pedestal, which are also observed in H-mode. However since the physics of type-II ELMs is not well understood, their designation may refer to different instabilities. Indeed, small high-n ballooning modes, occuring when a strong shaping of the plasma is achieved, as well as the ELMs mitigated by Resonant Magnetic Perturbations (section 1.4), are referred to as type-II ELMs, even though the underlying physics is different.

1.3.2.2 Theoretical understanding of the ELMs

The Edge Localized Modes have been theoretically identified as plasma magneto-hydro dynamic (MHD) instabilities triggered either by the large edge pressure gradient (so-called "ballooning modes") or by the large edge current (so-called "peeling modes") present in H-mode. MHD is a fluid description of the magnetized plasma, presented further in section 2.2, which is believed to be accurate to describe fast large scale instabilities such as ELMs. The linearization of the MHD equations *Eqs.* (2.9-2.12) around an equilibrium state, while assuming that resistivity is negligible (ideal MHD), allows for expressing all the variables (density, temperature, magnetic flux, velocity) as a function of the plasma displacement ξ. We can then express the potential energy δW as an only function of ξ. The so-called "energy principle" states that the plasma is stable if δW is positive for any displacement ξ [Freidberg 1982]. δW is calculated as an integral on the domain including the plasma, surrounded by a vacuum region, itself surrounded by an ideally conducting wall. δW is thus expressed as the sum of the plasma ("P"), the vacuum ("V") and the plasma-vacuum interface ("S" for surface) components:

$$\delta W = \delta W_P + \delta W_V + \delta W_S \tag{1.6}$$

The vacuum and surface terms are always positive, thus their contribution is only stabilizing. So we can only consider the plasma component, expressed as ([Freidberg 1982]):

$$\delta W_P = \frac{1}{2} \int \int \int_P \Big(\frac{|\boldsymbol{Q}_\perp|^2}{\mu_0} + \frac{B^2}{\mu_0}|\nabla \cdot \boldsymbol{\xi}_\perp + 2\boldsymbol{\xi}_\perp \cdot \boldsymbol{\kappa}|^2 + \gamma P |\nabla \cdot \boldsymbol{\xi}|^2$$
$$- (\boldsymbol{\xi}_\perp \cdot \nabla P)(2\boldsymbol{\xi}_\perp^* \cdot \boldsymbol{\kappa}) - j_{||}(\boldsymbol{\xi}_\perp^* \times \boldsymbol{b}) \cdot \boldsymbol{Q}_\perp \Big) dV \tag{1.7}$$

$\boldsymbol{Q}$ is the linear perturbation of the magnetic field $\boldsymbol{B}$, $\boldsymbol{\kappa}$ is the curvature of the equilibrium magnetic field, $\gamma = 5/3$ is the adiabatic index (ratio of the specific heats), P is the plasma pressure, $j_{||}$ is the parallel current density and μ_0 is the vacuum permeability. The $||$ and $\perp$ symbols respectively designate the parallel and perpendicular components (with respect to the equilibrium magnetic field), and stars designate the complex conjugate quantities. The first term represents the energy associated with the bending of the magnetic field lines and it is the dominant term for the shear Alfvén wave. The second term represents the energy associated with the compression of the magnetic field and is dominant for the compressional Alfvén wave. The third term represents the energy associated with the compression of the plasma, it is the main source of energy for the sound wave. Those three terms are always positive and therefore stabilizing. The remaining two terms have indefinite sign and are the ones that drive the instabilities, one is proportional to the pressure gradient and will be associated with pressure-driven modes, the other is proportional to $j_{||}$ and is associated with current-driven modes.

In the framework of ideal MHD, it was shown that type-I ELMs are ideal instabilities driven both by the pressure gradient ("ballooning modes") and the parallel current ("peeling modes") in the pedestal [Snyder 2004, Zohm 1996, Huysmans 2007]. The ideal stability boundary of an ELM can thus be plotted in a $(\nabla P, j)$ diagram, called 'peeling-
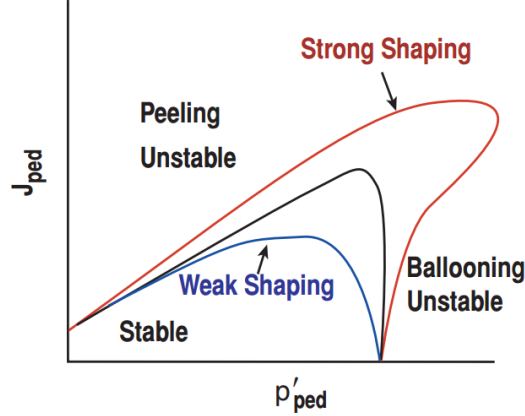
Figure 1.12: Peeling-ballooning diagram showing the stability limit of an ELM. Fig. from [Snyder 2004].

ballooning" (or P-B) diagram (an example is given in Fig. 1.12).

As for the type-III ELMs, they are regarded either as peeling modes (occuring at large current but rather low density and thus low pressure gradient) or as resistive peeling-ballooning instabilities. In the framework of the resistive MHD, "resistive type-III ELMs" are found to be driven by the edge pressure gradient ("resistive ballooning modes") and the parallel current ("peeling modes"), similarly to type-I ELMs [Sartori 2004].

So for both type-I and type-III ELMs, the cyclical dynamics is theoretically understood as follows: the edge pressure gradient and/or the edge current – whose bootstrap component is proportional to the pressure gradient – increase with the applied heating power. When the ideal (for type-I) or resistive (for type-III) P-B stability boundary is crossed, an ELM (P-B instability) is triggered. Thus the instability grows until the relaxation of the profiles occurs, bringing back the plasma to the stable region. Then the applied heating power progressively rebuilds the pedestal. The pedestal reconstruction increases again the edge current and pressure gradient, until the P-B boundary is crossed another time, generating another ELM. This theoretical interpretation proved to be consistent with the experimental observations above mentionned.

1.4 ELM control

1.4.1 Extrapolation of the ELM size in ITER

Owing to its good confinement properties, the ELMy H-mode configuration has been chosen as reference mode of operation for ITER [Shimada 2007]. Thus several studies have estimated the size that type-I ELMs should have in ITER (the type-I are a bigger concern than the other ELM types since they induce the largest heat loads on PFCs). In particular, the amount of energy released from the pedestal during an ELM ΔW_{ELM} has been estimated to depend on the electron pedestal collisionality ν^*, given by $\nu^* = q_{95}R_0\varepsilon^{-3/2}/\lambda_{e,e}$, where q_{95} is the safety factor at the edge (for $\psi_N = 95\%$), $\varepsilon = r/R_0$ is the

inverse aspect ratio and $\lambda_{e,e}$ is the electron-electron collision mean free path [Loarte 2002]. Fig. 1.13 shows a clear scaling of ΔW_{ELM} normalized against the pedestal energy W_{ped} with respect to the collisionality: ΔW_{ELM} increases when ν^* is decreased. In ITER, ν^* is foreseen to be rather low (~ 0.1) thus the energy load on the divertor due to an ELMs could reach up to 15% of the pedestal energy ($W_{ped} = 110J$), so $\Delta W_{ELM} = 17MJ$ [Loarte 2003]. Laboratory experiments have reproduced the heat load that ELMs would generate on the ITER divertor: over $1MJ$, the Tungsten tiles of the divertor might melt, as shown in Fig. 1.14. This means that uncontrolled ELMs would drastically reduce the divertor life time; therefore the ELM control (either mitigation or suppression) will be mandatory in ITER and future reactors [Hawryluk 2009].
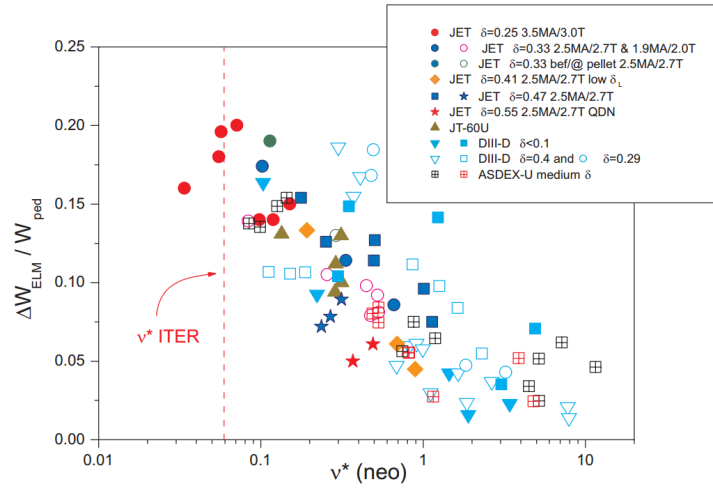
Figure 1.13: ELM energy ΔW_{ELM} divided by the pedestal energy W_{ped} as a function of the collisionality ν^* in existing tokamaks, and predicted value for ITER. Plot from [Loarte 2003].

Figure 1.14: Melted Tungsten divertor after an ITER-like ELM. Picture from [Linke 2007].

However, the ELMs also have a beneficial role: they are able to flush the impurities and fusion ashes out of the plasma. As the impurities are likely to be at the origin of other instabilities like disruptions, this beneficial role is not negligible. Therefore the question if the ELMs have to be either suppressed or mitigated is an important question.

A first step towards the answer is to find reliable mitigation/suppression techniques and to understand their physical mechanism.

1.4.2 ELM control techniques

Three ELM-control methods have been successfully tested in the current tokamaks. Two methods allow for mitigating the ELMs: they are likely to induce smaller ELM relaxations and thus smaller transient heat loads on the divertor.

- First, the repetitive injection of D-D or D-T ice pellets in the plasma [Lang 2007, Pégourié 2007, Baylor 2009] aims at locally increasing the pressure gradient in the area where the pellet ablation occurs: thus, the plasma locally becomes peeling-balooning unstable, and ELMs are triggered by the pellet injection. The goal is to trigger more frequent but smaller ELMs, at the frequency of the pellet injection. If the pellet injection frequency is larger than the natural ELM frequency, the ELMs triggered by pellets will be more frequent and thus the energy loss per ELM will be reduced. This method presents the double advantage of controlling the ELM frequency and to provide the particle fueling of the plasma, provided the 'fuel" can penetrate deep into the core. However the mechanism of the pellet ablation in the plasma depending on the pellet size and the speed and position of the injection is not yet fully understood: research is on the way to improve the system.

- Second, fast vertical displacements of the plasma, called "vertical kicks" [Degeling 2003, Gerhardt 2010], can be periodically induced by the modification of the magnetic field in the coils dedicated to the control of the vertical plasma position. The periodical vertical plasma displacement is likely to perturb the magnetic field and thus trigger ELMs at the frequency of the "kicks". As for the pellet injection, high frequency kicks induce more frequent but smaller ELMs, which results in a lower peak power deposition on divertor. The major drawback of this method is that it may lead to trigger instabilities called "vertical displacement events" which can potentially induce a total loss of confinement.

- This thesis focuses on the third promising method: the ELM control by Resonant Magnetic Perturbations (RMPs). Contrary to the two first methods, RMPs can not only induce the ELM mitigation, but also the total ELM suppression. The RMP technique consists in applying small non-axisymmetric magnetic perturbations (of the order of 10^3 or 10^4 lower than the total magnetic field), using dedicated coils called "RMP coils". This concept, which aims at generating a stochastic region at the plasma boundary, drew inspiration from the ergodic divertor experiments in the Tore Supra tokamak [Ghendrih 1996] and was first proposed for DIII-D in [Grosman 2003]. It proved to be successful in either suppressing the ELMs in the DIII-D [Evans 2004a, Fenstermacher 2008, Evans 2008], ASDEX Upgrade [Suttrop 2011] and KSTAR tokamaks [Jeon 2012] or in mitigating the ELM power in JET [Liang 2007a], MAST [Kirk 2010] and NSTX [Canik 2010], which validated its use for ITER operation. Depending on the RMP coil geometry, a toroidal wave

number of the magnetic perturbation $n = 1, 2, 3, 4$ or 6 is applied. In ITER, 3 rows of 9 coils (presented in Fig. 1.15) are designed and foreseen to apply a $n = 3$ or $n = 4$ toroidal perturbation [Hawryluk 2009]. The concept of this method is described in more detail in the next section.

In ITER, both pellet and RMP methods are foreseen to be used to control ELMs [Hawryluk 2009]. As for the vertical kicks, they might also be used in ITER, e.g. during the plasma current ramp-up [De la Luna 2009].
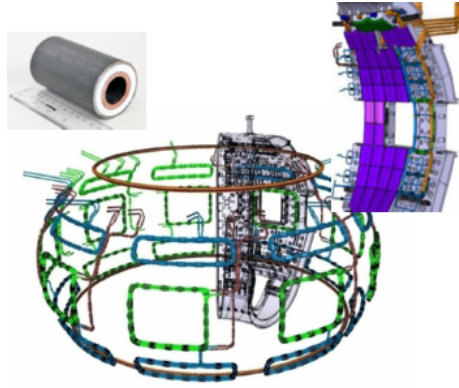
Figure 1.15: 3 rows of 9 RMP coils designed for ITER

1.4.3   ELM control by RMPs

When the plasma is at equilibrium, the magnetic surfaces are nested into each other, and the field lines close on themselves on the rational surfaces $q = m/n$ located inside the separatrix (m and n being the poloidal and toroidal mode numbers, as defined in section 1.2). The transport of heat and particles principally follows the magnetic field line: the parallel transport along the magnetic field is around 10^6 times larger than the perpendicular transport.

However when a magnetic perturbation is applied, the magnetic field lines deviate radially, which induces magnetic island chains on the rational surfaces – also called resonant surfaces –, as plotted on Fig. 1.16. In this schematic example, $n = 1 - 2$ magnetic perturbations generate the formation of magnetic islands on the surfaces $q = 2/1$ and $q = 3/2$. At rather low perturbation (Fig. 1.16 (a)), the two consecutive island chains do not interfere. Yet at larger applied perturbation (Fig. 1.16 (b)), the two island chains overlap, which generates a chaotic (also called ergodic or stochastic) magnetic field between the two rational surfaces. In the stochastic region, the magnetic field lines are no more defined. Thus this region with "broken" field lines is characterized by a largely enhanced radial transport of heat and particles. Since type-I ELMs are mostly triggered by the large edge pressure gradient in H-mode, the aim of the RMPs is thus to generate an ergodic region at the edge (in the pedestal) in order to enhance the radial transport ans subsequently to slightly reduce the edge pressure gradient under the ELM-triggering threshold.
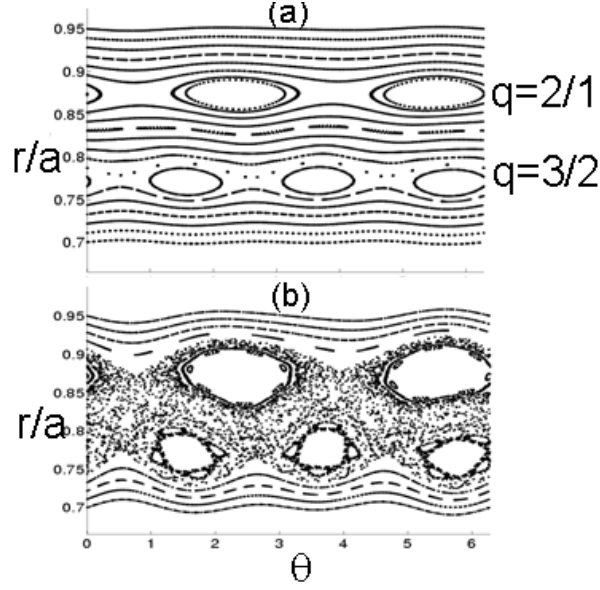
Figure 1.16: Magnetic topology at low (a) and high (b) magnetic perturbation: island chains are formed on the rational surfaces $q = 2/1$ and $q = 3/2$. For a large perturbation (b), the two rows of islands overlap which generate an ergodic magnetic field in between. The x- and y-axes respectively follow the poloidal angle θ and the radial direction r/a, with the definitions given in Fig. 1.6.

The ELM suppression by RMPs was first obtained in DIII-D [Evans 2004a]. Fig. 1.17 shows that depending on the intensity of the applied magnetic perturbation, RMPs can induce either the ELM mitigation (under a threshold in RMP current) or the full ELM suppression (over a threshold in current applied in RMP coils).

A single criterion was established to predict when there should be ELM suppression by RMPs. The magnetic field induced by a toroidal n perturbation was calculated in the vacuum with Biot-Savart law. (Note that usually the RMP coils are disposed so that a single n number is dominant, contrary to the example given in Fig. 1.16.) Then the level of ergodization was usually characterized by the Chirikov parameter σ, calculated as follows ([Nardon 2007]):

$$\sigma = \frac{\delta_{m,n} + \delta_{m+1,n}}{\Delta_{m,m+1}} \tag{1.8}$$

$\delta_{m,n}$ is the half-width (in the radial direction) of an island of the surface $q = m/n$, expressed as :

$$\delta_{m,n} = \left(\frac{8q^2 |b^1_{m,n}|}{mq'} \right)^{1/2} \tag{1.9}$$

where $b^1_{m,n}$ is the (m, n) Fourier harmonic of the radial perturbation of the magnetic field $b^1 = \frac{\boldsymbol{B} \cdot \nabla \psi^{1/2}}{\boldsymbol{B} \cdot \nabla \varphi}$ on the resonant surface, and $q' = dq/d\psi^{1/2}$ is the magnetic shear. $\Delta_{m,m+1}$ is the distance between the two consecutive rational surfaces $q = m/n$ and $q = (m+1)/n$, approximately given by: $\Delta_{m,m+1} = \frac{q}{mq'}$. Thus the larger the magnetic perturbation is induced on the rational surfaces, the more magnetic islands grow, since the island size
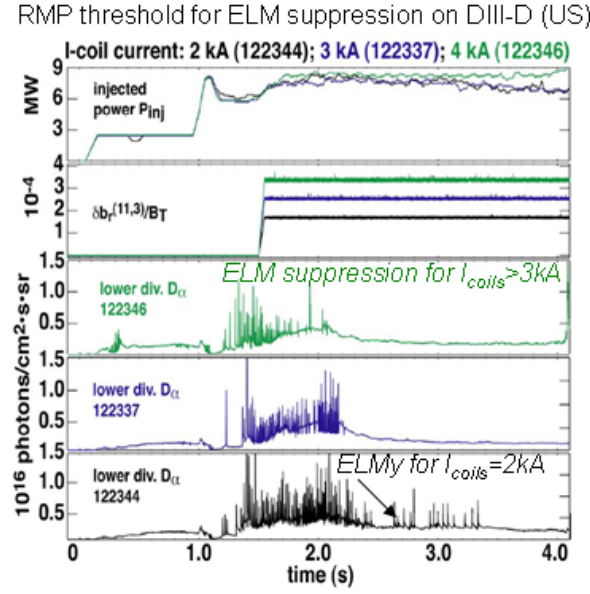
Figure 1.17: Application of the RMPs in DIII-D. For a sufficient current I in the RMP coils ($I > 3kA$, in blue and green), ELMs were suppressed (no D_α burst). For $I = 2kA$, ELMs are only mitigated. From [Evans 2008].

is proportional to the square root of the magnetic perturbation. For a sufficiently large magnetic perturbation, the islands exceed a critical size (corresponding to the Chirikov parameter equals to 1), thus the magnetic island chains overlap and an ergodic field is induced by RMPs. So for a sufficiently large current applied in RMP coils, it was thought that if $\sigma > 1$ then the ELMs could be suppressed by RMPs [Fenstermacher 2008].
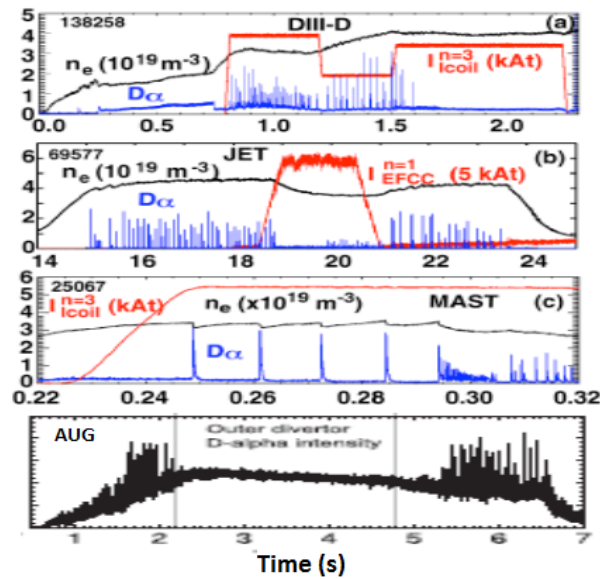
Figure 1.18: Effect of the RMPs on ELMs for a same vacuum-like ergodization in different tokamaks. Fig. adapted from [Fenstermacher 2010] and [Suttrop 2011].

However the physics at stake is actually found to be much more complicated. For a same level of ergodization calculated in the vacuum, the RMP application, tested on several tokamaks, leads to different results Fig. 1.18: whereas the ELM suppression by RMPs was obtained in DIII-D (a) and AUG (d), "only" the ELM mitigation was obtained in JET (b), and on the contrary ELMs were triggered by RMPs in MAST (c) [Fenstermacher 2010, Liang 2007a, Suttrop 2011]. This panel of different results is due to the fact that the level of ergodization was calculated for a vacuum magnetic field perturbation: thus it shows that the plasma response to RMPs has to be considered to accurately assess the effect of RMPs. This motivates the in-depth investigation among the fusion community, looking for the theoretical understanding of the plasma response to RMPs: [Fitzpatrick 1998, Heyn 2008, Bécoulet 2008, Izzo 2008, Strauss 2009, Nardon 2010, Liu 2010b, Yu 2011, Bécoulet 2012, Ferraro 2012, Waelbroeck 2012, Orain 2013].

As for the experimental results, which have been prolific as well during the last decade, a brief non-exhaustive overview can be given. Generally, a different mechanism of the ELM mitigation by RMPs was found depending on the electron collisionality ν^*. In DIII-D, the ELM suppression was obtained at low ν^* with a maximum ($n = 3$) resonant MP spectrum (in even parity). The ELM suppression was associated with a strong density pump-out induced by RMPs: the pedestal density is reduced by $\approx 20\%$, which implies a small degradation of the confinement. The low collisionality is besides due to the low density. However, at high collisionality, ELMs are "only" mitigated by RMPs (in odd configuration: with a non-resonant MP spectrum). Mitigated ELMs correspond to small type-II ELMs, characterized by small magnetic fluctuations and small density oscillations at the edge; yet no density pump-out is observed. In both low/high ν^* cases, RMPs have little or no effect on the temperature profile [Osborne 2005, Moyer 2005]. In JET, when a ($n = 1 - 2$) spectrum is applied by Error field correction coils (EFCCs), this distinction between high and low ν^* is also observed: at low ν^*, even though the ELM suppression is not obtained, the ELMs mitigation is observed, associated with density pump-out. Yet at high ν^*, type-I ELMs are replaced by small high-frequency ELMs ($f \sim 0.2 kHz$) without density pump-out, similarly to the DIII-D observations at high ν^* [Liang 2007a, Liang 2012]. In AUG, a threshold in density (and thus maybe in collisionality) is observed: at high density, the type-I ELMs have been suppressed by ($n = 3$) RMPs and replaced by small fluctuations. No density pump-out was induced by RMPs [Suttrop 2011]. This regime might be similar to the high ν^* regime in DIII-D, but it does not seem to depend on the resonant/ non resonant MP spectrum applied. However the ELM suppression by RMPs was not found at low density, until recently: depending on the phase of the applied RMPs, the ELM mitigation with pump-out could be observed at low density/low collisionality during the 2014 experimental campaign [Suttrop 2014, Kirk 2014].

1.5 Thesis plan

The aim of this thesis is to study numerically the ELMs and RMPs, while self-consistently taking into account the plasma response. In numerical simulations, the plasma parameters are taken as close as possible to the experimental configuration, using JET, DIII-D and MAST data. The parameters foreseen for the ITER standard scenario are also used to give "predictions" for ITER.

In chapter 2, the reduced extended MHD model implemented in the JOREK code [Huysmans 2009], including the newly added effects to self-consistently describe the plasma flows [Orain 2013], is presented. As well, the numerical tools used for the simulation runs with JOREK will be introduced. Then the three following chapters will present respectively the simulations of:

- the RMP penetration into the plasma (without ELMs).

- the ELM dynamics without RMPs.

- the interaction between ELMs and RMPs.

Concerning the RMP penetration, the current understanding is that depending on plasma parameters, and particularly on the plasma rotation, RMPs can be either screened or amplified. So the interaction between plasma flows has to be carefully studied and understood to make reliable predictions for ITER. Thus the interaction between plasma flows and RMPs (without ELMs) will be first described in chapter 3. This chapter will be introduced by simulations performed in simplified cylindrical geometry for DIII-D parameters with the Reduced MHD code RMHD [Bécoulet 2012]. These cylindrical simulations will allow to present the generic features of the plasma response to RMPs and the importance of several plasma parameters. Then JOREK simulations of the interaction between RMPs and plasma flows will be presented in realistic toroidal geometry successively for JET, MAST and ITER parameters [Orain 2013].

Furthermore, before studying the impact of RMPs on ELMs, it is worth considering the ELM dynamics alone. In chapter 4, simulations of the ELM dynamics will be presented for a JET configuration. The impact of the flows on this ELM dynamics – precursors, filaments, power reaching the divertor – will be stressed. Moreover, we will present the first reproduction of the cyclical ELM dynamics obtained in modeling, and show that the introduction of the realistic flows in the model allows for obtaining the ELM cycles.

Last, the modeling of the interaction between ELMs and RMPs will be presented in chapter 5. The first simulations of the ELM mitigation and ELM suppression by RMPs will be shown in a JET case. The mechanism of the ELM mitigation by RMPs will be carefully described.

Physical model and numerical tools

Contents

2.1   Aim of the chapter

The ELM and RMP simulations are performed with the JOREK code which resolves a system of reduced MHD equations. This chapter aims first at describing the initial model used in JOREK [Huysmans 2009] and the main hypotheses made to develop the set of equations. Then the new effects introduced in the model in order to obtain a self-consistent description of the plasma flows and of the radial electric field – namely the diamagnetic bi-fluid effects, the neoclassical effects and a source of parallel rotation – are presented. Third, the boundary conditions are described, which are important since they affect e.g. the plasma flows and the RMP penetration. Last, the different steps of a JOREK computation are given, with a description of the numerical tools used during these steps.

2.2   Reduced Magneto-Hydro Dynamic model

2.2.1   MHD equations

In plasma physics, two different approaches are used to describe the plasma dynamics: the kinetic and the fluid approaches. In the kinetic description, the Boltzmann equation

is solved for the probability distribution function of each species s (ions and electrons):

$$\frac{\partial f_s}{\partial t} + \boldsymbol{u} \cdot \nabla f_s + \frac{q_s}{m_s}(\boldsymbol{E} \times \boldsymbol{B}) \cdot \nabla_u f_s = \left(\frac{\partial f_s}{\partial t}\right)_{coll} \tag{2.1}$$

$f_s(\boldsymbol{r}, \boldsymbol{u}, t)$ is the probability distribution function as a function of the position $\boldsymbol{r}$, the particle velocity $\boldsymbol{u}$ and the time t; q_s and m_s are respectively the charge and mass of the species s.

$\left(\dfrac{\partial f_s}{\partial t}\right)_{coll}$ is the collision operator which denotes the friction between particles.

This 6-dimensional equation is coupled to the Maxwell equations describing the evolution of the electric $\boldsymbol{E}$ and magnetic $\boldsymbol{B}$ fields:

$$\nabla \cdot \boldsymbol{E} = \frac{\sigma}{\varepsilon_0} \tag{2.2}$$

$$\nabla \cdot \boldsymbol{B} = 0 \tag{2.3}$$

$$\nabla \times \boldsymbol{E} = -\frac{\partial \boldsymbol{B}}{\partial t} \tag{2.4}$$

$$\nabla \times \boldsymbol{B} = \mu_0 \boldsymbol{J} + \frac{1}{c^2}\frac{\partial \boldsymbol{E}}{\partial t} \approx \mu_0 \boldsymbol{J} \tag{2.5}$$

where σ and J are the charge and current densities, μ_0 is the magnetic permeability, ε_0 the vacuum permittivity and c the light speed. Even though *Eq.* (2.1) can be reduced to a 5-dimensional equation by averaging the motion of particles around the gyrocenter, the resolution of kinetic – or gyrokinetic – equations is very expensive in term of computational time. Thus this approach is generaly used to describe small-scale phenomena, such as the plasma turbulence, which affects the quality of the confinement.

However, to study larger scale phenomena affecting the stability of the plasma, such as ELMs, we rather use the framework of the magnetohydrodynamics, which is a fluid approach. MHD equations are obtained by taking the moments of the Boltzmann equation – *i.e.* multiplying by powers of $\boldsymbol{u}$ and integrating over the whole velocity space – as well coupled to the Maxwell equations *Eqs.* (2.2-2.5).

The fluid quantities, namely the density n, the fluid velocity $\boldsymbol{v}$ and the pressure tensor $\bar{P}$, are defined from the distribution function as follows:

$$n_s = \int f_s d^3\boldsymbol{u} \tag{2.6}$$

$$\boldsymbol{v}_s = \frac{1}{n_s} \int \boldsymbol{u} f_s d^3\boldsymbol{u} \tag{2.7}$$

$$\bar{P}_s = \int m_s(\boldsymbol{u} - \boldsymbol{v}_s) \times (\boldsymbol{u} - \boldsymbol{v}_s) f_s d^3\boldsymbol{u} \tag{2.8}$$

The pressure tensor can be decomposed into the scalar pressure P and the stress tensor $\bar{\bar{\Pi}}_i$, which contains the anisotropic and off-diagonal terms of the pressure tensor: $\bar{P} = P\bar{I} + \bar{\bar{\Pi}}_i$, where $\bar{I}$ is the identity tensor. We also define the mass density of a species $\rho_s = m_s n_s$ and the fluid mass density $\rho = m_i n_i + m_e n_e$.

The integration of Boltzmann equation (*Eq. (2.1)*) over the velocity space for a species s and summed over both species (electrons+ions) yields the continuity equation:

$$\frac{\partial \rho}{\partial t} + \nabla \cdot (\rho \boldsymbol{v}) = 0 \tag{2.9}$$

If there is no creation of particles, the integration of the collision operator over velocity space is indeed zero.

Multiplying *Eq. (2.1)* by $\boldsymbol{u}$ and integrating over the velocity space yields the momentum equation (summed over both species):

$$\rho \frac{\mathrm{d}}{\mathrm{d}t} \boldsymbol{v} = \boldsymbol{J} \times \boldsymbol{B} - \nabla P - \nabla \cdot \bar{\Pi}_i \tag{2.10}$$

where the *convective derivative* is defined as $\frac{\mathrm{d}}{\mathrm{d}t} = \left(\frac{\partial}{\partial t} + \boldsymbol{v} \cdot \nabla \right)$ and the plasma current is given by $J = \sum_s n_s q_s \boldsymbol{v}_s$. Since we consider only the ion-electron and electron-ion collisions, the integrated collision operator for ions and electrons $\boldsymbol{R}_{ie}$ and $\boldsymbol{R}_{ei}$ are opposite: they translate the momentum transfer from a species to the other, thus their sum vanishes.

Multiplying *Eq. (2.1)* by $\boldsymbol{u^2}$ and integrating gives the energy equation. However, we notice that each equation involves the moment at the next order: the continuity equation involves velocity, the momentum equation involves pressure, and on the same way, the energy equation involves the third order moment (the heat flux), and so on. Therefore a closure is necessary to solve the equations. A common closure, used in the JOREK code, is to assume that the system is adiabatic. This way, the energy equation is written as:

$$\frac{\mathrm{d}}{\mathrm{d}t} \left(\frac{P}{\rho^\gamma} \right) = 0 \tag{2.11}$$

where $\gamma = 5/3$ is the ratio of the specific heats. Note that numerous closures have been developed in litterature, which depend on the physics the model aims at addressing. The adiabatic closure is a simplified version of the Braginskii closure for the energy equation [Braginskii 1965], derived in appendix B.4. To these three equations (*Eqs. (2.9-2.11)*), a fourth equation is added to complete the MHD equations. This fourth equation is the Ohm's law, obtained by coupling the momentum equation for electrons with the Maxwell equations:

$$\boldsymbol{E} = -\frac{\partial \boldsymbol{A}}{\partial t} - \nabla \phi = -\boldsymbol{v} \times \boldsymbol{B} - \eta \boldsymbol{J} \tag{2.12}$$

where $\boldsymbol{A}$ and ϕ are respectively the vector and scalar potential, and η is the resistivity defined as

$$\eta = \frac{m_e}{n_e e^2 \tau_e} \tag{2.13}$$

τ_e being the electron collision time. The "ideal MHD" assumes that the resistivity is negligible ($\eta = 0$). Using this approximation, the linearization of the ideal MHD allows to obtain the form of the energy principle given in section 1.3.2.2. However, the "resistive MHD", which does not neglect the resistivity, is more complex but more realistic. The

framework of resistive MHD is used in JOREK.

The full derivation of the MHD equations can be found e.g. in [Goedbloed 2004]. As described in section 2.2.2, *ad hoc* terms of diffusion (of heat and particle, corresponding to the Fick's law), the classical viscosity (considering the plasma as a newtonian fluid) as well as sources (of heat, particle and parallel momentum) are added into the resistive MHD equations. These terms must be added in MHD codes both to give a phenomenological description of the transport (even though the transport is studied more accurately in the kinetic description) and for numerical reasons: diffusion and viscosity allow for suppressing small structures that cannot be numerically resolved in MHD codes.

It is important to note that several assumptions have been made to obtain the set of MHD equations:

- MHD as well as most fluid descriptions of the plasma are valid for collisional plasmas. Indeed, the closure of the moments of the Botzmann equation at the second order is a good approximation of the kinetic equations if the higher moments are negligible. So when we neglect the higher moments, we suppose that the distribution function is rather well described by the two first moments and the closure is done assuming that the distribution function is close to a Maxwellian. This implies that the plasma is highly collisional: collisions relax the perturbed distribution function to a Maxwellian in a timescale smaller than the thermal propagation time of the plasma. This is expressed by the inequality: $v_{th,s}\tau_s/a << 1$.

- The approximation made in *Eq.* (2.5) corresponds to the hypothesis that the thermal velocities are non-relativistic: $v_{th,s} << c$, which is the case in the phenomena described by our MHD simulations.

- The electron inertia is neglected compared to the ion inertia, since $m_i/m_e >> 1$. Thus the fluid mass density $\rho = m_i n_i + m_e n_e \approx m_i n_i$ and the fluid velocity $\boldsymbol{v}$ is approximately equal to the ion velocity $\boldsymbol{v}_i$.

- The quasineutrality of the plasma is assumed, ensuring that:

$$n = n_e = n_i \tag{2.14}$$

This means that the electron and ion density are locally equal, which is true if we consider a "portion" of the plasma whose characteristic length is much larger than the Debye length $\lambda_d \sim 10^{-5} m$, corresponding to the distance over which the electrostatic potential of a particle is "not seen" by the surrounding particles. In our simulations, the space is discretized into elements which are actually much larger than λ_d.

2.2.2 Reduction of the equations

In order to simplify the resistive MHD model (the final aim being to reduce the computational time as much as possible), the MHD equations are reduced into a set of scalar

equations. The reduced MHD model implemented in JOREK [Huysmans 2009] is inspired from the four-field model [Strauss 1997]. First, in the framework of the reduced MHD, we assume that the toroidal magnetic field is constant in time and that the poloidal magnetic field is smaller than the toroidal component (which is actually the case in tokamaks). The magnetic field is therefore decomposed in toroidal and poloidal components as follows:

$$\boldsymbol{B} = F_0 \nabla\varphi + \nabla\psi \times \nabla\varphi \tag{2.15}$$

with $\dfrac{B_{pol}}{B_\varphi} = \dfrac{|\nabla\psi|}{F_0} << 1$. φ is the toroidal angle, ψ is the poloidal flux defined in Eq. (1.4) and $F_0 = R_0 B_{\varphi 0}$ is approximately constant; R_0 is the major radius and $B_{\varphi 0}$ is the toroidal magnetic field amplitude at the magnetic axis. In the reduced model, the toroidal component of the vector potential given by $\boldsymbol{B}_{pol} = \nabla \times \boldsymbol{A}$ is also considered to be dominant over the poloidal components, thus:

$$\boldsymbol{A} = A_\varphi \boldsymbol{e}_\varphi = \frac{\psi}{R}\boldsymbol{e}_\varphi \tag{2.16}$$

As for the velocity $\boldsymbol{v}$, it is decomposed into the parallel and poloidal component. Thus the reduced MHD equations solved in JOREK are the continuity equation *Eq.* (2.9), the parallel and perpendicular projection of the momentum equation *Eq.* (2.10), the energy equation *Eq.* (2.11) and the projection of the Ohm's law *Eq.* (2.12) in the toroidal direction. The unknowns of the 5 equations are respectively the mass density ρ, the parallel (ion) velocity $v_{\|,i}$, the electric potential u, the temperature T and the magnetic flux ψ. Note that in the model used in this thesis, the electron and ion temperatures T_e and T_i are assumed to be equal ($= T$). The semi-developed form of the equations, normalized in JOREK units (the normalizations are described below), is the following:

$$\frac{\partial\rho}{\partial t} = -\nabla(\rho\boldsymbol{v}) + \nabla \cdot (D_\perp \nabla_\perp \rho) + S_\rho \tag{2.17}$$

$$\rho\frac{F_0}{R}\frac{\partial v_{\|,i}}{\partial t} = \boldsymbol{b} \cdot \Big(-\rho(\boldsymbol{v}\cdot\nabla)(\boldsymbol{v}_{\|,i} + \boldsymbol{v}_E)) - \nabla P$$
$$- \bar{\nabla} \cdot \bar{\Pi}_{i,neo} \Big) + \mu_\| \Delta v_{\|,i} + S_{v_\|} \tag{2.18}$$

$$\boldsymbol{e}_\varphi \cdot \nabla \times \Big(\rho\frac{\partial\boldsymbol{v}_E}{\partial t} = -\rho(\boldsymbol{v}\cdot\nabla)(\boldsymbol{v}_{\|,i} + \boldsymbol{v}_E)$$
$$+ \boldsymbol{J} \times \boldsymbol{B} - \nabla P - \bar{\nabla}\cdot\bar{\Pi}_{i,neo} + \mu_\perp \Delta v \Big) \tag{2.19}$$

$$\rho\frac{\partial T}{\partial t} = -\rho\boldsymbol{v}\cdot\nabla T - (\gamma - 1)P\nabla\cdot\boldsymbol{v} + \frac{1}{2}v^2 S_\rho$$
$$+ \nabla \cdot (\kappa_\| \nabla_\| T + \kappa_\perp \nabla_\perp T) + (1 - \gamma)S_T \tag{2.20}$$

$$\frac{1}{R^2}\frac{\partial\psi}{\partial t} = -\boldsymbol{B}\cdot\nabla_\| u + \frac{\tau_{IC}}{\rho}\boldsymbol{B}\cdot\nabla_\| P + \frac{\eta J}{R^2} \tag{2.21}$$

where the parallel gradient is defined as

$$\nabla_{\parallel}\alpha = (\boldsymbol{B}/B^2)\boldsymbol{B}\cdot\nabla\alpha$$
$$= \frac{\boldsymbol{b}}{B}\Big(\frac{F_0}{R^2}\partial_\varphi\alpha + \nabla\varphi\cdot\nabla\alpha\times\nabla\psi\Big) \qquad (2.22)$$

To these 5 equations, 2 simple equations are added for the toroidal current j and the toroidal vorticity W:

$$j = -R^2\boldsymbol{J}\cdot\nabla\varphi = -R^2\nabla\times\boldsymbol{B}\cdot\nabla\varphi = \Delta^*\psi \qquad (2.23)$$

$$W = \nabla\varphi\cdot(\nabla\times\boldsymbol{v}_\perp) \approx \nabla_\perp^2 u \qquad (2.24)$$

The full derivation of the developed equations is given in appendix B. The normalization of the variables in JOREK units (noted with superscript $\sim$) is the following: time is defined as $t = \tilde{t}\sqrt{\rho_0\mu_0}$, mass density is $\rho = \tilde{\rho}\rho_0$, temperature is $T(eV) = m_i/(\rho_0\mu_0 e)\tilde{T}$, the total pressure is $\tilde{P} = \mu_0 P = \tilde{\rho}\tilde{T}$ and the toroidal current is $\tilde{J} = \mu_0 J$. Note that the toroidal current density is defined in $Eq.$ (2.23) in the direction opposite to the magnetic field and hence in JOREK system a co-current injection corresponds to a negative source of parallel velocity. The electrostatic potential $\tilde{u}$ is related to the electric field as $\boldsymbol{E} = -F_0\nabla\tilde{u}/\sqrt{\rho_0\mu_0}$. For each species s, the parallel and perpendicular components of the velocity are $v_{\parallel,i} = \tilde{v}_{\parallel,i}B/\sqrt{\rho_0\mu_0}$ ($\tilde{v}_{\parallel,i}$ has no dimension) and $v_\perp = \tilde{v}_\perp/\sqrt{\rho_0\mu_0}$ ($\tilde{v}_\perp$ is expressed in Tesla).

Compared to the full MHD equations described in section 2.2.1, diffusive terms for the density and heat are added in the continuity and energy equations, as well as viscosity in the momentum equation. Sources of particle, heat and velocity are also added in the model. These diffusive and source terms are necessary to reproduce phenomenologically (and more simply) diffusive effects induced e.g. by turbulence which are not present in the model. They also allow for damping the small structures that may appear numerically. $D_\perp$ is the perpendicular particle diffusion, $\mu_{\parallel}$ and $\mu_\perp$ are the parallel and perpendicular anomalous viscosity coefficients, $\kappa_{\parallel}$ and $\kappa_\perp$ are the parallel and perpendicular heat diffusivity and η is the resistivity. These parameters are normalized as $\tilde{D}_\perp = D_\perp\sqrt{\rho_0\mu_0}$, $\tilde{\kappa}_{(\parallel,\perp)} = \kappa_{(\parallel,\perp)}\sqrt{\rho_0\mu_0}$, $\tilde{\mu}_{(\parallel,\perp)} = \mu_{(\parallel,\perp)}\sqrt{\mu_0/\rho_0}$ and $\tilde{\eta} = \eta\sqrt{\rho_0/\mu_0}$. Both viscosity and resistivity follow a Spitzer-like $(T/T_0)^{-3/2}$ dependence ([Wesson 2011], p.71) and the parallel heat diffusivity varies as $(T/T_0)^{5/2}$ ([Braginskii 1965], p.215-217). In the core plasma, for a particle density $n_0 = 6\times 10^{19}m^{-3}$ (JET case), the typical values used in simulations are $D_\perp = \kappa_\perp = 2m^2/s$, $\kappa_{\parallel}/\kappa_\perp = 2\times 10^8$, $\mu_\perp = 4\times 10^{-7}kg/(m.s)$, $\mu_{\parallel}/\mu_\perp = 10$ and $\eta \sim 10^{-7}\Omega.m$. S_ρ, $S_{V_{\parallel}}$ and S_T are sources of particles, parallel momentum and heat respectively. Reproducing realistic sources of heat and particle is a difficult issue [Sarazin 2010]. We have opted here for a simple approach: the particle source is constant throughout the plasma and the radial profile of the heat source is everywhere proportional to the temperature profile. As for the source of parallel velocity, is it described further below in section 2.3.3. As well, the different components of the velocity and the neoclassical tensor are detailed in section 2.3.1 and section 2.3.2 respectively.

2.3 Implementation of realistic flows

Several effects were added in the original JOREK model in order to self-consistently describe the plasma flows interacting with ELMs and RMPs, namely the diamagnetic drifts (section 2.3.1), the neoclassical friction (section 2.3.2) and a source of toroidal rotation (section 2.3.3).

2.3.1 Bi-fluid diamagnetic effects

The MHD ordering only considers the parallel and $E \times B$ drift components of the fluid velocity, resulting in a single fluid system of equations. In our model, two-fluid effects called diamagnetic effects are added to the initial model [Huysmans 2009]: the diamagnetic velocity $\boldsymbol{V}_s^* = -\nabla P_s \times \boldsymbol{B}/(\rho e_s B^2/m_i)$ – due to the pressure gradient perpendicular to the magnetic field – is taken into account for each species s (electrons and ions) and is of special importance in the pedestal where the pressure profile is steep. Both diamagnetic and $E \times B$ components are actually of the same order of magnitude. The decomposition of the velocity of a species s then writes:

$$\boldsymbol{v}_s = \boldsymbol{v}_{||,i} + \boldsymbol{v}_E + \boldsymbol{v}_s^* \tag{2.25}$$

where $\boldsymbol{v}_E = \boldsymbol{E} \times \boldsymbol{B}/B^2$ is the electric drift velocity.

Once normalized, the decomposition of the fluid (ion) velocity $Eq.$ (2.25) becomes:

$$\boldsymbol{v} = \boldsymbol{v}_i = v_{||,i}\boldsymbol{B} - R^2\nabla u \times \nabla\varphi - \frac{R^2\tau_{IC}}{\rho}\nabla P \times \nabla\varphi \tag{2.26}$$

where the diamagnetic parameter (inverse of the normalized ion cyclotron frequency) is defined as

$$\tau_{IC} = \frac{m_i}{2F_0 e\sqrt{\rho_0\mu_0}} \tag{2.27}$$

And the electron velocity is:

$$\boldsymbol{v}_e = v_{||,e}\boldsymbol{B} - R^2\nabla u \times \nabla\varphi + \frac{R^2\tau_{IC}}{\rho}\nabla P \times \nabla\varphi \tag{2.28}$$

Using the definition of the current, in SI units, we have: $\boldsymbol{v}_{||,e} = \boldsymbol{v}_{||,i} - \frac{\boldsymbol{J}_{||}}{ne}$, which gives in JOREK normalized units: $v_{||,e}\boldsymbol{B} = v_{||,i}\boldsymbol{B} - \frac{2F_0\tau_{IC}\boldsymbol{J}_{||}}{\rho} \approx v_{||,i}\boldsymbol{B} + \frac{2F_0\tau_{IC}j}{\rho}\nabla\varphi$. The definition of the JOREK toroidal current given in $Eq.$ (2.23) has been used. Thus the electron velocity is:

$$\boldsymbol{v}_e = v_{||,i}\boldsymbol{B} + \frac{2F_0\tau_{IC}}{\rho}j\nabla\varphi - R^2\nabla u \times \nabla\varphi + \frac{R^2\tau_{IC}}{\rho}\nabla P \times \nabla\varphi \tag{2.29}$$

Note that in $Eqs.$ (D.33-2.29) we have used the fact that we assume $T_e = T_i = T$ and thus $P_e = P_i = P/2$, so $\boldsymbol{v}_e^* = -\boldsymbol{v}_i^*$

We will see in this thesis that the diamagnetic drifts play a key role in order to

consistently study the RMP penetration and the ELM dynamics.

2.3.2   Neoclassical transport

The second important terms added correspond to the so-called "neoclassical effects". When the particles gyrate around the twisted field lines, they see a larger magnetic field B near the inside wall (High Field Side or HFS) and a smaller B near the outside wall (Low Field Side LFS), due to the fact that the toroidal magnetic field is proportional to $1/R$ ($B_\varphi(R) = F_0/R$). Therefore, if the ratio of the parallel velocity of a particle over the perpendicular one is too small, the particle undergoes a "mirror effect" and bounces back from the high field region, instead of sampling all poloidal angle. As the trajectory of these trapped particles projected on the poloidal plane has a banana shape, they are called "banana particles" (see Fig. 2.1). Because of the collisions between trapped and passing particles, the particles are successively trapped and untrapped (passing particles becoming trapped and vice versa) or move from one banana orbit to another. The diffusion of particles is thus enhanced by the presence of banana orbits: this is called the "neoclassical transport".
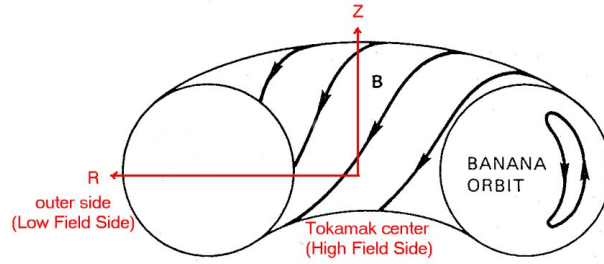
Figure 2.1: Banana orbit of the trapped particles due to the fact that $B_\varphi \propto 1/R$

One of the important "neoclassical" effects in tokamaks is the generation of a parallel current (so-called "bootstrap current") due to the finite banana orbit width in the region of density and temperature gradients. The real bootstrap current is not yet implemented in the JOREK model, but a source of toroidal current reproducing the profile induced by the bootstrap effects is included in the Ohm's law, such that the current profile is "hooked" to the initial profile containing a bootstrap component, using the Krook operator: $\eta\left(j - (j_{0,classical} + j_{0,bootstrap})\right)$, where η is the resistivity.

As for the neoclassical poloidal friction, describing the friction between the trapped and passing particles, it is translated into the equations as an anisotropy of the pressure tensor in the momentum equation. Indeed, the pressure tensor is written as $\bar{P} = \bar{I}P + \bar{\Pi}_{i,neo} + \bar{\Pi}_{i,gv}$. The cancellation of the gyroviscous tensor $\nabla \cdot \bar{\Pi}_{i,gv}$ with the time derivative of the diamagnetic velocity $d\boldsymbol{v}_i^*/dt$ [Hazeltine 1985a] is used, and the divergence of the neoclassical tensor is given by the heuristic closure taken from [Gianakon 2002]:

$$\nabla \cdot \bar{\Pi}_{i,neo} = \rho\mu_{i,neo}\frac{B^2}{B_\theta^2}(v_\theta - v_{\theta,neo})\boldsymbol{e}_\theta \qquad (2.30)$$

where $\mu_{i,neo}$ is the neoclassical friction. The so-called neoclassical tensor constrains the poloidal velocity v_θ to approach the value predicted by the neoclassical theory: $v_{\theta,neo} = -k_i \nabla T_i \times \boldsymbol{B}/eB^2 \cdot \boldsymbol{e}_\theta$, where k_i is the neoclassical heat diffusivity.

We have used the following definition of the unit vector in the poloidal direction:

$$\boldsymbol{e}_\theta = (\nabla\psi \times \nabla\varphi)\frac{R}{|\nabla\psi|} \tag{2.31}$$

Note that this definition implies that the orthonormal basis $(\boldsymbol{e}_\psi, \boldsymbol{e}_\theta, \boldsymbol{e}_\varphi) = (\frac{\nabla\psi}{|\nabla\psi|}, (\nabla\psi \times \nabla\varphi)\frac{R}{|\nabla\psi|}, R\nabla\varphi)$ is left handed, and the poloidal magnetic field therefore writes

$$B_\theta = B \cdot \boldsymbol{e}_\theta = |\nabla\psi|/R \tag{2.32}$$

The projection of *Eq.* (D.33) along the poloidal direction ($\boldsymbol{e}_\theta$ *Eq.* (2.31)) gives the expression of the poloidal velocity:

$$v_\theta = -\frac{1}{B_\theta}\Big(\nabla_\perp\psi \cdot \nabla_\perp u + \frac{\tau_{IC}}{\rho}\nabla_\perp\psi \cdot \nabla_\perp P - v_{||,i}B_\theta^2\Big) \tag{2.33}$$

The combination of *Eq.* (2.33) and *Eq.* (2.31) with the expression of the normalized neoclassical velocity $v_{\theta,neo} = -\dfrac{k_i\tau_{IC}}{B_\theta}(\nabla_\perp\psi \cdot \nabla_\perp T)$ leads to the developed form of the neoclassical tensor *Eq.* (2.30):

$$\nabla \cdot \bar{\bar{\Pi}}_{i,neo} = \mu_{i,neo}\rho\frac{B^2}{B_\theta^4}\Big(-v_{||,i}B_\theta^2 + \nabla_\perp\psi \cdot \nabla_\perp u$$
$$+ \frac{\tau_{IC}}{\rho}\big(\nabla_\perp\psi \cdot \nabla_\perp P + k_i\rho\nabla_\perp\psi \cdot \nabla_\perp T\big)\Big)(\nabla\psi \times \nabla\varphi) \tag{2.34}$$

Realistic radial profiles of the neoclassical parameters $\mu_{i,neo}$ and k_i (calculated from [Kessel 1994]) which depend both on the aspect ratio and on the collisionnality, are used in the simulations in chapter 3 for the JET case (section 3.3). For the sake of simplicity, these coefficients are taken constant in the ITER case (in chapter 3, section 3.4) and in the JET case in chapter 4 and chapter 5, where typical values $\tilde{\mu}_{i,neo} = \mu_{i,neo}\sqrt{\rho_0\mu_0} = 10^{-5}$ and $k_i = -1$ [Bécoulet 2012] are used. In the MAST case, the neoclassical friction is not included in the model.

Note that another neoclassical effect exists, which is the toroidal momentum damping by the neoclassical toroidal viscosity (NTV), occuring in presence of error fields. In order to improve the study of the plasma rotation in presence of RMPs (chapter 3), the physics of the toroidal momentum damping by NTV should also be taken into account. In relatively recent NTV papers and modeling [Cole 2008, Park 2009, Sun 2010, Becoulet 2009, Liu 2012], NTV is estimated in MHD codes *a posteriori* using an analytic solution of the drift-kinetic equation for trapped particles at different collisionality regimes. The solution strongly depends both on the perturbed magnetic field – which was usually computed in vacuum, or in approximation of ideal MHD response (no-islands) [Park 2009] – and on the radial electric field which defines the $E \times B$ drift frequency. It should therefore be

calculated taking into account the plasma response. However, so far we no consensual agreement seems to appear between the modeling using analytical approximate kinetic solution and the experiments. The reason is multiple: the collision operator within the drift-kinetic framework is quite complex and only simplified versions of it are used, which give different NTV predictions. At the same time, the plasma response itself, determined through MHD codes, needs to be considered and gives an additional level of complexity in predicting the NTV. The time coupling between kinetic and MHD computations is thus a thorny problem. For these reasons, such a kinetic-MHD computation is currently beyond the scope of the available models. As for the experimental side, the toroidal torque is composed of several parts (intrinsic turbulent rotation, NTV, ripple and other sources) thus the comparison of the NTV part of the toroidal rotation alone against the theorethical NTV value is not straightforward.

2.3.3 Source of parallel rotation

The last effect implemented to described self-consistent plasma flows is a source of parallel rotation that mimics the realistic parallel rotation profile. The source of parallel rotation, implemented as $\tilde{S}_{v_{||}} = -\tilde{\mu}_{||}\Delta\tilde{v}_{||,t=0}$, forces the parallel velocity to keep close to the experimental rotation profile and compensates the losses due to the parallel viscosity.

Consequently the parallel and perpendicular flows, constrained by the source of parallel rotation, the neoclassical and diamagnetic effects, self-consistently evolve towards an equilibrium. This results in the self-consistent evolution of the radial electric field, expressed by the radial force balance (in JOREK units):

$$E_r = \frac{\tau_{IC}}{\rho}\frac{\nabla_\perp\psi\cdot\nabla_\perp P}{|\nabla\psi|} + \frac{1}{F_0}\big(v_\theta B_\varphi - B_\theta v_\varphi\big) \tag{2.35}$$

with v_θ close to $v_{\theta,neo}$ and $v_\varphi \approx v_{\varphi,source}$ in the bulk plasma. As for the Scrape-Off Layer flows, they are mostly affected by the Bohm boundary conditions described in section 2.4.

2.4 Boundary conditions

The boundary of the computational domain is chosen to follow the closed magnetic field lines everywhere, except on the divertor target plates where the boundary crosses open field lines. On the closed field lines, Dirichlet conditions are used for all the variables: $variable(x) = constant(x)$ on the boundary. On the divertor targets, the Dirichlet conditions also apply for the variables u, j, W and ψ. However, Bohm conditions are set there for the parallel velocity $v_{||}$, the temperature T and the density ρ: the parallel velocity is imposed to be equal to the sound speed on the divertor: $v_{||} = c_s = \sqrt{\gamma T_e/m_i}$), and the temperature and density outflow is left free.

Moreover, in RMP simulations, the application of the RMPs is modeled by a change in boundary conditions for the magnetic flux perturbation $\psi(n \neq 0)$. The vacuum RMP spectrum is previously calculated with the ERGOS code [Bécoulet 2008] and applied as boundary conditions of the computational domain for the magnetic flux perturbation.

RMPs are progressively switched on in time: the amplitude of the perturbation is gradually increased in the typical timescale $t \sim 1000t_A$. That way, the magnetic perturbation gradually penetrates inside the plasma, which self-consistently adapts in the process. Also this method avoids possible problems with hysteresis effects that could occur if the simulation was started with a fully penetrated magnetic perturbation [Nishimura 2012]: the bifurcation from a fully penetrated state to a partially penetrated state might lead to a different plasma response. Note that this approach does not enable the plasma to modify the magnetic field perturbation at the boundary of the computational domain. Yet as this boundary is located far from the confined plasma (in the far SOL or at the wall) the "vacuum" approximation at the boundary may not be too far from reality. A more correct way to proceed is to include the real field generated by the RMP coils in a "free boundary" domain. This is under implementation and should be used in future works.

2.5 The JOREK code structure

JOREK is mainly composed of numerical computations on 3D data. The grid is discretized in 2D bi-cubic Bézier finite elements [Czarny 2008, Huysmans 2009] in the poloidal plane, and the toroidal direction is decomposed in Fourier series. Each Bézier element has its local coordinates (s, t) and the local system (s, t, φ) is related to the global cylindrical (R, Z, φ) coordinate system in which the equations are defined, using the co- and contra-variant vectors.

A JOREK computation is run as follows:

First an initial polar grid is generated for the Bezier elements (Fig. 2.2).

Figure 2.2: Initial polar grid for Bezier elements (poloidal plane) in the ITER case (standard H-mode scenario $15MA/5.3T$, described in section 3.4).

Second the equilibrium flux surfaces, including the X-point, are calculated while solving the Grad-Shafranov equation for the magnetic flux:

$$\Delta^*\psi = -\mu_0 R^2 \frac{dP}{d\psi} - F\frac{dF}{d\psi} \tag{2.36}$$

$F(\psi)$ is the current function related to the poloidal current: $j_{pol} = \nabla \times (F\nabla\varphi)$ and the Grad-Shafranov operator is defined as:

$$\Delta^*\psi = R^2\nabla \cdot \left(\frac{1}{R^2}\nabla\psi\right) = R\frac{\partial}{\partial R}\left(\frac{1}{R}\frac{\partial\psi}{\partial R}\right) + \frac{\partial^2\psi}{\partial Z^2} \tag{2.37}$$

The radial profiles of the pressure $P(\psi)$ and of the $F\frac{dF}{d\psi}$ function are obtained from equilibrium codes computing data extracted from experiments. These functions injected into *Eq.* (2.36) thus determine the equilibrium flux surfaces. The 2-D elements of the poloidal grid, presented in Fig. 2.3, are modified so that they are aligned to these equilibrium flux surfaces.

Note that the intrinsic flux aligned coordinate system $(\nabla\psi, \nabla\theta, \nabla\varphi)$ is also used in this thesis, as it is more convenient for the physical understanding. The equilibrium poloidal flux ψ is obtained from the Grad-Shafranov equation and the intrinsic poloidal angle θ is obtained from the equation: $d\theta/d\varphi = -1/q$ where q is the safety factor.

As for the boundary of the computational domain, it is usually chosen to be aligned to a magnetic field line located in the far Scrape-Off Layer, except in the divertor, where the boundary follows the divertor target plates, as shown in Fig. 2.3.
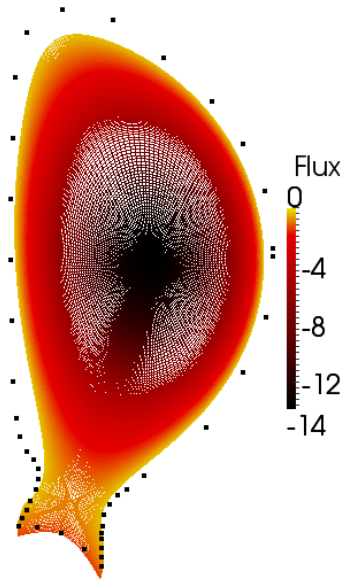
Figure 2.3: Final ITER equilibrium flux-aligned final mesh used in modeling. The squares represent the position of the wall and divertor.

Third the equilibrium flows are established in a time scale of $\sim 10^3$ Alfven times t_A. These flows develop due to the Bohm boundary conditions, the diamagnetic and neoclassical effects, as well as the toroidal source of rotation. Due to the initially large velocity gradients e.g. on the divertor where $v_{||} = c_s$, the time step has to be very low at the beginning ($\sim 10^{-3} t_A$), and is progressively increased, until the equilibrium state is reached. The example of the equilibrium radial electric field ($n = 0$) is given in the ITER case in Fig. 2.4.
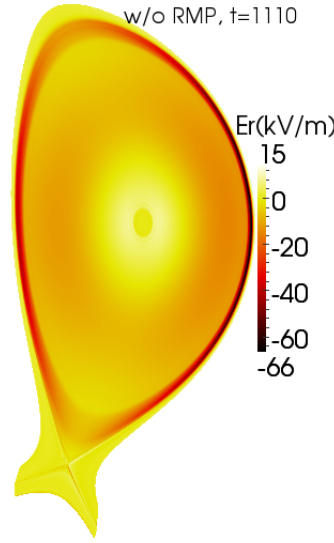
Figure 2.4: Poloidal profile of the radial equilibrium electric field in ITER ($n = 0$, without RMPs or ELMs)

Fourth once the equilibrium flows are obtained, the perturbation modes ($n \neq 0$) – due e.g. to the ELMs and/or the RMPs – are added in the simulation (Fig. 2.5). In RMP simulations, this implies a change in the boundary conditions, as described in section 2.4.

The simulation time varies between a few thousand of t_A and several tens of thousand of t_A, and the time stepping evolves between 10^{-2} and 1 t_A. The weak form of the equations *Eqs.* (2.17-2.21) are solved fully implicitely at each time step, using either the Crank-Nicholson or the Gear scheme [Hölzl 2012]. The numerical scheme used involves a direct solver on a large sparse matrix as a main computation of one time step. The matrix is inverted with the PaStiX sparse matrix library (Parallel Sparse matriX package, [Hénon 2002]), using the interating method GMRES [Saad 1986]. The JOREK code is massively parallelized with MPI and OpenMP, and a typical run requires around $10^4 - 10^5$ CPU.h.

Last after the simulation, post-processing calculations are done to extract data such as average profiles, Fourier harmonics and Poincaré plots.
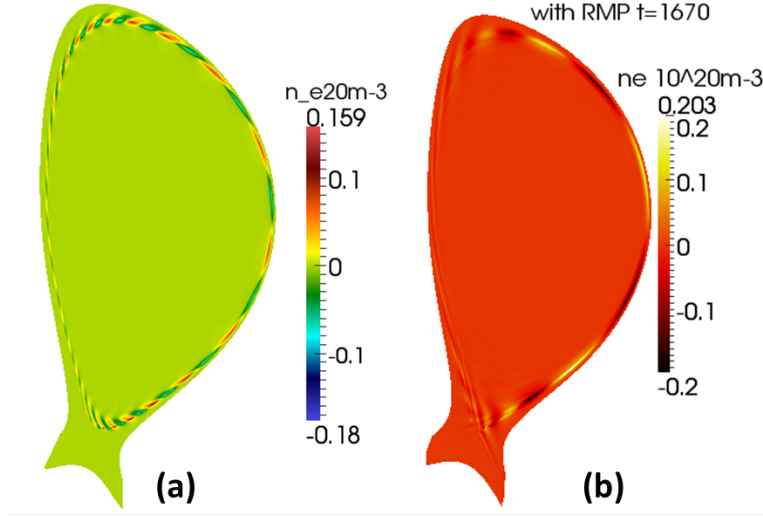
Figure 2.5: Time integration for all n harmonics in ITER: example of the density perturbation either due to the growth of an ELM ($n = 9$, left) or to the RMP penetration ($n = 3$, right, see section 3.4).

2.6   Summary

Modeling is performed with the reduced MHD code JOREK. The diamagnetic bi-fluid velocity, the neoclassical friction and a source of parallel rotation are added to the initial standard MHD model. We will see in chapter 3 that these effects, as well as the sheath conditions set as boundary conditions on the divertor targets, allow for describing self-consistently the plasma flows. The RMPs have also been implemented in JOREK: vacuum RMPs, previously calculated with the ERGOS code, are imposed as boundary conditions for the magnetic flux perturbation ψ_n. This way, RMPs can penetrate in the plasma while self-consistently taking into account the plasma response.

During a JOREK simulation, the poloidal grid – composed of Bézier elements – is aligned on the flux-surfaces, including the X-point and the SOL, and the toroidal direction is decomposed in Fourier series. On this grid, the equilibrium plasma flows ($n = 0$) are first calculated; then the modes of perturbation $n \neq 0$ are added in simulation, describing the time evolution of either the RMP penetration (chapter 3), or the ELM dynamics (chapter 4) or the ELM interaction with RMPs (chapter 5).

Interaction between RMPs and plasma flows

Contents

3.1 Introduction

The various results obtained (ELM suppression, ELM mitigation, ELM triggering or no effect) when RMPs were applied in different tokamaks – in spite of a similar theoretical ergodization calculated in vacuum – showed that the vacuum theory was not sufficient, as described in section 1.4.3. Thus it became clear that the plasma response to RMPs had to be taken into consideration.

The screening of externally applied static resonant magnetic perturbations was first developed theoretically by Fitzpatrick [Fitzpatrick 1998]. This theory is summarized in appendix C. The main idea is that a rotating plasma in presence of error fields can evolve in two different ways:

- either the RMPs are screened by the plasma rotation: the rotating plasma generates strong eddy currents on the resonant surfaces $q = m/n$ (n being the toroidal number of the RMPs), in response to the RMPs. These currents induce a magnetic perturbation opposite to the applied RMPs, thus the magnetic perturbation is screened (or shielded) on the rational surfaces.

- either the RMPs penetrate on the rational surfaces: the interaction between the plasma and the RMPs induce an electromagnetic torque which generates the "resonant" braking of the plasma rotation at the vicinity of the resonant surfaces, until the plasma rotation becomes close to zero on the rational surfaces. Thus the eddy currents become weak and RMPs induce magnetic islands on the rational surfaces.

If the RMP amplitude is gradually increased, the bifurcation from the screened to the penetrated state can occur, accompanied by the braking of the plasma rotation around the resonant surfaces. Also a backward transition can be obtained when the RMP amplitude is decreased. However the backward transition occurs for a lower threshold in amplitude, resulting in an hysteresis cycle of screening or penetration of RMPs. In [Fitzpatrick 1998], eleven different regimes are described depending on three parameters: the plasma rotation, the viscosity and the resistivity. In these regimes, the "inward" bifurcation (*i.e.* from the screened to the penetrated state) is found to occur for a different threshold in RMP amplitude, which depends on these three parameters.

This theory was developed for a singular layer (one poloidal harmonic m is considered), thus 2D and 3D effects of the plasma/RMP interaction cannot be described. However it gives an accurate analytical background and it provides a good basis for the understanding of the plasma response to RMPs.

In this chapter, the plasma response to RMPs is studied numerically in 3 dimensions. In section 3.2, we start with a preliminary modeling of the plasma response in simplified cylindrical geometry, using the reduced MHD code RMHD [Bécoulet 2012]. DIII-D parameters are used. This study allows for understanding the main features of the plasma response to RMPs, and to point out what impact the amplitude of the applied RMPs as well as different plasma parameters (the electron perpendicular rotation, the resistivity, the neoclassical friction which can be associated to the viscosity) may have on the RMP penetration.

Then the interaction between RMPs and plasma flows is studied in realistic toroidal geometry, including the X-point and the SOL, through JOREK simulations. The flow patterns present in X-point tokamaks are described, and different regimes of RMP penetration are found depending on the flows. The 3D-corrugation of the pedestal profiles as well as the lobe structures near the X-point, induced by RMPs, are described. The simulations are performed successively for realistic JET (section 3.3), ITER (section 3.4)

and MAST (section 3.5) parameters. The resonant rotation braking is also addressed in the MAST case.

3.2 Preliminary cylindrical modeling of the RMP penetration

In this section, a preliminary modeling is done in simplified cylindrical geometry with the reduced MHD code RMHD [Bécoulet 2012]. The RMHD model is similar to the one implemented in the JOREK code, but the simplified cylindrical geometry (without X-point or SOL) makes that the RMHD simulations are much shorter and easier to run than the JOREK simulations, even though some physical phenomena are missing. The RMHD modeling presented in this section is performed with parameters corresponding to the DIII-D tokamak [Evans 2004a]: $R_0 = 1.8m$, $a = 0.6m$, the central density, temperature, and toroidal rotation are $n_{e,0} = 8 \times 10^{19} m^{-3}$, $T_{e,0} = 1.5keV$ and $V_0 = 72km/s$. The resistivity profile follows a $T^{-3/2}$ dependence with a central resistivity $\eta_0 = 1/S = 10^{-8}$: this value is one order of magnitude larger than the experimental value because of numerical restrictions. Even though the neoclassical friction is a purely toroidal phenomenon, they have been included artificially in the cylindrical model (in the sense that poloidal velocity is constrained to approach the neoclassical poloidal velocity), as well as the diamagnetic effects. The neoclassical coefficients are taken constant: $\mu_{neo} = 5 \times 10^{-5}$ and $k_i = -0.8$. The spectrum of magnetic perturbations induced by the DIII-D I-coils (characterized by a coil current $I = 4kAt$ and an $n = 3$ even parity configuration) is first calculated in the vacuum with the ERGOS code [Bécoulet 2008], and then applied at the boundary of the computational domain. Both toroidal and poloidal directions are discretized in Fourier harmonics. An $(n = 3, m = 6 - 10)$ spectrum of RMPs is applied.

3.2.1 Generic features of the plasma response to RMPs

In order to give a picture of the plasma response to RMPs, the magnetic topology generated by the application of the $(n = 3, m = 6 - 10)$ RMP spectrum is modeled in two different cases: Fig. 3.1 presents the RMPs penetration, either in the vacuum (on the left) or in the DIII-D plasma (on the right). Note that the RMP screening by the plasma is found to be negligible at high resistivity [Bécoulet 2008], so the vacuum-like simulation is actually performed for a high resistivity $\eta_0 = 10^{-4}$.

In the vacuum, RMPs induce the formation of magnetic islands on the resonant surfaces $q = m/n$, and the overlap of the consecutive island rows 9/3 and 10/3 generates an ergodic zone at the edge. However, when RMPs are applied in the plasma (on the right), magnetic island chains are formed only on the rational surfaces $q = 7/3$ and $q = 10/3$: this represents the screening of the magnetic perturbations by the plasma on the resonant surfaces, except the harmonics $m = 7$ and $m = 10$ which penetrate in the plasma.

As explained in section 3.1, the plasma in rotation is likely to screen the RMPs on the rational surfaces: the plasma generates eddy currents on these surfaces in response to the
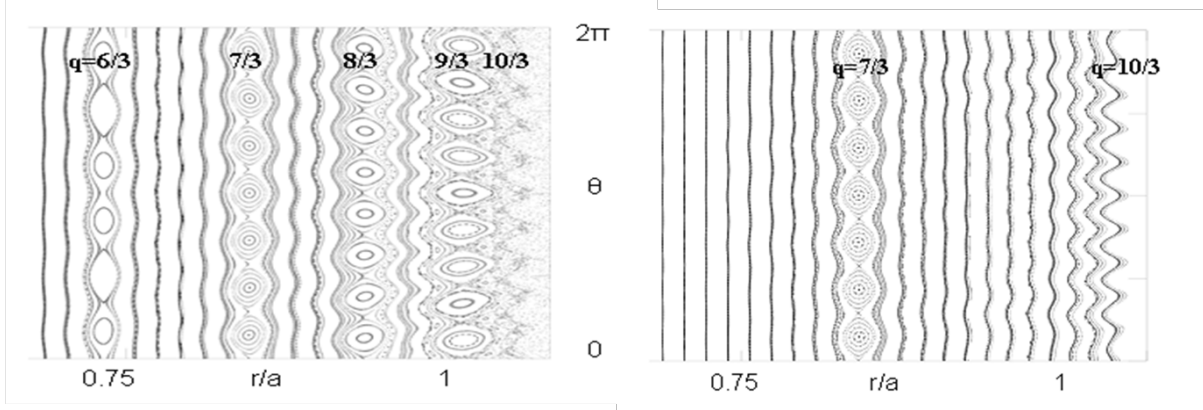
Figure 3.1: Formation of magnetic island chains on the resonant surfaces $q = m/n$ due to RMPs in the vacuum-like case (left) and in the plasma (right)

magnetic perturbation, and these eddy currents induce a magnetic perturbation opposite to the applied perturbation. In fact, the response currents have been found to be linked with the electron perpendicular rotation $v_{\perp,e}$ [Nardon 2010, Bécoulet 2012]: when $v_{\perp,e}$ is close to zero on a rational surface $q = m/n$, the response currents vanish and the (m, n) harmonic of RMPs penetrates, resulting in the formation of (m, n) magnetic islands on the rational surface. This relation between the response currents and the electron perpendicular velocity – found analytically by linearizing the Ohm's law (*Eq.* (2.21)) and demonstrated in appendix A – writes:

$$imv_{\perp,e}\psi_{m,n} = \eta J_{m,n} \qquad (3.1)$$

$\psi_{m,n}$ and $J_{m,n}$ are respectively the magnetic and current perturbation, and the perpendicular electron velocity is the sum of the electric $v_{E \times B}$ and electron diamagnetic v_e^* drifts:

$$v_{\perp,e} = v_e^* + v_{E \times B} \qquad (3.2)$$

In light of *Eq.* (3.1), the penetration of the two poloidal harmonics $m = 7$ and $m = 10$ of the RMPs can be explained by a different reason for each harmonic. First, the resonant surface $q = 7/3$ is located in the region of the plasma where the perpendicular electron velocity $v_{\perp,e}$ is close to zero, as illustrated in Fig. 3.2. Thus the current perturbation $J_{7,3}$ which would prevent the RMPs from penetrating cancels on the surface $q = 7/3$, and the RMPs can penetrate in the plasma.

Note that the cancellation of $v_{\perp,e}$ highly depends on the radial electric field, whose evolution modifies the $E \times B$ drift and subsequently the perpendicular velocity. So it is important to study the self-consistent evolution of the electric field to determine if the RMPs will be screened or not. In our example, the radial electric field is modified by the RMPs which induce an electromagnetic torque on the surface $q = 7/3$. Subsequently, on this surface, the electric drift evolves such that it compensates the diamagnetic velocity,

leading to penetration of the $m = 7$ component of the magnetic perturbation. The role of the evolution of the electric field will be illustrated in section 3.2.2.2.
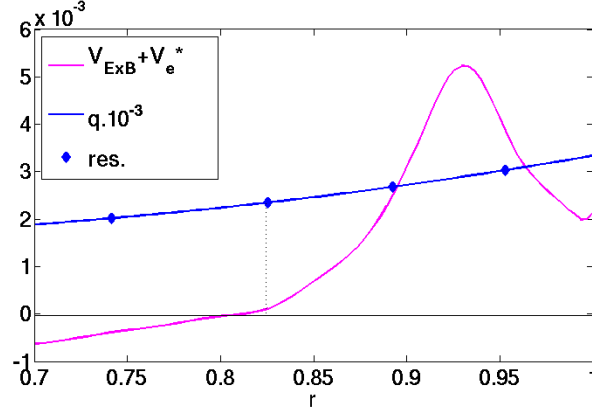
Figure 3.2: Radial profile of the electron perpendicular velocity (in pink): $v_{\perp,e}$ cancels at the resonant surface $q = 7/3$. The q-profile is plotted in blue and the diamonds indicate the resonant surfaces.

Eq. (3.1) can also explain the penetration of the $m = 10$ harmonic on the resonant surface $q = 10/3$. Indeed, the surface $q = 10/3$ is located at the very edge of the plasma where the resistivity is the highest (since η depends on $T^{-3/2}$, and T is low at the edge). In Eq. (3.1), the left hand side has to compensate the right hand side ($= \eta J_{m,n}$). Thus the very large resistivity η at the edge (close to the vacuum resistivity) constrains the current perturbation $J_{m,n}$ to remain at a very low level. Consequently, the RMPs can penetrate at the edge almost as well as in the vacuum, which explains the formation of the magnetic islands on the surface $q = 10/3$. A resistivity scan, given in section 3.2.2.3, illustrates in more detail the role of the resistivity.

This example allows to point out the importance of the perpendicular electron velocity and the resistivity regarding the RMP penetration. Experimentally, for a given H-mode profile, it is hardly possible to modify the resistivity in the pedestal, but the idea took hold of positioning a rational surface precisely where the perpendicular electron velocity cancels, at the top of the pedestal, in order of obtain the RMP penetration [Nardon 2010]. An important parameter for the RMP experiments and simulations is the safety factor at 95% of the edge q_{95}. This q_{95} factor is inversely proportional to the plasma current and therefore translates the "working point" depending on the injected current. So, in the experiments, it is possible to make a q_{95}–scan corresponding to the variation of the plasma current. A variation of the q_{95} parameter will indicate a modification of the q-profile and will then shift the position of the resonances. In particular, a resonant surface $q = m/n$ can be shifted to a position where the electron perpendicular velocity cancels by modifying the plasma current. This allows to obtain the penetration of the (n, m) harmonic characterized by the formation of magnetic islands on the surface $q = m/n$.

In Fig. 3.3, a simulation is presented where the resonant surface $q = 8/3$ (dash line) is located either on a surface where $v_{\perp,e} \neq 0$ (for $q_{95} = 3.15$, black case) or where $v_{\perp,e} = 0$ (for $q_{95} = 3.44$, red case). In the first situation, a current perturbation $J_{m,n}$ (left) is

induced on the resonant surface by the plasma perpendicular rotation. This current perturbation induces a magnetic field that compensates the RMPs, leading to the RMP screening: the $(n = 3, m = 8)$ Fourier component of the magnetic perturbation ψ_{nm} is zero on the resonant surface $q = 8/3$. However, in the second case (red), there is no current perturbation on the resonant surface, inducing the penetration of the $m = 8$ harmonic. Note that in this second penetrated case, the current perturbation has a tearing parity around the resonant surface, which is characteristic of the formation of magnetic islands.
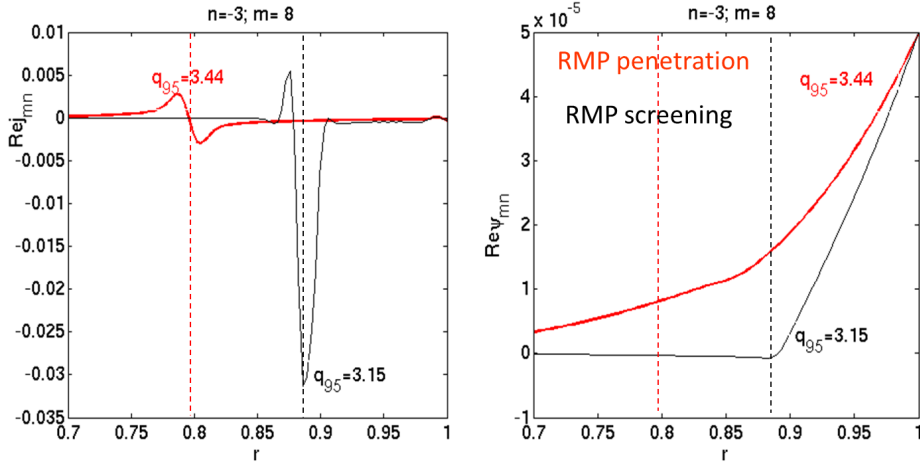
Figure 3.3: $(n = 3, m = 8)$ Fourier component of the current perturbation (left) and of the magnetic perturbation (right) for two different q-profiles.

Moreover, if the RMP penetration is obtained for a large "operational window" in terms of plasma current (and thus in terms of q_{95}), then it is easier to actually observe the RMP penetration in experiments. So it is interesting to study the range of the edge safety factor values Δq_{95} on which RMPs penetrate. In the following section 3.2.2, we will see that this range depends both on the amplitude of the applied RMPs and on the neoclassical friction rate. The values of these parameters as well as the value of the plasma resistivity are scanned to assess their impact on the RMP penetration.

3.2.2 Influence of plasma parameters on the RMP screening

3.2.2.1 Amplitude of the applied magnetic perturbation

First, the RMP penetration is studied for two different amplitudes of the applied magnetic perturbation ($\psi_{m,n}(1) = 2.5 \times 10^{-5}$ and 5×10^{-5}) for the single mode $(n = 3, m = 8)$. We notice first that when RMPs penetrate, the amplitude of the mode (m, n) on the corresponding $q = m/n$ resonant surface is approximately two times larger for a two times larger applied perturbation (as presented in Fig. 3.4). Indeed, when the magnetic perturbation penetrates on a resonant surface, the penetration is total and the amplitude of the perturbation on the resonant surface $|\psi_{m,n}|_{res}$ is similar as the "vacuum" perturbation thus when the penetration occurs, $|\psi_{m,n}|_{res}$ scales linearly with the applied perturbation.

Second, Fig. 3.4 shows that the range of edge safety factor values Δq_{95} for which RMPs penetrate is larger for a larger input perturbation. Indeed, for the mode $(n = 3, m = 8)$, the penetration window is $\Delta q_{95} \sim 1.1$ for a perturbation $\delta\psi_{m,n} = 5 \times 10^{-5}$, compared to $\Delta q_{95} \sim 0.5$ for a two times lower perturbation. This penetration window is centred around the position where $v_{\perp,e}$ cancels. As we move away from this position, the bifurcation from the screened to the penetrated state becomes "harder". Thus at larger RMP amplitude, the bifurcation is more easily overcome when the perpendicular velocity is not exactly zero, which explains the enlargement of the Δq_{95} when the RMP amplitude is increased. Other modeling with RMHD (not presented here) shows that this Δq_{95} window is shifted depending on the mode m considered. So, in the aim of obtaining the ergodization of the edge, it is necessary to have a large enough window Δq_{95} for two consecutive modes: this way, the two consecutive modes penetrate, and thus the magnetic islands can overlap and ergodize the region. Consequently, the RMP penetration and ergodization should be more problable at larger RMP amplitude. However, over a certain threshold in amplitude, RMPs and error fields are likely to trigger locked tearing modes which can then induce disruptions [Kirk 2010, Liang 2007b]. So the RMP amplitude should be high enough to obtain the RMP penetration, but not too high in order to avoid reaching the locked-mode triggering threshold.
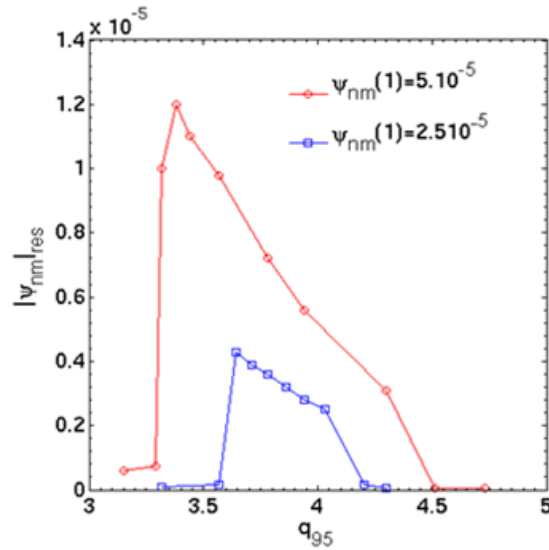
Figure 3.4: Amplitude of the harmonic $(n = 3, m = 8)$ for an applied perturbation $\delta\psi_{m,n} = 5 \times 10^{-5}$ (in red) and for a two times smaller $\delta\psi_{m,n} = 2.5 \times 10^{-5}$ (in blue)

3.2.2.2 Neoclassical friction

Let us consider again a single mode $(n = 3, m = 8$, Figs. 3.5-3.7) for three different values of the neoclassical friction rate $\mu_{neo} = 10^{-5}, 5 \times 10^{-5}$ and 10^{-4}. A q_{95}–scan, presented in Fig. 3.5 for these different values of μ_{neo}, shows that the window Δq_{95} for which RMPs penetrate becomes narrower when the neoclassical friction rate is increased. The physics
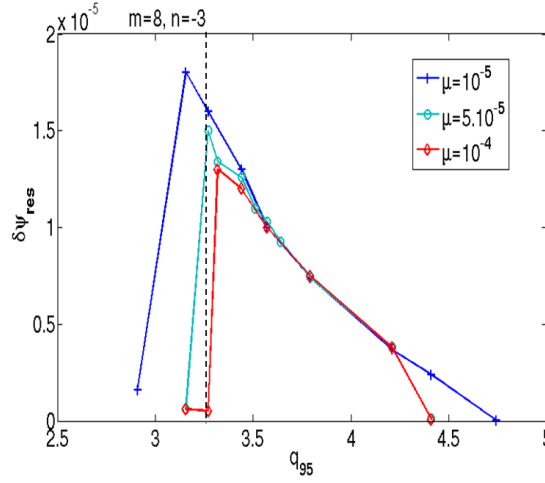
Figure 3.5: Influence of the strength of the neoclassical friction rate μ_{neo} on the range of penetration of the RMPs. For a larger μ_{neo} (in red), the penetration window Δq_{95} is smaller (as compared to a ten times smaller μ_{neo} in blue)

at stake is studied in the case corresponding to $q_{95} = 3.27$ (dashed line in Fig. 3.5): the $m = 8$ penetrates for a small neoclassical friction $\mu_{neo} = 10^{-5}$, but is screened for a 10 times larger neoclassical friction rate $\mu_{neo} = 10^{-4}$. When the neoclassical effects are small (in blue), the non-linear interaction of the RMPs with the electric field is stronger (Fig. 3.6) and the electric field becomes more positive on the resonance surface. Consequently, the $E \times B$ drift compensates the diamagnetic velocity on the resonance (Fig. 3.7), and thus the current perturbation is suppressed. This allows for the mode of RMPs to penetrate. However, a larger neoclassical friction rate (in red) prevents the radial electric field from evolving significantly in presence of RMPs. Thus the perpendicular electron velocity and subsequently the current perturbation cannot cancel: so the magnetic perturbation is screened. Actually, the neoclassical friction, similarly to the viscosity, induce a viscous torque which counteracts the electromagnetic torque (*i.e.* the resonant braking) induced by RMPs. So the neoclassical friction, as well as viscosity, reduce the modification of the electric field by RMPs and the resonant braking, and then act against the RMP penetration.

3.2.2.3   Plasma resistivity

The resistivity follows a radial dependence $\eta(r) = \eta_0 (T(r)/T_0)^{3/2}$. Thus the screening of the RMPs depends on the central value η_0. In this section, the impact of the value of η_0 on the RMP penetration is tested for the application of a single mode ($n = 3, m = 10$).

When RMPs are applied, the magnetic perturbation on the resonant surface $\psi_{m,n}$ grows exponentially, until it saturates to a certain level corresponding to the saturation of the island size. In the "vacuum-like" case (for $\eta_0 = 10^{-4}$), RMPs quickly penetrate, and the saturation amplitude of the perturbation on the resonant surface is close to the applied one (in blue on Fig. 3.8). The vacuum case is compared to the plasma, where the realistic central resistivity is much lower ($\eta = 10^{-8} - 10^{-9}$). Even though this realistic
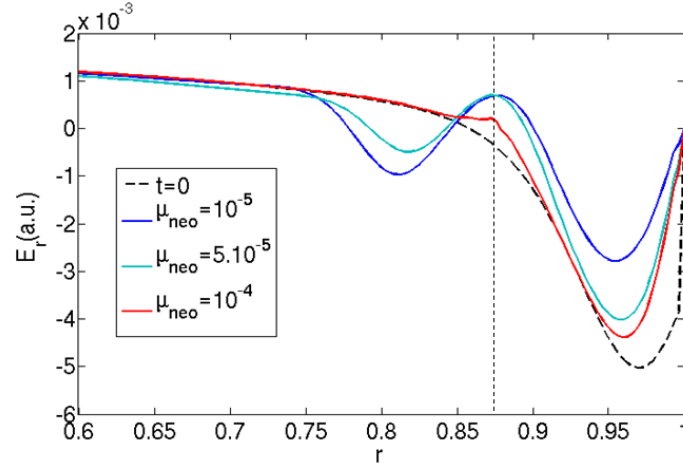
Figure 3.6: For $q_{95} = 3.27$ (dashed line on Fig. 3.5), the radial electric field E_r is less affected by the RMPs for a larger $\mu_{neo} = 10^{-4}$ (in red) than for $\mu_{neo} = 10^{-5}$ (in blue) on the resonant surface $q = 8/3$ ($r = 0.87$). The initial E_r (without RMPs, in black) is the same for each simulation.
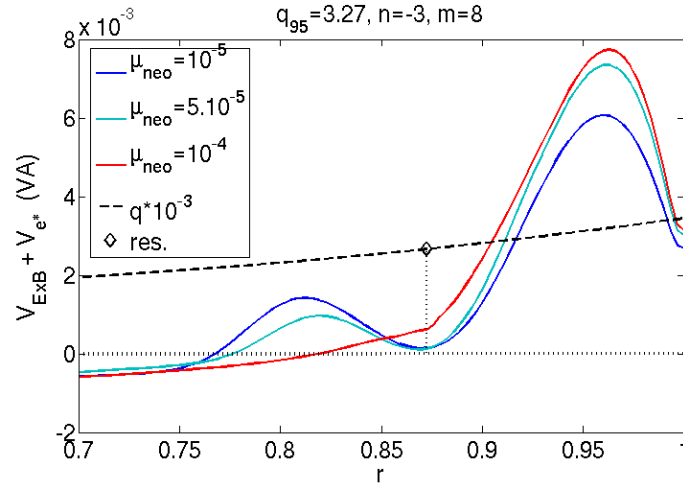
Figure 3.7: On the resonant surface $q = 8/3$ (diamond), the $E \times B$ drift does not compensate the diamagnetic drift for $\mu_{neo} = 10^{-4}$ (in red) due to the lower electric field (Fig. 3.6) On the contrary, the condition ($v_{E \times B} + v_e^* \approx 0$) is satisfied for $\mu_{neo} = 10^{-5}$ (in blue) due to the larger electric field.

resistivity cannot be reached in simulations for numerical reasons, a resistivity scan can give us the trend of the evolution of the RMP penetration as a function of η_0. We observe that the penetration time is longer and the amplitude on the resonance surface is lower when the resistivity is lower (in Fig. 3.8, the "low resistivity" $\eta_0 = 0.25 \times 10^{-8}$, in black, is compared to a larger plasma resistivity $\eta_0 = 10^{-8}$, in red). This is also seen in Fig. 3.9, where the radial dependence of the amplitude of the $m = 10$ mode is plotted depending on η_0: on the resonant surface $q = 10/3$, the amplitude of the magnetic perturbation is lower when the resistivity is lower. The explaination is similar to the one given in section 3.2.1: for a given perpendicular electron velocity and magnetic perturbation in

Eq. (3.1), a large resistivity forces the current perturbation $J_{m,n}$ to remain low, and allows the RMPs for penetrating. Yet for a lower resistivity, these currents are less "constrained" and are likely to grow, which reduces the RMP penetration.
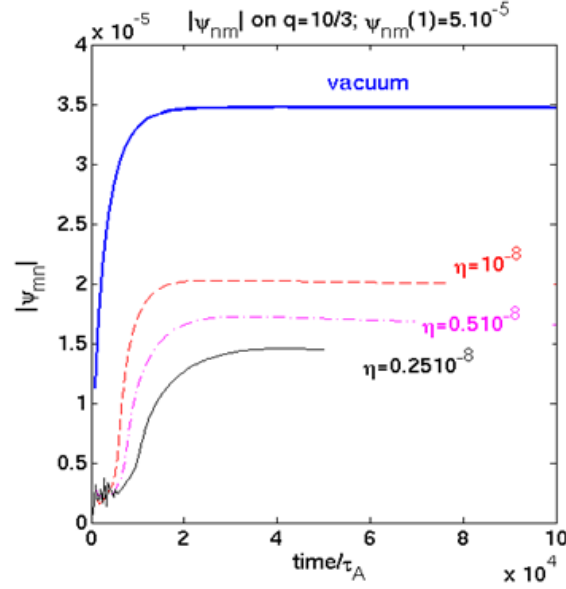
Figure 3.8: The penetration time (in x-axis) is increased for a lower resistivity η_0 (in black), and the amplitude on the resonant surface is also lower.
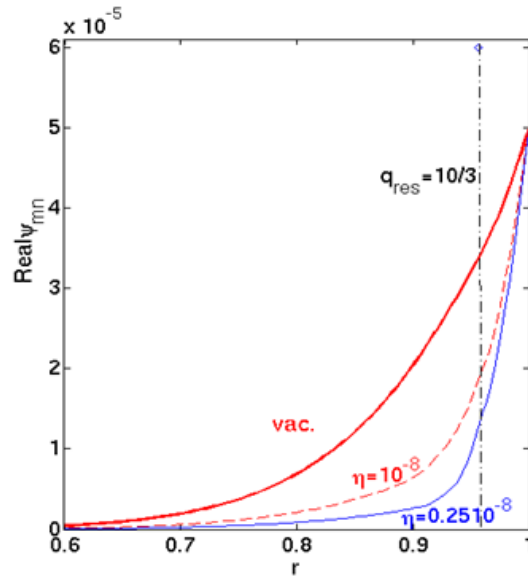
Figure 3.9: The screening of the perturbation is larger for a lower resistivity (in black): the amplitude of the Fourier component of the magnetic pertubation $\psi_{n,m}$ on the resonant surface $q = 10/3$ is lower.

3.2.3 Conclusion of the cylindrical modeling

The cylindrical modeling with the reduced MHD code RMHD, including diamagnetic and neoclassical effects, allows for observing the main features of the plasma response to RMPs. When RMPs are applied in a rotating plasma, either RMPs penetrate and magnetic island chains are formed on the rational surfaces, or they can be screened by the plasma flows which induce response currents on the rational surfaces, counteracting the applied RMPs.

The cancelation of the electron perpendicular velocity at the vicinity of a resonant surface $q = m/n$ has been identified as the condition which enables the formation of magnetic island chains on the resonant surface, due to the RMP penetration. RMPs also penetrate at the edge where the high resistivity ($\propto T^{-3/2}$) prevents the screening currents from growing.

When RMPs penetrate, the RMP penetration is accompanied by the braking of the electron perpendicular rotation which makes the penetration easier. This braking is due to the non-linear evolution of the radial electric field induced by RMPs. The poloidal neoclassical friction is found to act similarly as a viscous force: it reduces the modification of the radial the electric field by RMPs and thus prevents the resonant braking: so the neoclassical friction reduces the "penetration window" Δq_{95} where the RMPs penetrate around the surface where the electron perpendicular velocity cancels.

The RMP penetration is facilitated by a larger applied RMP amplitude, which also enlarges the "penetration window" Δq_{95}. Since this penetration window depend on the rational surface and thus on the poloidal harmonic m considered, two poloidal harmonic should be able to penetrate if the amplitude of the RMPs is large enough. The overlapping of these two following island chains can then generate an ergodic zone, where the radial transport is increased: this allows for locally reducing the pressure gradient under the triggering threshold. However, the maximum amplitude of the applied RMPs is limited by the risk of triggering "locked modes" which are deleterious for the plasma operation. The plasma response to RMPs is given for realistic JET parameters, as well as for the parameters foreseen for the ITER standard H-mode scenario in [Bécoulet 2012].

Nevertheless, these statements have to be either confirmed or review in more realistic toroidal geometry. Moreover, the interaction between RMPs and ELMs cannot be raised here. This motivates the studies presented in the following.

3.3 RMP screening by flows in JET in toroidal geometry

Several parameters – such as the electron perpendicular rotation, the plasma resistivity, the neoclassical friction and the amplitude of the applied RMPs – have been highlighted to impact the RMP penetration in cylindrical geometry. However in the cylindrical modeling, several elements of physics, such as the SOL transport and the impact of the X-point, have been neglected. As well, only current instabilities were included in the cylindrical model and all curvature effects and hence balloonning modes (ELMs) were

neglected. Thus it is necessary to verify the above mentioned results in realistic toroidal geometry.

This motivates the use of the JOREK code – which addresses these missing elements of physics – to simulate the plasma response to RMPs in realistic geometry, including the X-point and the SOL. In the following, JOREK simulations are presented, first for JET realistic parameters, then for the parameters foreseen in the ITER H-mode reference scenario, and last for MAST parameters. Note that the interaction between RMPs and ELMs, which can also be addressed by JOREK simulations, will be presented in chapter 5.

3.3.1   Input parameters

In this section, JOREK simulations are run for JET-like plasma parameters: $R = 3m, a = 1m, B_t = 2.9T, q_{95} \sim 3$ in toroidal geometry including the X-point and the SOL. Typical H-mode density and temperature initial profiles are chosen: the central electron density is $n_{e,0} = 6 \times 10^{19} m^{-3}$, the central temperature is $T_{e,0} = 5keV$ and the central toroidal rotation is $\Omega \sim 9kHz$. Input profiles are given in Fig. 3.10. Realistic profiles of the neoclassical coefficients are used in this section, given in Fig. 3.11. The RMP spectrum generated by the external Error Field Correction Coils (EFCC) [Liang 2007b] is considered in the simulations, with the following configuration: a toroidal symmetry $n = 2$ is taken and a current $I_{coil} = 40kAt$ is injected in the EFCC. The vacuum magnetic flux perturbation calculated with ERGOS is given in Fig. 3.12.
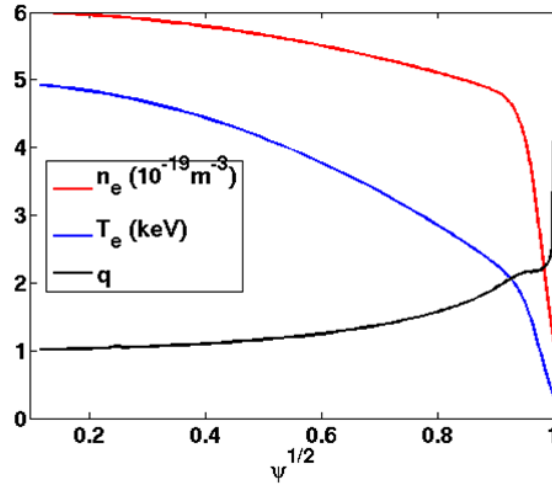
Figure 3.10: Initial radial profiles at $t = 0$ for JET-like simulations: electron temperature T_e in keV, density n_e in $10^{19} m^{-3}$ and safety factor q. These profiles are typical experimental JET profiles (previously used in simulations in [Huysmans 2009]); the q-profile is almost flat in the pedestal due to the bootstrap current.
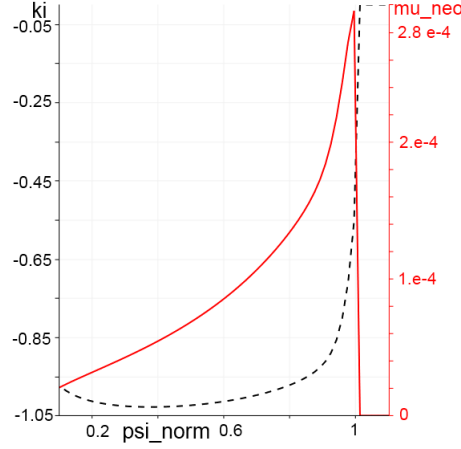
Figure 3.11: Realistic radial profiles of the neoclassical coefficients k_i (left axis) and $\mu_{i,neo}$ (right axis) used for simulations in the JET case.
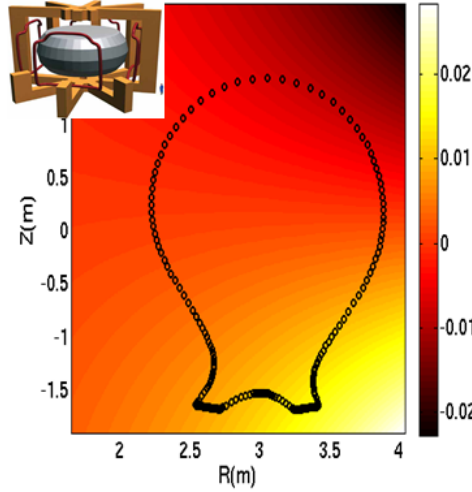
Figure 3.12: cosine component of the $n = 2$ magnetic flux perturbation generated by EFCC for $I_{coil} = 40kAt$. The black dots correspond to the boundary of the computational domain where the perturbations are applied.

3.3.2 Equilibrium plasma flows

The modeling of the plasma flows in a consistent way is primordial since they impact the penetration or the screening of the RMPs. In this subsection, equilibrium plasma flows are first studied without RMPs, in order to highlight the patterns generated by the different effects both in the scrape-off layer and the pedestal, in the poloidal and toroidal directions.

In the SOL, the poloidal and toroidal flows are mainly set by the sheath boundary conditions: the parallel $Mach = 1$ condition ($V_\parallel = \pm C_s$, where C_s is the ion sound speed) set on the divertor targets results in the evolution of the parallel velocity in the SOL until an equilibrium parallel flow is reached, characterized by an opposite direction in the low and high field sides and a "stagnation point" located at the top of the SOL

(Fig. 3.13). The divergence-free condition of the velocity thus constrains also the poloidal flow pattern (Fig. 3.14) in the SOL.
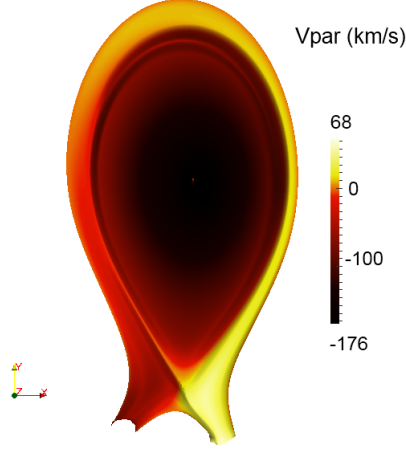
Figure 3.13: Parallel velocity (in km/s) in the JET case
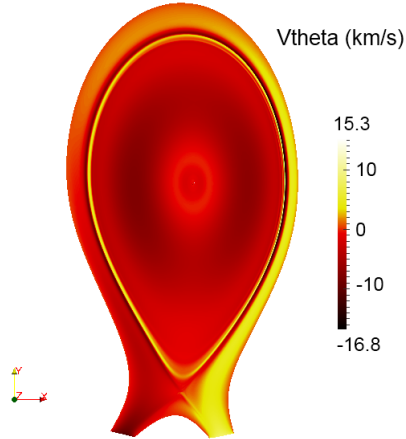
Figure 3.14: Poloidal velocity (in km/s) in JET

As for the central plasma, the parallel velocity (Fig. 3.13) is constrained by the source of parallel velocity which mimics the experimental profiles. In the poloidal direction, the flows (Fig. 3.14) are close to their neoclassical prediction (Fig. 3.15), especially in the strong temperature gradient pedestal region where neoclassical damping is strong.

The radial electric field E_r (Fig. 3.16) resulting from the equilibrium force balance (*Eq.* (2.35)) adapts accordingly. In particular, in the pedestal, a deep electric field well is generated by the diamagnetic terms (Fig. 3.16), reaching up to $-10^5 V/m$, which is in the ballpark of the values measured in the experiments [Andrew 2008]. Note that E_r has been estimated only in a few papers, so we compare our case with another pulse, presented in *Ref.* [Andrew 2008], corresponding to different pedestal profiles which are anyhow comparable.The absolute value of E_r at the bottom of the well is five times larger in our simulation than in the pulse considered in *Ref.* [Andrew 2008], yet this
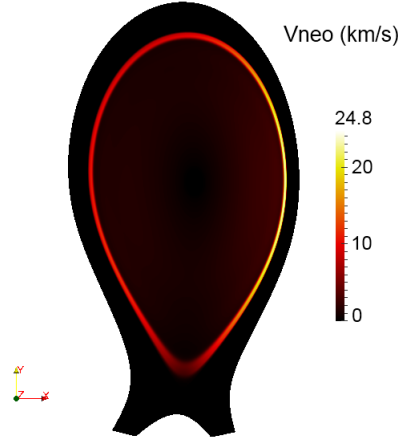
Figure 3.15: Neoclassical velocity (in km/s) in JET
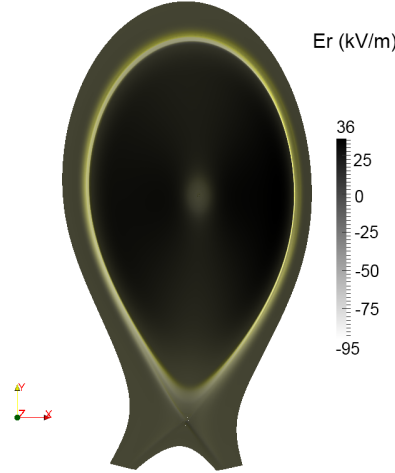
Figure 3.16: Radial electric field (in kV/m) in JET with diamagnetic effects, neoclassical effects and the source of toroidal rotation

is consistent with the fact that the pedestal is much higher in our case and thus the diamagnetic velocity is larger than in *Ref.* [Andrew 2008]. Indeed, the values of the density $(5 \times 10^{19} m^{-3})$ and temperature $(2keV)$ at the top of the pedestal are 2-3 times larger in our simulation than in the experimental pulse considered in *Ref.* [Andrew 2008]. Therefore the pressure gradient and consequently the diamagnetic velocity are around 5 times larger in our case. So the value at the bottom of the E_r well obtained in our simulation – which is approximately proportional to v^* – is consistently 5 times larger than in *Ref.* [Andrew 2008]. Fig. 3.16 also shows that the toroidal source of rotation $(f_{tor} = 9kHz)$ combined with the neoclassical effects make the radial electric field positive in the core. Indeed, in the core plasma, the pressure gradient is close to zero and the poloidal velocity is close to the neoclassical value (proportional to the low temperature gradient), so the radial electric field approximates $E_r = -B_\theta v_\varphi$ in order to satisfy the radial force balance *Eq.* (2.35). The radial electric field is thus positive in the core and negative in the pedestal, so the perpendicular electron velocity $v_{\perp,e} = v_{E \times B} + v_e^*$

(depending on E_r) is zero on a particular surface at the top of the pedestal. If this surface is a rational surface ($q = m/n$, n being the mode driven by the RMPs), the magnetic perturbation is likely to fully penetrate [Nardon 2010, Bécoulet 2012, Orain 2012]. The radial profiles of the parallel, poloidal, neoclassical and perpendicular velocities and the radial electric field are given in Fig. 3.17 (Low Field Side) and Fig. 3.18 (High Field Side) at the midplane.
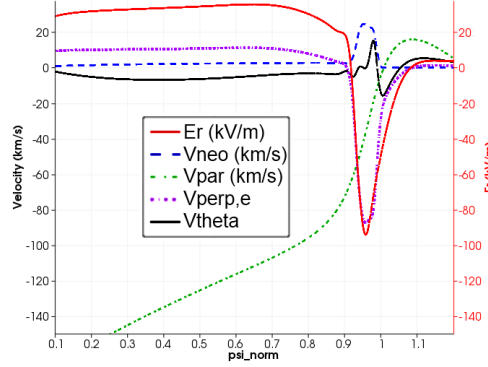
Figure 3.17: Radial profiles of the parallel, poloidal and neoclassical velocities and radial electric field at the Low Field Side at the midplane
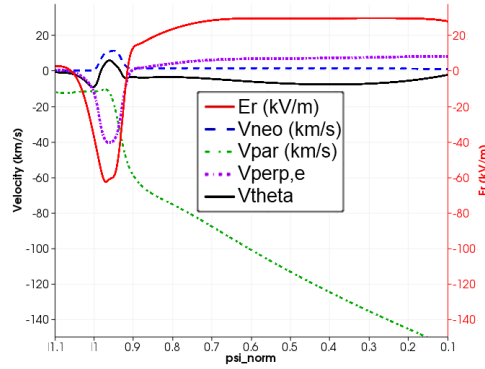
Figure 3.18: Radial profiles of the parallel, poloidal and neoclassical velocities and radial electric field at the High Field Side at the midplane

3.3.3 RMP screening by large diamagnetic rotation and low resistivity

Once the equilibrium flows are established, RMPs ($n = 2$, generated by EFCC, $I_{coil} = 40kAt$) are progressively increased at the boundary in $\sim 1000 t_A$. Without RMPs, the $n = 2$ mode is marginally stable (Fig. 3.19). In the presence of RMPs, the flux of magnetic perturbation (Fig. 3.20) penetrates inside the plasma: the energy of the $n = 2$ toroidal mode grows, until a quasi-steady state is reached (Fig. 3.19). On the resonant surfaces ($q = m/n, n = 2, m \geq 3$), magnetic islands grow up to the saturation, due to reconnection

forced by magnetic perturbations. Parallel current perturbations (Fig. 3.21) are induced on these resonant surfaces in response to the magnetic perturbations and allow for the screening of the RMPs: if the response current is in phase with the radial magnetic perturbation on a given resonant surface, the corresponding RMP harmonic is screened. If the magnetic and current perturbations are in antiphase, the magnetic perturbation penetrates on the corresponding resonant surface as in vacuum and can even be amplified [Bécoulet 2012].
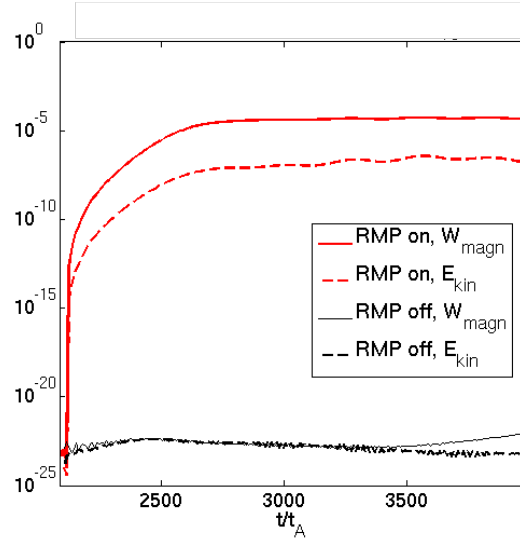
Figure 3.19: Time evolution of the magnetic and kinetic energies (in arbitrary units) of the $n = 2$ mode without/with RMPs, at high resistivity $\eta_0 = 10^{-7}$ and slow diamagnetic rotation ($\tau_{IC} = 10^{-3}$). Time is normalized to the Alfvén time t_A.
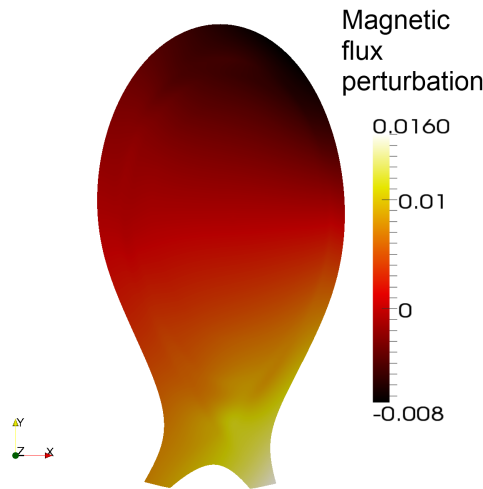
Figure 3.20: $n = 2$ magnetic flux perturbation $\psi_{n=2}$ penetrating in the plasma ($\eta_0 = 10^{-7}$, $\tau_{IC} = 10^{-3}$)
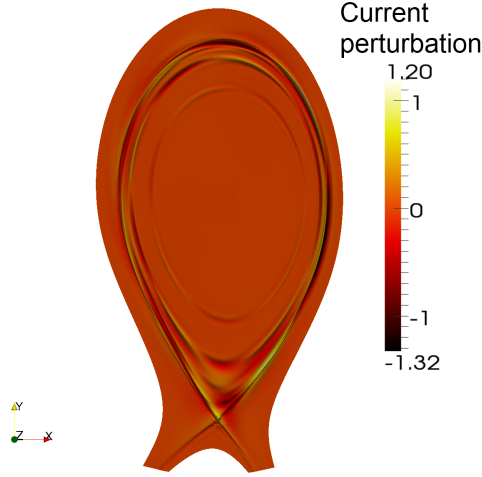
Figure 3.21: Response toroidal current perturbation $J_{n=2}$ on the resonant surfaces due to RMPs ($\eta_0 = 10^{-7}$, $\tau_{IC} = 10^{-3}$)

These induced currents depend both on the plasma flows and on the resistivity, so the different terms influencing the flows (diamagnetic velocity, neoclassical friction and source of parallel rotation) and affecting the plasma response to RMPs are progressively added in the simulation. The central resistivity is scanned between $\eta_0 = 10^{-7}$ and $\eta_0 = 5 \times 10^{-8}$ (in JOREK units). Note that for numerical reasons these values are taken $1 - 2$ orders of magnitude larger than the realistic (Spitzer) value in JET ($\sim 10^{-9}$).

The effects of the diamagnetic flow and the resistivity are first studied ; the source of parallel momentum and then the neoclassical friction are added in the model over a second phase. In all the studied cases, the central harmonic of the perturbation located on the resonant surfaces $q = 3/2$ is screened. The Poincaré plot of the magnetic topology is given in Fig. 3.22 (here for low poloidal rotation $\tau_{IC} = 10^{-3}$ and high resistivity $\eta_0 = 10^{-7}$). Note that θ_{geom} (only used in the Poincaré plots) represents the geometric poloidal angle, which differs from the intrinsic angle θ defined in section 2.5. θ_{geom} is defined as follows:

$$\theta_{geom} = \begin{cases} \arctan((Z - Z_0)/(R - R_0)) & \text{for} R > R_0 \\ (\pi - \arctan|\frac{Z-Z_0}{R-R_0}|) \times \text{sign}(Z - Z_0) & \text{otherwise} \end{cases}$$

The Poincaré plot (Fig. 3.22) shows that small islands are generated on the resonant surface $q = 4/2$: this means that the screening of the ($m = 4, n = 2$) harmonic is only partial. However the magnetic perturbation mostly penetrates at the very edge of the plasma where the resistivity is higher (Fig. 3.22). In these simulations, the magnetic shear is strong for $q \geq 2.5$ (Fig. 3.10) so the proximity of the surfaces $q = 5/2$ and $q = 6/2$ explains the formation of a stochastic layer at the edge, for $\psi \geq 0.97$ (Fig. 3.22). Yet, since the modes $m \geq 6$ are located too close to the separatrix, only the $m = 5$ mode seems to develop significantly, as suggested by the structure of the density and temperature
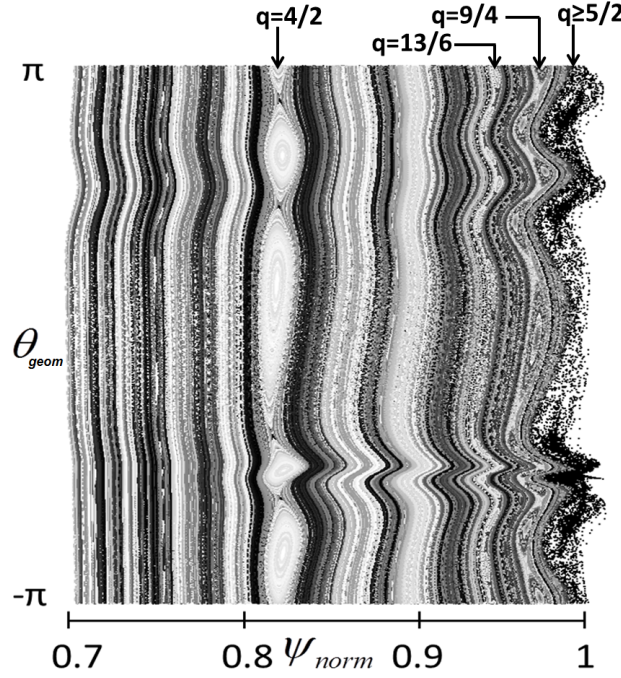
Figure 3.22: Poincaré plot of the magnetic topology in (ψ_0, θ_{geom}) coordinates ($\eta_0 = 10^{-7}$, $\tau_{IC} = 10^{-3}$).

perturbations presented in Fig. 3.24 and Fig. 3.25. It is also interesting to note that the coupling of the modes generates secondary islands on the rational surface $q = 9/4$ and even tertiary islands on $q = 13/6$ (Fig. 3.22). The observation of these secondary and tertiary islands can be explained by the flat q-profile in this area (Fig. 3.10), since the island size is inversely proportional to the magnetic shear $dq/d\psi$ ([Lieberman 1983]). The secondary islands are the result of the non-linear coupling between the $n = 2$ mode with itself whilst the tertiary islands correspond to the coupling between this resulting $n = 4$ component with $n = 2$. Even though the $n = 4$ and $n = 6$ modes are not explicitly included in these simulations, they appear nonetheless as a result of non-linear couplings.

From the resistivity scan and the progressive addition of the different flows, we find that the diamagnetic rotation and the resistivity are the two main parameters affecting the penetration of the RMPs, and three different regimes are identified depending on these two parameters (Fig. 3.26).

At low diamagnetic rotation ($\tau_{IC} = 10^{-3}$, which is half the realistic value) and high resistivity ($\eta_0 = 10^{-7}$), the generated islands rotate in the electron diamagnetic direction at the ion poloidal rotation frequency $f^* \sim m\frac{V_\theta}{2\pi r_{res}}$, where m is the poloidal mode number corresponding to the resonant surface. The main poloidal mode generated being the $m = 5$ mode (Fig. 3.24 and Fig. 3.25), the oscillation of the magnetic energy of the $n = 2$ mode (Fig. 3.26) mainly corresponds to the rotation of the magnetic islands on the surface $q = 5/2$ at the frequency $f^* \sim 6kHz$. The amplitude of these islands oscillates at the same frequency f^*: indeed, while they are rotating with the plasma, they successively face maxima and minima of external static magnetic perturbations, which explains the
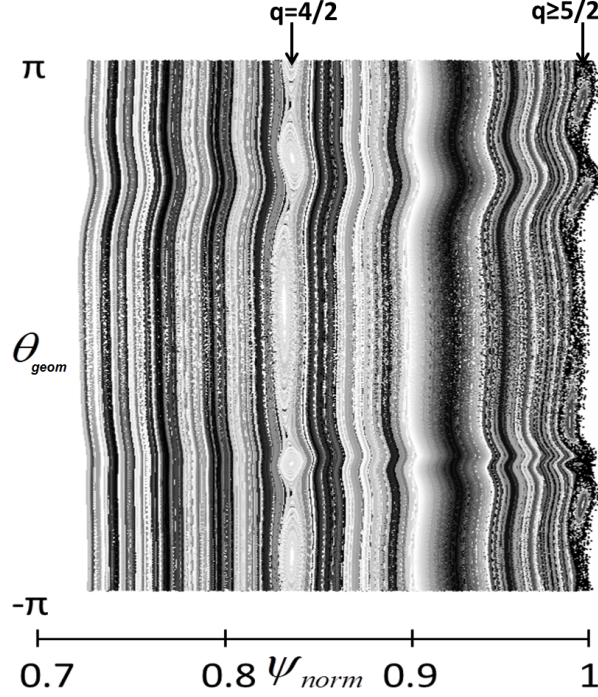
Figure 3.23: Poincaré plot of the magnetic topology in (ψ_0, θ_{geom}) coordinates at larger diamagnetic rotation $\tau_{IC} = 2 \times 10^{-3}$ (Resistivity is kept $\eta_0 = 10^{-7}$). Note that the islands generated by the RMPs are smaller compared to Fig. 3.22, which points out the larger screening induced by the large diamagnetic (poloidal) rotation.
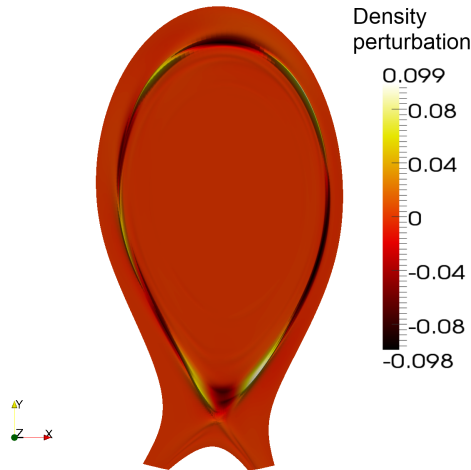
Figure 3.24: $n = 2$ density perturbation with RMPs, mainly located on the resonant surface $q = 5/2$ ($\eta_0 = 10^{-7}$, $\tau_{IC} = 10^{-3}$)

fluctuation of the island size at the frequency f^*. This mode is probably related to the Rutherford regime described in the Fitzpatrick theory [Fitzpatrick 1998] and such an oscillating regime is also found in simulations with toroidal rotation included [Izzo 2008].
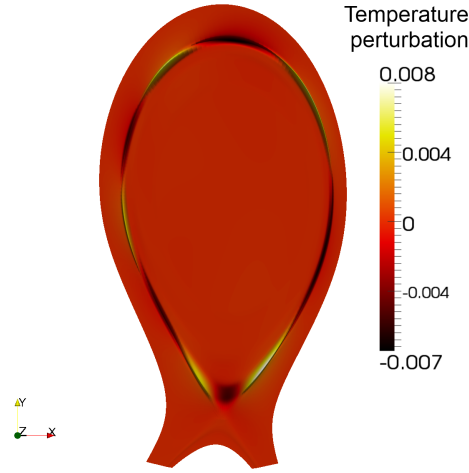
Figure 3.25: $n = 2$ temperature perturbation with RMPs, mainly located on the resonant surface $q = 5/2$ ($\eta_0 = 10^{-7}$, $\tau_{IC} = 10^{-3}$)
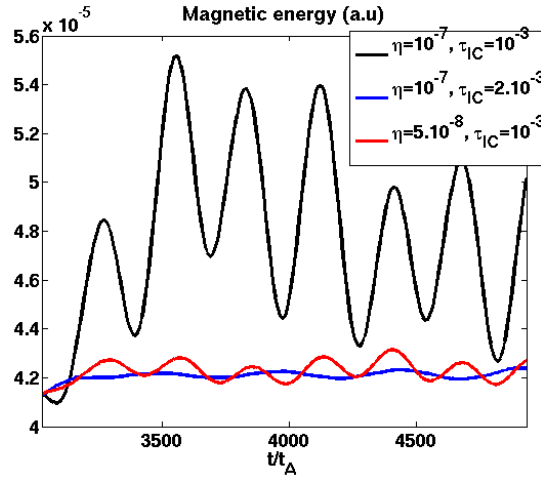
Figure 3.26: Three different regimes of penetration of the RMPs: magnetic energy of the $n = 2$ mode depending on the diamagnetic parameter τ_{IC} and the plasma resistivity η_0

Small fluctuations of the SOL density and temperature are observed in this regime to rotate at the same frequency as the magnetic flux fluctuations (Fig. 3.27, solid line). Note that the volume integrated density and temperature in the SOL increase when switching on the RMPs, suggesting an enhancement of the density and heat transport due to the formation of an ergodic region at the edge (Fig. 3.22). However no significant changes in plasma density and temperature profiles were observed in modeling ; the density pump-out has not been observed so far: less than 1% of the pedestal density is lost in the simulations, as compared to up to 20% in the experiments [Evans 2008, Liang 2007a]. The regime of oscillating islands is possibly related to the ELM suppression regimes at high collisionality (characterized by a smaller pedestal, a smaller diamagnetic rotation and a high resistivity [Suttrop 2011, Moyer 2005]), but more modeling of realistic experimental

cases is needed to confirm this statement.
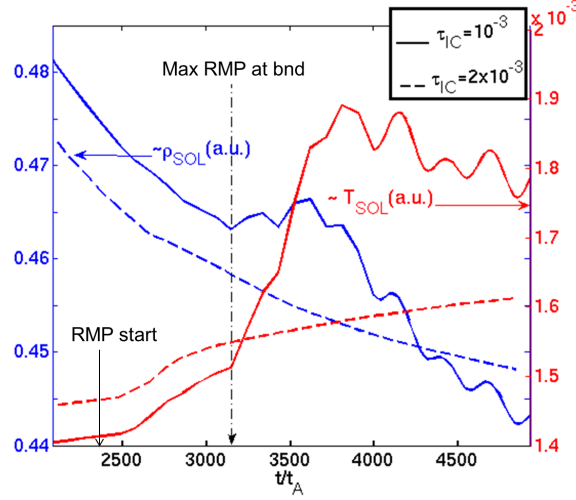
Figure 3.27: Volume integrated electron density and temperature in the Scrape-off layer at resistivity $\eta_0 = 10^{-7}$ for two different diamagnetic velocities ($\tau_{IC} = 10^{-3}$ and 2×10^{-3}).

At larger diamagnetic rotation ($\tau_{IC} = 2 \times 10^{-3}$, corresponding to the realistic value) and high resistivity ($\eta_0 = 10^{-7}$), the driven mode is on the contrary static and "locked" to the external RMPs. The Poincaré plot (Fig. 3.23) shows that the islands generated on the rational surface $q = 4/2$ are smaller at larger τ_{IC}, which means that the RMPs are more screened by the diamagnetic flow. As for the secondary and tertiary islands, they are totally invisible in this case. Consistently, the magnetic energy of the $n = 2$ mode is decreased as compared to the oscillating case (Fig. 3.26). Nonetheless, an ergodic layer is formed at the very edge (for $\psi \geq 0.98$), but its width is smaller and the deformation of the boundary is reduced. The heat transport, slightly enhanced by RMP application (as suggested by the increase in SOL temperature in Fig. 3.27, dash line), is weak compared to the previous case, due to the smaller ergodization of the edge.

An intermediate regime is also found at lower resistivity ($\eta_0 = 5 \times 10^{-8}$) with $\tau_{IC} = 10^{-3}$: the magnetic islands are quasi-static and slightly oscillate at the ion poloidal rotation frequency. The screening level is approximately the same as in the static case.

RMP screening is quantified in these three cases in Fig. 3.28, where the Fourier harmonics ($n = 2, m = 3 - 6$) of the magnetic flux perturbation are plotted. In the three cases, the central islands ($m = 3-4$) are screened on the corresponding resonant surfaces. Yet the Fourier harmonics $|\psi_{mn}|$ ($m = 3-4$) do not totally vanish on the resonant surfaces (which is consequent with the formation of small islands on $q = 4/2$), contrary to the previous modeling in cylindrical geometry [Bécoulet 2012] where the central harmonics were totally screened. The discrepancy between cylindrical and toroidal modeling is not really understood, but will be discussed in section 3.4. Regarding the edge harmonics ($m = 5 - 6$), the amplitude of the Fourier harmonics $|\psi_{mn}|$ is 2-3 times lower in the cases at low resistivity or high diamagnetic rotation than it is in the oscillating case, which means that the corresponding island size, proportional to $|\psi_{mn}|^{1/2}$, is reduced.
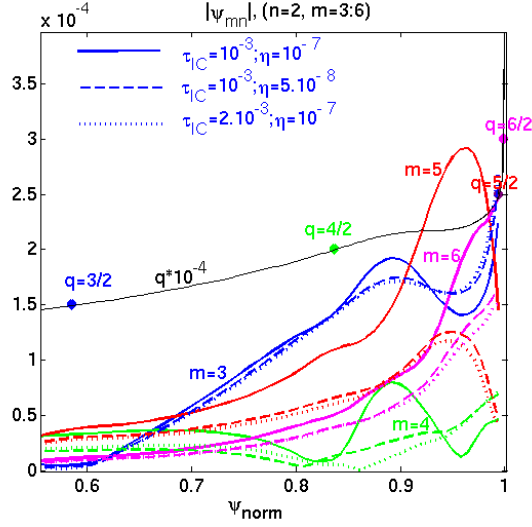
Figure 3.28: Fourier harmonics of the magnetic flux ($n = 2, m = 3 - 6$) depending on the resistivity and the diamagnetic rotation for $t \sim 4950 t_A$.

From now, the source of parallel momentum is added in the model. If the screening effect provided by high diamagnetic rotation and/or low resistivity is clear in the JET case, the effect of the parallel rotation is more complex (Fig. 3.29). As the parallel rotation does not directly affect the screening of RMPs, an increased parallel rotation does not necessarily imply an increased screening of RMPs. Indeed, at low resistivity ($\eta_0 = 5 \times 10^{-8}$), in the slightly oscillating regime characterized by low diamagnetic rotation ($\tau_{IC} = 10^{-3}$), the parallel rotation increases both the average island size and the fluctuation of the island width: this can explain the larger fluctuation of the magnetic energy of the $n = 2$ mode in Fig. 3.29. The oscillation frequency of the islands is also modified by the parallel rotation, probably because of the induced change in the radial electric field and the poloidal rotation. On the contrary, at higher diamagnetic rotation ($\tau_{IC} = 2 \times 10^{-3}$), the energy of the $n = 2$ mode is lower when the parallel velocity source is added, showing a slightly stronger screening by parallel velocity.

Last, in our simulations with the realistic diamagnetic rotation ($\tau_{IC} = 2 \times 10^{-3}$) and the source of parallel rotation (at $\eta_0 = 10^{-7}$), the addition of the neoclassical effects in the model modifies the plasma response. For a same simulation without neoclassical friction, the magnetic islands generated on $q = 5/2$ are static; however with neoclassical effects the generated islands are first static and then progressively rotate in the ion flow direction, until they reach the electron perpendicular rotation frequency f^* (Fig. 3.30). The island width also oscillates at the frequency f^*. We are thus in the same regime of plasma response as for the case at low diamagnetic rotation. The change in the regime of plasma response is not due to a modified perpendicular rotation (in both cases without and with neoclassical effects, the perpendicular velocity is the same at the vicinity of the resonant surface $q = 5/2$). The reason why this regime is obtained at large diamagnetic rotation with neoclassical friction is not really understood, but it may be explained by a change in viscosity resulting from the balance between the neoclassical friction force and
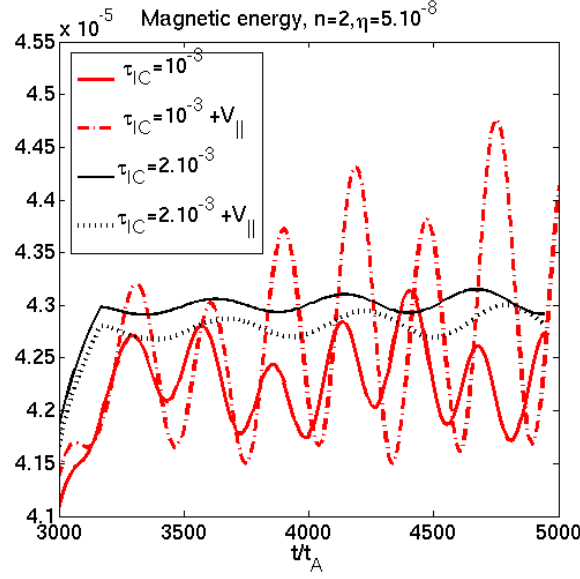
Figure 3.29: Effect of the source of parallel rotation on the magnetic energy of the driven mode $n = 2$ (resistivity $\eta_0 = 5 \times 10^{-8}$) at low ($\tau_{IC} = 10^{-3}$) and high ($2 \times 10^{-3}$) diamagnetic rotation
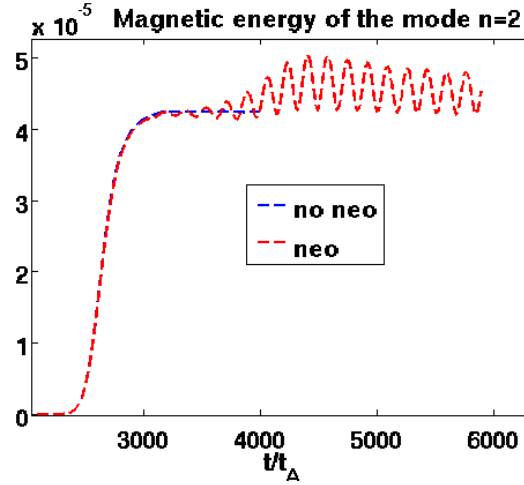
Figure 3.30: Effect of the neoclassical friction on the magnetic energy of the driven mode $n = 2$ (resistivity $\eta_0 = 10^{-7}$) at large diamagnetic rotation (2×10^{-3}). Without neoclassical effects in the model (in blue), the islands are static. With neoclassical friction included (in red), the generated islands are first static but finally rotate at the ion perpendicular rotation frequency.

the viscous force in the momentum equation. More modeling would be necessary to give a global interpretation of the phenomena at stake. The Poincaré plot of the magnetic topology of this case is given in Fig. 3.31. Compared to Fig. 3.23 (case without source of parallel rotation or neoclassical friction), the island width and the size of the ergodic layer is similar. Actually, in all cases, the position where perpendicular velocity cancels (red dashed line on Fig. 3.31) is located between $q = 4/2$ and $q = 5/2$ and does not match

a resonant surface. It explains why the perturbations significantly penetrate only at the very edge ($\psi \geq 0.97$) where resistivity is higher and where the perpendicular rotation is dominated by the diamagnetic effects.
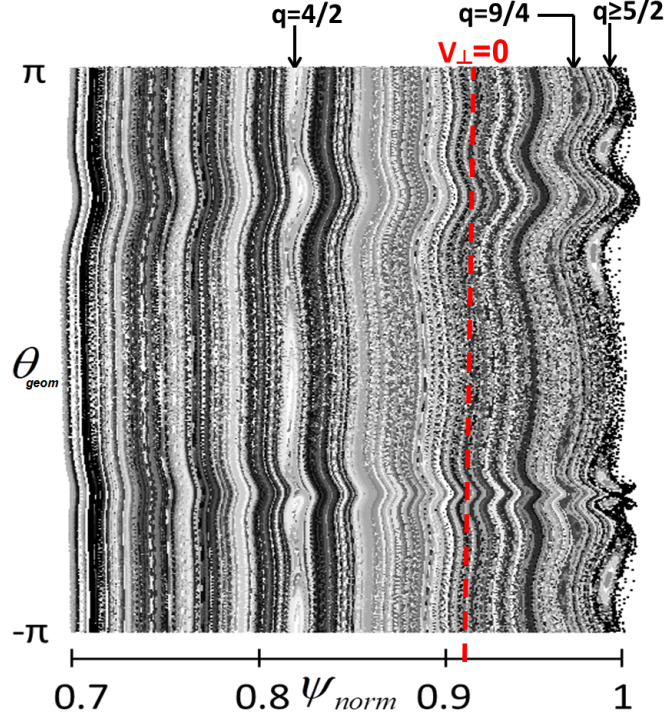
Figure 3.31: Poincaré plot of the magnetic topology in (ψ_0, θ_{geom}) coordinates with diamagnetic rotation ($\tau_{IC} = 2 \times 10^{-3}$), parallel source of rotation and neoclassical friction (resistivity $\eta_0 = 10^{-7}$). The surface where the perpendicular velocity $V_\perp$ cancels (indicated by the red dashed line) does not match a resonant surface, which explains that the RMPs do not fully penetrate.

3.4   Predictions for ITER

3.4.1   Input parameters and equilibrium plasma flows

In this section, the equilibrium and plasma parameters of the ITER standard H-mode scenario $15MA/5.3T$ are used. The machine dimensions are $R = 6.2m, a = 2m$ and the safety factor is $q_{95} = 3.5$. The density, temperature and toroidal rotation profiles are given in Fig. 3.32. Central density is $n_{e,0} = 8 \times 10^{19} m^{-3}$, central temperature is $T_0 = 27.8 keV$ and the initial toroidal rotation profile is similar to the temperature profile with a central arbitrary rotation frequency $\sim 0.9 kHz$, which is in the range of the expected value in ITER. The flux-aligned mesh used for modeling is given in Fig. 2.3. The resonant magnetic flux perturbations generated by In-Vessel Coils, in the configuration $n = 3$ and a current $I_{coil} = 54 kAt$ (Fig. 3.33, [Schaffer 2008]) are calculated from the vacuum code ERGOS [Bécoulet 2008] and are applied as boundary conditions in $10^3 t_A$ in the same way as in the previous section.
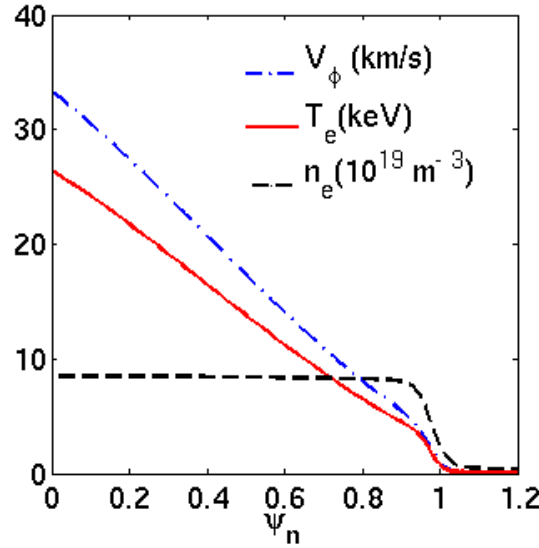
Figure 3.32: ITER input density, temperature and toroidal rotation profiles

Equilibrium plasma flows are computed for a central resistivity $\eta_0 = 10^{-8}$, which is, for numerical reasons, 100 times higher than the normalized Spitzer value calculated for ITER ($\eta_0 = 10^{-10}$). As the diamagnetic parameter is inversely proportional to $F_0 = R_0 B_{\varphi 0}$, the value for ITER $\tau_{IC} = 5 \times 10^{-4}$ is 4 times smaller than in the JET simulation. Neoclassical coefficients are taken constant in this part for simplicity: $\mu_{neo} = 10^{-5}$ and $k_i = -1$ [Bécoulet 2012]. The profiles of the parallel, poloidal and neoclassical velocities along the midplane are given in Fig. 3.34. The equilibrium radial electric field $E_r = -\nabla_\perp u \cdot \nabla\psi/|\nabla\psi|$, with the characteristic well in the pedestal, is plotted in Fig. 2.4.
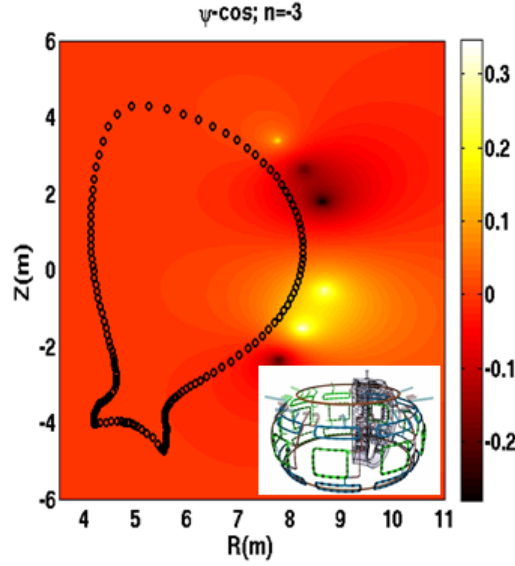
Figure 3.33: Vacuum solution for the magnetic flux perturbation ($n = 3$, IVC at max $I_{coil} = 54kAt$) from the ERGOS code, JOREK boundary in black and sketch of the ITER RMP coils in the bottom right corner
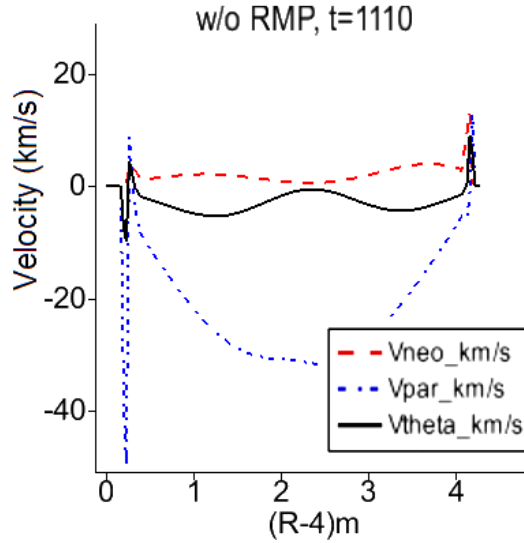
Figure 3.34: Profiles of the parallel, poloidal and neoclassical velocities along the midplane in ITER simulations

3.4.2 RMP screening in ITER

When the RMPs are not activated, the $n = 3$ mode remains stable: as shown in Fig. 3.35, the magnetic energy of the $n = 3$ mode is negligible. When RMPs are switched on (Fig. 3.33) at the boundary of the computational domain, the energy of the $n = 3$ toroidal harmonics grows until it saturates, corresponding to the saturation of the size of the magnetic islands generated by the RMPs on the resonant surfaces $q = m/3, m \geq 4$. These magnetic islands are static: they are "locked" to the external RMPs and their

size is constant. The magnetic flux perturbation $n = 3$ is given in Fig. 3.36. The plasma response is manifested by a perturbation of the parallel current induced on the resonant surfaces (Fig. 3.37). The perturbation of density (Fig. 2.5 (b)) and temperature (Fig. 3.38) mainly develops at the very edge ($q = m/3, m \geq 10$) where the resistivity is higher ; on the more internal resonant surfaces ($q = 4/3 \rightarrow 9/3$), the perturbation vanishes, which means that the central harmonics are screened. The temperature and density perturbations and the stochastization of the edge (for $\psi \geq 0.96$, as shown on the Poincaré plot Fig. 3.42) slightly increase the edge heat and particle transport, resulting in a small degradation of the pedestal (Fig. 3.39).
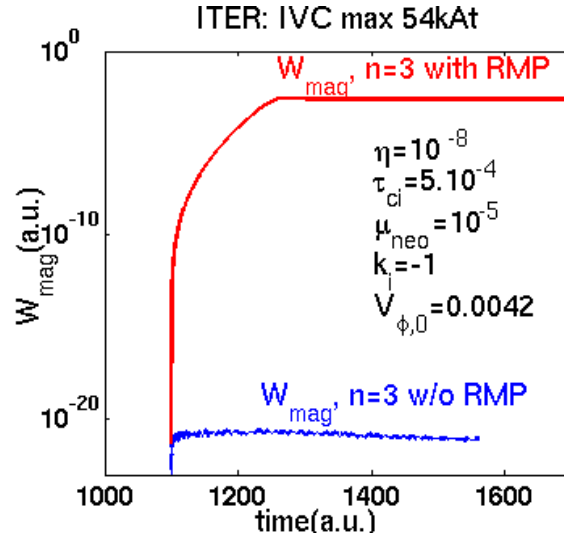
Figure 3.35: Magnetic energy of the $n = 3$ mode without/with RMPs
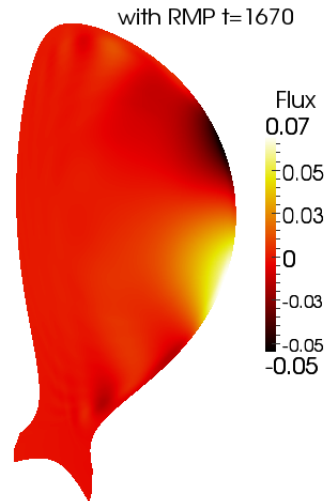
Figure 3.36: Static $n = 3$ magnetic flux perturbation due to RMPs in ITER

The profiles of the Fourier coefficients of the magnetic perturbation $\psi_{m,n}$ calculated with JOREK in presence of the plasma response are compared to the coefficients calculated in the vacuum with the code ERGOS. Compared to the vacuum case
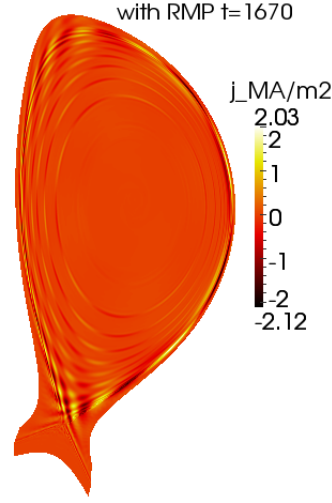
Figure 3.37: $n = 3$ toroidal current perturbation appearing in response to RMPs in ITER
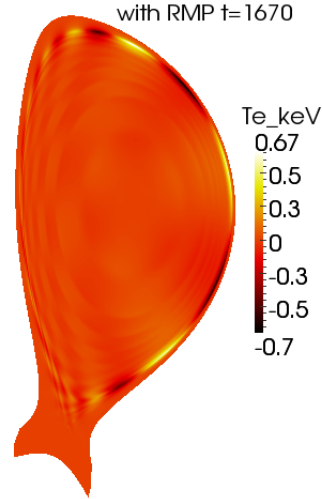
Figure 3.38: $n = 3$ temperature perturbation due to RMPs in ITER

[Bécoulet 2012], the central harmonics $m = 4 - 9$ (Fig. 3.40, Fig. 3.41) are screened by the rotating plasma on the corresponding resonant surfaces $q = m/n$. Yet it is important to note that the screening of the resonant part of the magnetic perturbations is only partial and that the screening factor $|\psi_{m,n}|/|\psi_{m,nvacuum}|$ on the resonance reaches $\sim 10\%$ for $m = 4 - 9$. This partial penetration is consistent with the fact that small magnetic islands are formed on the resonant surfaces (Fig. 3.42). The screening factor is much larger here than in the cylindrical modeling where the resonant component was reduced under 2% [Bécoulet 2012]. Comparatively, other simulations made with toroidal codes [Ferraro 2012, Liu 2010b] also found a similar screening factor ($\sim 10 - 20\%$), which is larger than the results in cylindrical approximation [Heyn 2008, Nardon 2010, Bécoulet 2012] and in the analytical calculations from layer theory [Waelbroeck 2012], where the screening factor ranges between one per mil and a few percent. The discrepancy between modeling in realistic geometry and simpler models is not fully understood.
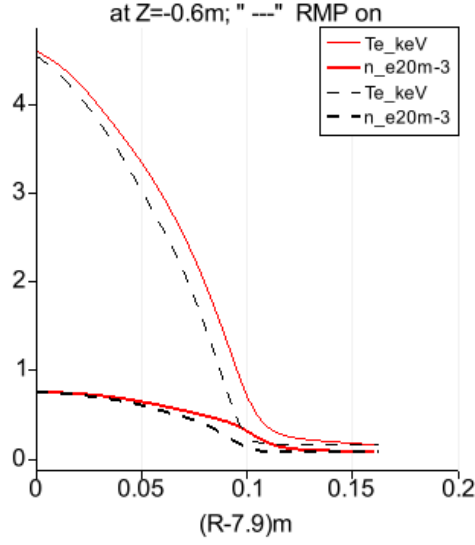
Figure 3.39: Density and temperature profiles at the edge for Z=-0.6m without (full line) and with RMPs (dash)
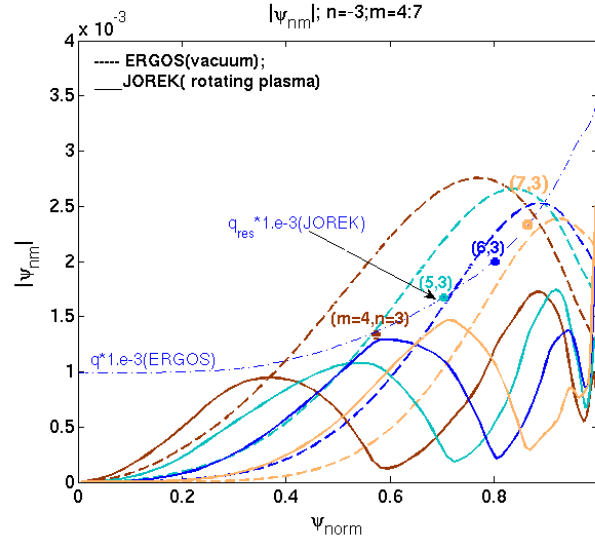
Figure 3.40: Fourier harmonics of the magnetic flux perturbation $|\psi_{m,n}|$, $n = 3$, $m = 4-7$ in the vacuum case (ERGOS code, dash) and taking into account the plasma response (JOREK, full line). The q-profile is given and the positions of the resonant surfaces are indicated by the dots. Note that compared to the vacuum case, all these harmonics $m = 4 - 7$ are screened on the corresponding resonant surfaces $q = m/n$ in presence of the rotating plasma.

Yet in cylindrical geometry, the current profile is less sheared than in toroidal geometry, thus the cylindrical current and q profiles cannot be taken consistently with experiments. Thus in cylindrical modeling we must either keep the cylindrical current profile and thus the q-profile is less sheared, hence moving resonances towards the plasma center; or we
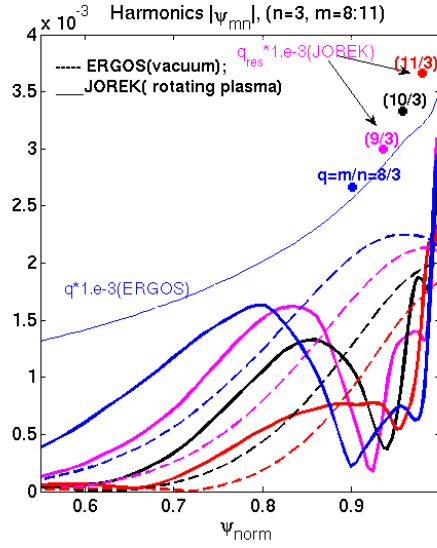
Figure 3.41: Fourier harmonics of the magnetic flux perturbation $|\psi_{m,n}|$, $n = 3$, $m = 8-11$ in the vacuum case (ERGOS code, dash) and taking into account the plasma response (JOREK, full line). The q-profile is given and the positions of the resonant surfaces are indicated by the dots. The edge harmonics $m = 10 - 11$ have a comparable amplitude on the resonant surfaces $q = 10 - 11/3$ in the ERGOS and JOREK cases, showing the penetration of these harmonics in the plasma.

have to use an artificial current to keep the resonant surfaces at the right radial position. This inconsistency may explain the discrepancy between cylindrical and toroidal modeling, however other parameters such as toroidal effects, compressibility or differences in resistivity and viscosity might also play a role.

Another new phenomenon pointed out in toroidal simulations (Fig. 3.40, Fig. 3.41 and [Liu 2010b]) is the amplification of the non-resonant harmonics due to the so-called resonant field amplification (RFA). Indeed, the amplitude of the magnetic perturbations in the core is larger with plasma response than in the vacuum modeling, due to the resonant response of a marginally stable kink mode [Liu 2010a]. At the edge, the amplitude of the resonant harmonics $m = 10 - 11$ (Fig. 3.41) have the same order of magnitude in both vacuum and plasma cases. The magnetic perturbation thus significantly penetrates only at the very edge where the resistivity is the highest, which is similar to the cylindrical non-linear MHD modeling results [Bécoulet 2012].

3.4.3   Stochasticity at the edge

The RMP penetration at the edge generates the formation of islands on the resonant surfaces $q = m/3$, $m \geq 10$. As the edge resonant surfaces are close to each other due to strong magnetic shear, the islands overlap and therefore form an ergodic layer at the edge for $\psi \geq 0.96$, as suggests the Poincaré plot of the magnetic topology in (ψ, θ) coordinates Fig. 3.42.

The formation of the ergodic layer is correlated with a splitting of the separatrix [Joseph 2008].
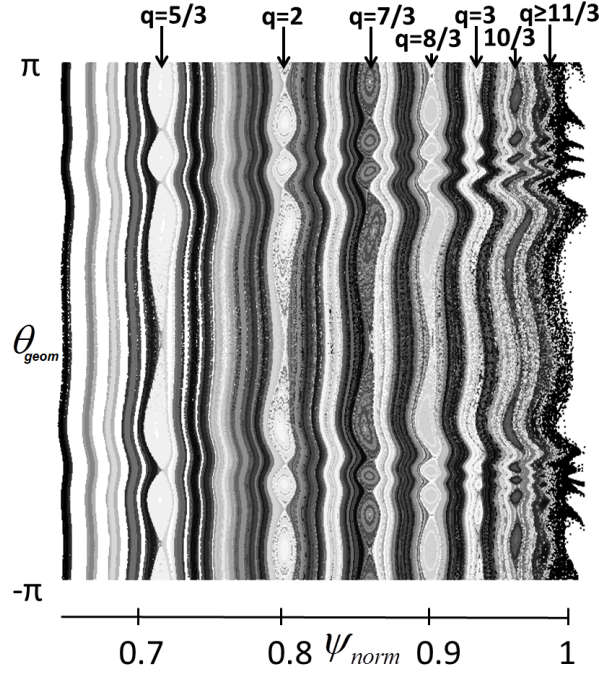
Figure 3.42: Poincare plot of the magnetic topology with RMPs in (ψ_0, θ_{geom}) coordinates: magnetic field lines (starting at the edge inside the separatrix) integration after 200 toroidal turns at $\varphi = 0$. Resonant surfaces $q = m/3, m \geq 5$ are indicated. A stochastic layer is formed for $\psi \geq 0.96$

The separatrix under the RMP transforms into a homoclinic tangle defining the plasma edge [Evans 2005], manifesting itself as lobe structures ($\sim 20cm$) near the X-point (Fig. 3.43) and as smaller finger-like structures ($\sim 6cm$) at the top of the plasma (Fig. 3.44). The homoclinic tangle is defined as the intersection of the two stable and unstable invariant manifolds associated with the X-point, which stem from the splitting of the unperturbed separatrix due to the magnetic perturbation [Evans 2004b, Guckenheimer 1983]. The superposition of the magnetic topology with the plot of the homoclinic tangle (stable and unstable manifolds) defining the deformation of the separatrix is given in Fig. 3.45. These lobes near the X-point are observed in the experiments, either directly ([Kirk 2012], [Chapman 2012]) or as the footprints of high heat and/or particle fluxes where the lobes intersect the divertor [Cahyna 2013b, Evans 2007, Schmitz 2008, Nardon 2011]. Models of plasma response based on a simplified assumption of screening currents on resonant surfaces [Cahyna 2011] or on a linear MHD model [Cahyna 2013a] predict significant shortening of the lobes when the RMP is screened by the plasma response. Shortening is observed in the magnetic field topology [Cahyna 2013a, Nardon 2011, Cahyna 2011] and through the reduction of fluxes [Schmitz 2013, Frerichs 2012] and generally increases with the increase of the width of the plasma region where the RMP is screened [Cahyna 2011]. The shortening of lobes currently represent the most convenient way to quantify experimentally the screening of RMPs. In the same way, in our simulations, the size of the lobes qualifies the screening of the RMPs by plasma flows. In
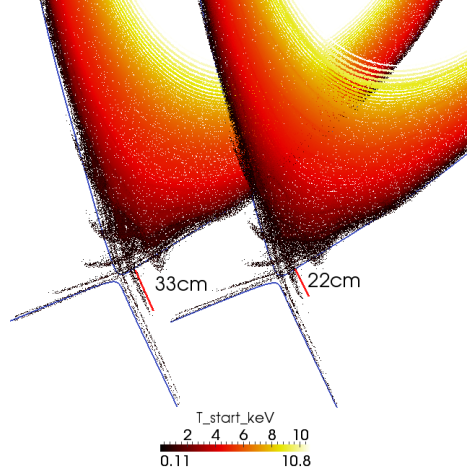
Figure 3.43: Magnetic topology near the X-point in (R, Z) coordinates. A lobe structure characteristic of the ergodicity in X-point geometry is observed. On the left, a RMP simulation without neoclassical, diamagnetic flows or toroidal rotation is run for a central resistivity $\eta_0 = 10^{-7}$. On the right, the same RMP simulation is run with all flows included for a central resistivity $\eta_0 = 10^{-8}$: the resulting lobe size is smaller by $1/3$ compared to the the case without flows.
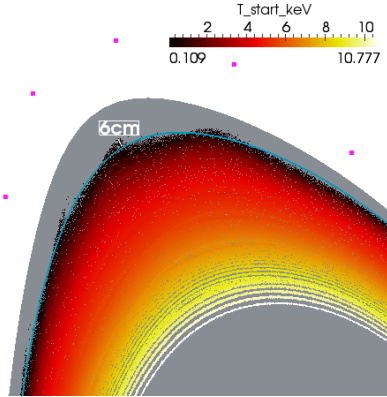
Figure 3.44: Magnetic topology at the top of the machine. Small deformations of the separatrix ($\sim 6cm$) are observed.

Fig. 3.43, a simulation with the same input RMP amplitude is run in two cases: with SOL flows only (induced by sheath conditions) and with all flows included (neoclassical and diamagnetic flows, source of toroidal rotation). The addition of the flows in the simulation shortens the length of the lobe structures near the X-point by $\sim 1/3$, which corroborates the hypothesis (so far deduced from simpler models) that the RMP screening by plasma flows is correlated to lobe/footprint shortening.

A 3D-deformation of the density, temperature and pressure profiles is observed. The deformation of the pressure profile close to the separatrix is found to be due to the mode ($n = 3, m \sim 12$), Fig. 3.46. A small degradation of the density and temperature profiles is
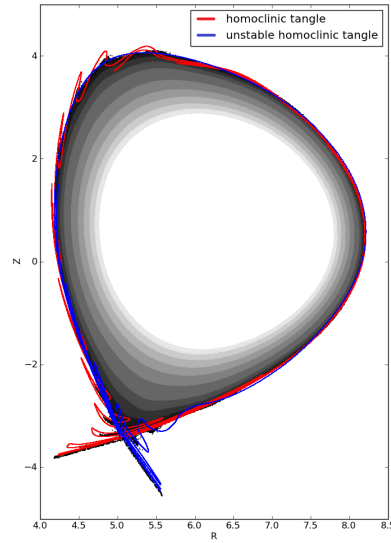
Figure 3.45: Superposition of the Poincaré plot of the magnetic topology in (R, Z) coordinates with the stable (red) and unstable (blue) homoclinic tangles defining the deformation of the separatrix.
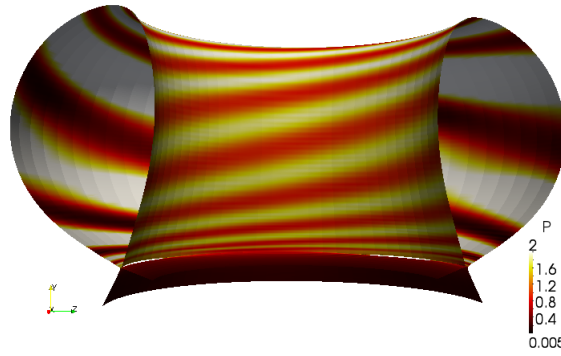
Figure 3.46: 3D-plot of the pressure on an initial equilibrium flux surface without RMP near the separatrix. The 3D-deformation corresponds to a mode $(n = 3, m \sim 12)$.

also observed near the X-point when RMPs are applied. The comparison of the density profile with (Fig. 3.47) and without RMPs (Fig. 3.48) shows the enhancement of the particle transport towards the divertor targets by the RMPs. A similar enhancement of the heat transport is observed. This increase in heat and particle fluxes subsequently generates a small splitting of the strike points on the divertor targets, mostly on the outer target (Fig. 3.49).
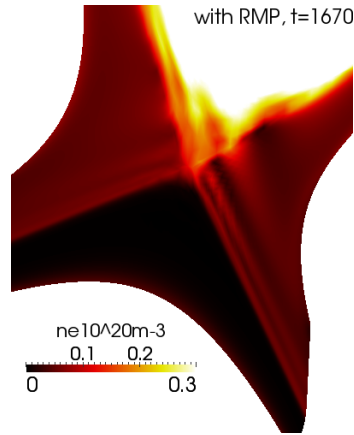
Figure 3.47: Degradation of the density profile near the X-point due to RMPs
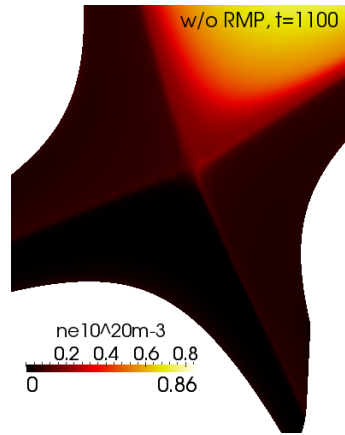
Figure 3.48: Density near the X-point without RMPs
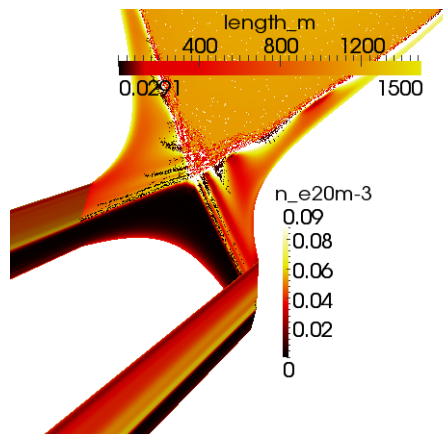
Figure 3.49: 2D-Poincaré plot (in the poloidal plane) of the magnetic topology (connection length) near the X-point, plotted together with the electron density on the divertor targets (toroidal section). Note the induced splitting of the strike points on the outer divertor target.

3.5   Effects of RMPs on MAST in DND configuration

3.5.1   Input parameters
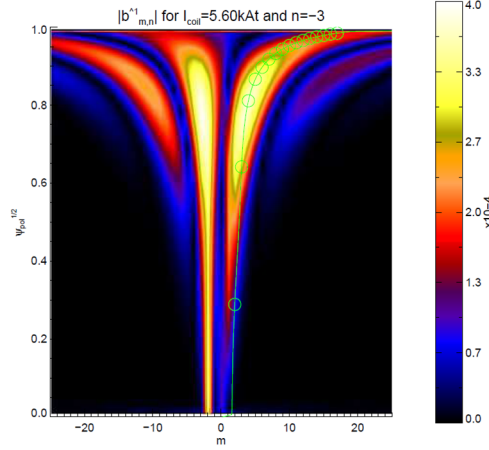
Figure 3.50: Fourier harmonics of the radial magnetic field generated by the RMP coils in disposition "90L": in this configuration, the magnetic perturbation is maximal on the resonances $(m, n = 3)$
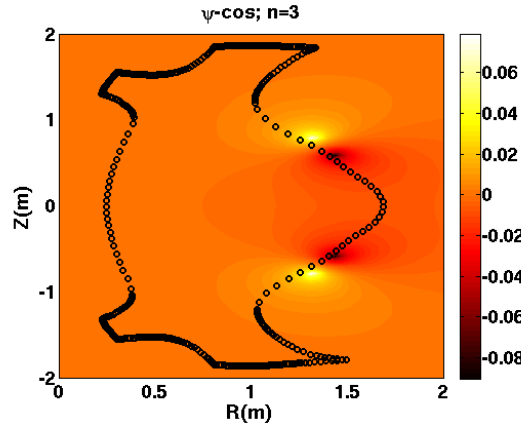
Figure 3.51: Input resonant magnetic perturbation generated by the RMP coils calculated in the vacuum with the ERGOS code and applied as boundary conditions of the computational domain (in black)

RMP penetration in MAST is studied in Double Null Divertor (DND) configuration with plasma parameters corresponding to the shot #24763 (previously considered in [Pamela 2013]). The central density is $n_{e,0} = 4.25 \times 10^{19} m^{-3}$, the central electron temperature is $T_{e,0} = 1.04 keV$ and the central resistivity is taken $\eta_0 = 10^{-7}$ (this is two orders of magnitude larger than the normalized Spitzer value). The disposition of the RMP coils chosen is the "90L" configuration, since it corresponds to a maximal amplitude of the radial magnetic field (generated by the RMPs) located on the resonant surfaces,

as shown in Fig. 3.50. The $n = 3$ Fourier component of the vacuum RMP field imposed at the boundary of the computational domain is given in Fig. 3.51. For numerical reasons, in the simulation the current circulating in the RMP coils is taken to be 1/10 of the experimental value. The reason is that during the transitory phase when RMPs are switched on progressively at the boundary, toroidal currents $J = \Delta\psi$ appear close to the boundary and dissipate when the stationary solution is reached. If the RMP amplitude is too large, these toroidal currents evolve on a very fast time scale, setting a stringent constraint on the allowed time step. For the moment, we did not succeed in optimizing the numerical scheme for the realistic MAST parameters.

Two different cases are studied and compared: first, the simulation is run with only the SOL flows generated by sheath conditions. Second, the diamagnetic effects are added, with a diamagnetic parameter $\tau_{IC} = 10^{-2}$ (note that the large rotation in MAST implies a realistic diamagnetic parameter $\tau_{IC} = 5 \times 10^{-2}$, *ie* 100 times the one of the ITER case, but a lower value is taken here for numerical reasons: as the very large value of τ_{IC} again imposes a severe constraint on the time step, we opted here for intermediate well resolved values; realistic values are left for future work). In this section, neither the source of parallel rotation nor the neoclassical poloidal friction are included in the model so as to focus on the effects of the diamagnetic rotation on RMP penetration.

3.5.2 RMP penetration

In both cases (with or without diamagnetism), a static $n = 3$ mode grows due to the RMPs (Fig. 3.52). The magnetic energy of the mode is a few percent higher in the case including the diamagnetic flow, which means that the diamagnetic effects slightly amplify the magnetic perturbations in this MAST configuration.
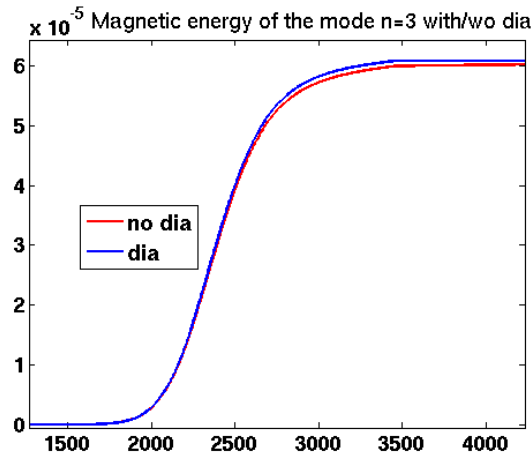
Figure 3.52: Magnetic energy of the $n = 3$ mode driven by RMPs in the 2 cases: without and with diamagnetic effects

The penetration of the magnetic flux perturbation is given in Fig. 3.53 and the induced current perturbations on the resonant surfaces is shown in Fig. 3.54 (case without diamagnetic flow). The electron density (Fig. 3.55) and temperature perturbations (Fig. 3.56,
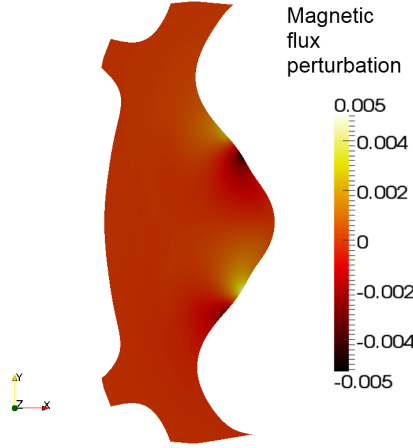
Figure 3.53: Magnetic flux perturbation penetrating in the plasma (without diamagnetic effects)
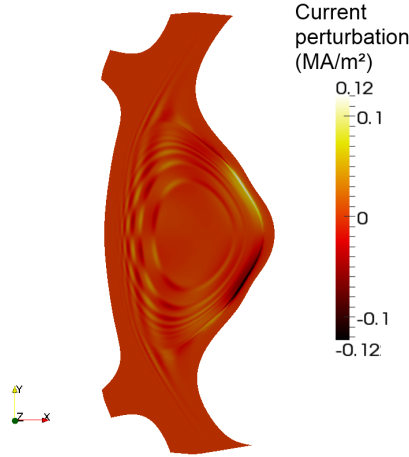
Figure 3.54: Current perturbation generated on the resonant surfaces $q = m/n$, $n = 3$ (without diamagnetic effects)

$n = 3$) represent up to 10% of the central average value and are mainly located at the edge on the LFS, at the proximity of the RMP coils.

The radial profiles of the Fourier harmonics of the magnetic flux perturbation $|\psi_{m,n}|$ ($n = 3$, $m = 4-12$), are presented Fig. 3.57 and Fig. 3.58 for both cases with and without diamagnetic flow. In both cases, the central resonant harmonics $m = 4 - 9$ are screened near the corresponding surfaces $q = m/n$. The screening of the resonant harmonics is only partial (reduced to $\sim 10\%$ of the vacuum perturbation) and magnetic islands are thus generated on the resonant surfaces in both cases (without Fig. 3.59 and with diamagnetic effects Fig. 3.60). These islands are larger in the core plasma in the simulation without diamagnetic rotation: the amplitude of the low poloidal numbers is reduced by the rotation. Also the amplification of the non-resonant magnetic perturbation due to
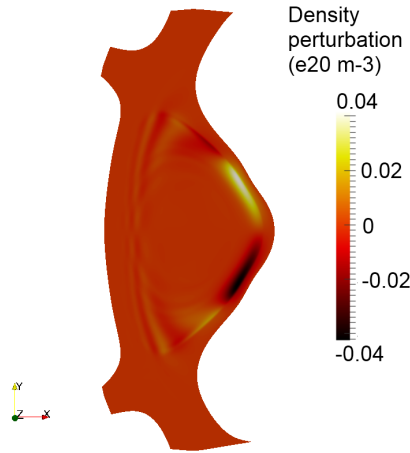
Figure 3.55: Density perturbation with $n = 3$ RMPs in MAST (without diamagnetic effects)
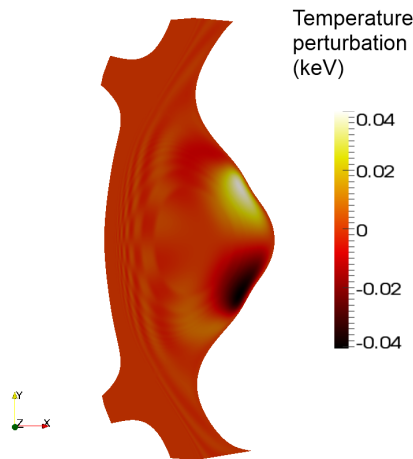
Figure 3.56: Electron temperature perturbation with $n = 3$ RMPs in MAST (without diamagnetic effects)

RFA is observed in the core. At the edge, the harmonics $m = 10 - 12$ penetrate in both cases, but the amplitude is larger in the diamagnetic case (Fig. 3.58): the diamagnetic flow seems to amplify the perturbation at the edge. Indeed the resonant components of the Fourier harmonics $m = 9 - 12$ are slightly larger with diamagnetic effects on the corresponding resonant surfaces $q = m/n$ (Fig. 3.59-Fig. 3.60).

3.5.3 Ergodization and 3D-effects

The penetration of the external RMP harmonics creates an ergodic layer at the edge for $\psi \geq 0.95$ (Fig. 3.59-Fig. 3.60). Related to the ergodization are lobe structures formed near the X-point, as shown in Fig. 3.61 (case with diamagnetic flows included). It is interesting to notice that the presence of the two separatrices in DND configuration
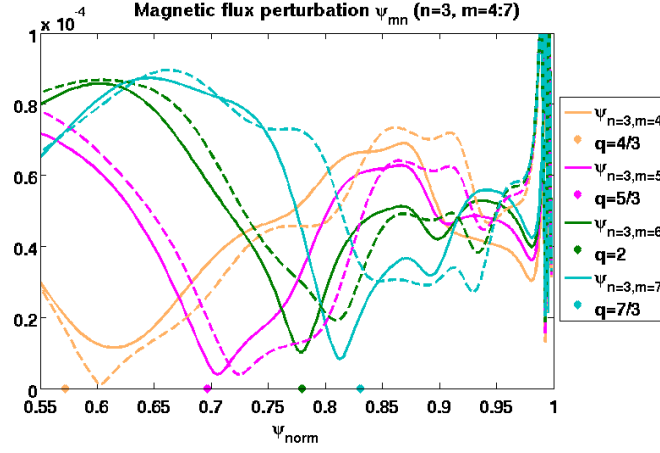
Figure 3.57: Radial profile of the Fourier harmonics of the magnetic perturbation $|\psi_{m,n}|$, $m = 4-7$ in both cases: without diamagnetic effects (dash) and with diamagnetic effects included (full line). The approximate position of the resonant surfaces $q = m/n$ are represented by the dots. All the central harmonics $m = 4 - 7$ are screened near their corresponding resonant surfaces in both cases
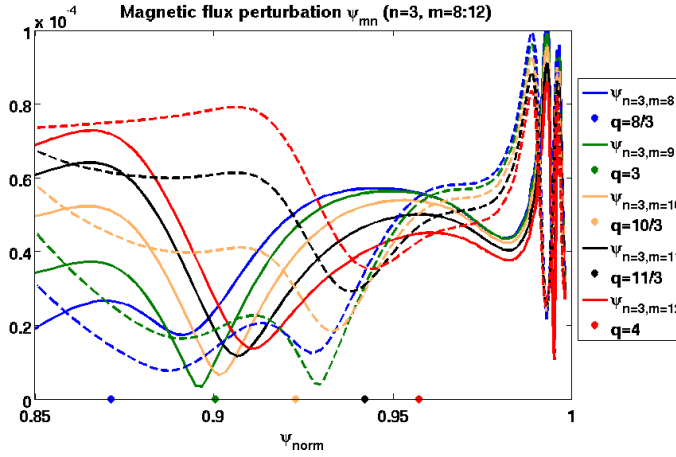
Figure 3.58: Radial profile of the Fourier harmonics of the magnetic perturbation $|\psi_{m,n}|$, $m = 8 - 12$ in both cases: without diamagnetic effects (dash) and with diamagnetic effects included (full line). The approximate position of the resonant surfaces $q = m/n$ are represented by the dots. The more central harmonics $m = 8-9$ are screened near their corresponding resonant surfaces in both cases, whereas the external ones ($m = 10 - 12$) penetrate close to the surface $q = m/n$ in both cases but are slightly more amplified in the case including the diamagnetic effects.

constrains the trajectories of the magnetic field lines so the lobes are only formed in the LFS. This phenomenon is also observed in MAST DND experiments with the fast camera. The size of the lobes in the LFS are comparable in both studied cases (with and without diamagnetic effects).

The 3D-deformation following a $n = 3$ toroidal mode number is observed in both sim-
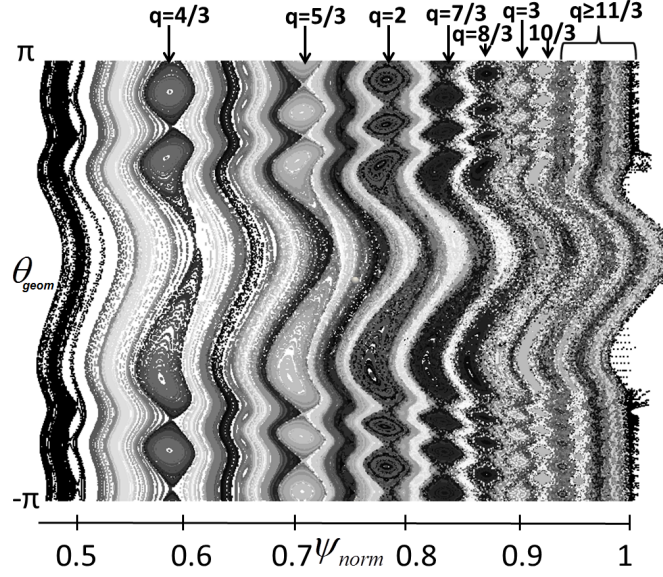
Figure 3.59: Poincare plot of the magnetic topology in MAST without diamagnetic rotation, in (ψ_0, θ_{geom}) coordinates: magnetic field lines integration after 200 toroidal turns. The resonant surfaces $q = m/3, m \geq 4$ are indicated. A stochastic layer is formed for $\psi \geq 0.96$
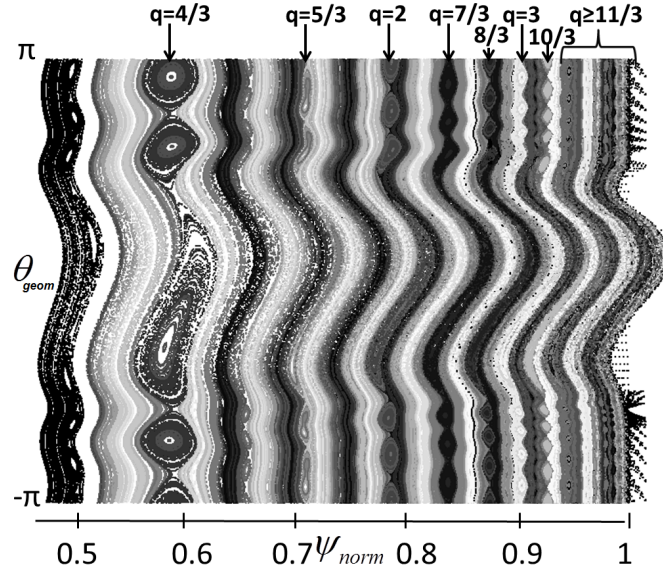
Figure 3.60: Poincare plot of the magnetic topology in MAST with diamagnetic rotation included, in (ψ_0, θ_{geom}) coordinates: magnetic field lines integration after 200 toroidal turns. The resonant surfaces $q = m/3, m \geq 4$ are indicated. A stochastic layer is formed for $\psi \geq 0.96$

ulations in the LFS. The separatrix is displaced towards the interior by a few centimeters at the midplane: $\sim 2 - 3cm$ without diamagnetism and $\sim 1.5cm$ in the diamagnetic
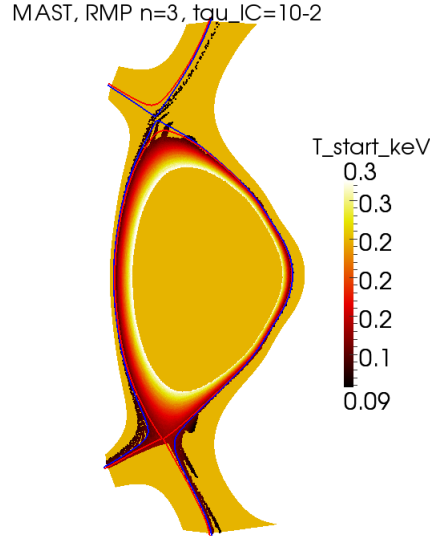
Figure 3.61: Poincare plot of the magnetic topology with diamagnetic flow. The color represents the temperature of the starting point of the field line inside the separatrices. The length of the lobes near the X-points is sensibly the same in the case without diamagnetic flow
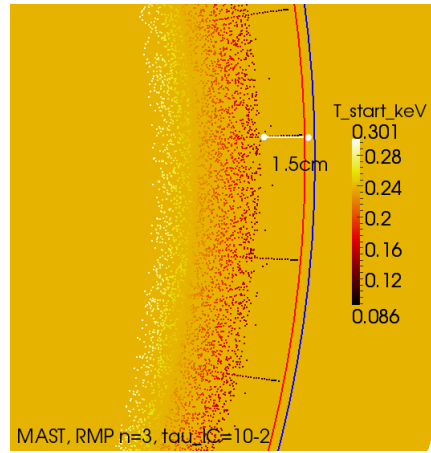
Figure 3.62: Zoom in Poincare plot Fig. 3.61 around the midplane (case with diamagnetic flow): the displacement of the last closed flux surface due to RMPs at the toroidal angle $\varphi = 0°$ is approximately $1.5cm$

case (Fig. 3.62) for a toroidal angle $\varphi = 0°$. The inward displacement of the electron density and temperature profiles at the midplane in the LFS (Fig. 3.63) is maximum for a toroidal angle $\varphi = 0°$ (position where the RMP coils deliver the largest negative flux perturbation) and minimum for $\varphi = 180°$ (angle where the maximum positive flux perturbation is applied). Compared to the density and temperature profiles without RMPs, the gradients are lower in the pedestal when the RMPs are applied, showing a small degradation of the confinement by the RMPs: this can be explained by the enhancement of the heat and particle transport due to the ergodicity at the edge. The 3D-corrugation
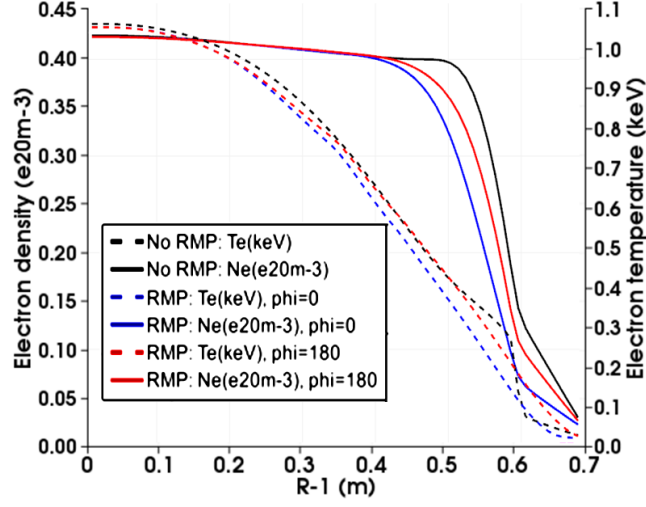
Figure 3.63: Radial profiles of the electron temperature (dash) and the density (full line) at the midplane without RMPs (black), with RMPs at the toroidal angles $\varphi = 0°$ (blue) and 180° (red): note the small degradation of the pedestal and the 3D-deformation of density and temperature due to RMPs
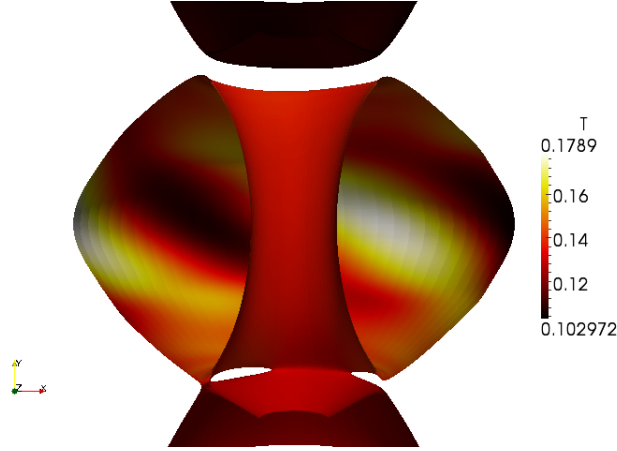
Figure 3.64: 3D-deformation of the electron temperature near the separatrix due to RMPs

of the electron density and temperature profiles are observed: the deformation of the temperature near the separatrix is given in Fig. 3.64.

Last, it is observed in the experiments that the radial electric field is made more positive by RMP application ([Kirk 2011]). This phenomenon was found in simulations in the cylindrical case (section 3.2 and [Bécoulet 2012]) and is also found in our toroidal simulations with JOREK, as plotted in Fig. 3.65 in the LFS (diamagnetic effects are included). The braking of the perpendicular electron velocity $v_{\perp,e}$ induced by RMPs is also evidenced in JOREK simulations (Fig. 3.66), following the same trend as in the experiments ([Kirk 2013a], [Chapman 2012]). If the plasma brakes until $v_{\perp,e}$ becomes zero on the resonant surfaces, the magnetic perturbations are not screened on the resonant surfaces, as it was found in [Nardon 2010, Bécoulet 2012, Orain 2012] and in section 3.2
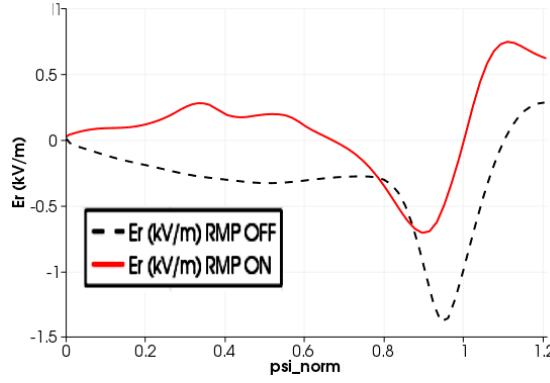
Figure 3.65: Radial profile of the radial electric field at the midplane in the LFS without RMPs (- - black) and with RMPs (red)
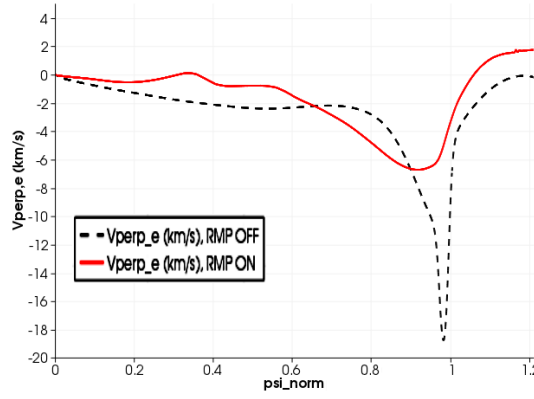
Figure 3.66: Radial profile of the electron perpendicular velocity at the midplane in the LFS without RMPs (- - black) and with RMPs (red)

in cylindrical geometry and here demonstrated in appendix A for toroidal geometry. Fig. 3.66 shows that the damping of the perpendicular electron rotation occurs close to the resonant surface $q = 4/3$ ($\psi \sim 0.58$), which enables the growth of the 4/3 magnetic islands (Fig. 3.60).

It is important to note that this study for the MAST case is a preliminary study, and can only give trends of the effect of RMPs on the plasma in this particular case of a spherical tokamak in DND configuration. Clearly, the size of the displacements calculated here cannot be quantitatively compared to the experiments, since numerical limits imposed us to "minimize" two antagonist effects: on the one hand, the realistic RMP amplitude (10 times the one used in our simulations) should generate much larger penetration, on the other hand the realistic diamagnetic rotation (5 times the one used here) is likely to have much larger screening effects on the RMPs. However these results can be compared qualitatively to the experimental trends.

3.6 Conclusion and discussion

First, the cylindrical modeling of the plasma response to RMPs was presented as an introductory study. Typically, the RMP penetration occurs in a narrow region near the separatrix due to higher resistivity. However, at certain plasma parameters or/and because of the non-linear evolution of the radial electric field due to RMPs, the electron perpendicular velocity $v_{\perp,e} = v_e^* + v_{E \times B}$ can vanish on a rational surface $q = m/n$. In this case, the (m,n) harmonic of the RMPs penetrates locally, which generates magnetic island chains on the resonant surface $q = m/n$. The generic feature of the RMP interaction with a rotating plasma is the following: a larger RMP amplitude, a larger resistivity, a lower electron perpendicular rotation and a lower neoclassical poloidal friction are favourable factors for the RMP penetration.

The will to study the RMP interaction with more realistic plasma flows in a realistic tokamak configuration, as well as to be able to study the impact of RMPs on ELMs, motivated us to carry out the study in toroidal geometry with the JOREK code.

Thus the penetration of the RMPs in the plasma was studied through JOREK simulations – in toroidal geometry including the X-point and the SOL –, taking into account the plasma flows generated by the diamagnetic and neoclassical effects, by a source of toroidal rotation and by the sheath boundary conditions on the divertor. The screening of the RMPs on the resonant surfaces is observed in the center of the plasma in all the studied cases (JET, ITER, MAST) but the screening is only partial. The factor $|\psi_{m,n}|/|\psi_{m,n,vacuum}|$ on the resonance is larger than in the previous cylindrical modeling. The perturbation however significantly penetrates at the edge: magnetic islands grow on the resonant surfaces and eventually form an ergodic layer at the edge (for $\psi \geq 0.95$ in the three studied cases).

In JET geometry, a low plasma resistivity and a large diamagnetic rotation are found to increase the screening of the RMPs. Three regimes of RMP penetration are found depending on these two parameters: at low diamagnetic rotation and high resistivity, the generated islands co-rotate with the plasma electron flow and their size fluctuate at the same frequency. At larger diamagnetic rotation, the islands are static and "locked" to the external static RMPs; a stronger screening of the perturbations is observed. An intermediate regime is observed at lower resistivity, in which the generated island are quasi-static and slightly oscillate. The possible link between these regimes and the difference in ELM mitigation at high and low collisionality [Evans 2008, Moyer 2005] is under investigation. As for the toroidal rotation, depending on the plasma parameters (in particular on the resistivity), it can either reduce or amplify the RMP penetration. Also, contrary to the JET case, the magnetic perturbation seems to be slightly amplified by the diamagnetic rotation at the edge in MAST simulations.

In MAST and ITER cases, static magnetic islands are formed on the resonant surfaces due to $n = 3$ magnetic perturbations. The presence of lobe structures related to the ergodization at the edge are evidenced in both cases ($\sim 20cm$ in ITER, $\sim 7cm$ in MAST). In ITER, the comparison of simulations run with and without flows demonstrates that the plasma rotation reduces the length of the lobes by 1/3. The heat and particle transport is enhanced by the ergodicity near the X-point, resulting in the lo-

cal degradation of the electron density and temperature profiles and the splitting of the strike points on the divertor targets, mostly in the LFS. In MAST, the separatrix follows a $(n = 3, m \sim 11)$ 3D-corrugation (the last close flux surface is moved inward by $\sim 3cm$ at the midplane for a zero poloidal angle). The pedestal position follows the same inward movement, accompanied by a small degradation of the pedestal (relaxation of the density and temperature gradients). Last, the radial electric field evolution and the braking of the electron perpendicular velocity is observed, following the same trend as in the experiments.

The two main limits of this study are the following: first, for numerical reasons, the resistivity was taken around two orders of magnitude larger than the experimental resistivity, however it is the smallest value that can be used so far in computations run with the existing MHD codes. Second, even though the particle transport is found to be increased by the stochastic layer formed by RMPs at the edge, no clear density pump-out was observed in our simulations: less than 1% of the pedestal density is lost, as compared to up to 20% in the experiments [Evans 2008, Liang 2007a]. This might be due to some missing physics in our model. Indeed, several papers, e.g. Ref [Waelbroeck 2012], have shown that the gradient of the parallel current, which appears in the **electron** density equation, plays a major role in the pump-out of density in the plasma when RMPs are applied: the parallel current flowing along perturbed magnetic field lines (phenomenon called "magnetic flutter") generates an enhanced radial transport of the electron density. This parallel current does not appear in the **ion** density equation considered in our model, however the ion and electron density equations should be equivalent. The inclusion of several components of the fluid (ion) velocity so far neglected, such as the polarization drift and the velocity induced by the neoclassical friction, should therefore be added in the ion flux (in the ion density equation) to make these equations fully consistent. This is the ambipolarity constraints, raised e.g. in [Tokar 2008], which imposes for the ion flux to be equal to the electron flux: this way, an enhanced electron transport should also induce an enhanced ion transport. The purpose of an ongoing study, presented in appendix D, is thus to implement the magnetic flutter in the JOREK code, either by implementing the electron density equation – including the gradient of parallel current – instead of the ion equation, or by adding the corrective terms of the ion velocity in the ion density equation. The increased particle transport induced by magnetic flutter might then allow for the observation of the density pump-out generated by RMPs in JOREK simulations, consistently with experimental observations.

ELM cyclical dynamics

Contents

4.1   Introduction

Experimentally, ELM relaxations consist in a cyclical phenomenon, resulting in the quasiperiodic deposition of energy on the divertor target plates. Modeling this phenomenon requires to reproduce this cyclical behavior. Besides, the simulation of ELM cycles rather than a single ELM crash which depends on the initial unstable pressure profile involves different physical mechanisms. Indeed, after the first ELM crash, memory of the choice for the initial state is lost. The phase coherence between modes that determines the ELM instability growth has reorganized and is now consistently determined by the dynamics rather than imposed through the choice of initial conditions. And so is the energy content within the bath of toroidal harmonics. In this respect, an ELM crash starting from such a coherent state is significantly different from a first initial relaxation triggered by the choice of an initial state. This chapter discusses the specificities of the multiple ELM dynamics starting from self-consistent inter-ELM states (section 4.5) with respect to the single ELM relaxation from an initial chosen condition (section 4.2).

    The ELM dynamics without RMPs is studied through JOREK simulations performed for JET-like plasma parameters and geometry, similarly to chapter 3. First, a simulation of a single ELM crash is presented without diamagnetic flows in section 4.2. Even though the simulation without diamagnetic flows does not allow for obtaining an ELM cycle, it

gives a relatively acurate picture of the dynamics of a single ELM, from the growth of the peeling-ballooning instabilities to the crash of the pressure profile. In a second time, the diamagnetic rotation is included in simulation. The diamagnetic effects are known to reduce the growth rate of ideal and resistive instabilities [Drake 1983, Huysmans 2001] and thus have a stabilizing effect on plasma instabilities. The stabilizing effect of the diamagnetic rotation on ELMs is discussed in section 4.3.1 and the impact of the diamagnetic flow on the rotation of the ELM precursors and filaments is described in section 4.3.2. Then we show in section 4.4 that ELM simulations with diamagnetic flows present a near-symmetric ELM power deposition on the inner and outer divertor target plates, which is in closer agreement with the experimental observations, as compared to the previous simulations without diamagnetic flow. Finally, we present in section 4.5 the first simulations of multi-ELM cycles obtained in realistic geometry. The diamagnetic flows have been evidenced to be a key parameter for simulating cycles of sawtooth crashes [Halpern 2011]; we show in this chapter that they also enable to simulate cycles of ELM crashes.

4.2   Dynamics of a single ELM without flows: growth and crash

In order to compare the ELM dynamics either in presence or in absence of diamagnetic flows, an ELM simulation is first performed without diamagnetic drifts, for the JET-like parameters given in chapter 3. In the following sections, the diamagnetic drifts will be added and compared to this reference case. The simulation starts from a chosen typical unstable H-mode pedestal profile. As an example, we consider the dynamics of a single harmonic $n = 8$ unstable mode.

The ELM is triggered due to the initial large pressure gradient and the current (bootstrap-like) profile at the edge: the initial state is slightly over the peeling-ballooning threshold. As shown in Fig. 4.1, the ELM starts with the exponential growth of the $n = 8$ mode – characterized by a constant linear growth rate γ –, until non-linear effects saturate the mode and generate the relaxation of the pedestal profiles that brings back the system below the peeling-ballooning stability boundary. During the linear growth, an $n = 8$ perturbation of density and temperature develops, which induces the ballooning structure of the edge density and temperature profiles, mainly located on the low field side (see Fig. 4.2 (b)). Then, as described in [Huysmans 2009], the $n = 8$ mode saturates due to the non-linear generation of an $n = 0$ flow, induced by the Maxwell stress $[\psi_{n=8}, j_{n=8}]$ in the momentum equation. This $n = 0$ flow – corresponding to the $n = 0$ kinetic energy in Fig. 4.1 – distorts and shears the density pattern (Fig. 4.2 (c)), inducing the expelling of sheared filaments of density from the pedestal.

Meanwhile, the $n = 8$ magnetic perturbation due to the ELM generate the magnetic reconnection of the edge. As shown by the Poincaré plot Fig. 4.3, the magnetic field is fully reconnected in the pedestal: the magnetic field is ergodic for a normalized flux $\psi > 0.9$. Note that the Poincaré plot in (ψ, θ) coordinates (Fig. 4.3) also highlights
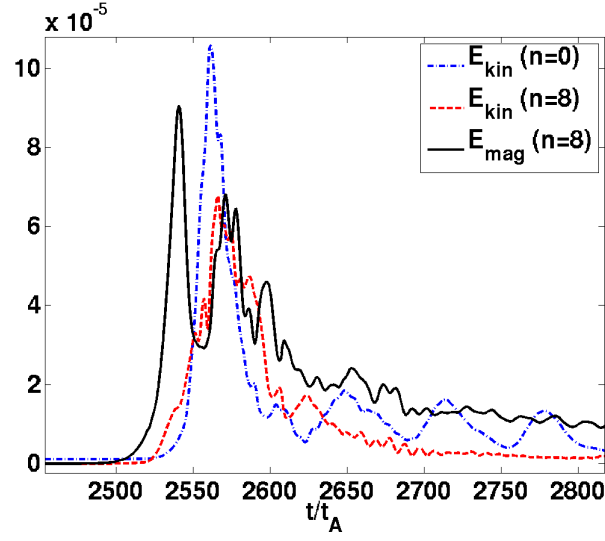
Figure 4.1: Time variation of the magnetic energy of the $n = 8$ mode and kinetic energies of the modes $n = 8$ and $n = 0$ during an $n = 8$ ELM without diamagnetic effects. Time is normalized to the Alfvén time t_A.
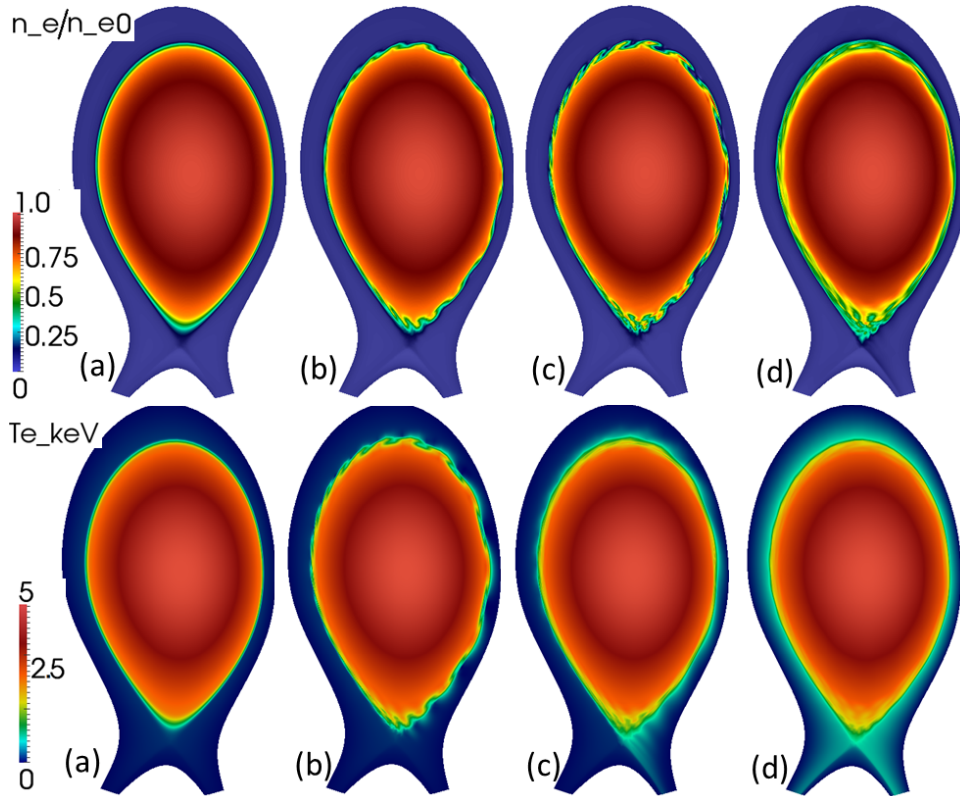
Figure 4.2: Normalized density (top) and electron temperature (bottom, in keV) at the equilibrium (a), just before the ELM crash (b), during the crash (c) and at the end of the crash (d).

the ballooning deformation on the low field side. The ergodization of the edge magnetic field largely enhances the heat diffusive transport at the edge, hence the temperature transport through the pedestal and in the scrape-off layer is increased first on the low field side (Fig. 4.2 (c)) and then on both field sides (Fig. 4.2 (d)).
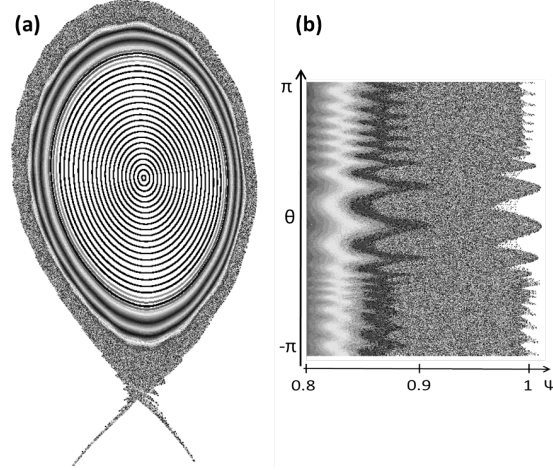
Figure 4.3: Poincaré plot of the magnetic topology at the onset of the ELM crash: (a) in (R,Z) coordinates; (b) in (ψ, θ) coordinates, zoomed at the edge (for $\psi > 0.8$).

As a result, due to the enhancement of both the convection of density by the $n = 0$ flow and the diffusion of temperature by the ergodization, the pedestal pressure has significantly reduced at the edge at the end of the ELM crash, as plotted in Fig. 4.4: the edge pressure profile has flattened due to the expelled energy that has reached the divertor targets.
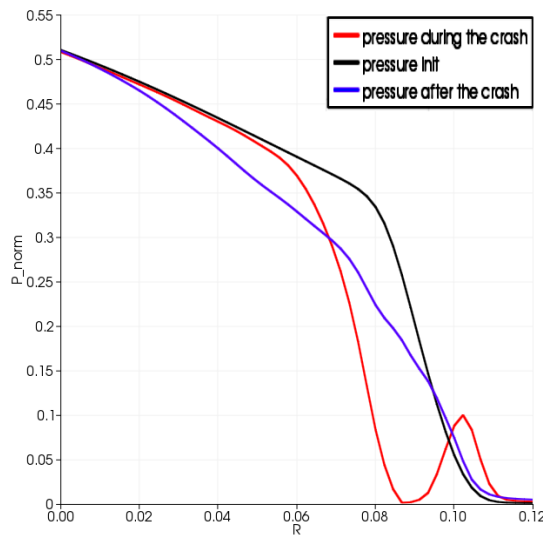
Figure 4.4: Edge pressure profile at the midplane before an ELM (black), during an ELM (red) and after an ELM (blue). The pressure is normalized to the central value.

The single ELM simulations obtained without diamagnetic flows reproduce quite well

e.g. the ballooning deformation, the expelling of density filaments and the flattening of the pressure profile observed in experiments [Gohil 1988, Kirk 2004, Kirk 2006]. However, we show that the diamagnetic drifts are necessary to improve the theoretical description of the ELMs. In particular, ELM simulations with diamagnetic drifts give a more accurate picture (in the sense that they better reproduce experimental facts) of the rotation of precursors and filaments (section 4.3.2), of the power deposition on the divertor due to an ELM (section 4.4) and of the cyclical dynamics of the ELMs (section 4.5).

4.3 Diamagnetic effects: ELM stabilization and ELM rotation

4.3.1 Diamagnetic stabilization

The diamagnetic effects strongly affect the ELM dynamics. The first well know effect of the diamagnetic rotation is the stabilization of the MHD modes and in particular the stabilization of ideal and resistive ballooning modes [Drake 1983, Rogers 1999, Diamond 1985, Huysmans 2001]. Indeed, it is found theoretically that the growth rates of medium and high n modes is reduced by the diamagnetic stabilization. The high $n \to \infty$ ballooning modes are even fully stabilized by the diamagnetic rotation for a large enough value of τ_{IC} [Huysmans 2001] and thus medium n numbers are the most unstable modes. The diamagnetic stabilization is also observed in our simulations. As compared to ELM simulations without diamagnetic drifts where the highest n number was the most unstable mode [Pamela 2013], in the ELM modeling with diamagnetic rotation we find that the most unstable modes are medium n numbers, between around 6 and 12 depending on the cases. As an example, the linear growth rate of a single harmonic ELM is plotted for the JET-like case in Fig. 4.5, depending on the toroidal mode number considered. The growth rate is largest for an $n = 8$ ELM, which means that the $n = 8$ mode will dominate the linear growth of a multi-harmonic ELM simulation made for these parameters. However, it is possible that the other mode numbers may be non-linearly more unstable.

Moreover, the linear growth rate of an $n = 8$ ELM is calculated for different plasma diamagnetic velocity characterized by the τ_{IC} parameter (see Fig. 4.6). The realistic value – used in all other JET-like simulations – is $\tau_{IC} = 2 \times 10^{-2}$. The linear growth rate of the $n = 8$ mode is divided by $\sim 3 - 4$ with diamagnetic rotation (compared to the case without rotation), and it decreases if τ_{IC} is increased. Note that the toroidal number n of the most unstable mode also depends on the diamagnetic rotation. An analytical estimation of n_{max} depending on τ_{IC} is given in [Huysmans 2001]. We show in the next subsection that the diamagnetic rotation does not only affect the growth rate of the ELM, but also its rotation frequency.

4.3.2 ELM rotation: precursors and filaments

The rotation of the ELM and their associated filaments has recently been measured during the ELM crash in KSTAR [Yun 2011] and in ASDEX Upgrade [Classen 2013]. It
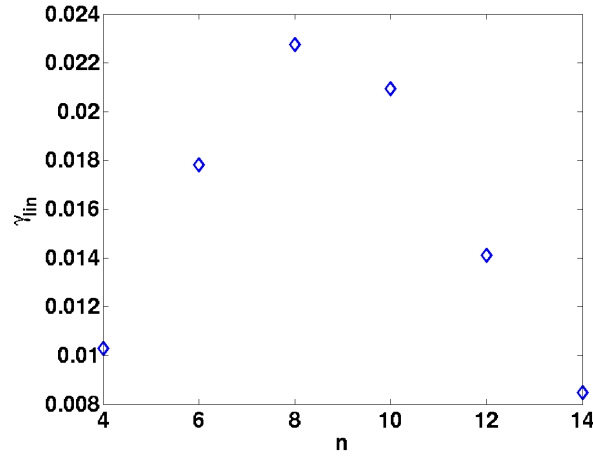
Figure 4.5: Linear growth rate of a single harmonic ELM depending on its toroidal mode number n with diamagnetic effects.
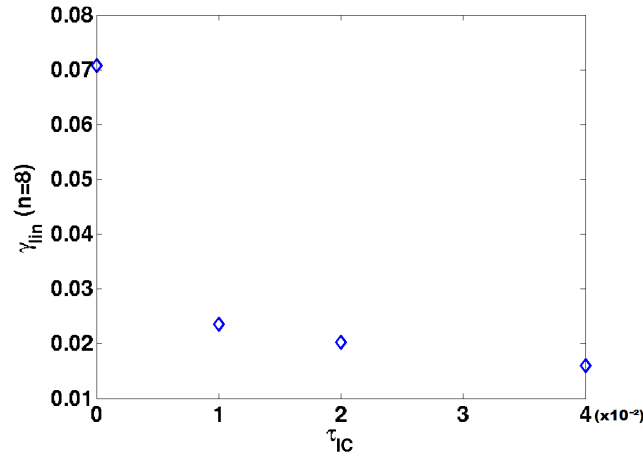
Figure 4.6: Linear growth rate of an $n = 8$ ELM depending on the diamagnetic parameter τ_{IC}.

is unclear which mechanism is responsible for the ELM rotation, either the $E \times B$ or the diamagnetic velocity during the growth phase of the ELM. Also the experimentally observed deceleration [Yun 2011] and reversal [Classen 2013] of the filament rotation at the ELM crash remains unexplained.

Here, we study the impact of the $E \times B$ and diamagnetic rotation on the ELM rotation. The JOREK simulations are performed using the parameters of a realistic JET shot (#77329, described in [Bécoulet 2012]) and compared to an analytical calculation, given in more details in [Morales 2014]. The rotation of an $n = 6$ ELM is studied during its linear growth, either without or with diamagnetic drift. As presented in Fig. 4.7, without diamagnetic rotation, the instability is almost static while growing. However, with diamagnetic rotation, the ELM precursor (*i.e.* during the linear growth) rotates in the the electron diamagnetic or $E \times B$ direction (anticlockwise).
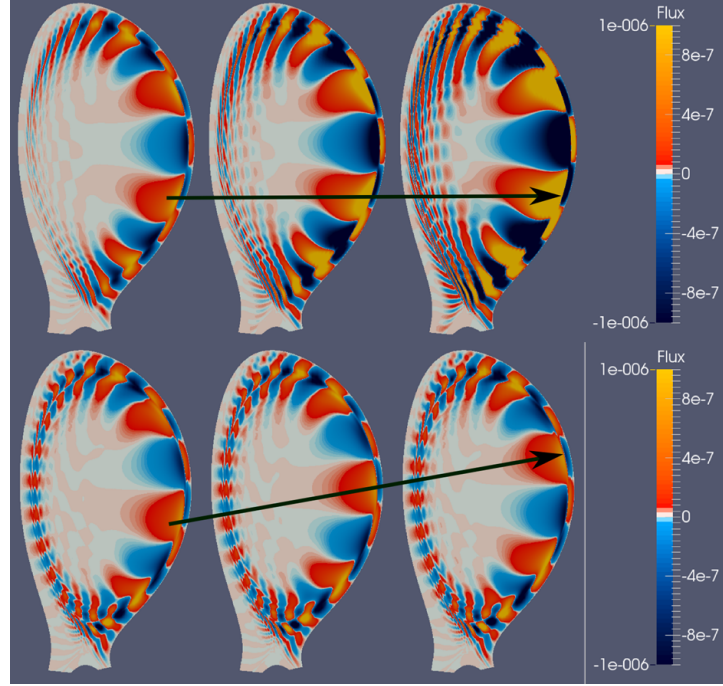
Figure 4.7: Rotation of the ELM precursors without (top) or with (bottom) diamagnetic rotation. The $(n = 6)$ magnetic flux perturbation is plotted for three different times separated by $20 t_A$.

In comparison, the analytical calculation [Morales 2014] using the ballooning representation (see e.g. [Connor 1978]) demonstrates that in the zero resistivity and low shear limit, the ELM frequency is equal to half the ion diamagnetic velocity $(\omega_i^*/2)$ in the plasma reference frame. Thus the mode rotates at the following velocity:

$$\boldsymbol{v}_{mode} = \boldsymbol{v}_{E\times B} + \boldsymbol{v}_{\|} + \frac{\boldsymbol{v}_i^*}{2} \tag{4.1}$$

Thus in the poloidal direction, $\boldsymbol{v}_{mode,\theta} \approx \boldsymbol{v}_{E\times B} + \boldsymbol{v}_i^*/2$. Yet in the pedestal the $E \times B$ drift scales as $\boldsymbol{v}_e^*$ since the electron pressure gradient term is dominant in the equilibrium force balance (*Eq.* (2.35)). Thus the poloidal velocity of the mode is approximately equal to $\boldsymbol{v}_e^* + \boldsymbol{v}_i^*/2 = \boldsymbol{v}_e^*/2$: the mode rotates in the electron diamagnetic direction at the frequency $\omega^*/2$. This velocity direction and the magnitude of the speed of the ELM rotation (several km/s) are in agreement with the experimental observations of the rotating ELM precursors [Yun 2011, Classen 2013].

In the non-linear stage, the mode velocity $v^*/2$ is added to the $n = 0$ flow, which is non-linearly induced by the Maxwell stress, as described in section 4.2. Qualitatively, the mechanism of the filament shearing remains comparable to the one observed without diamagnetic drift: the pedestal plasma rotates in the electron diamagnetic direction, while the plasma displaced towards the SOL rotates in the ion diamagnetic direction, as plotted in Fig. 4.8. Therefore the density filaments are sheared off from the plasma and expelled in the ion diamagnetic direction. However the advection of filaments is modified

by the diamagnetic drifts, thus more density is expelled towards the inner divertor plates, as explained as follows.
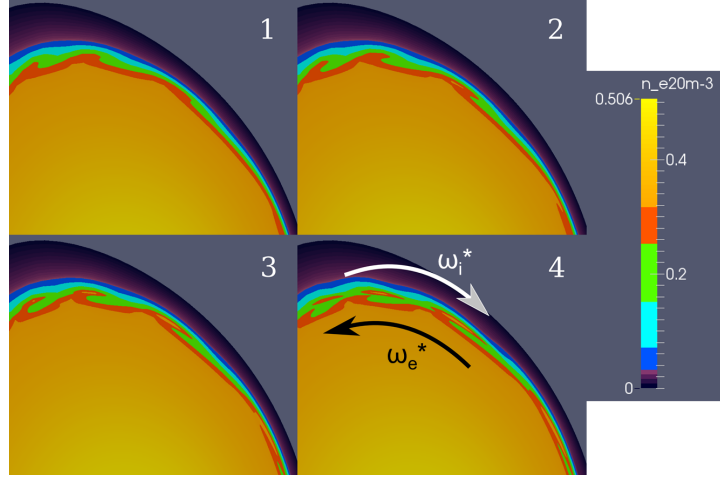
Figure 4.8: Expelling of the ELM filaments on the non-linear stage of an ELM with diamagnetic effects. $10t_A$ separate two pictures.

4.4   Power deposition on divertor

During an ELM, the temperature is conducted by the heat diffusivity from the reconnected edge plasma to the divertor plates, whereas the density is convected by the $E \times B$ and diamagnetic rotation. Experimentally, the deposition of the heat flux due to an ELM is either symmetric on the inner/outer divertor target plates, or the inner target receives twice more power [Pitts 2007, Eich 2003]. In the previous modeling performed without diamagnetic drifts, the outer target received almost all the ELM power deposition, which was contrary to the experimental observations.

As an example, an $n = 2 - 8$ ELM simulation is performed with realistic JET parameters (shot #77329) for two different cases: one without including flows in the model (Fig. 4.9 (a)) and one with diamagnetic effects, neoclassical friction and toroidal source of rotation included (Fig. 4.9 (b)). In the case without flows, almost all the heat flux generated by the ELM filaments is deposited on the outer divertor, whereas in the case where flows are included in the model, the deposited heat flux is near-symmetric on the inner and outer. A cut along the radial direction of the divertor targets, given in Fig. 4.10, shows the large difference of the power deposition in the cases without/with flows.

This difference can be explained by the fact that the diamagnetic velocity advects more density towards the inner divertor plate than the outer plate, hence the heat flux reaching the divertor at the sound speed is deposited near-symmetrically in the inner and outer divertor plates: even though the temperature is larger on the outer than on the inner side, the density is larger in the inner region so a similar power, proportional to both the plasma temperature and density, reaches the inner and outer divertor target
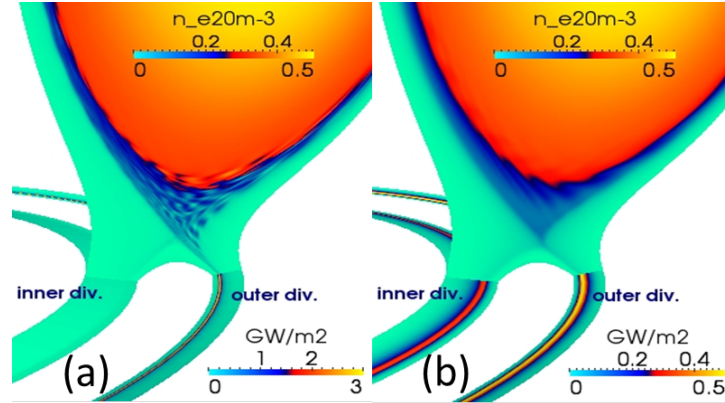
Figure 4.9: Heat flux (in MW/m^2) reaching the inner and outer divertor target plates after an ELM: without flows (a) or with diamagnetic, neoclassical and toroidal flows (b).
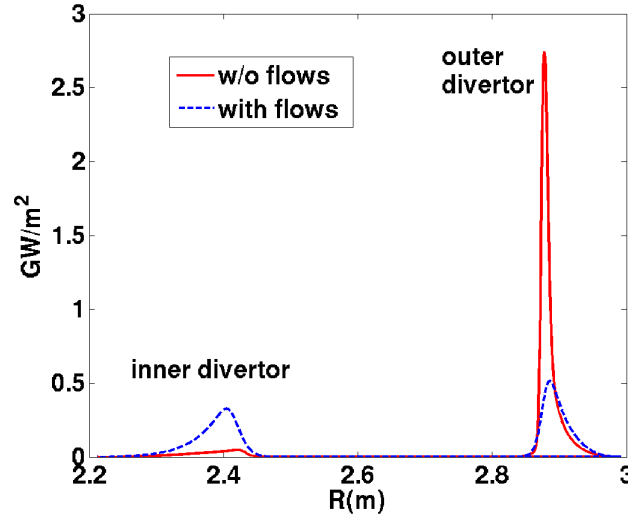
Figure 4.10: Radial section of the heat flux reaching the inner and outer divertor target plates along the divertor: almost all flux reaches the outer divertor (full line) without flows whereas the deposition is near-symmetric with flows (dash line).

plates due to an ELM. Thus simulations with diamagnetic drifts allow for reproducing more realistically the dynamics of an ELM up to the deposition on the divertor.

4.5 Non-linear cyclical dynamics

Last but not least, in this section, we show that the diamagnetic drifts is also a key ingredient which allows for reproducing the ELM cyclical dynamics. In the modeling without diamagnetic drifts (section 4.2), the ELM crash is generated by the chosen initially unstable pressure profile. After the crash, the unstable modes remain unstable, and the residual magnetic activity expels the plasma outside the separatrix, which prevents the pedestal from building-up again. As an example, the simulation of the $n = 8$ mode without dia-

magnetic effects (described in section 4.2) is continued during several thousands of Alfvén times: we observe that a significant MHD activity remains after the crash. Indeed, the magnetic and kinetic energies of the $n = 8$ mode, plotted in Fig. 4.11, is not completely damped after the crash. Because of this magnetic activity, magnetic island chains remain after the crash for $\psi > 0.85$ and an ergodic layer subsists at the very edge ($\psi > 0.95$), as shown in Fig. 4.12, plotted for $t \sim 7 \times 10^3 t_A$. This perturbed magnetic structures and particularly the edge stochastization increase both the heat parallel diffusivity and the $E \times B$ convection of particles. The enhanced transport prevents the reconstruction of the pedestal profiles and keeps the plasma below the peeling-ballooning stability limit, thus a second ELM cannot be obtained in the simulations without diamagnetic effects.
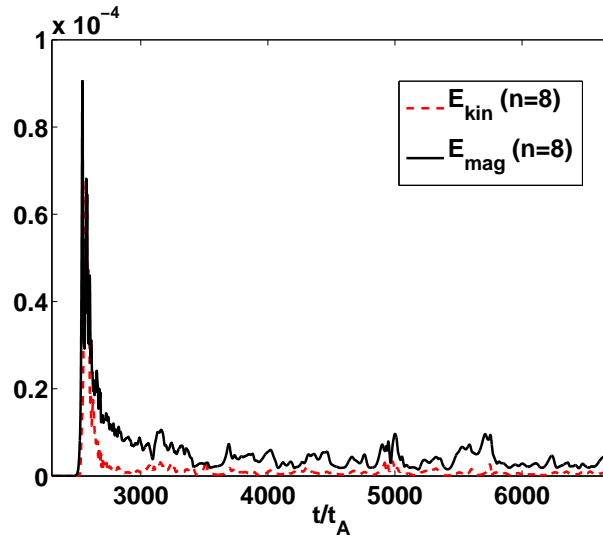
Figure 4.11: Time variation of the magnetic and kinetic energies of the mode $n = 8$ without diamagnetic effects. A large magnetic activity remains after the crash.

4.5.1   Cyclical self-consistent evolution

However, the inclusion of the diamagnetic rotation induces two major stabilizing effects on ELMs. First, it reduces the amplitude of the ELM perturbation and crash. Indeed, compared to the simulation without diamagnetism (Fig. 4.11), the magnetic and kinetic energies of the same $n = 8$ ELM with diamagnetic drifts included (Fig. 4.13) are 1-2 orders of magnitude lower. In Fig. 4.13, the multi-harmonic simulation of the modes $n = 0, 2, 4, 6$ and 8 with diamagnetic drifts is presented. The most unstable $n = 8$ mode is hardly coupled with the other modes during the first ELM crash and the energy of the other modes remain several orders of magnitude lower than the energy of the $n = 8$ mode. So the dynamics of the first ELM is almost only governed by the $n = 8$ mode. Note that the modes $n > 9$ are less unstable than the $n = 8$ mode due to the diamagnetic stabilization of the high toroidal numbers section 4.3.1; for this reason and in order to reduce the time-consumption of the simulation, the highest $n > 9$ modes were not kept in simulation. The odd modes were not included either to reduce the time-consumption.
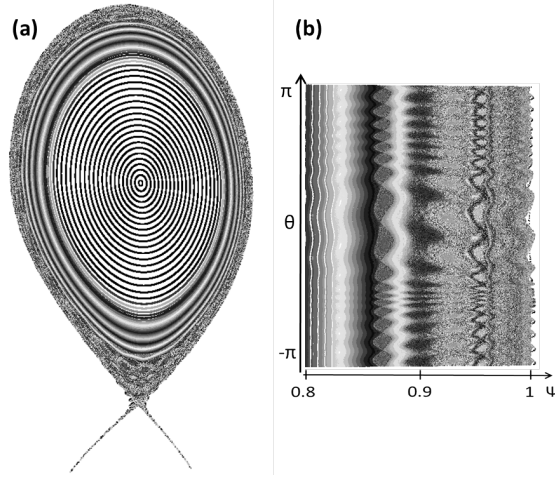
Figure 4.12: Poincaré plot of the magnetic field topology long after the $n = 8$ ELM crash without diamagnetic effect, at $t \sim 7 \times 10^3 t_A$: (a) poloidal projection; (b) at the plasma edge (normalized flux $\psi \geq 0.8$).
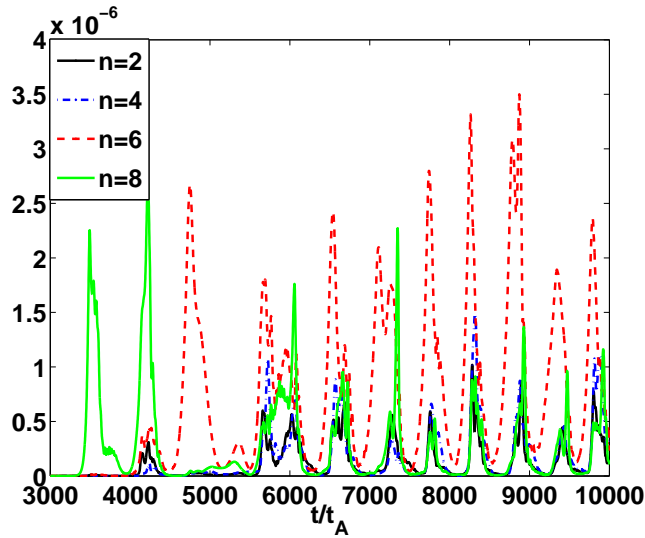
Figure 4.13: Kinetic energy of the modes $n = 2 - 8$ in the multi-harmonic $n = 0 : 2 : 8$ simulation with diamagnetic effects.

After the first ELM crash, we observe the second major role of the diamagnetic stabilization: instead of remaining unstable after the crash, the plasma is stabilized by the diamagnetic rotation (Fig. 4.13). Only when the pressure profile is built up by the applied heating power, the plasma is destabilized again. The ballooning modes are growing again until a threshold in pressure gradient is reached, triggering the second ELM relaxation. Therefore the ELM dynamics results from a competition between the diamagnetic stabilization and the destabilization of the plasma by the heat and particle sources filling the pedestal and steepening the pressure profile. The ELM cycles obtained in simulation Fig. 4.13 can be decomposed into two periods. The first three transient ELMs are largely dominated by the most unstable modes ($n = 8$ during the first two

ELMs then $n = 6$), and their triggering threshold is dependent on the initial chosen state. However, after 3-4 ELMs, the memory of the initial state is lost, and a quasi-periodic regime of ELM crashes is obtained. These ELMs are characterized by a strong non-linear coupling between the $n = 2-8$ modes. The $n = 6$ mode is growing first, directly followed by the other modes. After a crash in this quasi-periodic regime, the plasma reorganizes into a self-consistent state. Thus, the ELM frequency does not depend any more on initial conditions, but depends on intrinsic parameters: the diamagnetic rotation (which have a stabilizing effect on ELMs) and the applied heating power (destabilizing), as described in the next section 4.5.2. The competition between these two parameters governs the cyclical dynamics of the ELMs. Each ELM in the quasi-periodic regime can be decomposed into three steps (Fig. 4.14): first, the instability grows as the pressure gradient (and in a smaller extent the edge current) increase. Second, the ELM crash occurs when a limit of pressure gradient is reached. And third, the pedestal profiles relax: particles and energy are expelled out of the plasma, and the pressure gradient collapses, as presented in Fig. 4.14 (a). Note that the bootstrap current is not included in the model (the current is forced to tend to the initial realistic current profile via a current source, but does not depend on the pressure gradient evolution, as it is in experiments), so the dynamics of the instabilities simulated here shows only a small dependence on the pedestal current (Fig. 4.14 (b)).
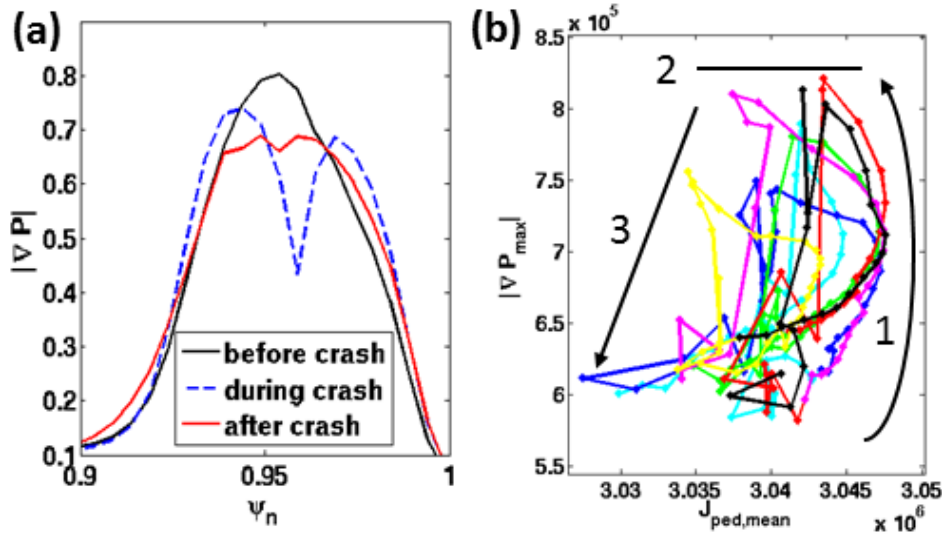
Figure 4.14: In quasi-periodic regime: (a) Edge pressure gradient before, during and after an ELM. (b) Peeling-ballooning diagram of the ELMs.

After a small delay ($\sim 100 t_A$) corresponding to the ion parallel time $\tau_{\parallel,i} = \pi q R/c_s$ (where c_s is the sound speed), the energy and particles due to the ELM filaments reach the divertor target plates at the sound speed. The distinction between the first transient ELMs and the quasi-periodic regime is also observed on the plot of the integrated power reaching the divertor after an ELM (Fig. 4.15): although the power deposition due to the four first ELMs is very variable, the integrated peak power deposited by an ELM on the divertor (Fig. 4.15) is approximately the same for all the ELMs in quasi-periodic regime

($\sim 5 - 6MW$ on the outer divertor, $\sim 2 - 3MW$ on the inner divertor). This again shows that the first ELMs before reorganization are singular. Note that in quasiperiodic regime, the peak power deposition on the inner divertor is slightly delayed (by $\sim 50t_A$) compared to the outer deposition: because of the ballooning character of the instabilities, the filaments are mostly expelled from the Low Field Side, so the filaments first hit the outer target.

Furthermore, the deposition on the inner and outer divertor targets is near-symmetric in this simulation: the integrated deposited power has the same order of magnitude on both targets, even though roughly two-times more power is deposited on the outer divertor target.
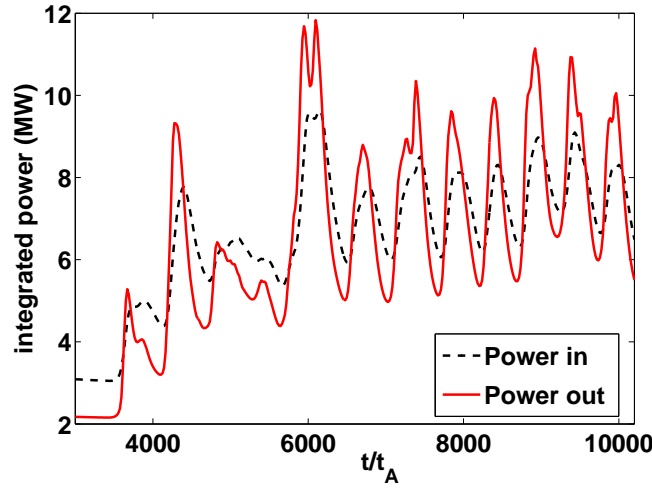
Figure 4.15: Integrated power reaching the inner (dash line) and outer (full line) divertor plates.

4.5.2   Characterization of the ELM frequency

The ELM frequency obtained in Fig. 4.13 is about $3kHz$. This frequency depends on both the stabilizing effect of the diamagnetic rotation and the destabilization by the steepening of the pressure profile due to the heat source. To assess these effects, simulations are performed first with a twice larger heat source and second with a twice larger diamagnetic parameter τ_{IC}. First, we notice that the enhanced heat source has the effect of raising the maximal pressure gradient reached at the ELM crash, which is about 5% larger with the enhanced source (Fig. 4.16). This can be explained by two combined effects. First, whilst the peeling-ballooning modes are growing, the enhanced heating power induce a quicker increase in the edge pressure gradient during the delay needed by the non-linear effects to induce the pedestal relaxation. Second, due to the larger heating power, the mean equilibrium (inter-ELM) temperature T_0 is raised after several ELMs. Consequently, the resistivity (proportional to $T_0^{-3/2}$) is reduced, so the boundary stability is improved. For both reasons, a larger pressure gradient develops in the pedestal before the ELM crash,

which induces a larger amount of particles and energy expelled by the ELM. Subsequently, the power reaching the divertor (Fig. 4.17) is increased. This means that the pedestal has lost more energy and that more time is needed to reconstruct the pedestal. Therefore the ELM frequency is decreased as the heat power is increased. This behavior is similar to the type-III ELMs observed in experiments [Sartori 2004].
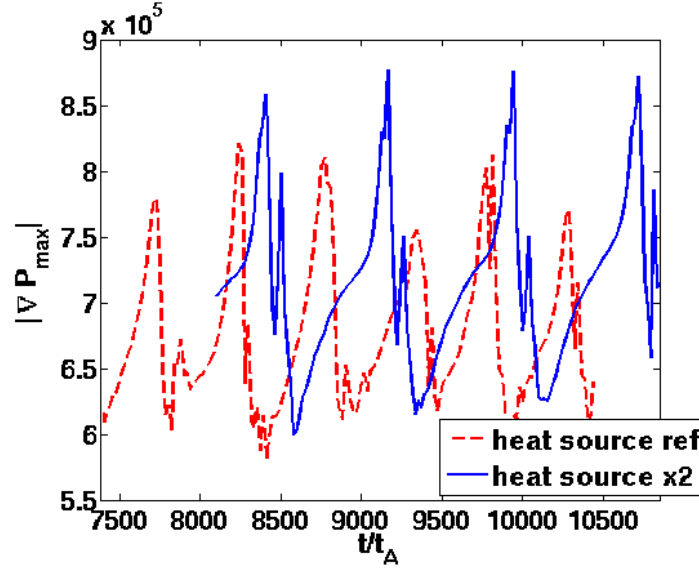
Figure 4.16: Time variation of the maximal edge pressure gradient in quasi-periodic $n = 8$ ELMy regime in the reference case (dash) and with a double injected power.
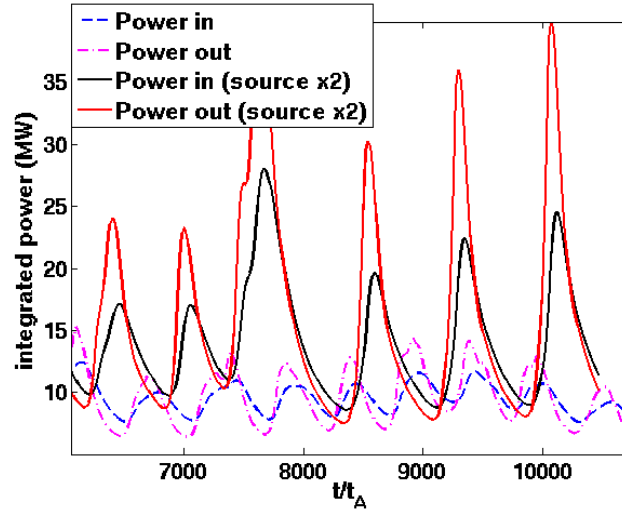
Figure 4.17: Integrated power on the inner and outer divertor plates in quasi-periodic $n = 8$ ELMy regime in the reference case (dash) and with a double injected power.

Second, simulations at larger diamagnetic rotation present a larger ELM frequency. Actually, due to the diamagnetic stabilization, smaller instabilities develop at the edge

plasma and a smaller energy is expelled from the pedestal. So the plasma after the crash remains just below the stability limit, such that less time is needed to cross again the stability threshold, which explains a larger ELM frequency. In the case with a diamagnetic parameter twice larger than the realistic one (Fig. 4.18), not only the ELM frequency (obtained after the transient phase) is increased, but the large diamagnetic rotation gradually decreases the amplitude of the ELMs, so that in terms of peeling-ballooning cycles, the plasma moves from the initially unstable state towards a "fix point" in the P-B diagram by doing smaller and smaller cycles. As it represents a bifurcation from a cycling dynamics towards a stable state, it may present similarities with the so-called dithering cycles [Zohm 1996].
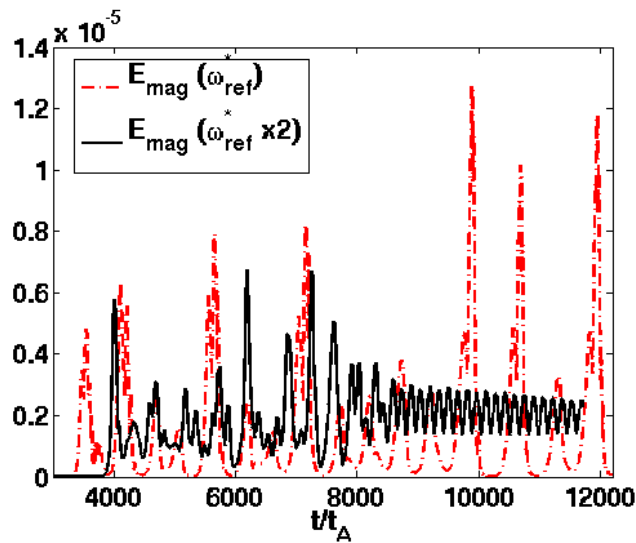
Figure 4.18: Magnetic energy of the $n = 8$ ELM depending on the diamagnetic parameter: realistic value (dash) and doubled (full)

4.6   Conclusion of the chapter

In this chapter, the ELM cyclical dynamics was reproduced in non-linear modeling performed with JOREK. The main limitations of our model is the large resistivity which is two orders of magnitude larger than the experimental value due to computational limitations and the *ad hoc* heat and particle sources taken in simulation that affect the ELM frequency. In spite of these restrictions, the modeling of these resistive ELMs represents a significant step forward in the understanding of the cycling dynamics.

In the ELM modeling without diamagnetic drifts, the overall dynamics of a single ELM crash is rather well reproduced: the growth of the peeling-ballooning modes induces the deformation of the plasma edge until density filaments are sheared and expelled out of the pedestal. Meanwhile, the edge ergodization induced by the ELM enhances the heat transport through the ETB. As a result, the collapse of the edge pressure profile occurs. This description matches quite accurately the experimental observations.

However several experimental observations, such as the rotation of the ELM precursors
and the symmetric ELM power deposition on the divertor targets, are not reproduced
in simulation without diamagnetic rotation. As well, an ELM cycle cannot be obtained
without dimagnetic drifts since the plasma remains unstable after the ELM crash: the
residual edge transport prevents the pedestal from rebuilding, and thus a second ELM
cannot grow.

The addition of the bi-fluid diamagnetic rotation in the model allows to improve
significantly the decription of the ELM dynamics, summarized in the following.

The diamagnetic rotation has a stabilizing effect on the plasma instabilities, and in
particular on the ballooning modes: it reduces the linear growth rates of medium and high
n modes and even fully stabilizes the high n modes. Subsequently the ELM dynamics – at
least during the linear growth – is dominated by the medium ($6 \leq n \leq 12$) modes, which
is relatively consistent with the experimental measurements of the toroidal mode number
[Kirk 2006, Classen 2013]. Note that larger toroidal mode numbers have been measured
in some experiments (e.g. up to $n = 35$ in [Yu 2008]); this may indicate that larger n
modes are likely to be non-linearly more unstable. Regrettably, non-linear simulations at
large n number are numerically very costly (since it requires to simulate a larger number
of harmonics and to have a very fine meshing), so the non-linear effect of these large n
modes could not be tested in this work.

During the linear growth, the edge localized mode rotates in the electron diamagnetic
direction at the frequency $\omega^*/2$. This velocity direction and the magnitude of the speed
of the ELM rotation (several km/s) are in agreement with the experimental observations
of the rotating ELM precursors [Yun 2011, Classen 2013]. In the non-linear stage, an
$n = 0$ flow, which is non-linearly induced by the Maxwell stress, is added to the velocity
$v^*/2$ of the mode. This flow shears off the density filaments in the pedestal plasma and
expels them in the SOL in the ion diamagnetic direction. The advection of filaments due
to the diamagnetic and $E \times B$ drifts expels more density towards the inner divertor plate
than towards the outer plate. As for the temperature, whose transport is enhanced by
the ergodization of the edge magnetic field during the ELM, it is larger on the outer than
on the inner side. Due to the compensation of the inner/outer asymmetry of the density
and temperature profiles, the heat flux – proportional to the plasma density multiplied
by temperature – reaching the divertor at the sound speed, is almost equally deposited
on the inner and outer target plates. As a comparison, in the experiments, either the
ELM power deposition is symmetric, or twice as much power reaches the inner plate than
the outer plate. Thus the modeling with diamagnetic drifts is closer to the experimental
observations compared to simulations without diamagnetic drifts where the outer plate
receives almost all the power.

Last, the diamagnetic flows appear to be a key parameter for the simulation of ELM
cycles, since they allow for the stabilization of the plasma after an ELM relaxation. After
the first ELM crash, the stabilized plasma reorganizes and memory of the initial chosen
profiles is lost. The phasing and the energy repartition between modes is consistently
determined. The steepening of the pressure profile generated by the pedestal recon-
struction destabilizes again the edge plasma until the edge pressure gradient reaches the

ELM-triggering threshold: a new ELM growth and crash then occurs. Similar coupling between modes, similar maximum pressure gradient reached when the crash occurs and similar power deposition on the divertor plates are cyclically recovered for all the ELMs in the quasiperiodic regime. These differ much from the first transient ELMs, pointing out the importance of simulating cycles rather than a single ELM crash.

The diamagnetic rotation and the applied heating power are found to be two main parameters affecting the cyclical ELM dynamics. If the diamagnetic rotation is increased, the ELM frequency is increased and the ELM size is progressively reduced, so that the plasma gravitates towards an attracting point in the peeling-ballooning diagram. In our particular case of resistive (type-III like) ELMs, an enhanced heat source leads to a larger maximum pressure gradient reached at the ELM crash, resulting in a larger ELM frequency and a larger heat flux reaching the divertor.

Contents

5.1   Introduction

In chapter 3, we found that RMPs interact with the plasma, resulting in either the screening or the penetration of RMPs. This can lead to the simple idea that if they are screened, the applied RMPs may have no effect on ELMs and on the contrary if they penetrate they should be able to mitigate or even suppress them. However studying the RMP penetration alone does not give a clue on the actual mechanism of the ELM mitigation of RMPs. Therefore this motivates the study of the interaction between RMPs and ELMs. In addition, we have seen that the plasma rotation strongly affects both the RMP penetration and the ELM dynamics, so the ELM/RMP interaction has to be studied while self-consistently taking into account the plasma rotation. In this chapter, we present the first non-linear simulations of the ELM mitigation and suppression by RMPs. The plasma diamagnetic rotation and the RMP amplitude are found to impact the ELM mitigation/suppression.

In section 5.2, the modeling of the ELM mitigation by RMPs is presented in a typical case performed with JET experimental parameters. The RMP application is found to reduce the ELM power deposition on the divertor targets by a factor of ten. Then the mechanism of the ELM mitigation by RMPs is carefully described in section 5.3. Last, section 5.4 reports the effect of the RMPs on an ELM cycle, using similar parameters as in section 5.2, but with a larger diamagnetic velocity. We observe the bifurcation from a case where RMPs have no effect on ELMs (for a rather low applied RMP current) to a case where RMPs fully suppress the ELMs (for a two times larger applied RMP current).

5.2   Mitigation of the ELM power deposition on diver-tor by RMPs

In this chapter, experimental JET parameters – except the resistivity, two orders of magnitude larger than the experimental value – corresponding to the shot #77329 are used. Typical JET values are taken for the diamagnetic parameter and the neoclassical coefficients: the constant values given in section 2.3.2 are used. The ($n = 2$) RMP spectrum due to the error field correction coils (EFCC) is first calculated in the vacuum with the ERGOS code ([Bécoulet 2008]) and applied as boundary conditions for the magnetic flux perturbation in JOREK. Once the plasma response to ($n = 2$) RMPs has stabilized to an equilibrium (affected by RMPs), the other toroidal modes are added to the simulation. The effect of RMPs on ELMs is tested first in a simulation with $n = 0, 2, 4, 6$ and 8, the RMP coil current being scanned between 20 and $60kAt$. In the simulation run without RMPs, the most unstable mode is the $n = 8$, which leads to a large ELM crash (Fig. 5.1, left). When RMPs are applied, instead of this large ELM crash, a more continuous activity of the modes $n = 2, 4, 6$ and 8 coupled altogether is observed (Fig. 5.1). This activity starts with a peak of energy of the mode $n = 6$, which is the most unstable with RMPs. This peak is smaller compared to the peak of the $n = 8$ mode without RMPs thus it leads to a mitigated ELM with a smaller peak energy released. Moreover, as the RMP current is increased from 20 to $60kAt$, the $n = 6$ peak size is reduced, which means that a stronger ELM mitigation is obtained when the RMP current is larger. The power reaching the divertor in the $40kAt$ case is plotted in Fig. 5.2. The deposited power is divided by ten when RMPs are applied compared to the "natural" ELM (without RMPs).
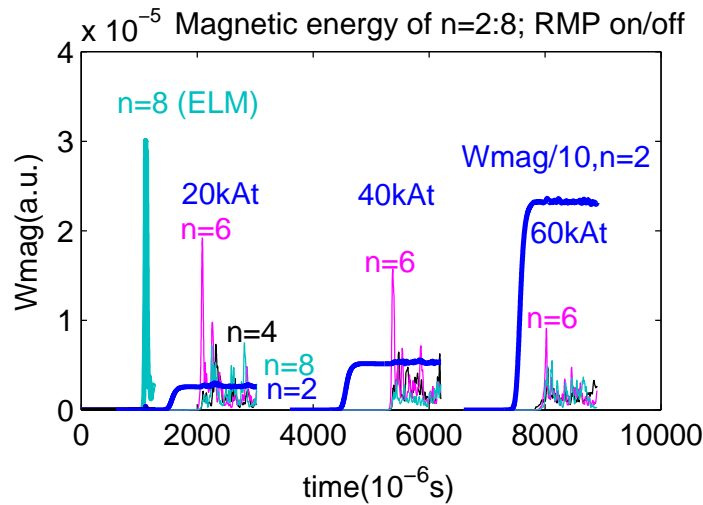
Figure 5.1: Magnetic energy of the modes $n = 2 - 8$; from left to right: without RMP, with RMP current $I_{coil} = 20kAt$, $40kAt$ and $60kAt$
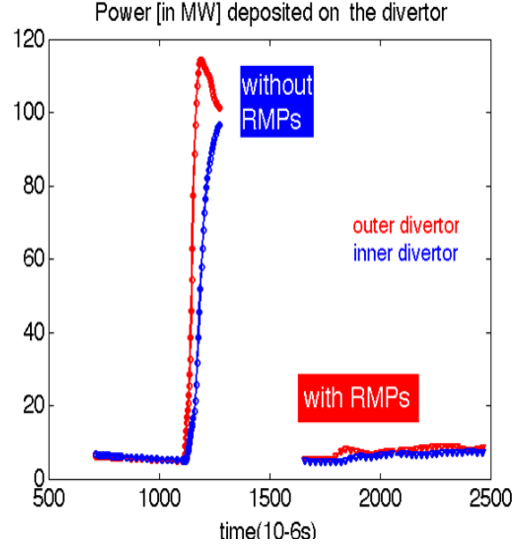
Figure 5.2: Power on inner/outer divertor targets without (left) and with RMPs (right) for $I_{coil} = 40kAt$

5.3 Mechanism of the ELM mitigation by RMPs

We try to understand the mechanism at stake in the ELM mitigation. The first hypothesis is that the edge ergodization due to RMPs which results in a lower edge pressure gradient (as shown in Fig. 5.3) may generate a (partial) stabilization of the ELMs. To test this hypothesis, a simulation is run without RMPs with a reduced pressure gradient similar to the pressure gradient obtained with RMPs (Fig. 5.3, line with crosses). In fact, the reduction of the edge pressure gradient delays the ELM crash (full line in Fig. 5.4) compared to the reference ELM (dashed line in Fig. 5.4), but still leads to a large ELM crash. So the only reduction of the pressure gradient by RMPs does not explain the observed ELM mitigation. The second tested hypothesis is that the modification of the magnetic topology due to RMPs induces the mitigation. A linear run of an ELM with RMPs is thus performed, where the magnetic topology is affected by both the ELM and the RMPs but where the RMPs and the unstable modes are not coupled. This linear run also leads to a large ELM crash.

   This proves that it is really the coupling between the ($n = 2$) RMPs and its harmonics (even modes) that generate the ELM mitigation. Fig. 5.5 presents the simulation at $60kAt$ with $n = 0 - 8$, where the odd modes are also included. We notice that the initial amplitude of the even modes $n = 4, 6$ and 8 is large due to the non-linear drive by ($n = 2$) RMPs. The magnetic energy between these even modes is equally redistributed after the first relaxation of the $n = 6$ modes and the magnetic energy non-linearly cascades from the naturally unstable $n = 8$ mode towards the lower n even modes [Biskamp 1997]. As for the odd modes (Fig. 5.5), they are totally damped due to the activity of the even modes driven by RMPs, and hence they remain at the noise level. The reduction of the ELM toroidal mode number when mitigated by RMPs was observed in KSTAR [Yun 2011], but not in the general case [Kirk 2013a]. Actually, in another simulation
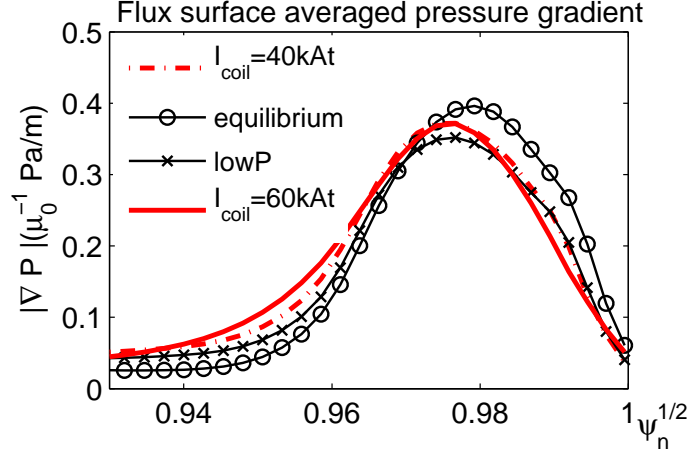
Figure 5.3: Edge pressure gradient: cases without RMP (circles), with RMP at $I_{coil} = 40kAt$ (dash-dot) and $60kAt$ (full line) and without RMP at reduced pressure gradient (crosses)
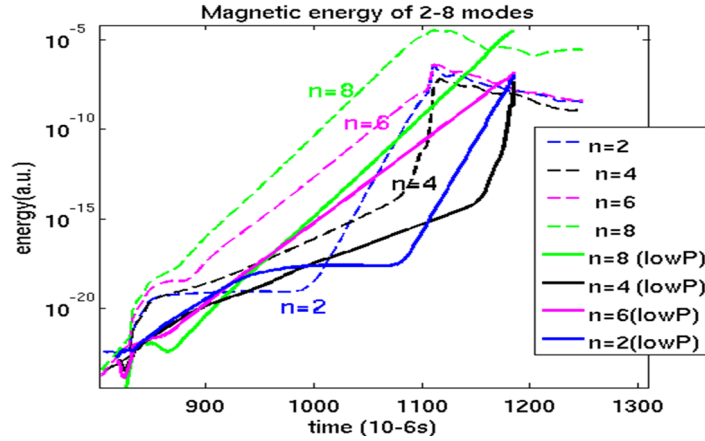
Figure 5.4: Magnetic energy of the modes $n = 2 - 8$ without RMP: in the simulation run at reduced pressure gradient (full line), the ELM crash is delayed compared to the reference case, but remains large.

performed at 15% larger diamagnetic rotation (not presented here), the $n = 6$ mode is the most unstable for the natural ELM due to the diamagnetic stabilization of the larger n modes, and remains the most unstable mode while non-linearly coupled with ($n = 2$) RMPs. Thus the energy cascade implies a redistribution between the non-linearly coupled modes but does not necessarily mean a reduction of the main toroidal mode number.

The coupling of ELM and RMPs induce a change in the edge magnetic structure, as plotted in Fig. 5.7. The magnetic topology of the natural ELM (Fig. 5.7 (a)) is dominated by the $n = 8$ ballooning perturbation that induces a large reconnection at the edge (for $\psi_{norm} > 0.85$). As well, the corresponding footprints in the outer divertor (Fig. 5.8 (a)) present a clear $n = 8$ structure. These structures rotate in the ion diamagnetic direction due to the rotation of the ELM filaments. In the case of RMPs without ELMs
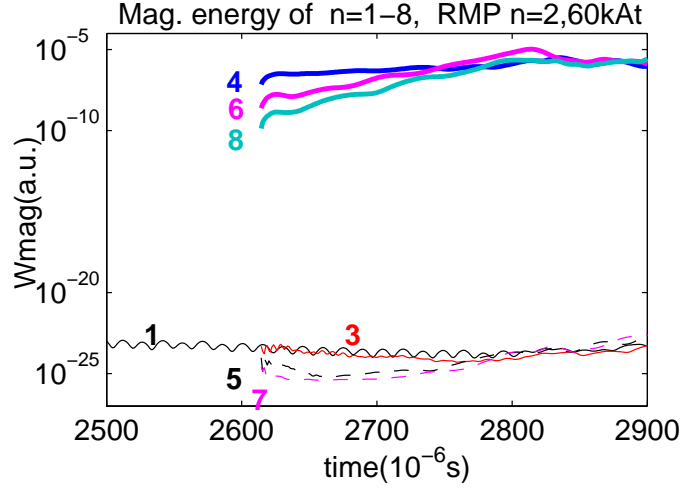
Figure 5.5: Magnetic energy of the modes $n = 1 - 8$ with RMPs ($I_{coil} = 60kAt$). The magnetic activity due to the even modes driven by RMPs totally damps the odd modes.
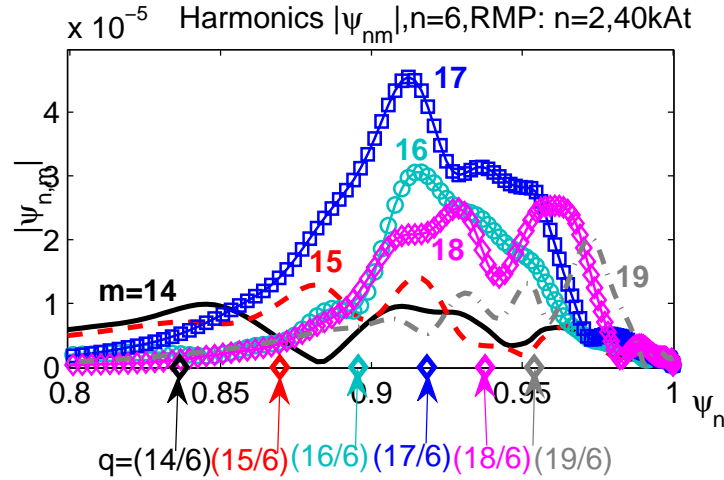
Figure 5.6: Radial profiles of the Fourier harmonics of the magnetic flux perturbation $|\psi_{mn}|$, for $n = 6$ and $14 < m < 19$. The rational surfaces $q = m/n$ are indicated by the diamonds.

(Fig. 5.7 (b)), $n = 2$ magnetic islands are formed on the rational surfaces $q = m/n$ due to the forced magnetic reconnection, and present a tearing-like parity ($\psi_{mn} \neq 0$ on the rational surfaces). It is important to notice that the perpendicular ($E \times B +$ diamagnetic) electron rotation is zero on the rational surface $q = 5/2$ (at $\psi_{norm} \approx 0.85$) which leads to the RMP penetration and the formation of large islands on this surface, as demonstrated in [Nardon 2010, Bécoulet 2012, Orain 2013] and in chapter 3. Moreover, the corresponding footprints in the outer divertor (Fig. 5.8 (b)) show a typical static $n = 2$ structure. As for the magnetic topology of the ELMs with RMPs (Fig. 5.7 (c)), it is clearly different from the topology of the natural ELM. The magnetic structure is dominated by the modes $n = 4$ and $n = 6$, with magnetic islands observed on the rational

surfaces $q = 9/4, 14/6$ and $15/6$. The overlapping of the surfaces $q = 16/6, 17/6$ and $18/6$ generates an ergodic zone deeper in the pedestal than in the case of RMPs alone. The $n = 4$ and 6 modes have a tearing-parity ($\psi_{mn} \neq 0$) on these rational surfaces that is imposed by the driving by RMPs (as plotted in Fig. 5.6), in place of the ballooning parity in the natural ELM case ($\psi_{mn} = 0$). The magnetic islands and above all the ergodic zone at the edge induces an enhanced transport at the edge that expels continuously the heat and particles out of the plasma. The corresponding footprints (Fig. 5.8 (c)) keep the $n = 2$ structure imposed by external RMPs, nevertheless they are modulated by the presence of the $n = 4$ and 6 modes during the small continuous relaxations that replaced the large $n = 8$ ELM crash without RMPs. This typical footprint structure of ELMs in presence of RMPs was reported in [Jakubowski 2009].
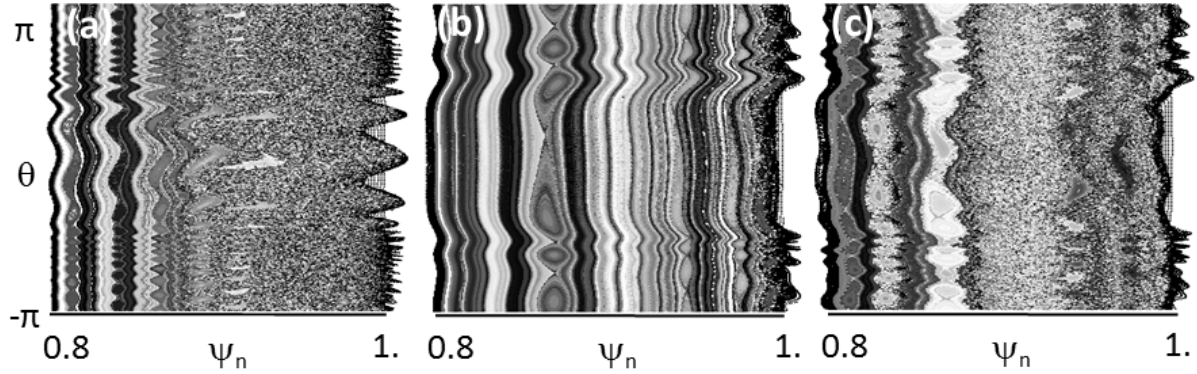
Figure 5.7: Magnetic topology at the edge ($0.8 < \psi_{norm} < 1$): in case of an ELM without RMP (a), in case of RMPs without ELM (b) and in case of an ELM with RMPs (c).

5.4   ELM cycles with RMPs

A multi-harmonic ($n = 2, 4, 6$ and 8) simulation of an ELM cycle with ($n = 2$) RMPs is performed for a larger diamagnetic rotation (this is done both by increasing the diamagnetic parameter τ_{IC} and by taking a steeper pressure profile). In this case, the most unstable mode without RMPs is the $n = 6$ mode (in red in Fig. 5.9) due to the diamagnetic stabilization of the larger mode numbers. At rather low applied RMP current ($40kAt$, left of Fig. 5.9), the ELMs are not mitigated by RMPs. Neither the ELM amplitude or frequency is affected by the RMPs. This may be explained by the large screening of RMPs at large diamagnetic (perpendicular) rotation, which does not allow for a large coupling between unstable modes and RMPs. However at twice larger applied RMP current ($80kAt$, left of Fig. 5.9), the modes $n = 4, 6$ and 8 are more strongly coupled to RMPs, thus they are now fully driven by $n = 2$ RMPs and present a large initial amplitude due to the coupling with RMPs. Contrary to the case presented in section 5.2, these coupled modes do not generate a turbulent MHD activity. Instead, static islands driven by RMPs are formed. The presence of these islands – reconnected at the edge –
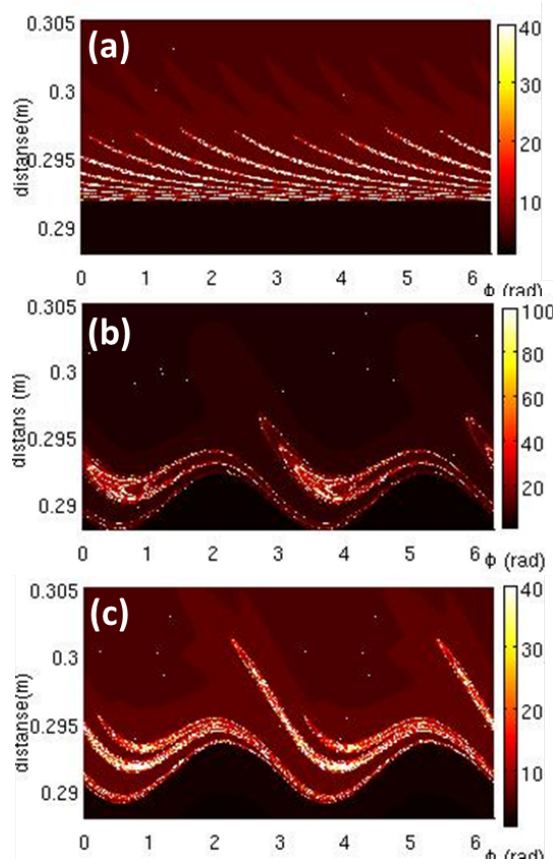
Figure 5.8: Footprints in the outer divertor obtained by the edge field lines integration until crossing with divertor plate: in case of an ELM without RMP (a), in case of RMPs without ELM (b) and in case of an ELM with RMPs (c). The colorbar represents the number of toroidal turns.
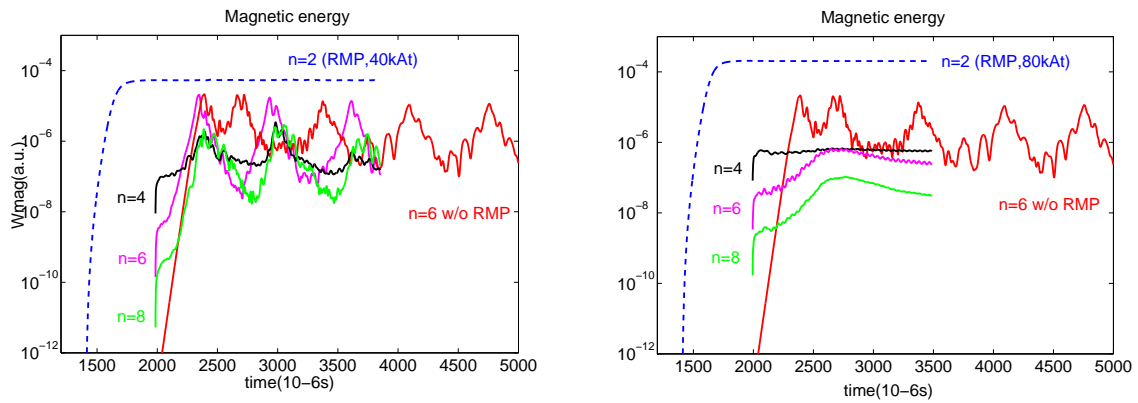
Figure 5.9: Comparison of the magnetic energy of the $n = 6$ mode without and with RMPs (in log scale). At "low" RMP current ($40kAt$, left), RMPs have no effect on the ELM amplitude and frequency, whereas at larger RMP current ($80kAt$, right), the ELM is fully stabilized by RMPs.

generate a permanently enhanced heat and particle transport, which reduces the edge

pressure gradient and thus keeps the plasma under the stability threshold. Therefore, by increasing the RMP current from 40 to $80kAt$, a bifurcation from a largely screened state toward a reconnected state takes place [Fitzpatrick 1998], which leads to the full ELM suppression. Subsequently we have observed three different regimes: ELM mitigation by RMPs, no effect of RMPs on ELMs and ELM suppression by RMPs. These regimes depend on both the RMP amplitude and the diamagnetic rotation. Future work will focus on quantifying more precisely the access to these different regimes.

5.5   Conclusion of the chapter

In this chapter, three regimes of ELM/RMP interaction have been found in JOREK simulations of the JET case with $n = 2$ RMPs. First, at rather low diamagnetic rotation, the ELM mitigation is obtained, where the large ELM crash is replaced by a continuous (in time) magnetic activity or turbulence, also called type-II ELMy activity [Evans 2008, Suttrop 2011, Jeon 2012]. The size of the small initial relaxation is reduced as the RMP coil current is increased. For $I_{coil} = 40kAt$, the integrated peak power on the divertor is found to be divided by a factor of ten. The ELM mitigation is not due to the reduction of the edge pressure gradient but is rather due to the non-linear coupling of the even modes which are driven by the $n = 2$ RMPs. These RMP-driven modes generate plasma reconnection – characterized by magnetic island chains in the pedestal and an edge ergodic zone – and thus continuously expel heat and particles out of the plasma. The footprint on the divertor target plates due to the mitigated ELMs exhibit essentially structures created by the $n = 2$ RMPs, however modulated by the presence of the other n modes.

Then, at larger diamagnetic rotation, two other regimes are observed in simulation. At rather low RMP current ($I_{coil} = 40kAt$), the RMPs have no effect on the ELM dynamics: the ELM amplitude and frequency are not affected by the RMPs since the RMPs are too "shielded" by the plasma rotation to be coupled with unstable modes. However, at larger RMP current ($I_{coil} = 80kAt$), RMPs penetrate and are strongly coupled with the even modes, such that these modes are "locked" to the RMP driving: hence the large permanent transport induced by these RMP-driven modes stabilizes the plasma under the stability threshold and the ELMs are fully suppressed. Current and future works are dedicated to a more precise understanding of the parameters that demarcate these three regimes.

Conclusion

Tokamak plasmas, in high confinement regime, undergo large periodical relaxations of the edge pressure profile, called Edge Localized Modes or ELMs. These ELMs induce a large transient heat load on the divertor target plates. In ITER, if they are not controlled, ELMs are foreseen in the nominal D-T 15MA scenario to represent a loss of $17MJ$ of energy, expelled from the bulk plasma and reaching the divertor. Since the divertor plates could be damaged over $1MJ$, uncontrolled ELMs represent a particular concern for the divertor limetime in ITER. This motivates research to achieve a better understanding of the nature of ELMs and of their dynamics, and to find reliable methods enabling to control the ELMs. This thesis has focused on a promising control method: the application of Resonant Magnetic Perturbations or RMPs. The purpose of RMPs is to induce magnetic island chains on particular magnetic surfaces called resonant surfaces; the overlapping of two consecutive island chains at the plasma edge should generate an ergodic zone where the radial heat and particle transport are enhanced. Since ELMs are believed to be peeling-ballooning modes, triggered by the large edge pressure gradient and/or the large edge current, the increased radial edge transport induced by RMPs should allow to reduce the edge pressure gradient under the peeling-ballooning triggering threshold. This method has already proven to be successful, yet the mechanisms of the ELM control by RMPs – far more complicated than this simple picture – is still not fully understood.

In this respect, this thesis aimed at improving this theoretical understanding through numerical simulations using parameters taken from experimental plasmas, following three axes:

- the interaction between RMPs and plasma flows.

- the ELM dynamics, in particular their cyclical behaviour.

- the interaction between ELMs and RMPs.

These numerical simulations were performed using the non-linear reduced magneto-hydrodynamic code JOREK, presented in chapter 2. New features were added to the original single fluid MHD model, in order to self-consistently decribe the plasma flows: the bi-fluid diamagnetic effects, the neoclassical poloidal friction and a source of parallel rotation. As well, RMPs have been implemented in the code as boundary conditions for the magnetic flux perturbation, to allow for simulating the RMP penetration inside the plasma while taking into account the plasma response.

In chapter 3, a preliminary modeling of the plasma response to RMPs in cylindrical geometry with the RMHD code was first presented. It shows that RMPs, which would

generate magnetic island chains on all rational surfaces in the vacuum, are actually fully screened by the plasma, except on particular rational surfaces where the electron perpendicular velocity cancels, and at the very edge where the plasma resistivity is large. RMPs non-linearly affect the radial electric field, which can evolve such that the electric drift compensates the electron diamagnetic velocity: then the RMP penetration occurs. A large RMP amplitude, a large resistivity, a small electron perpendicular velocity and a small neoclassical poloidal friction are found to be favorable conditions for the RMP penetration.

Then the RMP penetration has been modeled in toroidal geometry, including the X-point and the SOL, for JET, ITER and MAST parameters. In these three cases, the RMPs are found to be screened, except at the very edge ($\psi_N > 0.95$) where they induce an ergodic layer. The edge ergodization actually enhances the radial heat and particle transport, resulting in a small degradation of the edge density and temperature profiles. Note that even though magnetic perturbations are screened on central resonant surfaces, very small islands appear anyhow: this indicates that the screening is only partial, contrary to the previous cylindrical modeling. Another new feature observed in toroidal geometry is the amplification of the non-resonant component of the magnetic perturbation in the core plasma, associated with the so-called "Resonant Field Amplification". In the JET case, three different regimes of RMP penetration have been observed depending on the diamagnetic rotation and the resistivity: at low diamagnetic rotation and high resistivity, the generated islands co-rotate with the plasma ion flow and their size fluctuate at the same frequency. At larger diamagnetic rotation, the islands are static and "locked" to the external static RMPs; a stronger screening of the perturbations is observed. An intermediate regime is observed at lower resistivity, in which the generated island are quasi-static and slightly oscillate. In ITER and MAST, the regime of static magnetic islands prevails.

RMPs are also found to induce the 3D-displacement of the plasma boundary, characterized by the deformation of the separatric and the 3D-corrugation of the pedestal density and temperature profiles. Nevertheless, the plasma displacement is not large enough to reach the wall. The maximum displacement of the separatrix occurs near the X-points, where lobes structures are induced by RMPs. These lobe structures associated with the edge ergodization are responsible for the splitting of the strike points on the divertor targets. Last, the radial electric field evolution and the braking of the electron perpendicular velocity is observed, following the same trend as in the experiments.

In chapter 4, the ELM dynamics has been studied for JET parameters and geometry. The diamagnetic rotation is found to be a key parameter which allows for depicting rather well the experimental behaviour of the ELMs in simulations. In particular, the diamagnetic stabilization enables to reproduce the cyclical dynamics of the ELMs, which has been modeled for the first time in toroidal geometry in this thesis. The dynamics of an ELM cycle is modeled as follows. The initial density and temperature profiles are chosen to be unstable, just over the peeling-ballooning stability threshold. Thus the first ELM is triggered by the initially large edge pressure gradient and edge density. Since

the diamagnetic rotation stabilizes the high-n modes, the ELM growth is dominated by the most unstable medium-n. The unstable modes grow in the pedestal and rotate in the electron diamagnetic direction at half the diamagnetic frequency $\omega^*/2$. Since the modes appear in the pedestal before the ELM crash, they are called ELM precursors. As these modes grow, the pedestal density takes the shape of "blobs", mostly in the Low Field Side ; An axisymmetric ($n = 0$) flow is induced by Maxwell stresses, which shear off the plasma density filaments and expel them through the external transport barrier. Thus the density filaments are advected by the $E \times B$ and diamagnetic drifts in the ion diamagnetic direction. Meanwhile, the temperature diffusive transport through the ETB is also largely enhanced by the ergodization of the pedestal induced by the ELM. Because of the advection of the density and of the heat diffusive transport, the pedestal profiles collapse: this is the ELM crash. Due to the ELM crash, a large heat flux reaches the divertor target. The temperature is larger in the LFS, yet since the diamagnetic velocity advects more density towards the inner divertor plate, the heat flux (proportional to both the density and temperature) is "distributed" near-symmetrically between the inner and outer divertor plates. The near-symmetric repartition is in closer agreement with the experimental repartition (either symmetric or twice more important in the inner side) compared to simulations without diamagnetic effects.

After the ELM crash, in simulations without diamagnetic effects, the plasma remained unstable and therefore the transport through the ETB remains large, preventing the pedestal from reconstructing. However when the diamagnetic drifts are present, they are found to stabilize the plasma after the ELM crash. Thus the plasma self-consistently reorganizes in a state which does not depend on the initial conditions: the phasing and the energy repartition between modes is now consistently determined. Due to the applied heating power, the pedestal gradually rebuilds and the edge profiles streepen until the ELM-triggering thresohold is reached: thus another ELM growth and crash occurs. After a few transient ELMs, a quasiperiodic ELMy regime is obtained, characterized by a similar coupling between modes, similar maximum pressure gradient reached when the crash occurs and similar power deposition on the divertor plates, cyclically recovered for all the ELMs. These differ much from the first transient ELMs, pointing out the importance of simulating cycles rather than a single ELM crash.

The ELM cycles, as drawn in peeling-ballooning diagrams, result in a competition between the diamagnetic stabilization of the plasma and the destabilization by the applied heating power. In our particular case, the ELM frequency is decreased when the applied heating power is increased, resulting in less frequent but larger ELMs: at larger applied power, more energy is lost during a crash so the pedestal needs more time to build-up again. This behaviour is simular to the type-III ELMs observed in experiments. However, if the diamagnetic rotation is significantly increased, the ELM frequency is progressively increased, and the energy loss per ELM is gradually decreased: this results in the gyration towards a fix point in the peeling-diagram. This may be related to the compound ELMs observed experimentally.

Last, the first modeling of the ELM mitigation and suppression by RMPs is presented

in chapter 5 for a JET configuration. The ELM mitigation by RMPs (generated by $n = 2$ EFCC) was obtained in JOREK simulations, resulting in a reduction of the ELM power reaching the divertor by a factor of ten. The mitigation is not due to the reduction of the edge pressure gradient by RMPs (observed in simulations), yet it is generated by the coupling between the RMPs and all the modes multiples of the RMP mode (here the even modes are "locked" with $n = 2$ RMPs). These modes couple together and generate magnetic reconnections on the resonant surfaces with a large ergodic zone, thus inducing a continuous transport through the ETB. Subsequently, in place of the large sudden relaxation that characterizes an ELM, a continuous turbulent MHD activity is induced by the ELMs mitigated by the RMPs.

When the diamagnetic rotation is increased, two other regimes of the ELM/RMP interaction are observed in modeling. At sufficiently low applied RMP amplitude, the RMPs have no effect on ELMs, since RMPs are shielded by the plasma rotation. However for a larger RMP amplitude, a bifurcation from the "shielded" state to a "reconnected" state occurs, in which the RMPs are found to fully suppress the ELMs. In this configuration, the even modes, coupled to the RMPs, induce a large permanent transport, which stabilizes the plasma under the P-B limit: thus ELMs are suppressed.

Perpectives

The simulations performed with the JOREK code have enabled to give a comprehensive picture of the ELM cyclical dynamics and of the ELM mitigation by RMPs. This constitutes a step forward in accurately simulating the ELMs and the RMPs, yet a certain number of questions remain open and some refinement of the model should be necessary to improve this theoretical description. A list of possible further investigations and developments is proposed below.

- In the short run, a realistic bootstrap current should be added to the model: when taken into account, the bootstrap current could significantly affect the ELM dynamics and change the peeling-ballooning description of the cycles.

- Also, as discussed in section 3.6 and in appendix D, the impact of the magnetic flutter on the density pump-out induced by RMPs is being investigated. A version of the code is under development, where the electron density equation is solved (including the current parallel gradient term, which is suspected to be responsible for the magnetic flutter) instead of the ion density equation. The ion/electron ambipolarity is assured by the vorticity equation. The influence these new terms have on the particle transport induced by the RMP application will be checked.

- The modeling of RMPs as boundary conditions for the magnetic perturbation does not allow for the magnetic perturbation to be amplified at the edge. A more realistic description of the RMPs will be developped in the coming years: RMP coils will be directly implemented in the JOREK-STARWALL model [Hölzl 2012], such that the perturbation induced by RMP coils will be modeled fully consistently.

- In the longer run, the detailed divertor recycling physics, including ionization and recombination processes, will be included in the JOREK model, in order to be able to compare quantitatively the heat fluxes reaching the divertor – in low and high recycling regimes – with experimental observations.

In parallel to these further developments of the code, the physics of the ELM cycles and the ELM mitigation by RMPs, modeled for the first time here, will be explored in depth for different realistic cases (AUG, JET, MAST, ITER). Particular emphasis with be placed in the comparison between modeling and experiments. The aim is to further understand the complex non-linear physics involved (among others the non-linear dynamics of the rotating precursors and filaments, the coupling between modes during ELM cycles, the demarcation between the regimes of ELM mitigation or suppression by RMPs...), and *in fine* to be able to give reliable predictions for ITER.

Linearization of the Ohm's law: non-screening of the RMPs when electron perpendicular velocity cancels

It was found that the cancellation of the perpendicular velocity (*Eq. (A.4)*) on the resonant surfaces implies the vanishing of the screening currents, which is the "no screening" condition for RMPs [Bécoulet 2012]. This can be shown by linearizing the Ohm's law (*Eq. (2.21)*) using the Fourier transform $A(\psi_{0,0}, \theta, \varphi) = A_{0,0}(\psi_{0,0}) + A_{m,n}(\psi_{0,0})e^{i(m\theta+n\varphi)}$ of the variables P, ψ and J. m and n are the poloidal and toroidal mode numbers respectively, and $\psi_{0,0}$ is the equilibrium poloidal flux (label of the flux surfaces). We consider a single mode (m, n) developing on the resonant surface $q = m/n$. The system is supposed to be at the steady state, which means that the growth of the mode has arrived at saturation. We also suppose that the density perturbation is low compared to the average value: $\rho \sim \rho_{0,0}$. In the framework of our model, we assume that electron and ion temperature are equal but the following calculation remains true if $T_i \neq T_e$. At the first order, the linearization of *Eq. (2.21)* yields:

$$
0 = \frac{F_0}{R^2}in(-u_{m,n} + \frac{\tau_{IC}}{\rho_{0,0}}P_{m,n}) + \frac{im}{R}\psi_{m,n}(-\partial_\psi u_{0,0}
$$
$$
+ \frac{\tau_{IC}}{\rho_{0,0}}\partial_\psi P_{0,0}) - \frac{im}{R}\nabla\psi_{0,0}(-u_{m,n} + \frac{\tau_{IC}}{\rho_{0,0}}P_{m,n}) + \frac{\eta}{R^2}J_{m,n} \tag{A.1}
$$

Using the definition of the safety factor $q = \dfrac{\vec{B} \cdot \nabla\varphi}{\vec{B} \cdot \nabla\theta} = \dfrac{F_0/R^2}{|\nabla\psi|/R} = \dfrac{F_0}{R|\nabla\psi|}$, *Eq. (A.1)* becomes:

$$
\frac{iF_0}{R^2}(\frac{\tau_{IC}}{\rho_{0,0}}P_{m,n} - u_{m,n})(\frac{m}{q} - n) + \frac{im}{R}\psi_{m,n}(\frac{\tau_{IC}}{\rho_{0,0}}\partial_\psi P_{0,0}
$$
$$
- \partial_\psi u_{0,0}) = \frac{\eta}{R^2}J_{m,n} \tag{A.2}
$$

On the resonant surface, the safety factor is equal to $q = m/n$, which implies that:

$$
\frac{im}{R}\psi_{m,n}(\frac{\tau_{IC}}{\rho_{0,0}}\partial_\psi P_{0,0} - \partial_\psi u_{0,0}) = \frac{\eta}{R^2}J_{m,n} \tag{A.3}
$$

We can write the perpendicular component of the electron velocity:

$$
\begin{aligned}
V_{\perp,e} &= (\vec{V}_e^* + \vec{V}_{E\times B}) \cdot \vec{e}_\theta \\
&= \Big(\frac{R^2 \tau_{IC}}{\rho} \nabla P \times \nabla \varphi - R^2 \nabla u \times \nabla \varphi \Big) \cdot \vec{e}_\theta \\
&= R \Big(\frac{\tau_{IC}}{\rho} \nabla_\perp P - \nabla_\perp u \Big) \cdot \frac{\nabla \psi}{|\nabla \psi|} \\
&= R \Big(\frac{\tau_{IC}}{\rho_{0,0}} \partial_\psi P_{0,0} - \partial_\psi u_{0,0} \Big)
\end{aligned}
\tag{A.4}
$$

The combination of *Eq.* (A.4) with *Eq.* (A.3) yields:

$$
im V_{\perp,e} \psi_{m,n} = \eta J_{m,n}
\tag{A.5}
$$

This relation shows that the current perturbation which appears on the resonant surface $q = m/n$ in response to the magnetic perturbation is proportional to the local electron perpendicular velocity $V_{\perp,e}$. Therefore it appears that the cancellation of the perpendicular flow on a resonant surface is the non-screening condition of the corresponding RMP harmonics (m,n) by the plasma rotation. The surfaces where this condition is fulfilled can be found *via* a q_{95}-scan, which shifts the radial position of the resonant surfaces.

Derivation of the reduced MHD equations with diamagnetic and neoclassical effects implemented in JOREK

Contents

In this appendix the set of reduced MHD equations with diamagnetic and neoclassical effects, implemented in the JOREK code, is derived. To simplify the MHD system of equations, a reduction of the problem is done. This allows to write the vector differential equations as scalar differential equations, a non negligible simplification of the problem.

First we present the reduction of the induction equation followed by the reduction of the density, momentum and temperature equations.

B.1 Induction equation

The magnetic field is separated between a toroidal and a poloidal component. The toroidal component is considered constant

$$
\begin{aligned}
\boldsymbol{B} &= \boldsymbol{B}_\varphi + \boldsymbol{B}_{Pol} \\
&= \boldsymbol{B}_\varphi + \nabla\psi \times \nabla\varphi \\
&= \frac{F_0}{R}\boldsymbol{e}_\varphi + \nabla\psi \times \nabla\varphi \\
&= F_0\nabla\varphi + \nabla\psi \times \nabla\varphi,
\end{aligned}
\tag{B.1}
$$

with $\nabla\varphi = 1/R\,\boldsymbol{e}_\varphi$, φ the toroidal direction. R is the horizontal direction along the major radius and Z is the vertical direction. The three dimensional cylindrical coordinate system convention is $(R,\,Z,\,\varphi)$ that could be noted (1, 2, 3). The magnetic flux $\psi = R(\boldsymbol{A}\cdot\boldsymbol{e}_\varphi)$ with $\boldsymbol{A}$ the vector potential. Note that in the general case we have $\boldsymbol{B} = \nabla\times\boldsymbol{A}$.

The magnetic field is considered to be axisymmetric. The total current density is assumed to be mainly toroidal so we can write, using Ampère's law

$$
\boldsymbol{j} = -\frac{1}{\mu_0 R}\Delta^*\psi\,\boldsymbol{e}_\varphi,
\tag{B.2}
$$

with

$$
\Delta^* = R^2\nabla\cdot\left(\frac{1}{R^2}\nabla_\perp\right) = \left(R\frac{\partial}{\partial R}\left(\frac{1}{R}\frac{\partial}{\partial R}\right) + \frac{\partial^2}{\partial Z^2}\right).
\tag{B.3}
$$

The induction equation is the following

$$
\frac{\partial\boldsymbol{B}_{Pol}}{\partial t} = -\nabla\times\boldsymbol{E}.
\tag{B.4}
$$

The poloidal magnetic field can also be written

$$
\boldsymbol{B}_{Pol} = \nabla\psi\times\nabla\varphi = \nabla\times\left(\psi\nabla\varphi\right),
\tag{B.5}
$$

thus if the magnetic field is replaced by the magnetic flux ψ we have

$$
\nabla\times\left[\partial_t\left(\psi\nabla\varphi\right) + \boldsymbol{E}\right] = 0.
\tag{B.6}
$$

The expression inside brackets can be expressed as the gradient of a scalar potential u. So that,

$$
\partial_t(\psi\nabla\varphi) = -\boldsymbol{E} - F_0\nabla u.
\tag{B.7}
$$

The F_0 coefficient has been added to simplify the final formulation of the $\boldsymbol{E}\times\boldsymbol{B}$ velocity $(\boldsymbol{v}_E)$. The expression for the electric field $\boldsymbol{E}$ can be derived from the generalized Ohm's law (see for instance [Goedbloed 2004]),

$$
\boldsymbol{E} = -\frac{1}{en}\nabla P_e - \boldsymbol{v}\times\boldsymbol{B} + \frac{1}{en}(\boldsymbol{j}\times\boldsymbol{B}) + \eta\boldsymbol{j} - \frac{m_e}{e}\frac{d\boldsymbol{v}_e}{dt}.
\tag{B.8}
$$

with e the electron charge, $n = n_e = n_i = \rho/m_i$ the particle density (m^{-3}), m_i and m_e respectively the ion and electron mass (kg). In this equation we have kept the pressure term because there is an important macroscopic gradient in the pressure profile. On the other hand the electron inertia term is neglected.

The induction equation becomes

$$\partial_t(\psi\nabla\varphi) = \frac{m_i}{\rho e}\nabla P_e + \boldsymbol{v}\times\boldsymbol{B} - \frac{m_i}{\rho e}(\boldsymbol{j}\times\boldsymbol{B}) - \eta\boldsymbol{j} - F_0\nabla u. \tag{B.9}$$

Projecting this equation along the magnetic field $\boldsymbol{B}$, we obtain

$$\frac{1}{R}\frac{\partial\psi}{\partial t}B_\varphi = \frac{m_i}{\rho e}\nabla P_e\cdot\boldsymbol{B} - F_0\nabla u\cdot\boldsymbol{B} + \frac{\eta}{\mu_0 R}\Delta^*\psi B_\varphi \tag{B.10}$$

The terms $\boldsymbol{v}\times\boldsymbol{B}$ and $\boldsymbol{j}\times\boldsymbol{B}$ are perpendicular to $\boldsymbol{B}$. Also we have replaced the current density by its expression as a function of the magnetic flux (see *Eq.* (B.2)).

Using the Poisson bracket notation we have

$$[a,\psi] = \boldsymbol{e}_\varphi\cdot(\nabla a\times\nabla\psi) = \nabla a\cdot(\nabla\psi\times\boldsymbol{e}_\varphi) = R\nabla a\cdot\boldsymbol{B}_{Pol} \tag{B.11}$$

and the scalar product with $\boldsymbol{B}$ is:

$$\nabla a\cdot\boldsymbol{B} = \frac{F_0}{R^2}\frac{\partial a}{\partial\varphi} + \frac{1}{R^2}[a,\psi] \tag{B.12}$$

Thus using *Eq.* (B.12) and knowing that $B_\varphi = F_0/R$, *Eq.* (B.10) becomes:

$$\frac{1}{R^2}\frac{\partial\psi}{\partial t} = \frac{\eta}{\mu_0 R^2}\Delta^*\psi + \frac{m_i}{\rho e F_0}\left(\frac{F_0}{R^2}\frac{\partial P_e}{\partial\varphi} + \frac{1}{R}[P_e,\psi]\right) - \frac{F_0}{R^2}\frac{\partial u}{\partial\varphi} - \frac{1}{R}[u,\psi] \tag{B.13}$$

t	$=$	$\tilde{t}\sqrt{\rho_0\mu_0}$	$\boldsymbol{j}$	$=$	$\tilde{\boldsymbol{j}}/\mu_0$
ρ	$=$	$\tilde{\rho}\rho_0$	D	$=$	$\tilde{D}/\sqrt{\rho_0\mu_0}$
η	$=$	$\tilde{\eta}\sqrt{\mu_0/\rho_0}$	P_e	$=$	$P/(1+T_i/T_e)$
φ	$=$	$\tilde{u}F_0/\sqrt{\rho_0\mu_0}$	P	$=$	$\tilde{P}/\mu_0$
$\boldsymbol{v}_\perp$	$=$	$\tilde{v}_\perp/\sqrt{\rho_0\mu_0}$	$v_\|$	$=$	$\tilde{v}_\|\|\boldsymbol{B}\|/\sqrt{\rho_0\mu_0}$
$\mu_{i,neo}$	$=$	$\tilde{\mu}_{i,neo}/\sqrt{\rho_0\mu_0}$	S_ρ	$=$	$\tilde{S}_\rho\sqrt{\rho_0/\mu_0}$

Table B.1: JOREK normalization. The superscripts $\sim$ represent the JOREK normalized variables.

In JOREK the normalization presented in Tab. B.1 is used. Writing *Eq.* (B.13) as a

function of the normalized variables we obtain

$$\frac{1}{\sqrt{\rho_0\mu_0}R^2}\frac{\partial\psi}{\partial\tilde{t}} = \frac{\tilde{\eta}}{\sqrt{\rho_0\mu_0}R^2}\Delta^*\psi + \frac{1}{\sqrt{\rho_0\mu_0}}\frac{m_i}{F_0e\sqrt{\rho_0\mu_0}(1+T_i/T_e)}\frac{1}{\tilde{\rho}}\left(\frac{F_0}{R^2}\frac{\partial\tilde{P}}{\partial\varphi} + \frac{1}{R}\left[\tilde{P},\psi\right]\right)$$
$$-\frac{F_0}{\sqrt{\rho_0\mu_0}R^2}\frac{\partial\tilde{u}}{\partial\varphi} - \frac{1}{\sqrt{\rho_0\mu_0}R}\left[\tilde{u},\psi\right] \quad (B.14)$$

For simplicity, in the following, the tildes are omitted. The previous normalized expression simplifies to

$$\frac{1}{R^2}\frac{\partial\psi}{\partial t} = \frac{\eta}{R^2}\Delta^*\psi + \tau_{IC}\frac{1}{\rho}\left(\frac{F_0}{R^2}\frac{\partial P}{\partial\varphi} + \frac{1}{R}\left[P,\psi\right]\right) - \frac{F_0}{R^2}\frac{\partial u}{\partial\varphi} - \frac{1}{R}\left[u,\psi\right] \quad (B.15)$$

with

$$\tau_{IC} = \frac{m_i}{F_0e\sqrt{\rho_0\mu_0}(1+T_i/T_e)}$$

B.2   Density equation

The normalized continuity equation (noted without the tilde symbols) is

$$\frac{\partial\rho}{\partial t} = -\nabla\cdot(\rho\boldsymbol{v}) + \nabla\cdot(D\nabla\rho) + S_\rho \quad (B.16)$$

The normalized velocity can be decomposed as

$$\boldsymbol{v} = v_{||}\boldsymbol{B} + \boldsymbol{v}_E + \boldsymbol{v}_i^*$$
$$= v_{||}\boldsymbol{B} + R^2\nabla\varphi\times\nabla u + \tau_{IC}\frac{R^2}{\rho}\left(\nabla\varphi\times\nabla P\right) \quad (B.17)$$

We recall that the parallel velocity normalization (dimensionless) is different from the perpendicular component normalization (Tesla, $[\boldsymbol{B}]$ units). Thus to recover the homogeneity in the expression the parallel velocity is multiplied by the magnetic field. The

first term in the right hand side of *Eq.* (B.16) can be decomposed in

$$
\begin{aligned}
\nabla \cdot (\rho \boldsymbol{v}) =& \nabla \cdot \left(-\rho R^2 \nabla u \times \nabla \varphi + \rho v_{||} \boldsymbol{B} + \tau_{IC} R^2 \left(\nabla \varphi \times \nabla P \right) \right) \\
=& -\nabla \left(\rho R^2 \right) \cdot \nabla u \times \nabla \varphi - \rho R^2 \underbrace{\nabla \cdot (\nabla u \times \nabla \varphi)}_{=0} + \nabla (\rho v_{||}) \cdot \boldsymbol{B} + \rho v_{||} \underbrace{\nabla \cdot \boldsymbol{B}}_{=0} \\
& + \tau_{IC} \nabla P \cdot \left(\nabla \times (R^2 \nabla \varphi) \right) \\
=& -\nabla \varphi \cdot \nabla \left(\rho R^2 \right) \times \nabla u + \left(\nabla_{Pol}(\rho v_{||}) + \partial_\varphi (\rho v_{||}) \nabla \varphi \right) \cdot (\nabla \psi \times \nabla \varphi + F_0 \nabla \varphi) \\
& - 2\tau_{IC} \partial_Z P \\
=& \frac{1}{R} [u, \rho R^2] + \nabla \varphi \cdot \nabla (\rho v_{||}) \times \nabla \psi + \frac{F_0}{R^2} \partial_\varphi (\rho v_{||}) - 2\tau_{IC} \partial_Z P \\
=& \frac{1}{R} [u, \rho R^2] + \frac{1}{R} [\rho v_{||}, \psi] + \frac{F_0}{R^2} \partial_\varphi (\rho v_{||}) - 2\tau_{IC} \partial_Z P \\
=& -R[\rho, u] - 2\rho \partial_Z u + \frac{\rho}{R} [v_{||}, \psi] + \frac{v_{||}}{R} [\rho, \psi] + \frac{F_0}{R^2} v_{||} \partial_\varphi \rho + \frac{F_0}{R^2} \rho \partial_\varphi v_{||} - 2\tau_{IC} \partial_Z P
\end{aligned}
$$

$$(B.18)$$

Thus the full ion density equation is solved:

$$
\begin{aligned}
\frac{\partial \rho}{\partial t} =& R[\rho, u] + 2\rho \partial_Z u + \frac{\rho}{R} [\psi, v_{||}] + \frac{v_{||}}{R} [\psi, \rho] - \frac{F_0}{R^2} v_{||} \partial_\varphi \rho - \frac{F_0}{R^2} \rho \partial_\varphi v_{||} + 2\tau_{IC} \partial_Z P \\
& + \nabla \cdot \left(D_{||} \nabla_{||} \rho \right) + \nabla \cdot (D_\perp \nabla_\perp \rho) + S_\rho
\end{aligned}
$$

$$(B.19)$$

B.3   Momentum equation

B.3.1   Developed form of the momentum equation and gyro-viscous cancellation

We start with the momentum equation for a single fluid ($\approx$ ion) taking into account the 'cross' or gyro-viscous stress tensor and the neoclassical tensor,

$$
\frac{\partial (\rho \boldsymbol{v})}{\partial t} + \nabla \cdot (\rho \boldsymbol{v} \otimes \boldsymbol{v}) = -\nabla P + \boldsymbol{j} \times \boldsymbol{B} - \nabla \cdot \overline{\overline{\boldsymbol{\Pi}}}_{gv} - \nabla \cdot \overline{\overline{\boldsymbol{\Pi}}}_{neo} \tag{B.20}
$$

with ρ the ion mass density and $\overline{\overline{\boldsymbol{\Pi}}}_{gv}$ the gyro-viscous tensor. We have neglected the electron inertia and the parallel and perpendicular stress tensors. The neoclassical tensor $\overline{\overline{\boldsymbol{\Pi}}}_{neo}$ and the viscosity $\mu \Delta \boldsymbol{v}$ are first neglected, but will be added at the end of the subsection. For more details about these tensors see e.g. Ref. [Schnack 2006] and references therein.

Let us consider the continuity equation neglecting the diffusive terms:

$$
\frac{\partial \rho}{\partial t} = -\nabla \cdot (\rho \boldsymbol{v}) + S_\rho \tag{B.21}
$$

This equation allows us to simplify the inertial term in the momentum equation *Eq.* (B.20) as follows

$$\rho\frac{\partial \boldsymbol{v}}{\partial t} + \boldsymbol{v}\left[\frac{\partial \rho}{\partial t} + \nabla\cdot(\rho\boldsymbol{v})\right] + \rho(\boldsymbol{v}\cdot\nabla)\boldsymbol{v} = -\nabla P + \boldsymbol{j}\times\boldsymbol{B} - \nabla\cdot\overline{\overline{\boldsymbol{\Pi}}}_{gv}$$

$$\rho\frac{\partial \boldsymbol{v}}{\partial t} + \boldsymbol{v}S_\rho + \rho(\boldsymbol{v}\cdot\nabla)\boldsymbol{v} = -\nabla P + \boldsymbol{j}\times\boldsymbol{B} - \nabla\cdot\overline{\overline{\boldsymbol{\Pi}}}_{gv} \tag{B.22}$$

Then the velocity vector can be decomposed as:

$$\boldsymbol{v} = v_{\parallel}\boldsymbol{B} + \boldsymbol{v}_E + \boldsymbol{v}_i^*$$

$$= v_{\parallel}\boldsymbol{B} + R^2\nabla\varphi\times\nabla u + \tau_{IC}\frac{R^2}{\rho}\left(\nabla\varphi\times\nabla P\right) \tag{B.23}$$

Developing the material derivative, the momentum equation can be written

$$\rho\left[\partial_t\left(\boldsymbol{v}_E + \boldsymbol{v}_i^* + v_{\parallel}\boldsymbol{B}\right) + \left[\left(\boldsymbol{v}_E + \boldsymbol{v}_i^* + v_{\parallel}\boldsymbol{B}\right)\cdot\nabla\right]\left(\boldsymbol{v}_E + \boldsymbol{v}_i^* + v_{\parallel}\boldsymbol{B}\right)\right] =$$

$$-\nabla P + \boldsymbol{j}\times\boldsymbol{B} - \nabla\cdot\overline{\overline{\boldsymbol{\Pi}}}_{gv} - \boldsymbol{v}S_\rho \tag{B.24}$$

Separating the $\boldsymbol{v}_i^*$ from the other components in the material derivative we find

$$\rho\left[\partial_t\left(\boldsymbol{v}_E + v_{\parallel}\boldsymbol{B}\right) + \left[\left(\boldsymbol{v}_E + v_{\parallel}\boldsymbol{B} + \boldsymbol{v}_i^*\right)\cdot\nabla\right]\left(\boldsymbol{v}_E + v_{\parallel}\boldsymbol{B}\right)\right]$$

$$+ \rho\left[\partial_t\boldsymbol{v}_i^* + \left[\left(\boldsymbol{v}_E + v_{\parallel}\boldsymbol{B} + \boldsymbol{v}_i^*\right)\cdot\nabla\right]\boldsymbol{v}_i^*\right]$$

$$= -\nabla P + \boldsymbol{j}\times\boldsymbol{B} - \nabla\cdot\overline{\overline{\boldsymbol{\Pi}}}_{gv} - \boldsymbol{v}S_\rho \quad \text{(B.25)}$$

The utility of the introduction of the gyro-viscous tensor is that it algebraically cancels a significant part of the advection acceleration. In fact we can write the *gyro-viscous cancellation* as [Schnack 2006]

$$\rho\left[\partial_t\boldsymbol{v}_i^* + \left[\left(\boldsymbol{v}_E + v_{\parallel}\boldsymbol{B} + \boldsymbol{v}_i^*\right)\cdot\nabla\right]\boldsymbol{v}_i^*\right] + \nabla\cdot\overline{\overline{\boldsymbol{\Pi}}}_{gv} \approx \nabla\chi - \rho\left(\boldsymbol{v}_i^*\cdot\nabla\right)v_{\parallel}\boldsymbol{B} \tag{B.26}$$

Replacing this expression in *Eq.* (B.25) we find

$$\rho\partial_t(\boldsymbol{v}_E + v_{\parallel}\boldsymbol{B}) + \rho\left[\left(\boldsymbol{v}_E + v_{\parallel}\boldsymbol{B} + \boldsymbol{v}_i^*\right)\cdot\nabla\right]\left(\boldsymbol{v}_E + v_{\parallel}\boldsymbol{B}\right) =$$

$$-\nabla(P + \chi) + \boldsymbol{j}\times\boldsymbol{B} + \rho\left(\boldsymbol{v}_i^*\cdot\nabla\right)v_{\parallel}\boldsymbol{B} - \boldsymbol{v}S_\rho \tag{B.27}$$

The gradient term $(\nabla\chi)$ is introduced in the gradient of the pressure (in *Eq.* (B.25)) and χ can be considered as negligible in comparison to the pressure value (P). We have then the material derivative of the diamagnetic velocity 'cancelled' by the gyro-viscous tensor. We note that the actual calculation of *Eq.* (B.26) is complex [Hazeltine 1985b, Hsu 1986, Chang 1992] and as stated in Ref. [Schnack 2006] "*it seems to have been carried out only under restricted conditions (i.e., uniform magnetic field , sheared slab geometry , uniform temperature, etc...). Further, there is not universal agreement on the exact form of the cancellation. Some authors* [Hazeltine 1985b, Hsu 1986] *find additional terms on the right hand side of Eq.* (B.26)." For our case we are interested in the most simplified

formulation, so we keep the above presented cancellation.

In JOREK, we also add the viscosity, as if plasma was a newtonian fluid, and a source of rotation S_v. The neoclassical friction can also be added (see the description below), which gives the full momentum equation:

$$
\rho \partial_t \left(\boldsymbol{v}_E + v_\| \boldsymbol{B} \right) + \rho \left[\left(\boldsymbol{v}_E + v_\| \boldsymbol{B} + \boldsymbol{v}_i^* \right) \cdot \nabla \right] \boldsymbol{v}_E + \rho \left[\left(\boldsymbol{v}_E + v_\| \boldsymbol{B} \right) \cdot \nabla \right] v_\| \boldsymbol{B}
$$
$$
= -\nabla P + \boldsymbol{j} \times \boldsymbol{B} - \nabla \cdot \overline{\overline{\Pi}}_{neo} + S_v - \boldsymbol{v} S_\rho + \mu \Delta \boldsymbol{v}. \quad \text{(B.28)}
$$

To get the perpendicular momentum equation (derived in section B.3.3), we apply the operator $\nabla \varphi \cdot \nabla \times [R^2 ...]$ on *Eq.* (B.28). And the parallel momentum equation (derived in section B.3.4) is the projection of *Eq.* (B.28) along the magnetic field $\boldsymbol{B}$.

B.3.2 Addition of the neoclassical tensor

The divergence of the neoclassical tensor is given by the heuristic closure taken from Ref. [Gianakon 2002]:

$$
\nabla \cdot \overline{\overline{\Pi}}_{i,neo} = \rho \mu_{i,neo} \frac{B^2}{B_\theta^2} (v_\theta - v_{\theta,neo}) \, \boldsymbol{e}_\theta \quad \text{(B.29)}
$$

where $\mu_{i,neo}$ is the neoclassical friction. This formulation expresses the friction between trapped and passing particles and constrains the poloidal velocity v_θ to approach the neoclassical value $v_{\theta,neo} = -k_i \nabla T_i \times \boldsymbol{B} / eB^2 \cdot \vec{e}_\theta$, where k_i is the neoclassical heat diffusivity. We have used the following definition of the unit vector in the poloidal direction:

$$
\boldsymbol{e}_\theta = (\nabla \psi \times \nabla \varphi) \frac{R}{|\nabla \psi|} \quad \text{(B.30)}
$$

Note that this definition implies that the orthonormal basis $(\boldsymbol{e}_\psi, \boldsymbol{e}_\theta, \boldsymbol{e}_\varphi) = (\frac{\nabla \psi}{|\nabla \psi|}, (\nabla \psi \times \nabla \varphi) \frac{R}{|\nabla \psi|}, R \nabla \varphi)$ is left handed, and the poloidal magnetic field therefore writes

$$
B_\theta = \boldsymbol{B} \cdot \boldsymbol{e}_\theta = |\nabla \psi| / R \quad \text{(B.31)}
$$

The projection of *Eq.* (B.17) along the poloidal direction $\boldsymbol{e}_\theta$ *Eq.* (B.30) gives the expression of the poloidal velocity:

$$
v_\theta = -\frac{1}{B_\theta} \left(\nabla_\perp \psi \cdot \nabla_\perp u + \frac{\tau_{IC}}{\rho} \nabla_\perp \psi \cdot \nabla_\perp P - v_\| B_\theta^2 \right) \quad \text{(B.32)}
$$

The combination of *Eq.* (B.32) and *Eq.* (B.30) with the expression of the normalized neoclassical velocity $v_{\theta,neo} = -\frac{k_i \tau_{IC}}{B_\theta} (\nabla_\perp \psi \cdot \nabla_\perp T)$ leads to the normalized developed

form of the neoclassical tensor *Eq.* (B.29):

$$
\nabla \cdot \overline{\overline{\Pi}}_{i,neo} = \mu_{i,neo}\rho \frac{B^2}{B_\theta^4}\Big(-v_{\|}B_\theta^2 + \nabla_\perp\psi \cdot \nabla_\perp u
$$
$$
+ \frac{\tau_{IC}}{\rho}\big(\nabla_\perp\psi \cdot \nabla_\perp P + k_i\rho\nabla_\perp\psi \cdot \nabla_\perp T\big)\Big)(\nabla\psi \times \nabla\varphi) \tag{B.33}
$$

Where we have used the normalization defined in (B.1)

B.3.3   Derivation of the perpendicular momentum equation

B.3.3.1   Derivation of the diamagnetic term

The new term which comes from the introduction of the diamagnetic effects is

$$
\rho\left(\boldsymbol{v}_i^* \cdot \nabla\right)\boldsymbol{v}_E \tag{B.34}
$$

In JOREK the perpendicular momentum equation is written as a function of the toroidal vorticity defined as

$$
W = \nabla\varphi \cdot (\nabla \times \boldsymbol{v}_E) = \nabla \cdot \nabla_\perp u \tag{B.35}
$$

We then express the term in *Eq.* (B.34) in terms of toroidal vorticity. To do so we apply the following operator

$$
\nabla\varphi \cdot \nabla \times \left[R^2 \dots \right. \tag{B.36}
$$

The details of this calculation are presented in the following. Here we consider this term on the right hand side of *Eq.* (B.28) so a minus sign is added

$$
-\nabla\varphi \cdot \nabla \times \left[R^2\rho\left(\boldsymbol{v}_i^* \cdot \nabla\right)\boldsymbol{v}_E\right] = \nabla \cdot \left(\nabla\varphi \times \left[R^2\rho\left(\boldsymbol{v}_i^* \cdot \nabla\right)\boldsymbol{v}_E\right]\right)
$$
$$
= \nabla \cdot \left(\nabla\varphi \times \left[\tau_{IC}R^4\left(\nabla\varphi \times \nabla P\right)\cdot\nabla\right]\boldsymbol{v}_E\right) \tag{B.37}
$$

Projecting the diamagnetic velocity in the cylindrical coordinates (R, Z, φ) we get the following form

$$
-\nabla\varphi \cdot \nabla \times \left[R^2\rho\left(\boldsymbol{v}_i^* \cdot \nabla\right)\boldsymbol{v}_E\right] = \nabla \cdot \left(\nabla\varphi \times \left[\tau_{IC}R^4\left(\nabla\varphi \times \nabla P\right)\cdot\nabla\right]\boldsymbol{v}_E\right)
$$
$$
= \nabla \cdot \left(\nabla\varphi \times \tau_{IC}R^3\left[-\partial_Z P\,\partial_R + \partial_R P\,\partial_Z\right](v_{E_R}\boldsymbol{e}_R + v_{E_Z}\boldsymbol{e}_Z)\right). \tag{B.38}
$$

Writing the $\boldsymbol{E} \times \boldsymbol{B}$ velocity terms as a function of the scalar u function we get

$$
v_{E_R} = -R\partial_Z u \qquad \text{and} \qquad v_{E_Z} = R\partial_R u. \tag{B.39}
$$

Replacing in *Eq.* (B.38) and developing we have

$$
-\nabla\varphi\cdot\nabla\times\left[R^2\rho\left(\boldsymbol{v}_i^*\cdot\nabla\right)\boldsymbol{v}_E\right]=\nabla\cdot\Bigg(\tau_{IC}R^2\Big[\left[R\partial_Z P\partial_{RR}-R\partial_R P\partial_{RZ}+\partial_Z P\partial_R\right]u\,\boldsymbol{e}_R
$$
$$
+\left[R\partial_Z P\partial_{RZ}-R\partial_R P\partial_{ZZ}+\partial_Z P\partial_Z\right]u\,\boldsymbol{e}_Z\Big]\Bigg)\quad\text{(B.40)}
$$

Using the divergence operator in cylindrical coordinates we find

$$
-\nabla\varphi\cdot\nabla\times\left[R^2\rho\left(\boldsymbol{v}_i^*\cdot\nabla\right)\boldsymbol{v}_E\right]=\tau_{IC}\Bigg(R^3\left[\partial_Z P\partial_{RRR}+\partial_Z P\partial_{RZZ}-\partial_R P\partial_{RRZ}-\partial_R P\partial_{ZZZ}\right]u
$$
$$
+R^2\left[\partial_Z P\partial_{RR}-\partial_R P\partial_{RZ}\right]u-R\partial_Z P\partial_R u
$$
$$
+R^2\left[\partial_{RZ}P\partial_R+\partial_Z P\partial_{RR}+\partial_{ZZ}P\partial_Z+\partial_Z P\partial_{ZZ}\right]u+R\partial_Z P\partial_R u
$$
$$
+R^3\left[\partial_{RZ}P\partial_{RR}-\partial_{RR}P\partial_{RZ}+\partial_{ZZ}P\partial_{RZ}-\partial_{RZ}P\partial_{ZZ}\right]u
$$
$$
+3R^2\left[\partial_Z P\partial_{RR}-\partial_R P\partial_{RZ}+\partial_Z P\frac{\partial_R}{R}\right]u\Bigg)
$$
$$
\text{(B.41)}
$$

Using the Poisson bracket notation this last expression can be written

$$
-\nabla\varphi\cdot\nabla\times\left[R^2\rho\left(\boldsymbol{v}_i^*\cdot\nabla\right)\boldsymbol{v}_E\right]=\tau_{IC}\Bigg\{R^3\left[W,\,P\right]+R^2\nabla\cdot\left(\partial_Z P\nabla_{Pol}u\right)
$$
$$
-R^3\left[\partial_{RZ}u\left(\partial_{RR}P-\partial_{ZZ}P\right)-\partial_{RZ}P\left(\partial_{RR}u-\partial_{ZZ}u\right)\right]
$$
$$
+3R^3\left[\left(\frac{1}{R}\partial_R u\right),\,P\right]\Bigg\}
$$
$$
\text{(B.42)}
$$

B.3.3.2 Implementation of the other terms in the perpendicular momentum equation

The time derivative terms are the following:

$$
\begin{aligned}
\nabla\varphi \cdot \nabla \times \left[R^2 \rho \frac{\partial \boldsymbol{v}_E}{\partial t} \right] &= \nabla\varphi \cdot \nabla \times \left[R^2 \rho \frac{\partial}{\partial t}(-R^2 \nabla u \times \nabla\varphi) \right] \\
&= \nabla \cdot \nabla\varphi \times \left[R^4 \rho \frac{\partial}{\partial t}(\nabla u \times \nabla\varphi) \right] \\
&= \nabla \cdot \left[R^4 \rho \frac{\partial}{\partial t}\left(\frac{\nabla_\perp u}{R^2} \right) \right] \\
&= \nabla \cdot \left(R^2 \rho \nabla_\perp \frac{\partial u}{\partial t} \right)
\end{aligned}
\tag{B.43}
$$

$$
\begin{aligned}
\nabla\varphi \cdot \nabla \times \left[R^2 \rho \frac{\partial (v_\| \boldsymbol{B})}{\partial t} \right] &= -\nabla \cdot \nabla\varphi \times \left[R^2 \rho \frac{\partial (v_\| \boldsymbol{B})}{\partial t} \right] \\
&= -\nabla \cdot \left[R^2 \rho \frac{\partial}{\partial t}(v_\| \nabla\varphi \times \boldsymbol{B}) \right] \\
&= -\nabla \cdot \left[R^2 \rho \frac{\partial}{\partial t}\left(\frac{\nabla_\perp \psi}{R^2} \right) \right] \\
&= -\nabla \cdot \left(\rho \nabla_\perp \frac{\partial}{\partial t}(v_\| \nabla_\perp \psi) \right)
\end{aligned}
\tag{B.44}
$$

This second term is neglected as the parallel component of the velocity projected on the poloidal plane is considered negligible as compared to the perpendicular component of the velocity.

The advection terms, quite complicated, are developed below. We write $\hat{\rho} = R^2 \rho$ and we use the identity $(\boldsymbol{v} \cdot \nabla)\boldsymbol{v} = \nabla(\boldsymbol{v^2}/2) - \boldsymbol{v} \times (\nabla \times \boldsymbol{v})$. The advection, on the right hand side of the equation, is:

$$
\begin{aligned}
\nabla\varphi \cdot \nabla \times \left[R^2 \left(-\rho \left(\boldsymbol{v}_E \cdot \nabla \right) \boldsymbol{v}_E \right) \right] &= -\nabla\varphi \cdot \nabla\hat{\rho} \times (\boldsymbol{v}_E \cdot \nabla)\boldsymbol{v}_E + \hat{\rho}\nabla\varphi \cdot \nabla \times (\boldsymbol{v}_E \cdot \nabla)\boldsymbol{v}_E \\
&= -\nabla\varphi \cdot \nabla\hat{\rho} \times \nabla(\boldsymbol{v}_E^2/2) + \nabla\varphi \cdot \nabla\hat{\rho} \times (\boldsymbol{v}_E \times (\nabla \times \boldsymbol{v}_E)) \\
&\quad - \nabla\varphi\hat{\rho}\underbrace{\nabla \times \nabla(\boldsymbol{v}_E^2/2)} + \nabla\varphi\hat{\rho}\nabla \times (\boldsymbol{v}_E \times \nabla \times \boldsymbol{v}_E) \\
&= \frac{1}{R}\left[\frac{\boldsymbol{v}_E^2}{2}, \hat{\rho} \right] - \nabla\hat{\rho} \cdot \underbrace{\nabla\varphi \times (\boldsymbol{v}_E \times \boldsymbol{w}_E)}_{(\boldsymbol{w}_E \cdot \boldsymbol{a}^3)\boldsymbol{v}_E - (\boldsymbol{v}_E \cdot \boldsymbol{a}^3)\boldsymbol{w}_E} - \hat{\rho}\nabla \cdot \underbrace{\nabla\varphi \times (\boldsymbol{v}_E \times \boldsymbol{w}_E)}_{(\boldsymbol{w}_E \cdot \boldsymbol{a}^3)\boldsymbol{v}_E} \\
&= \frac{1}{2R}\left[R^4 |\nabla_\perp u|^2, \hat{\rho} \right] + (\boldsymbol{w}_E \cdot \boldsymbol{a}^3)R^2 \nabla\hat{\rho} \cdot (\nabla u \times \nabla\varphi) \\
&\quad - \hat{\rho}(\boldsymbol{w}_E \cdot \boldsymbol{a}^3)\nabla \cdot \boldsymbol{v}_E - \hat{\rho}\boldsymbol{v}_E \cdot \nabla(\boldsymbol{w}_E \cdot \boldsymbol{a}^3)
\end{aligned}
\tag{B.45}
$$

We calculate the developed form of the $\boldsymbol{E} \times \boldsymbol{B}$ velocity and the vorticity:

$$\boldsymbol{v}_E = \begin{cases} -R\frac{\partial u}{\partial Z} \\ +R\frac{\partial u}{\partial R} \\ 0, \end{cases}$$

$$\boldsymbol{w}_E = \nabla \times \boldsymbol{v}_E = \begin{cases} -\frac{\partial}{\partial \varphi}\frac{\partial u}{\partial R} \\ -\frac{\partial}{\partial \varphi}\frac{\partial u}{\partial Z} \\ R\nabla \cdot \nabla_\perp u \end{cases}$$

Thus $(\boldsymbol{w}_E \cdot \boldsymbol{a}^3) = \nabla \cdot \nabla_\perp u = w_E$. Furthermore, we use: $\nabla \cdot \boldsymbol{v}_E = -2\frac{\partial u}{\partial Z}$ which gives the following term:

$$\begin{aligned}
\nabla\varphi \cdot \nabla \times \left[R^2\left(-\rho\left(\boldsymbol{v}_E \cdot \nabla\right)\boldsymbol{v}_E\right)\right] &= \frac{1}{2R}\left[R^4|\nabla_\perp u|^2, \hat{\rho}\right] + Rw_E\left[\hat{\rho}, u\right] + 2\hat{\rho}w_E\frac{\partial u}{\partial Z} - \hat{\rho}\boldsymbol{v}_E \cdot \nabla w_E \\
&= \frac{1}{2R}\left[R^4|\nabla_\perp u|^2, \hat{\rho}\right] + Rw_E\left[\hat{\rho}, u\right] + 2\hat{\rho}w_E\frac{\partial u}{\partial Z} + \hat{\rho}R\left[w_E, u\right] \\
&= \frac{1}{2R}\left[R^4|\nabla_\perp u|^2, \hat{\rho}\right] + R\left[\hat{\rho}w_E, u\right] + 2\hat{\rho}w_E\frac{\partial u}{\partial Z}
\end{aligned}$$

$$(B.46)$$

Where we have used the following identity:

$$\boldsymbol{v}_E \cdot \nabla w = -R^2\nabla u \times \nabla\varphi \cdot \nabla w = -R\left[w, u\right]. \tag{B.47}$$

We can show that $R\left[\hat{\rho}w, u\right] + 2\hat{\rho}w\frac{\partial u}{\partial Z} = \frac{1}{R}\left[\hat{\rho}wR^2, u\right]$, then we can also write the term as:

$$\nabla\varphi \cdot \nabla \times \left[R^2(-\rho(\boldsymbol{v}_E \cdot \nabla)\boldsymbol{v}_E)\right] = \frac{1}{2R}\left[R^4|\nabla_\perp u|^2, \hat{\rho}\right] + \frac{1}{R}\left[\hat{\rho}wR^2, u\right] \tag{B.48}$$

The terms $\nabla\varphi \cdot \nabla \times R^2\left[-\rho\left(\boldsymbol{v}_\| \cdot \nabla\right)\boldsymbol{v}_E\right]$ and $\nabla\varphi \cdot \nabla \times R^2\left[-\rho\left(\boldsymbol{v}_\| \cdot \nabla\right)\boldsymbol{v}_\|\right]$ are neglected as they are small compared to the terms involving the perpendicular velocity: $\{\nabla\varphi \cdot \nabla \times R^2(-\rho\left[(\boldsymbol{v}_E + \boldsymbol{v}_i^*) \cdot \nabla\right]\boldsymbol{v}_E)\}$. However they are not zero and a laborious calculation can show that they are expressed as follows (see the full development in Emmanuel Franck's paper [Frank 2014]):

$$R\nabla\varphi \cdot \nabla \times R^2\left(-\rho\boldsymbol{v}_\| \cdot \nabla\boldsymbol{v}_\|\right) =$$

$$\left[\rho v_\|^2 j, \psi\right] + \left[\rho v_\|\left(\nabla_\perp v_\| \cdot \nabla_\perp \psi\right), \psi\right] + R\nabla \cdot \left(\rho\frac{F_0}{R^2}v_\|\partial_\varphi\left(v_\|\nabla_\perp\psi\right)\right) - \frac{1}{2}\left[\hat{\rho}, v_\|^2|\boldsymbol{B}_{pol}|^2\right]$$

$$(B.49)$$

and

$$
\begin{aligned}
R\nabla\varphi \cdot \nabla \times R^2 \left[-\rho \left(\boldsymbol{v}_{||} \cdot \nabla \boldsymbol{v}_E + \boldsymbol{v}_E \cdot \nabla \boldsymbol{v}_{||} \right) \right] =& \\
- \left[\rho, v_{||} \left(\nabla_{pol}\psi \cdot \nabla_{pol}u \right) \right] &+ \left[\rho v_{||}\omega_E, \psi \right] - \left[u, \rho v_{||}j \right] \\
- \left[u, \rho \left(\nabla_{pol}\psi \cdot \nabla_{pol}v_{||} \right) \right] &+ R\nabla \cdot \left(\rho \frac{F_0}{R^2} v_{||} \nabla_{pol} \left(\partial_\varphi u \right) \right).
\end{aligned}
\tag{B.50}
$$

The pressure term is the following:

$$
\begin{aligned}
\nabla\varphi \cdot \nabla \times \left[R^2(-\nabla P) \right] =& -\nabla\varphi \cdot (2R\nabla R \times \nabla P) - \nabla\varphi \cdot \cancel{(\nabla \times \nabla P)} \\
=& -2\frac{\partial P}{\partial Z}
\end{aligned}
\tag{B.51}
$$

The $\boldsymbol{J} \times \boldsymbol{B}$ term is derived as:

$$
\begin{aligned}
\nabla\varphi \cdot \nabla \times \left[R^2 \boldsymbol{J} \times \boldsymbol{B} \right] =& \nabla\varphi \cdot \left[(\boldsymbol{B} \cdot \nabla)\boldsymbol{J}R^2 - (\boldsymbol{J} \cdot \nabla)\boldsymbol{B}R^2 \right] \\
=& (\boldsymbol{B} \cdot \nabla) \underbrace{(\boldsymbol{J} \cdot \nabla\varphi)R^2}_{-\Delta^*\psi=-j} - (\boldsymbol{J} \cdot \nabla) \underbrace{(\boldsymbol{B} \cdot \nabla\varphi)R^2}_{F_0} \\
=& -\boldsymbol{B} \cdot \nabla j \\
=& -\frac{F_0}{R^2}\frac{\partial j}{\partial\varphi} + \frac{1}{R}[\psi, j]
\end{aligned}
\tag{B.52}
$$

The viscous term was first implemented using only the $\boldsymbol{E} \times \boldsymbol{B}$ vorticity. Yet the diamagnetic vorticity seems important to also consider, and there is as much a component due to the parallel velocity, which is non zero but is so far neglected. The $\boldsymbol{E} \times \boldsymbol{B}$ vorticity was calculated in the above paragraph. As for the diamagnetic vorticity, it is expressed as:

$$
\boldsymbol{w}_* = \nabla \times \boldsymbol{v}_* = \nabla \times \left(\tau_{IC}\frac{R}{\rho} \left\{ \begin{array}{c} -\frac{\partial p}{\partial Z} \\ \frac{\partial p}{\partial R} \\ 0 \end{array} \right. \right) = \tau_{IC} \left\{ \begin{array}{l} -\frac{1}{\rho}\frac{\partial}{\partial\varphi}\frac{\partial p}{\partial R} + \frac{1}{\rho^2}\frac{\partial\rho}{\partial\varphi}\frac{\partial p}{\partial R} \\ -\frac{1}{\rho}\frac{\partial}{\partial\varphi}\frac{\partial p}{\partial Z} + \frac{1}{\rho^2}\frac{\partial\rho}{\partial\varphi}\frac{\partial p}{\partial Z} \\ -\frac{R}{\rho^2}(\nabla_\perp p \cdot \nabla_\perp\rho) + \frac{R}{\rho}(\nabla \cdot \nabla_\perp p) \end{array} \right.
$$

The toroidal component of the diamagnetic vorticity is then:

$$
\boldsymbol{w}_* \cdot \nabla\varphi = -\frac{\tau_{IC}}{\rho^2}(\nabla_\perp p \cdot \nabla_\perp\rho) + \frac{\tau_{IC}}{\rho}(\nabla \cdot \nabla_\perp p) = \nabla \cdot \left(\frac{\tau_{IC}}{\rho}\nabla_\perp p \right).
\tag{B.53}
$$

As for the vorticity due to the parallel component of the velocity, we have:

$$
\begin{aligned}
\boldsymbol{w}_{||} =& \nabla \times (v_{||}\boldsymbol{B}) \\
=& v_{||}\nabla \times \boldsymbol{B} + \nabla v_{||} \times \boldsymbol{B} \\
=& v_{||}\boldsymbol{J} + F_0\nabla v_{||} \times \nabla\varphi + \nabla v_{||} \times \nabla\psi \times \nabla\varphi \\
=& v_{||}\boldsymbol{J} + F_0\nabla v_{||} \times \nabla\varphi - (\nabla v_{||} \cdot \nabla\psi)\nabla\varphi + (\nabla v_{||} \cdot \nabla\varphi)\nabla\psi.
\end{aligned}
\tag{B.54}
$$

Thus the toroidal component of this term is:

$$
\begin{aligned}
\boldsymbol{w}_{\parallel} \cdot \nabla \varphi =& v_{\parallel} \boldsymbol{J} \cdot \nabla \varphi - \frac{1}{R^2}(\nabla v_{\parallel} \cdot \nabla \psi) + \frac{1}{R^4}\frac{\partial v_{\parallel}}{\partial \varphi}\frac{\partial \psi}{\partial \varphi} \\
=& - v_{\parallel} \nabla \cdot \left(\frac{1}{R^2} \nabla_{\perp} \psi \right) - \frac{1}{R^2}(\nabla_{\perp} v_{\parallel} \cdot \nabla_{\perp} \psi).
\end{aligned}
\tag{B.55}
$$

Finally, the total toroidal component of the vorticity is expressed as follows:

$$
\boldsymbol{w} \cdot \nabla \varphi = \nabla \cdot \nabla_{\perp} u + \nabla \cdot \left(\frac{\tau_{IC}}{\rho} \nabla_{\perp} p \right) - v_{\parallel} \nabla \cdot \left(\frac{1}{R^2} \nabla_{\perp} \psi \right) - \frac{1}{R^2}(\nabla_{\perp} v_{\parallel} \cdot \nabla_{\perp} \psi).
\tag{B.56}
$$

The perpendicular viscous term is:

$$
\begin{aligned}
\nabla \varphi \cdot \nabla \times \left[R^2 \mu \Delta \boldsymbol{v} \right] =& \nabla \varphi \cdot \nabla \times \left[R^2 \mu \nabla(\nabla \cdot \boldsymbol{v}) - R^2 \mu \nabla \times (\nabla \times \boldsymbol{v}) \right] \\
=& \nabla \varphi \cdot \left[\cancel{R^2 \mu \nabla \times \nabla(\nabla \cdot \boldsymbol{v})} + \nabla(R^2 \mu) \times \nabla(\nabla \cdot \boldsymbol{v}) \right] - \nabla \varphi \cdot \nabla \times \left(R^2 \mu \nabla \times \boldsymbol{w} \right) \\
=& \nabla \varphi \cdot 2\mu R \nabla R \times \nabla(\nabla \cdot \boldsymbol{v}) - \nabla \varphi \cdot \left[\nabla(R^2 \mu) \times (\nabla \times \boldsymbol{w}) + R^2 \mu \underbrace{\nabla \times (\nabla \times \boldsymbol{w})}_{\cancel{\nabla(\nabla \cdot \boldsymbol{w})} - \nabla^2 \boldsymbol{w}} \right] \\
=& 2\mu \frac{\partial}{\partial Z}(\nabla \cdot \boldsymbol{v}) - \nabla \varphi \cdot \left[\nabla(R^2 \mu) \times (\nabla \times \boldsymbol{w}) \right] + R^2 \mu \nabla^2 \boldsymbol{w} \cdot \nabla \varphi
\end{aligned}
\tag{B.57}
$$

The term $-\nabla \varphi \cdot \left[\nabla(R^2 \mu) \times (\nabla \times \boldsymbol{w}) \right]$ is derived as follows:

$$
\begin{aligned}
-\nabla \varphi \cdot \left[\nabla(R^2 \mu) \times (\nabla \times \boldsymbol{w}) \right] =& - \nabla \varphi \cdot 2\mu R \nabla R \times (\nabla \times \boldsymbol{w}) \\
=& - 2\mu R(\nabla \times \boldsymbol{w}) \cdot \underbrace{\nabla \varphi \times \nabla R}_{\frac{1}{R}\nabla Z}
\end{aligned}
\tag{B.58}
$$

with $\nabla \times \boldsymbol{w} = \nabla \times (\nabla \times \boldsymbol{v}) = \nabla(\nabla \cdot \boldsymbol{v}) - \nabla^2 \boldsymbol{v}$. Thus:

$$
\begin{aligned}
-\nabla \varphi \cdot \left[\nabla(R^2 \mu) \times (\nabla \times \boldsymbol{w}) \right] =& - 2\mu \nabla(\nabla \cdot \boldsymbol{v}) \cdot \nabla Z + 2\mu \Delta \boldsymbol{v} \cdot \nabla Z \\
=& - 2\mu \frac{\partial}{\partial Z}(\nabla \cdot \boldsymbol{v}) + 2\mu \nabla^2 v_z
\end{aligned}
\tag{B.59}
$$

where the Z component of the velocity is:

$$
v_z = \boldsymbol{v} \cdot \nabla Z = R\frac{\partial u}{\partial R} + \frac{R}{\rho}\frac{\partial p}{\partial R} - \frac{v_{\parallel}}{R}\frac{\partial \psi}{\partial R}
\tag{B.60}
$$

We combine *Eqs.* B.56, B.57, B.59 and B.60 to obtain the following form of the

perpendicular viscous term:

$$
\begin{aligned}
\nabla\varphi \cdot \nabla \times \left[R^2 \mu \nabla^2 \boldsymbol{v} \right] =& 2\mu \Delta \boldsymbol{v}_z + R^2 \mu \nabla^2 \boldsymbol{w} \cdot \nabla\varphi \\
=& 2\mu \nabla^2 \left(R \frac{\partial u}{\partial R} + \frac{R}{\rho} \frac{\partial p}{\partial R} - \frac{v_\parallel}{R} \frac{\partial \psi}{\partial R} \right) + R\mu \nabla^2 \left[R \nabla \cdot \nabla_\perp u \right. \\
& \left. + R \nabla \cdot \left(\frac{\tau_{IC}}{\rho} \nabla_\perp p \right) - R v_\parallel \nabla \cdot \left(\frac{1}{R^2} \nabla_\perp \psi \right) - \frac{1}{R} (\nabla_\perp v_\parallel \cdot \nabla_\perp \psi) \right]
\end{aligned}
$$

$$\tag{B.61}$$

In the code, the term $2\mu \Delta \boldsymbol{v}_z$ is neglected, as well as the vorticity issued from the parallel component of the velocity, so the implemented term is:

$$
\nabla\varphi \cdot \nabla \times \left[R^2 \mu \Delta \boldsymbol{v} \right] = + R\mu \nabla^2 \left(R \nabla \cdot \nabla_\perp u + R \nabla \cdot \left(\frac{\tau_{IC}}{\rho} \nabla_\perp p \right) \right)
\tag{B.62}
$$

As for the neoclassical component, its derivation is:

$$
\begin{aligned}
\nabla\varphi \cdot \nabla \times \left[-R^2 \nabla \cdot \overline{\overline{\Pi}}_{i,neo} \right] =& \nabla\varphi \cdot \nabla \times \left[-R^2 \mu_{i,neo} \rho \frac{B^2}{B_\theta^4} \left(-v_\parallel B_\theta^2 + \nabla_\perp \psi \cdot \nabla_\perp u \right.\right. \\
& \left.\left. + \frac{\tau_{IC}}{\rho} \left(\nabla_\perp \psi \cdot \nabla_\perp P + k_i \rho \nabla_\perp \psi \cdot \nabla_\perp T \right) \right) (\nabla\psi \times \nabla\varphi) \right] \\
=& + \nabla \cdot \nabla\varphi \times \left[R^2 \mu_{i,neo} \rho \frac{B^2}{B_\theta^4} \left(-v_\parallel B_\theta^2 + \nabla_\perp \psi \cdot \nabla_\perp u \right.\right. \\
& \left.\left. + \frac{\tau_{IC}}{\rho} \left(\nabla_\perp \psi \cdot \nabla_\perp P + k_i \rho \nabla_\perp \psi \cdot \nabla_\perp T \right) \right) (\nabla\psi \times \nabla\varphi) \right] \\
=& + \nabla \cdot \left[\mu_{i,neo} \rho \frac{B^2}{B_\theta^4} \left(-v_\parallel B_\theta^2 + \nabla_\perp \psi \cdot \nabla_\perp u \right.\right. \\
& \left.\left. + \frac{\tau_{IC}}{\rho} \left(\nabla_\perp \psi \cdot \nabla_\perp P + k_i \rho \nabla_\perp \psi \cdot \nabla_\perp T \right) \right) \nabla_\perp \psi \right]
\end{aligned}
$$

$$\tag{B.63}$$

Where we have used the identity:

$$
\nabla\varphi \cdot (\nabla\psi \times \nabla\varphi) = |\nabla\varphi|^2 \nabla\psi - (\nabla\varphi \cdot \nabla\psi) = \frac{1}{R^2} \nabla_\perp \psi
\tag{B.64}
$$

The calculation of the divergence of this term is quite complicated, but the weak form

used in JOREK is much simpler:

$$\int_V \nabla\varphi \cdot \nabla \times \left[-R^2 \nabla \cdot \overline{\overline{\Pi}}_{i,neo}\right] dV = -\int_V (\nabla u^* \cdot \nabla_\perp \psi) \left[\mu_{i,neo}\rho\frac{B^2}{B_\theta^4}\left(-v_{||}B_\theta^2 + \nabla_\perp\psi\cdot\nabla_\perp u\right.\right.$$

$$\left.\left. + \frac{\tau_{IC}}{\rho}\left(\nabla_\perp\psi\cdot\nabla_\perp P + k_i\rho\nabla_\perp\psi\cdot\nabla_\perp T\right)\right)\right] dV$$

The full perpendicular momentum equation is the following:

$$\begin{aligned}
\nabla\cdot\left(R^2\rho\nabla_\perp\frac{\partial u}{\partial t}\right) = & \frac{1}{2R}\left[R^4|\nabla_\perp u|^2, \hat{\rho}\right] + \frac{1}{R}\left[\hat{\rho}w_E R^2, u\right]\\
& -2\frac{\partial P}{\partial Z} - \frac{F_0}{R^2}\frac{\partial j}{\partial\varphi} + \frac{1}{R}\left[\psi, j\right]\\
& +R\mu\nabla^2\left(R\nabla\cdot\nabla_\perp u + R\nabla\cdot\left(\frac{\tau_{IC}}{\rho}\nabla_\perp p\right)\right)\\
& +\tau_{IC}\left\{R^3\left[W, P\right] + R^2\nabla\cdot(\partial_Z P\nabla_\perp u)\right.\\
& -R^3\left[\partial_{RZ}u\left(\partial_{RR}P - \partial_{ZZ}P\right) - \partial_{RZ}P\left(\partial_{RR}u - \partial_{ZZ}u\right)\right]\\
& +3R^3\left[\left(\frac{1}{R}\partial_R u\right), P\right]\right\}\\
& +\nabla\cdot\left[\mu_{i,neo}\rho\frac{B^2}{B_\theta^4}\left(-v_{||}B_\theta^2 + \nabla_\perp\psi\cdot\nabla_\perp u\right.\right.\\
& \left.\left. +\frac{\tau_{IC}}{\rho}\left(\nabla_\perp\psi\cdot\nabla_\perp P + k_i\rho\nabla_\perp\psi\cdot\nabla_\perp T\right)\right)\nabla_\perp\psi\right]
\end{aligned} \tag{B.65}$$

Note that we have neglected the following terms: the term due to the time derivative of the parallel velocity, the cross terms $\left\{\left(v_{||}\boldsymbol{B}\cdot\nabla\right)\boldsymbol{v}_E\right\}$, $\left\{\left(\boldsymbol{v}_E\cdot\nabla\right)v_{||}\boldsymbol{B}\right\}$ and the $\frac{\partial}{\partial Z}(\nabla\cdot\boldsymbol{v})$ term. Also the vorticity issued from the parallel component of the velocity in the viscous term. We have also considered the visous coefficient μ as a constant whereas it is a temperature-dependent factor whose gradient might not be negligible.

B.3.4   Derivation of the parallel momentum equation

The parallel momentum equation does not contain new diamagnetic terms as the term in *Eq.* (B.34) is normally perpendicular to the magnetic field, so the projection along $\boldsymbol{B}$ is exactly zero. However we make the approximation that the perpendicular velocity is

poloidal:

$$
\begin{aligned}
\boldsymbol{v}_E =& \frac{\boldsymbol{E} \times \boldsymbol{B}}{B^2} = \frac{-F_0 \nabla u \times (F_0 \nabla \varphi + \nabla \psi \times \nabla \varphi)}{\frac{F_0^2}{R^2} + \frac{|\nabla \psi|^2}{R^2}} \\
\boldsymbol{v}_E =& \frac{-R^2 \nabla u \times \nabla \varphi}{1 + \frac{|\nabla \psi|^2}{F_0^2}} - \frac{RF_0}{F_0^2 + |\nabla \psi|^2} [u, \psi] \\
\boldsymbol{v}_E =& - R^2 \nabla u \times \nabla \varphi - \frac{R}{F_0} [u, \psi] + O\left(\frac{|\nabla \psi|^2}{F_0^2} \right) \\
\boldsymbol{v}_E =& - R^2 \nabla u \times \nabla \varphi + O\left(\frac{|\nabla \psi|}{F_0} \right) \\
\boldsymbol{v}_E \sim& - R^2 \nabla u \times \nabla \varphi = \boldsymbol{v}_{E,\ poloidal}
\end{aligned}
\tag{B.66}
$$

On the same way, the diamagnetic velocity at the following order is:

$$
\boldsymbol{v}_* = - R^2 \frac{\tau_{IC}}{\rho} \nabla p \times \nabla \varphi - \frac{R \tau_{IC}}{\rho F_0} [p, \psi] + O\left(\frac{|\nabla \psi|^2}{F_0^2} \right)
\tag{B.67}
$$

This approximation makes that finally the projection of the term $(\boldsymbol{v} \cdot \nabla) \boldsymbol{v}_E$ along $\boldsymbol{B}$ is actually not zero, but is neglected because it is small and unphysical. As well, the perpendicular component of the term $(\boldsymbol{v} \cdot \nabla) \boldsymbol{v}_{||}$ is not exactly zero and is also neglected.

The projection of the momentum equation *Eq.* (B.28) on $\boldsymbol{B}$ gives the parallel velocity equation:

$$
\rho \frac{\partial (v_{||} \boldsymbol{B})}{\partial t} \cdot \boldsymbol{B} + \rho \left((\boldsymbol{v}_E + v_{||} \boldsymbol{B}) \cdot \nabla \right) v_{||} \boldsymbol{B} \cdot \boldsymbol{B} = -\nabla P \cdot \boldsymbol{B} - \nabla \cdot \overline{\overline{\boldsymbol{\Pi}}}_{neo} \cdot \boldsymbol{B} + \boldsymbol{S}_v \cdot \boldsymbol{B} - \boldsymbol{v} \cdot \boldsymbol{B} S_\rho + \mu \Delta \boldsymbol{v} \cdot \boldsymbol{B}
\tag{B.68}
$$

The time derivative term is:

$$
\begin{aligned}
\rho \frac{\partial (v_{||} \boldsymbol{B})}{\partial t} \cdot \boldsymbol{B} =& \rho B^2 \frac{\partial (v_{||})}{\partial t} + \rho v_{||} \frac{\partial \boldsymbol{B}}{\partial t} \cdot \boldsymbol{B} \\
=& \rho B^2 \frac{\partial (v_{||})}{\partial t} + \rho v_{||} \frac{\partial (B^2/2)}{\partial t} \\
=& \rho B^2 \frac{\partial (v_{||})}{\partial t} + \frac{\rho v_{||}}{2R^2} \frac{\partial ((\nabla_\perp \psi)^2)}{\partial t} \\
=& \rho B^2 \frac{\partial (v_{||})}{\partial t} + \frac{\rho v_{||}}{R^2} \nabla_\perp \psi \cdot \nabla_\perp \frac{\partial \psi}{\partial t}
\end{aligned}
\tag{B.69}
$$

The second term is neglected as compared to the first one, since B^2 varies in a larger timescale as compared to the velocity.

The advection by the parallel velocity is:

$$
- \left(\rho \left(v_\| \boldsymbol{B} \cdot \nabla \right) v_\| \boldsymbol{B} \right) \cdot \boldsymbol{B} = - \rho \nabla \left(\frac{v_\|^2 \boldsymbol{B}^2}{2} \right) \cdot \boldsymbol{B} - \underbrace{\left(\nabla \times (v_\| \boldsymbol{B}) \right) \times v_\| \boldsymbol{B}}_{\perp \boldsymbol{B}} \cdot \boldsymbol{B}
$$

$$
= - \frac{\rho}{2} \left(F_0 \nabla \varphi \cdot \nabla (v_\|^2 B^2) + \nabla \psi \times \nabla \varphi \cdot \nabla (v_\|^2 B^2) \right) \quad \text{(B.70)}
$$

$$
= - \rho \frac{F_0}{2R^2} \frac{\partial (v_\|^2 B^2)}{\partial \varphi} - \frac{\rho}{2R} \left[v_\|^2 B^2, \psi \right]
$$

However the implementation in the code is simpler with the weak form. Writing the test function v^*, the weak form of this term is the following:

$$
\int_V - v^* \rho \nabla \left(\frac{v_\|^2 B^2}{2} \right) \cdot \boldsymbol{B} \, dV = \underbrace{\int_V - \nabla \left(v^* \rho \frac{v_\|^2 B^2}{2} \right) \cdot \boldsymbol{B} \, dV}_{\int_S \left(v^* \rho \frac{v_\|^2 B^2}{2} \right) \cdot d\boldsymbol{S} \cdot \boldsymbol{B} = 0} + \int_V - \nabla \left(v^* \rho \right) \cdot \boldsymbol{B} \frac{v_\|^2 B^2}{2} \, dV
$$

$$
= \int_V \left(\frac{F_0}{R^2} \frac{\partial \rho}{\partial \varphi} + \frac{1}{R} [\rho, \psi] + \frac{F_0}{R^2} \frac{\partial v^*}{\partial \varphi} + \frac{1}{R} [v^*, \psi] \right) \frac{v_\|^2 B^2}{2} \, dV
$$

$$
\text{(B.71)}
$$

The advection by the $\boldsymbol{E} \times \boldsymbol{B}$ velocity (so far neglected in the code) is expressed as:

$$
- \left(\rho \left(\boldsymbol{v}_E \cdot \nabla \right) v_\| \boldsymbol{B} \right) \cdot \boldsymbol{B} = - \rho \boldsymbol{v}_E \cdot \nabla (v_\| \boldsymbol{B}^2) + \rho \boldsymbol{v}_E \cdot (v_\| \underbrace{\boldsymbol{B} \nabla B}_{\nabla (B^2/2)})
$$

$$
= \rho R^2 \nabla u \times \nabla \varphi \cdot \nabla (v_\| \boldsymbol{B}^2) - \rho R^2 v_\| \nabla u \times \nabla \varphi \cdot \nabla \left(\frac{\boldsymbol{B}^2}{2} \right)
$$

$$
= \rho R [v_\| B^2, u] - \rho R v_\| \left[\frac{B^2}{2}, u \right] \quad \text{(B.72)}
$$

$$
= \rho R \left(v_\| [B^2, u] + B^2 [v_\|, u] \right) - \rho R v_\| \left[\frac{B^2}{2}, u \right]
$$

$$
= \rho R B^2 [v_\|, u] + \rho R v_\| \left[\frac{B^2}{2}, u \right]
$$

The pressure term projected on $\boldsymbol{B}$ is:

$$
- \boldsymbol{B} \cdot \nabla P = - \nabla P (F_0 \nabla \varphi + \nabla \psi \times \nabla \varphi)
$$

$$
= - \frac{F_0}{R^2} \frac{\partial p}{\partial \varphi} + \frac{1}{R} [\psi, P] \quad \text{(B.73)}
$$

The viscous term and the source terms are defined so that viscosity imposes the velocity to mimics the imposed rotation profile (corresponding to the experimental profile),

so both terms give:

$$\mu_{||}\Delta v_{||}B^2 + \boldsymbol{S}_v \cdot \boldsymbol{B} = \mu_{||}\Delta(v_{||} - v_{||,source})B^2 \tag{B.74}$$

The parallel projection of the divergence of the neoclassical tensor is given by:

$$
\begin{aligned}
-\boldsymbol{B} \cdot \left[\nabla \cdot \overline{\overline{\Pi}}_{i,neo} \right] = &- \boldsymbol{B} \cdot \left[\mu_{i,neo}\rho\frac{B^2}{B_\theta^4}\left(-v_{||}B_\theta^2 + \nabla_\perp\psi \cdot \nabla_\perp u \right. \right. \\
&\left. + \frac{\tau_{IC}}{\rho}\left(\nabla_\perp\psi \cdot \nabla_\perp P + k_i\rho\nabla_\perp\psi \cdot \nabla_\perp T \right) \right) (\nabla\psi \times \nabla\varphi) \Big] \\
= &-\mu_{i,neo}\rho\frac{B^2}{B_\theta^2}\left[-v_{||}B_\theta^2 + \nabla_\perp\psi \cdot \nabla_\perp u \right. \\
&\left. + \frac{\tau_{IC}}{\rho}\left(\nabla_\perp\psi \cdot \nabla_\perp P + k_i\rho\nabla_\perp\psi \cdot \nabla_\perp T \right) \right]
\end{aligned}
\tag{B.75}
$$

since $\boldsymbol{B} \cdot (\nabla\psi \times \nabla\varphi) = (\nabla\psi \times \nabla\varphi)^2 = \frac{|\nabla\psi|^2}{R^2} = B_\theta^2$

Finally, the total parallel velocity equation is:

$$
\begin{aligned}
\rho B^2\frac{\partial(v_{||})}{\partial t} + \frac{\rho v_{||}}{R^2}\nabla_\perp\psi \cdot \nabla_\perp\frac{\partial\psi}{\partial t} = &- \rho\frac{F_0}{2R^2}\frac{\partial(v_{||}^2 B^2)}{\partial\varphi} - \frac{\rho}{2R}\left[v_{||}^2 B^2, \psi \right] \\
&+ \rho R B^2[v_{||}, u] + \rho R v_{||}\left[\frac{B^2}{2}, u \right] - \frac{F_0}{R^2}\frac{\partial p}{\partial\varphi} + \frac{1}{R}[\psi, P] \\
&- \mu_{i,neo}\rho\frac{B^2}{B_\theta^2}\left(-v_{||}B_\theta^2 + \nabla_\perp\psi \cdot \nabla_\perp u \right. \\
&\left. + \frac{\tau_{IC}}{\rho}\left(\nabla_\perp\psi \cdot \nabla_\perp P + k_i\rho\nabla_\perp\psi \cdot \nabla_\perp T \right) \right) \\
&+ \mu_{||}\Delta(v_{||} - v_{||,source})B^2
\end{aligned}
\tag{B.76}
$$

The current equation implemented, neglecting the lowest order terms, is the following:

$$
\begin{aligned}
\rho B^2\frac{\partial(v_{||})}{\partial t} = &- \rho\frac{F_0}{2R^2}\frac{\partial(v_{||}^2 B^2)}{\partial\varphi} - \frac{\rho}{2R}\left[v_{||}^2 B^2, \psi \right] - \frac{F_0}{R^2}\frac{\partial p}{\partial\varphi} + \frac{1}{R}[\psi, P] \\
&- \mu_{i,neo}\rho\frac{B^2}{B_\theta^2}\left(-v_{||}B_\theta^2 + \nabla_\perp\psi \cdot \nabla_\perp u + \frac{\tau_{IC}}{\rho}\left(\nabla_\perp\psi \cdot \nabla_\perp P + k_i\rho\nabla_\perp\psi \cdot \nabla_\perp T \right) \right) \\
&+ \mu_{||}\Delta(v_{||} - v_{||,source})B^2
\end{aligned}
\tag{B.77}
$$

B.4 Energy equation

The energy equation from the moment of the Boltzmann equation at the second order, as in Ref. [Braginskii 1965]. This equation for a given species s is the following (using the Einstein notation)

$$\frac{\partial f_s}{\partial t} + \frac{\partial}{\partial x_\beta}\left(V_{s\beta}f_s\right) + \frac{\partial}{\partial V_{s\beta}}\left(\frac{F_{s\beta}}{m_s}f_s\right) = C, \tag{B.78}$$

with

$$F_s = e_s\boldsymbol{E} + e_s\left(\boldsymbol{V}\times\boldsymbol{B}\right),$$

f_s the distributtion function, $\boldsymbol{V}_s$ the total velocity for a given species and C is the collisions term. The quantity C is the change per unit time in the distribution function for particles of one species due to collisions with other particle species. To obtain the energy equation we follow the method given in [Braginskii 1965]. *Eq.* (B.78) is multiplied by $mV^2/2$ and it is integrated over the velocity. We find the following form for a species (hereinafter we ommit the subscript s for simplicity except in the charge e)

$$\frac{\partial}{\partial t}\left(\frac{mn}{2}\langle V^2\rangle\right) + \nabla\cdot\left(\frac{mn}{2}\langle V^2\boldsymbol{V}\rangle\right) - e_s n\,\boldsymbol{E}\cdot\boldsymbol{V} = \int\frac{mV^2}{2}Cd\boldsymbol{V} \tag{B.79}$$

with $V^2 = \|\boldsymbol{V}\|^2$ the squared norm of the velocity, m the mass (kg) and n the particle density (m^{-3}) for the consider species. To simplify and calculate the average in *Eq.* (B.79) we consider the total velocity divided between a mean and a fluctuating part, $\boldsymbol{V} = \boldsymbol{v} + \boldsymbol{v}'$. It is important to note that $\langle\boldsymbol{v}'\rangle = 0$. We recall that we note vectors with bold type (e.g. $\boldsymbol{v}$) or with a subscript (e.g. v_β) in this section. To simplify the previous equation we develop the averaged terms

$$\langle V^2\rangle = \langle v^2\rangle + 2\langle v\cdot v'\rangle + \langle v'^2\rangle$$
$$\frac{1}{2}\langle V^2 V_\beta\rangle = \frac{1}{2}v^2 v_\beta + \frac{1}{2}v_\beta\langle v'^2\rangle + v\langle v'_\alpha v'_\beta\rangle + \frac{1}{2}\langle v'_\beta v'^2\rangle \tag{B.80}$$

Now we introduce the isotropic pressure (P), the stress tensor ($\Pi_{\alpha\beta}$) and the mean change in the momentum by collisions between one species of particles with the other species ($\boldsymbol{R}$). These three quantities write

$$P = nT = \frac{nm}{3}\langle v'^2\rangle$$

$$\Pi_{\alpha\beta} = nm\left\langle v'_\alpha v'_\beta - \frac{v'^2}{3}\delta_{\alpha\beta}\right\rangle \tag{B.81}$$

$$\boldsymbol{R} = \int m\boldsymbol{v}'Cd\boldsymbol{v}$$

This three expressions are introduced in *Eq.* (B.79). We find the energy equation for a species

$$\frac{\partial}{\partial t}\left(\frac{nm}{2}v^2 + \frac{3}{2}P\right) + \frac{\partial}{\partial x_\beta}\left\{\left(\frac{nm}{2}v^2 + \frac{5}{2}P\right)v_\beta + \Pi_{\alpha\beta}\cdot v_\alpha + q_\beta\right\} = e_s n\,\boldsymbol{E}\cdot\boldsymbol{v} + \boldsymbol{R}\cdot\boldsymbol{v} + Q$$

(B.82)

with the notations

$$q_\beta = \frac{nm}{2}\langle v'_\beta v'^2\rangle$$

$$Q = \int \frac{mv'^2}{2}C d\boldsymbol{v}$$

The vector $\boldsymbol{q}$ is the flux density of heat carried by particles of a given species and represents the transport of the energy associated with the random motion in the coordinate system in which the particle gas as a whole is at rest at a given point in space. The quantity Q is the heat generated by collisions. This term compensate with the $(\boldsymbol{R}\cdot\boldsymbol{v})$ term that expresses the change of momentum due to collisions. The kinectic energy lost in a collision is converted into heat. Thus the two last terms on the right hand side of *Eq.* (B.82) compensate one another. We can write

$$\frac{\partial}{\partial t}\left(\frac{nm}{2}v^2 + \frac{3}{2}P\right) + \frac{\partial}{\partial x_\beta}\left\{\left(\frac{nm}{2}v^2 + \frac{5}{2}P\right)v_\beta + \Pi_{\alpha\beta}\cdot v_\alpha + q_\beta\right\} = e_s n\,\boldsymbol{E}\cdot\boldsymbol{v} \quad \text{(B.83)}$$

B.4.1 Total energy equation

We now combine the energy equation for the ions and electrons. Neglecting the electron mass, the electron stress tensor, considering $n = n_i = n_e$ and taking into account that $e = e_i = -e_e$, we find the following energy equation expression

$$\frac{\partial}{\partial t}\left(\frac{nm_i}{2}v_i^2 + \frac{3}{2}(P_i + P_e)\right) + \frac{\partial}{\partial x_\beta}\left\{\left(\frac{nm_i}{2}v_i^2 + \frac{5}{2}P_i\right)v_{i\beta} + \frac{5}{2}P_e v_{e\beta} + \Pi_{i\alpha\beta}\cdot v_{i\alpha} + q_{i\beta} + q_{e\beta}\right\}$$
$$= en\,\boldsymbol{E}\cdot\boldsymbol{v}_i - en\,\boldsymbol{E}\cdot\boldsymbol{v}_e \quad \text{(B.84)}$$

The energy equation can be written as a function of a single fluid pressure or temperature equation. The pressure is here defined as

$$P = \rho T \quad \text{with} \quad P = P_e + P_i \quad \text{and} \quad T = T_e = T_i. \quad \text{(B.85)}$$

Also we introduce the current density vector

$$\boldsymbol{j} = en(\boldsymbol{v}_i - \boldsymbol{v}_e) \quad \text{(B.86)}$$

Taking into account the total pressure P and the current density $\boldsymbol{j}$, *Eq.* (B.84) takes the

form

$$\frac{\partial}{\partial t}\left(\frac{nm_i}{2}v_i^2 + \frac{3}{2}P\right) + \frac{\partial}{\partial x_\beta}\left\{\left(\frac{nm_i}{2}v_i^2 + \frac{5}{2}P\right)v_{i\beta} - \frac{5}{2}\frac{P_e j_\beta}{en} + \Pi_{i\alpha\beta}\cdot v_{i\alpha} + q_{i\beta} + q_{e\beta}\right\} = \boldsymbol{E}\cdot\boldsymbol{j}$$
(B.87)

Taking into account Poynting theorem the single terme on the right hand side of *Eq.* (B.87) can be written

$$\boldsymbol{E}\cdot\boldsymbol{j} = -\frac{\partial}{\partial t}\left(\frac{B^2}{2\mu_0}\right) - \nabla\cdot\left(\frac{\boldsymbol{E}\times\boldsymbol{B}}{\mu_0}\right)$$
(B.88)

We consider the total heat flux

$$q_\beta = q_{i\beta} + q_{e\beta}$$
(B.89)

Therefore the total energy time evolution derived from *Eq.* (B.87) has the form (here we consider $\boldsymbol{v}\approx\boldsymbol{v}_i$ and $\rho = nm_i$)

$$\frac{\partial}{\partial t}E_{Total} + \frac{\partial}{\partial x_\beta}\left(q_{\beta\,Total}\right) = 0,$$
(B.90)

with

$$E_{Total} = \left\{\frac{\rho}{2}v^2 + \frac{3}{2}P + \frac{B^2}{2\mu_0}\right\},$$

$$q_{\beta\,Total} = \left\{\frac{\rho}{2}v^2 v_\beta + \frac{5}{2}Pv_\beta - \frac{5}{2}\frac{P_e j_\beta}{en} + \Pi_{i\alpha\beta}\cdot v_\alpha + q_\beta + \frac{\boldsymbol{E}\times\boldsymbol{B}}{\mu_0}\right\}.$$

B.4.2 Energy equation as a function of the total isotropic pressure P and temperature T

To write the energy equation as a function of the isotropic pressure we can take the energy equation for a single species (*Eq.* (B.82)) and replace the velocity terms using the momentum and the continuity equations. In fact the first and third term in the left hand side of *Eq.* (B.82) can be expressed (considering $\boldsymbol{v}\approx\boldsymbol{v}_i$ and $\rho = nm_i$)

$$\frac{\partial}{\partial t}\left(\frac{\rho}{2}v^2\right) + \frac{\partial}{\partial x_\beta}\left(\frac{\rho}{2}v^2 v_\beta\right) = \boldsymbol{v}\cdot\left\{\frac{\partial}{\partial t}\left(\rho\boldsymbol{v}\right) + \frac{\partial}{\partial x_\beta}\left(\rho\boldsymbol{v}v_\beta\right)\right\}.$$
(B.91)

And using the continuity equation

$$\frac{\partial\rho}{\partial t} + \nabla\cdot(\rho\boldsymbol{v}) = 0,$$
(B.92)

we can write

$$\boldsymbol{v}\cdot\left\{\frac{\partial}{\partial t}\left(\rho\boldsymbol{v}\right) + \frac{\partial}{\partial x_\beta}\left(\rho\boldsymbol{v}v_\beta\right)\right\} = \boldsymbol{v}\cdot\left\{\rho\left(\frac{\partial\boldsymbol{v}}{\partial t} + (\boldsymbol{v}\cdot\nabla)\boldsymbol{v}\right)\right\}.$$
(B.93)

Thus the first and the third term in *Eq.* (B.82) can be replaced by the right hand side of *Eq.* (B.93). And this last term can be expressed using the momentum equation for a single species (we recall that the subscript s indicating the species is not used except for the electric charge e). This momentum equation for a species s writes

$$\rho \left(\frac{\partial \boldsymbol{v}}{\partial t} + (\boldsymbol{v} \cdot \nabla) \boldsymbol{v} \right) = -\nabla P - \nabla \cdot \overline{\overline{\boldsymbol{\Pi}}} + e_s n \left(\boldsymbol{E} + \boldsymbol{v} \times \boldsymbol{B} \right) + \boldsymbol{R}. \tag{B.94}$$

Then the scalar product in the right hand side of *Eq.* (B.93) can be written, using the Einstein notation

$$v_\alpha \cdot \rho \left(\frac{\partial v_\alpha}{\partial t} + v_\beta \frac{\partial v_\alpha}{\partial x_\beta} \right) = -v_\alpha \cdot \frac{\partial P}{\partial x_\alpha} - v_\alpha \cdot \frac{\Pi_{\alpha\beta}}{\partial x_\beta} + v_\alpha \cdot e_s n E_\alpha + \underline{v_\alpha \cdot (\boldsymbol{v} \times \boldsymbol{B})_\alpha} + v_\alpha \cdot R_\alpha. \tag{B.95}$$

Replacing in *Eq.* (B.82) we obtain

$$\frac{3}{2}\frac{\partial P}{\partial t} + \frac{5}{2} v_\beta \frac{\partial P}{\partial x_\beta} + \frac{5}{2} P \frac{\partial v_\beta}{\partial x_\beta} + v_\alpha \cdot \frac{\partial \Pi_{\alpha\beta}}{\partial x_\beta} + \Pi_{\alpha\beta} \cdot \frac{\partial v_\alpha}{\partial x_\beta} + \frac{\partial q_\beta}{\partial x_\beta}$$

$$- v_\alpha \cdot \frac{\partial P}{\partial x_\alpha} - v_\alpha \cdot \frac{\Pi_{\alpha\beta}}{\partial x_\beta} + v_\alpha \cdot e_s n E_\alpha + v_\alpha \cdot R_\alpha = e_s n E_\alpha \cdot v_\alpha + R_\alpha \cdot v_\alpha + Q. \tag{B.96}$$

Then the energy equation for a single species simplifies to

$$\frac{3}{2}\frac{\partial P}{\partial t} + \frac{3}{2} v_\beta \frac{\partial P}{\partial x_\beta} + \frac{5}{2} P \frac{\partial v_\beta}{\partial x_\beta} + \Pi_{\alpha\beta} \cdot \frac{\partial v_\alpha}{\partial x_\beta} + \frac{\partial q_\beta}{\partial x_\beta} = Q. \tag{B.97}$$

Considering ions and electrons, we add the two energy equations for this two kind of particles to find the total energy equation as a function of the total isotropic pressure. We neglect the electron stress tensor and we write the electron velocity as a function of the current density. The sum of the ions and electrons energy equations yields

$$\frac{3}{2}\frac{\partial P}{\partial t} + \frac{3}{2} v_{i\beta} \frac{\partial P}{\partial x_\beta} - \frac{3}{2}\frac{j_\beta}{en}\frac{\partial P_e}{\partial x_\beta} + \frac{5}{2} P \frac{\partial v_{i\beta}}{\partial x_\beta} - \frac{5}{2}\frac{P_e}{en}\frac{\partial j_\beta}{\partial x_\beta} + \Pi_{i\alpha\beta}\frac{\partial v_{i\alpha}}{\partial x_\beta} + \frac{\partial}{\partial x_\beta}\left(q_{i\beta} + q_{e\beta} \right) = Q_i + Q_e. \tag{B.98}$$

Here we have considered that the charge conservation law is stationary thus the current density $\boldsymbol{j}$ is divergence free.

Finally we can write *Eq.* (B.98) taking into acccount that $\boldsymbol{v} \approx \boldsymbol{v}_i$ as

$$\frac{3}{2}\frac{\partial P}{\partial t} + \frac{3}{2}\boldsymbol{v} \cdot \nabla P + \frac{5}{2} P \left(\nabla \cdot \boldsymbol{v} \right) = -\nabla \cdot \boldsymbol{q} + \frac{3}{2}\frac{\boldsymbol{j} \cdot \nabla P_e}{en} + \sum Q. \tag{B.99}$$

The right hand side of this equation contains all heat sources, including the heating due to the viscosity, $\sum Q = Q_{Heating} + Q_{Viscosity}$.

We note that the left hand side of *Eq.* (B.99) can be written in the following form if

the continuity equation (*Eq.* (B.92)) is used

$$\frac{3}{2}\frac{\partial P}{\partial t} + \frac{3}{2}\boldsymbol{v}\cdot\nabla P + \frac{5}{2}P\left(\nabla\cdot v\right) = \frac{3}{2}\frac{dP}{dt} - \frac{5}{2}\frac{P}{\rho}\frac{d\rho}{dt}$$
$$= \frac{3}{2}P\frac{d}{dt}\left\{\ln\left(\frac{P}{\rho^{\gamma}}\right)\right\}$$

(B.100)

with the material derivative $d/dt = \partial/\partial t + \boldsymbol{v}\cdot\nabla$ and where $\gamma = 5/3$ is the adiabaticity index for a monoatomic gas.

If the characteristic time of the dissipative processes (electric resistance, thermal conductivity, viscosity, etc.) is large compared with the reciprocal frequency of the plasma motion (e.g. L/v) the dissipative terms are small. Under these conditions we can assume that the process is adiabatic and write as a first approximation

$$\frac{d}{dt}\left(\frac{P}{\rho^{\gamma}}\right) = 0.$$

(B.101)

From *Eq.* (B.99) we can write the energy equation introduced in JOREK

$$\frac{\partial P}{\partial t} = -\boldsymbol{v}\cdot\nabla P - \gamma P\left(\nabla\cdot\boldsymbol{v}\right) - \nabla\cdot\boldsymbol{q} + \frac{\boldsymbol{j}\cdot\nabla P_e}{en} + Q.$$

(B.102)

Taking into account only the total pressure P, considering the heat flux proportional to the temperature gradient and replacing the velocity by the $\boldsymbol{E}\times\boldsymbol{B}$, parallel and diamagnetic velocity we can write

$$\frac{\partial P}{\partial t} = R\left[P, u\right] - v_{||}\left(\frac{1}{R}\left[P,\psi\right] + \frac{F_0}{R^2}\partial_\varphi P\right)$$
$$+ 2\gamma P\partial_Z u + \gamma\tau_{IC}\frac{P}{\rho}\left(2\partial_Z P + \frac{R}{\rho}\left[P,\rho\right]\right) - \gamma P\left(\frac{1}{R}\left[v_{||},\psi\right] + \frac{F_0}{R^2}\partial_\varphi v_{||}\right) \quad \text{(B.103)}$$
$$- \nabla\cdot\left(\kappa_\perp\nabla_\perp T + \kappa_{||}\nabla_{||}T\right) + \frac{1}{2}\frac{\boldsymbol{j}\cdot\nabla P}{en} + S_P.$$

Writting *Eq.* (B.102) equation as a function of the total temperature (we recall here that $P = \rho T$) and taking into account the continuity equation (*Eq.* (B.92)) we have

$$\frac{\partial T}{\partial t} = -\boldsymbol{v}\cdot\nabla T + T\left(1 - \gamma\right)\left(\nabla\cdot\boldsymbol{v}\right) - \frac{1}{\rho}\nabla\cdot\boldsymbol{q} + \frac{3}{4}\frac{m_i}{e}\frac{\boldsymbol{j}\cdot\nabla P}{\rho^2} + Q.$$

(B.104)

Also taking into account the total pressure P and replacing in this last equation the velocity by the $\boldsymbol{E}\times\boldsymbol{B}$, parallel and diamagnetic velocity we find

$$\begin{aligned}
\frac{\partial T}{\partial t} &= R\left[T,u\right] - v_{\parallel}\left(\frac{1}{R}\left[T,\psi\right] + \frac{F_0}{R^2}\partial_\varphi T\right) \\
&\quad + T\left(1-\gamma\right)\left\{\frac{1}{R}\left[v_{\parallel},\psi\right] + \frac{F_0}{R^2}\partial_\varphi v_{\parallel} - 2\partial_Z u - 2\frac{\tau_{IC}}{\rho}\partial_Z\left(\rho T\right)\right\} \\
&\quad + \gamma\,\tau_{IC}\frac{T}{\rho}R\left[T,\rho\right] \\
&\quad - \nabla\cdot\left(\kappa_\perp\nabla_\perp T + \kappa_{\parallel}\nabla_{\parallel}T\right) + \frac{3}{4}\frac{m_i\,\boldsymbol{j}\cdot\nabla\left(\rho T\right)}{e\rho^2} + S_T.
\end{aligned} \tag{B.105}$$

Summary of Fitzpatrick's theory: from induction motor paradigm to rotating plasma states in presence of a static error-field

Contents

This appendix summarizes the original theory of the screening of error fields by rotating plasmas, proposed in [Fitzpatrick 1998]. In section C.1, the induction motor paradigm is first presented. The analogy between this induction motor and a rotating tokamak plasma with error field (or RMPs) will then be made in section C.2.

C.1 The induction motor paradigm

C.1.1 Assumptions

We consider an induction motor, sketched in Fig. C.1 composed of:
- a non-conducting stationary core
- a thin freely rotating conducting armature (radius r_a, rotation frequency ω_a, thickness

δ_a)
- a viscous fluid between the core and the armature (viscosity μ)
- rotating field coils at radius $r_c > r_a$
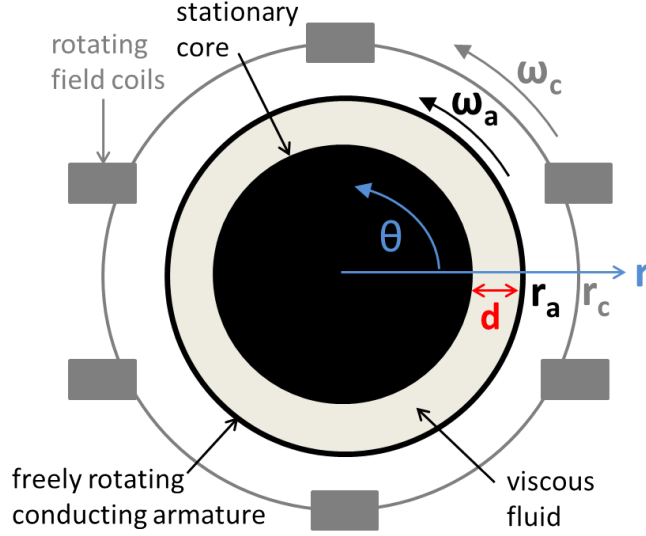
Figure C.1: Sketch of the induction motor considered in this section

The main idea is that the magnetic field produced by the rotating field coils crossed with the eddy currents induced in the armature will force the armature to co-rotate with the coils.

C.1.2   Calculation of the magnetic flux

The magnetic field perturbation is written in polar coordinates (r, θ, z):

$$\delta\vec{B} = \nabla\psi \times \vec{e_z} \tag{C.1}$$

and Maxwell-Faraday equation gives

$$\mu_0\delta\vec{j} = \nabla \times \delta\vec{B} = -\nabla_\perp^2\psi\vec{e_z} \tag{C.2}$$

The combination with Ohm's law in the armature's referential is

$$\nabla \times (\nabla \times \delta\vec{B}) = \mu_0\sigma\nabla \times (\delta\vec{E} + \vec{V}_{arm} \times \delta\vec{B}) \tag{C.3}$$

$$\nabla \times (\nabla_\perp^2\psi\vec{e_z}) = \mu_0\sigma(\frac{\partial}{\partial t}(\nabla\psi \times \vec{e_z}) - \nabla \times (\vec{V}_{arm} \times \delta\vec{B})) \tag{C.4}$$

and the projection on e_z direction is

$$\nabla_\perp^2\psi = \mu_0\sigma(\frac{\partial\psi}{\partial t} + r_a\omega_a\delta B_r) \tag{C.5}$$

The magnetic field is assumed to be dominated by one single poloidal harmonic m:

$$\psi = \psi(r).e^{i(m\theta - \omega_c t)} \tag{C.6}$$

and the linearization gives

$$\frac{1}{r}\frac{\partial}{\partial r}(r\psi') - \frac{m^2}{r^2}\psi = \mu_0\sigma(-i\omega_c + i\omega_a)\psi \tag{C.7}$$

This expression is then integrated across the armature, assuming that the magnetic flux is constant $(\psi(r) = \psi_a)$ and that the term in $\frac{m^2}{r^2}$ is negligible compared to the others. We finally get

$$[r\frac{d\psi}{dr}]^{r_a}_{r_a-\delta_a} = i\omega\tau_a\psi_a \tag{C.8}$$

where the time constant of the armature $\tau_a = \mu_0\sigma r_a\delta_a$ and the slip frequency $\omega = \omega_a - \omega_c$ have been defined. This slip frequency corresponds to the difference in rotation frequency between the armature and the coils.

Outside the armature, Faraday's law yields $\nabla^2_\perp\psi = 0$ since there is no current. The general solution of the equation is

$$\psi(r) = A(\frac{r}{r_a})^m + B(\frac{r}{r_a})^{-m} \tag{C.9}$$

The vacuum flux ψ_v is defined as the magnetic flux that would penetrate if there was no current: $\psi_v = \psi_c(\frac{r_a}{r_c})^m$, where ψ_c and r_c are respectively the magnetic flux and the radius of the coils. Using the boundary conditions $\psi(r_a) = \psi_a$ and $\psi(r_c) = \psi_c = \psi_v(\frac{r_c}{r_a})^m$, we have:

$$\psi(r) = \psi_a(\frac{r}{r_a})^m \tag{C.10}$$

for $r < r_a - \delta_a$ and

$$\psi(r) = \psi_v(\frac{r}{r_a})^m + (\psi_a - \psi_v)(\frac{r}{r_a})^{-m} \tag{C.11}$$

for $r_a < r < r_c$. The integration of Eq. (C.8) using Eq. (C.10) $[r = r_a - \delta_a]$ and Eq. (C.11) $[r = r_a]$ gives the expression of the magnetic flux perturbation induced in the armature, as a function of the vacuum magnetic perturbation:

$$\psi_a = \frac{2m\psi_v}{i\omega\tau_a + 2m} \tag{C.12}$$

Eq. (C.12) shows the value of the magnetic flux perturbation on the armature depending on the slip frequency ω. If the slip frequency is rather low $(\omega << 2m/\tau_a)$, then the magnetic flux perturbation penetrate the armature and the eddy currents induced by the difference of rotation between the armature and the external coils are low, and the magnetic flux penetrate almost as in vacuum: $\psi_a \approx \psi_v$. However, for a large slip frequency $(\omega >> 2m/\tau_a)$, the large eddy currents exclude the magnetic flux from the armature, and $\psi_a << \psi_v$.

C.1.3 Electromagnetic torque

The integrated electromagnetic torque per unit length acting on the armature is given by

$$T_{\theta,EM} = \int_{r_a-\delta_a}^{r_a} \oint_0^{2\pi} r\vec{e}_r \times \vec{F}_{EM}.\vec{e}_z r d\theta dr \tag{C.13}$$

$$\vec{F}_{EM}.\vec{e}_\theta = \frac{1}{2}\Re(\vec{j} \times \vec{B}^*).\vec{e}_\theta = \frac{1}{2}\Re(j_z \delta B_r^*) \simeq \frac{1}{2}\Re\left[-\frac{1}{\mu_0}\frac{1}{r}\frac{\partial}{\partial r}(r\psi').(-\frac{im}{r}\psi^*) \right] \tag{C.14}$$

$$\Rightarrow T_{\theta,EM} = \Re\left[\frac{im\pi}{\mu_0} \int_{r_a-\delta_a}^{r_a} \frac{\partial}{\partial r}(r\psi')\psi^* dr \right] = \Im\left[-\frac{m\pi}{\mu_0}\left[(r\psi')\right]_{r_a-\delta_a}^{r_a} \psi_a^* \right] \tag{C.15}$$

The combination of *Eq.* (C.8) and *Eq.* (C.15) yields

$$T_{\theta,EM} = -\frac{m\pi}{\mu_0}\omega\tau_a|\psi_a|^2 = -\frac{2m^2\pi|\psi_v|^2}{\mu_0}\frac{\omega\tau_a/2m}{1+(\omega\tau_a/2m)^2} \tag{C.16}$$

The electromagnetic torque is plotted as a function of the slip frequency in Fig. C.2. This torque always acts to reduce the slip frequency and forces the armature to co-rotate with the coils. The maximal torque is exerted when the slip frequency ω is equal to $2m/\tau_a$.
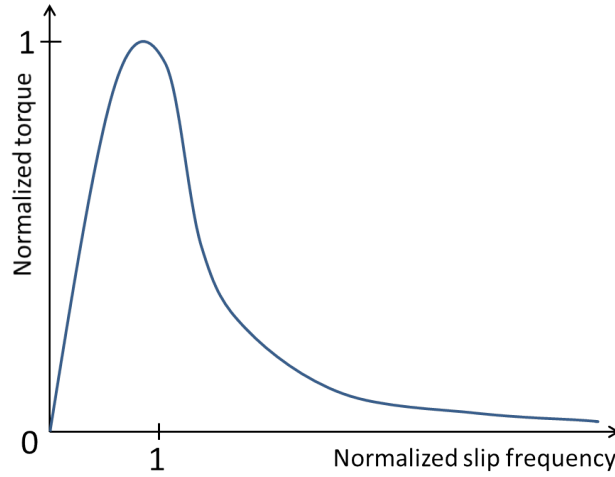
Figure C.2: Electromagnetic torque normalized to its maximul value $\pi m^2|\psi_v|^2/\mu_0$ as a function of the normalized slip frequency $\omega\tau_a/2m$.

C.1.4 Torque balance

We note d the distance between the armature and the non-rotating core. The viscous force per unit length exerted by the viscous fluid on the armature is written as follows:

$$F_{VS} = -\frac{\mu.2\pi r_a^2 \omega_a}{dm} \tag{C.17}$$

The corresponding torque is:

$$T_{\theta,VS} = -\frac{\mu.2\pi r_a^3 \omega_a}{dm} \tag{C.18}$$

The torque balance yields, at steady state:

$$T_{\theta,EM} + T_{\theta,VS} = 0 \tag{C.19}$$

$$\Rightarrow \omega_a = \frac{\tau_a m^2 d}{2\mu_0 r_a^3 \mu} |\psi_v|^2 \frac{\omega}{1 + (\omega \tau_a/2m)^2} \tag{C.20}$$

We assume in the following that ω_c is negative, so that the slip frequency is always positive. Thus we have $\omega_a = |\omega_c| - \omega$, and *Eq.* (C.20) writes:

$$|\omega_c| - \omega = \frac{|\psi_v|^2}{|\psi_{v1}|^2} \frac{\omega}{1 + (\omega \tau_a/2m)^2} \tag{C.21}$$

with $\psi_{v1} = \sqrt{\frac{2\mu_0 r_a^3 \mu}{\tau_a m^2 d}}$.

In the case where the coil frequency $|\omega_c|$ is under a critical value ($= 6\sqrt{3}m/\tau_a$), – which is correlated with a small value of $\omega << 2m/\tau_a$– we have $\omega/(1 + (\omega \tau_a/2m)^2) \sim \omega$, thus we obtain the simple equation:

$$\omega \approx \frac{|\omega_c|}{1 + |\psi_v|^2/|\psi_{v1}|^2} \tag{C.22}$$

In this case, the slip frequency remains low enough, so that the eddy currents are too low to exclude the magnetic flux from the armature.

However, over the critical value of ω_c, *Eq.* (C.21) presents two branches of solutions. The "high slip" branch, obtained for $\omega >> 2m/\tau_a$, is given by:

$$\omega \approx \frac{|\omega_c|}{2} \left(1 + \sqrt{1 - \frac{|\psi_v|^2}{|\psi_{v2}|^2}} \right) \tag{C.23}$$

where $\psi_{v2} = \psi_{v1}|\omega_c|\frac{\tau_a}{4m}$

As for the "low slip" branch, it verifies:

$$\frac{\omega \tau_a}{2m} \approx \frac{|\psi_v|^2}{|\psi_{v3}|^2} - \sqrt{\frac{|\psi_v|^4}{|\psi_{v3}|^4} - 1} \tag{C.24}$$

with $\psi_{v3} = \sqrt{\frac{|\omega_c|\tau_a}{m}}\psi_{v1}$.

In the high slip branch, the large slip frequency induce eddy currents which prevent the magnetic flux from penetrating the armature. However, when the coil field strength is progressively increased, the slip frequency is reduced, until a bifurcation towards the low slip branch occurs, when the field strength is equal to ψ_{v2}. The critical slip frequency of the bifurcation is $\omega = |\omega_c|/2$. In the low slip branch, the eddy currents remain low

enough to let the magnetic flux perturbation penetrate the armature. When the coil field strength is reduced, the slip frequency is gradually increased, until the backward bifurcation to the high slip branch occurs. The critical field when the transition occurs is equal to $\psi_{v3} < \psi_{v2}$, thus an hysteresis effect is observed, as plotted in Fig. C.3.
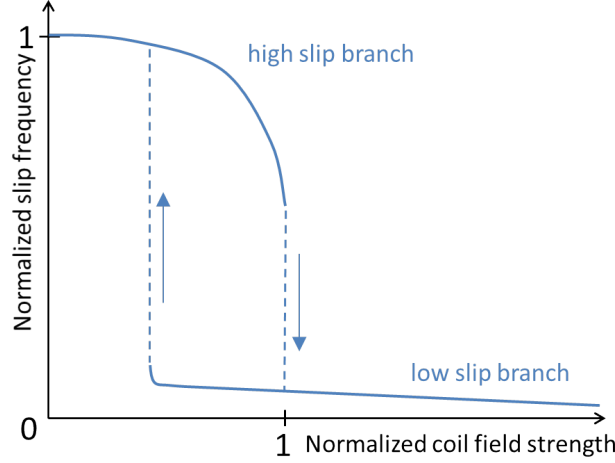
Figure C.3: Hysteresis cycle of the high and low branches of solutions of *Eq.* (C.20). The x- and y-axes respectively represent the normalized coil field strength $|\psi_v|^2/|\psi_{v2}|^2$ and the normalized slip frequency $\omega/|\omega_c|$.

C.2   The plasma induction motor

The anology is now made with a "plasma induction motor", where a tokamak plasma is approximated by a periodical cylinder. The toroidal direction, $2\pi R_0$ periodic, is described by the toroidal angle $\varphi = z/R_0$. Even though the error fields or RMPs are static in a tokamak, the plasma is rotating so there is still a differential velocity between the resonant surfaces of the plasma and the error field. Thus the error field can, similarly to the induction motor, exert a $\boldsymbol{j} \times \boldsymbol{B}$ torque on the rotating plasma by inducing eddy currents on the resonant surfaces.

C.2.1   Tearing mode equation

The equilibrium magnetic field and plasma current are given by:

$$\boldsymbol{B} = \left\{ \begin{array}{l} 0 \\ B_\theta(r) \\ B_\varphi \end{array} \right. \text{ and } \boldsymbol{j} = \left\{ \begin{array}{l} 0 \\ 0 \\ j_\varphi(r) \end{array} \right.$$

Maxwell-Faraday equation yields:

$$\mu_0 j_\varphi(r) = \mu_0 j_{0z} = \frac{1}{r}\frac{d(rB_\theta)}{dr} \tag{C.25}$$

We consider the plasma at the vicinity of a resonant field line characterized by its safety factor:

$$q(r) = \frac{d\varphi}{d\theta} = \frac{rB_\varphi}{RB_\theta} \tag{C.26}$$

and q on the resonant surface is given by

$$q_s = \frac{m}{n} \tag{C.27}$$

The equilibrium plasma is submitted to a static error-field (or static magnetic perturbations). We suppose that the plasma response has the same helicity as the error-field, and that the steady state equibrium – affected by the static error fields – is already reached:

$$\psi(r,\theta,\varphi,t) = \hat{\psi}(r)e^{i(m\theta-n\varphi)} \tag{C.28}$$

We separate the magnetic field and current into the equilibrium (without error field) and the pertubated parts: $\boldsymbol{B} = \boldsymbol{B_0} + \boldsymbol{\delta B}$ and $\boldsymbol{j} = \boldsymbol{j_0} + \boldsymbol{\delta j}$. The perturbed field are given by:

$$\boldsymbol{\delta B} = \nabla\psi \times \boldsymbol{e}_z = \begin{cases} \frac{im}{r}\psi \\ -\frac{\partial\psi}{\partial r} \\ 0 \end{cases} \quad\text{and}\quad \boldsymbol{\delta j} = \frac{1}{\mu_0}\nabla \times \boldsymbol{\delta B} = \frac{1}{\mu_0} \begin{cases} -\frac{in}{R}\frac{\partial\psi}{\partial r} \\ \frac{mn}{rR}\psi \\ -\nabla_\perp^2\psi = \mu_0\delta j_z \end{cases}$$

Then the equilibrium force balance writes in the ideal MHD assumption:

$$\nabla \times (\boldsymbol{j} \times \boldsymbol{B}) = \nabla \times \nabla P = \boldsymbol{0} \tag{C.29}$$

Using the identity $\boldsymbol{j} \times \boldsymbol{B} = \boldsymbol{j_0} \times \boldsymbol{\delta B} + \boldsymbol{\delta j} \times \boldsymbol{B_0}$, and the relation $B_\varphi = qRB_\theta/r$, the projection of *Eq.* (C.29) along $\boldsymbol{e}_z$ yields the so-called tearing mode equation:

$$\nabla_\perp^2\psi + \frac{\mu_0\psi q_s dj_{0z}/dr}{B_\theta(q-q_s)} = 0 \tag{C.30}$$

C.2.2 Invalidity of the ideal MHD on resonant surfaces

The electromagnetic torque due to the $\boldsymbol{j} \times \boldsymbol{B}$ force is:

$$\begin{aligned} T_{\theta,EM} &= \oint_{\theta=0}^{2\pi} \oint (r\boldsymbol{e}_r \times ((\boldsymbol{j_0}+\boldsymbol{\delta j}) \times (\boldsymbol{B_0}+\boldsymbol{\delta B}))) \cdot \boldsymbol{e}_z r d\theta R d\varphi \\ &= \oint \oint r^2 R_0 d\theta d\varphi \delta j_z \delta B_r \end{aligned} \tag{C.31}$$

since $\oint_\theta(\boldsymbol{j_0} \times \boldsymbol{\delta B} + \boldsymbol{\delta j} \times \boldsymbol{B_0})d\theta = \text{constant}(\theta)\oint_\theta \psi d\theta = 0$.
   Thus:

$$\begin{aligned} T_{\theta,EM} &= \oint \oint r^2 R_0 d\theta d\varphi \frac{1}{2}\Re\left(-\frac{\nabla_\perp^2\psi}{\mu_0}\left(-\frac{im}{r}\right)\psi^*\right) \\ &= -\frac{rR_0m}{2\mu_0}4\pi^2\Im\left(\nabla_\perp^2\psi\psi^*\right) \end{aligned} \tag{C.32}$$

Yet the tearing mode equation (*Eq.* (C.30)) gives:

$$\nabla_\perp^2 \psi \psi^* = -\frac{\mu_0 dj_{0z}/dr}{B_\theta(nq/m - 1)}|\psi|^2 \in \mathbb{R} \tag{C.33}$$

Thus $T_{\theta,EM} = 0$. It means that no electromagnetic torque can be exerted on the regions governed by ideal MHD. Except on the resonant surfaces, we consider that the ideal MHD is valid, so no torque is exerted outside the resonant surfaces. However, the tearing mode equation clearly presents a singularity on the resonant surfaces $q = m/n$, thus the ideal MHD is not valid any more on these surfaces. Indeed, if we write the magnetic perturbation as a function of the displacement $\boldsymbol{\xi}$ in the framework of ideal MHD, we have:

$$\boldsymbol{\delta B} = \nabla \times (\boldsymbol{\xi} \times \boldsymbol{B_0}) \tag{C.34}$$

thus the radial displacement of the plasma induced in response to the external error fields such that no eddy currents appear is given by:

$$\xi_r = \frac{\psi}{B_\theta(1 - nq/m)} \tag{C.35}$$

So, if there were no eddy currents appearing on the resonant surfaces $q = m/n$, then an infinite displacement ξ_r would be induced. Subsequently the ideal MHD is not valid at the vicinity of the rational surfaces, and a finite displacement occurs, due to the viscosity and the plasma inertia. This displacement is insufficient to prevent eddy currents from appearing, and the error-fields are capable to exert a torque on the rational surfaces.

C.2.3 Plasma response theory

We consider a resonant surface located on the radius r_s, with a thickness δ_s and a conductivity $\sigma(r_s)$. By analogy with section C.1, we define the time constant of the resonant layer:

$$\tau_s = \mu_0 \sigma(r_s) r_s \delta_s \tag{C.36}$$

On the same way, the slip frequency is defined:

$$\omega = m\Omega_\theta(r_s) - n\Omega_\varphi(r_s) \tag{C.37}$$

where $\Omega_\theta(r)$ and $\Omega_\varphi(r)$ are respectively the poloidal and toroidal rotation frequencies. The equivalent to the thin armature hypothesis (in the induction motor) is the assumption that ψ is constant over the layer, considered to be thin.

In this assumption, the following equation is verified, analogous to *Eq.* (C.8):

$$[r\frac{d\psi}{dr}]_{r_s-\delta_s/2}^{r_s+\delta_s/2} = i\omega\tau_s\psi_s \tag{C.38}$$

where $\psi_s = \psi(r_s)$ is the reconnected magnetic flux. If $\psi_s \neq 0$, then a magnetic island chain forms on the rational surface.

C.2.4 Asymptotic matching

Outside the resonant layer, the ideal MHD rather well describes the plasma dynamics, so the magnetic flux satisfies the tearing mode equation (*Eq.* (C.30)), and the plasma current is negligible. The solution to the tearing mode equation can be decomposed as follows:

$$\psi_{(}r) = \psi_s \psi_{plasma,N}(r) + \psi_{shield} \tag{C.39}$$

where the normalized plasma solution is $\psi_{plasma,N}(r) = \psi_{plasma}(r)/\psi(r_s)$. It satisfies the boundary conditions (at $r = 0$ and $r \to \infty$) corresponding to the boundary conditions in absence of the error fields.

The tearing stability index Δ' needs to be defined:

$$\Delta' = [r\frac{d\psi_{plasma,N}}{dr}]_{r_s^-}^{r_s^+} \tag{C.40}$$

If $\Delta' < 0$ then the plasma is tearing stable. Else if $\Delta' > 0$, the magnetic field spontaneously reconnects (without error fields) to form magnetic islands on the rational surface. The oscillation frequency of the magnetic field due to a spontaneously created island is:

$$\omega_0 = m\Omega_{\theta 0}(r_s) - n\Omega_{\varphi 0}(r_s) \tag{C.41}$$

Note that such islands are static in the frame of the plasma. So they rotate with the plasma in the laboratory frame. In the following, we consider that the plasma is tearing stable: $\Delta' < 0$.

As for the shielded solution ψ_{shield}, it is defined as the magnetic flux satisfying the boundary conditions in presence of error-field, assuming no magnetic reconnection has occured inside the plasma: $\psi_{shield}(r_s) = 0$. The vacuum magnetic flux is defined as in previous section, as in absence of plasma:

$$\psi_v = \psi_c \left(\frac{r_s}{r_c}\right)^m \tag{C.42}$$

where ψ_c is the magnetic flux at the coil. The error field coils are located outside the plasma thus their radius verifies $r_c > a$, a being the minor radius of the tokamak. Similarly to *Eq.* (C.9), the shielded solution verifies Faraday's law outside the resonant surface:

$$\psi_{shield}(r) = A(\frac{r}{r_s})^m + B(\frac{r}{r_s})^{-m} \text{ for } r_s < r < r_c. \tag{C.43}$$

Using the boundary conditions on $r = r_s$ and $r = r_c$, we find:

$$\psi_{shield}(r) = \psi_v \left[(\frac{r}{r_s})^m - (\frac{r}{r_s})^{-m}\right] \text{ for } r_s < r < r_c. \tag{C.44}$$

Both plasma and shielded solutions are plotted in Fig. C.4.

Using *Eq.* (C.39), *Eq.* (C.40) and *Eq.* (C.44), we obtain the equation governing the
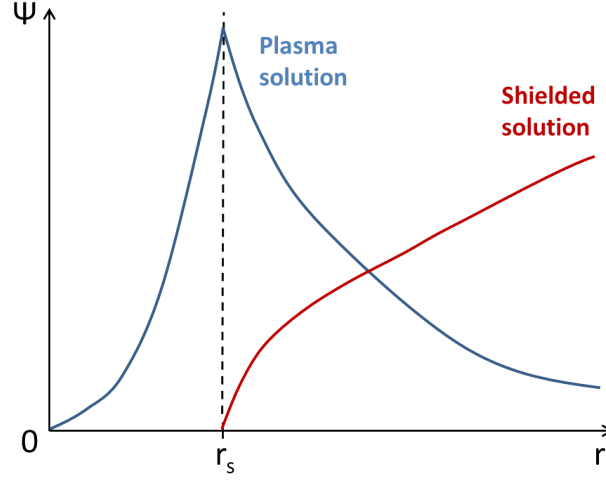
Figure C.4: Typical plasma and shielded solutions. The resonant surface is indicated by the dashed line.

region outside the resonant layer:

$$[r\frac{d\psi}{dr}]_{r_s^-}^{r_s^+} = \Delta'\psi_s + \underbrace{[r\frac{d\psi_{shield}}{dr}]_{r_s^-}^{r_s^+}}_{2m\psi_v|_{r^+} - 0|_{r^-}} \tag{C.45}$$

$$[r\frac{d\psi}{dr}]_{r_s^-}^{r_s^+} = \Delta'\psi_s + 2m\psi_v \tag{C.46}$$

Finally, the combination of *Eq.* (C.38) and *Eq.* (C.46) yields:

$$\psi_s = \frac{2m\psi_v}{-\Delta' + i\omega\tau_s} \tag{C.47}$$

Thus if the slip frequency ω is equal to zero, the reconnected flux takes its maximum value: $\psi_{s,max} = \left(\frac{2m}{-\Delta'}\right)\psi_v$. In the general case, $-\Delta' < 2m$ so $|\psi_s| > |\psi_v|$: this means that the error field is amplified on the resonant surface. Else if $\omega > \frac{-\Delta'}{\tau_s}$, eddy currents are generated on the rational surfaces, which suppress the magnetic reconnection, and the magnetic perturbation is screened: $|\psi_s| << |\psi_v|$.

C.2.5   Torque balance

The electromagnetic torque integrated over the rational surface is calculated, using *Eq.* (C.32):

$$
T_{\theta,EM} = \int_{r_{s-}}^{r_{s+}} \left(-\frac{2\pi^2 R_0 m}{\mu_0} \Im\big(\underbrace{r\nabla_\perp^2 \psi}_{\frac{\partial}{\partial r}\left(r\frac{d\psi}{dr}\right)} \psi^* \big) \right) dr
$$

$$
= -\frac{2\pi^2 R_0 m}{\mu_0} \Im\big([r\frac{d\psi}{dr}]_{r_s^-}^{r_s^+} \psi_s^*\big) \tag{C.48}
$$

Injecting *Eq.* (C.46) into *Eq.* (C.48), we get:

$$
T_{\theta,EM} = -\frac{2\pi^2 R_0 m}{\mu_0} \Im\big(i\omega\tau_s \underbrace{\psi_s \cdot \psi_s^*}_{|\psi_s|^2}\big) \tag{C.49}
$$

Finally, using *Eq.* (C.47), we obtain the formulation of the electromagnetic torque:

$$
T_{\theta,EM} = -\frac{8\pi^2 R_0 m^3}{\mu_0} \frac{\omega\tau_s}{(-\Delta')^2 + (\omega\tau_s)^2} |\psi_v|^2 \tag{C.50}
$$

Similarly to the induction motor, when the slip frequency is zero, no electromagnetic torque is exerted so no eddy currents are induced. The electromagnetic torque increases with the slip frequency, until the critical value of the slip frequency $\omega = (-\Delta')/\tau_s$ is reached. Over this value, the torque decreases with ω.

Actually, the neoclassical damping of the poloidal rotation is mostly due to the neo-classical friction ($v_\theta \to v_{\theta,neo}$) so the effect of the electromagnetic torque on the poloidal rotation may not be observed experimentally. However, the toroidal plasma velocity is not constrained as the poloidal velocity, so the electromagnetic torque has more effect on the toroidal rotation. The safety factor on the rational surface is:

$$
q_s = \frac{m}{n} = \frac{rB_\varphi}{RB_\theta} \approx -\frac{T_{\varphi,EM}}{T_{\theta,EM}} \tag{C.51}
$$

So the toroidal electromagnetic torque is expressed as:

$$
T_{\varphi,EM} \approx -\frac{n}{m}T_{\theta,EM} = \frac{8\pi^2 R_0 n m^2}{\mu_0} \frac{\omega\tau_s}{(-\Delta')^2 + (\omega\tau_s)^2} |\psi_v|^2 \tag{C.52}
$$

We consider the variation of toroidal angular rotation induced by the error fields, noted $\Delta\Omega_\varphi(r)$. The perpendicular viscosity acts to relax the toroidal rotation back to the unperturbed profile. The viscous force takes the form $F_v = \mu S \frac{\partial \Delta\Omega_\varphi}{\partial r}$, where $\mu(r)$ is the perpendicular viscosity and S the surface of the fluid layer. At the steady state, the force only acts on the resonant layer, so the variation of the force is zero outside the

resonant layer:

$$\frac{d}{dr}\left(r\mu\frac{\partial\Delta\Omega_\varphi}{\partial r}\right) = 0 \tag{C.53}$$

At the edge of the plasma, we also assume that the error field does not modify the plasma rotation: $\Delta\Omega_\varphi(a) = 0$. The integration of *Eq.* (C.53) yields:

$$\frac{\partial\Delta\Omega_\varphi}{\partial r} = \text{cst.}\frac{1}{r\mu(r)} \tag{C.54}$$

The integration using the boundary conditions yields the general solution:

$$\Delta\Omega_\varphi(r) = \begin{cases} \Delta\Omega_{\varphi_s} \text{ for } r < r_s \\ \Delta\Omega_{\varphi_s}\frac{\int_r^a \frac{dr}{\mu r}}{\int_{r_s}^a \frac{dr}{\mu r}} \text{ for } r_s < r < a \end{cases}$$

The integrated viscous torque acting on the resonant layer is given by:

$$T_{\varphi,VS} = 4\pi^2 R_0\left[r\mu R_0^2\frac{d\Delta\Omega_\varphi}{dr}\right]_{r_{s-}}^{r_{s+}} \tag{C.55}$$

Integrating the solution of $\Delta\Omega_\varphi$ into *Eq.* (C.55), the following expression of the viscous torque is obtained:

$$T_{\varphi,VS} = 4\pi^2 R_0\Delta\Omega_{\varphi_s}/\int_{r_s}^a\frac{dr}{r\mu} \tag{C.56}$$

The slip frequency, which is modified when the toroidal rotation is reduced by the error fields, is given by:

$$\omega = \omega_0 - n\Delta\Omega_{\varphi_s} \tag{C.57}$$

where we have used *Eq.* (C.37) and *Eq.* (C.41). We have assumed that the poloidal rotation is strongly damped (e.g. by the neoclassical poloidal friction). ω_0 is the oscillation frequency of a naturally unstable (m,n) tearing mode, also called "natural frequency".

The torque balance at the steady state is given by:

$$T_{\varphi,EM} + T_{\varphi,VS} = 0 \tag{C.58}$$

Using *Eq.* (C.52), *Eq.* (C.56) and *Eq.* (C.57), we have:

$$\frac{2n^2m^2\tau_s(\int_{r_s}^a dr/r\mu)}{\mu_0 R^2(-\Delta')^2}\frac{\omega}{1+[\omega\tau_s/(-\Delta')]^2}|\psi_v|^2 = \omega_0 - \omega \tag{C.59}$$

This equation is simular to *Eq.* (C.20) which governs the behaviour of the induction motor. In the same way, under a critical value of the natural frequency of the (m,n) tearing mode $\omega_{0,c} = 3\sqrt{3}(-\Delta')/\tau_s$, the slip frequency always remains low such that the response currents are too low to prevent the magnetic field from reconnecting. However, if the natural frequency is larger than this critical value – and it is always the case in tokamak plasmas –, then there are (as for the induction motor) two branches of solutions:

the unreconnected (high slip) branch where very little magnetic reconnection occurs due to the large slip frequency, and the fully reconnected (low slip) branch at low slip frequency. The bifurcation from the high slip to the low slip branch is similar as the one plotted in Fig. C.3.

C.3   Conclusion

When the error fields or RMPs are switched on and ramped up gradually, first no magnetic reconnection occurs, and eddy currents are induced on the resonant surfaces as a response to the error fields. These currents shield the induced magnetic perturbation, and are due to the rotation of the plasma.

The eddy currents generate an electromagnetic torque at the vicinity of the resonant surfaces, which acts to slow down the plasma rotation. Over a certain threshold in the error-field amplitude, the plasma rotation is damped up to half its original value, and the bifurcation to the reconnected state occurs: the electromagnetic torque brakes the plasma rotation to standstill on the resonant surfaces. Thus the eddy currents are sufficiently low to let magnetic island chains form on the rational surfaces: the magnetic field in fully reconnected. When the error field or the RMPs are reduced, the plasma progressively spins until the backward transition to the unreconnected state occurs. The error field has to be reduced to a much lower than the inward threshold, resulting in an hysteresis effect, as plotted in Fig. C.3.

This analysis is only a preliminary study, which demonstrates the bifurcation between the two states. In [Fitzpatrick 1998], eleven regimes are identified, which depend on the plasma resistivity, the plasma rotation and the plasma viscosity. For each of these regimes, the transition from the unreconnected to the fully reconnected state occur for a different amplitude of the applied error field. The aim of this appendix is not to describe all these regimes, but to understand why error field or RMPs can either be screened or penetrate, and to clarify the bifurcation phenomenon that actually occurs in the tokamak plasmas.

Towards simulation of the density pump-out induced by "magnetic flutter" in JOREK

Contents

D.1   Aim of the study

The density equation should be equivalent if we consider either ion or electron species. Yet in most MHD codes including JOREK, the particle fluxes induced by the polarization drift and the neoclassical velocity are neglected in the ion density equation, which makes the electron and ion density equations inconsistent. Several papers, e.g. Ref [Waelbroeck 2012], have shown that the gradient of the parallel current, which appears as an electron flux in the electron density equation, plays a major role in the pump-out of density in the plasma when RMPs are applied. Indeed, the following derivation shows that the parallel current flowing along perturbed magnetic field lines (phenomenon called magnetic flutter) is likely to generate an enhanced radial transport of electron density. Due to the ambipolarity constraints, raised e.g. in [Tokar 2008], the ion flux and the electron flux have to be equal, so that an enhanced electron transport will also induce an enhanced ion transport. This derivation shows that the terms inducing the magnetic

flutter can be added in the JOREK model in two different ways, depending on if we consider the electron or ion equation.

D.2   Density equation for electrons and ions

The density equation for electrons writes:

$$\frac{\partial n_e}{\partial t} + \nabla \cdot (n_e \boldsymbol{v_e}) = D_\perp \nabla_\perp^2 n_e + S_{n_e} \tag{D.1}$$

The density equation for ions is:

$$\frac{\partial n_i}{\partial t} + \nabla \cdot (n_i \boldsymbol{v_i}) = D_\perp \nabla_\perp^2 n_i + S_{n_i} \tag{D.2}$$

We will show that if assuming the quasineutrality of the plasma:

$$n_i = n_e = n \tag{D.3}$$

both equations may not be equivalent as we neglect several components of the velocity.

The momentum equation for ions leads to the expression of the fluid velocity, which is approximately equal to the ion velocity. The momentum equation for ions writes:

$$\begin{aligned}
m_i n_i \frac{d\boldsymbol{v}}{dt} &= e n_i (\boldsymbol{E} + \boldsymbol{v} \times \boldsymbol{B}) - \nabla P_i - \nabla \cdot \bar{\Pi}_i - m_e n_i \nu_{ei}(\boldsymbol{v_i} - \boldsymbol{v_e}) \\
m_i n \frac{d\boldsymbol{v}}{dt} &= e n (\boldsymbol{E} + \boldsymbol{v} \times \boldsymbol{B}) - \nabla P_i - \nabla \cdot \bar{\Pi}_i - e n \eta \boldsymbol{J}
\end{aligned} \tag{D.4}$$

where we have used the quasineutrality equation (*Eq.* (D.3)), the definition of the resistivity $\eta = \frac{m_e \nu_{ei}}{ne^2}$ and the definition of the current:

$$\boldsymbol{J} = ne(\boldsymbol{v_i} - \boldsymbol{v_e}) \tag{D.5}$$

Using the identity $(\boldsymbol{v} \times \boldsymbol{B}) \times \boldsymbol{B} = (\boldsymbol{B} \cdot \boldsymbol{v})\boldsymbol{B} - (\boldsymbol{B} \cdot \boldsymbol{B})\boldsymbol{v} = \boldsymbol{v}_\parallel B^2 - \boldsymbol{v}B^2$, the cross product of *Eq.* (D.4) with the magnetic field gives the expression of the fluid velocity:

$$\begin{aligned}
\boldsymbol{v} &= \boldsymbol{v}_{i,\parallel} + \frac{\boldsymbol{E} \times \boldsymbol{B}}{B^2} - \frac{\nabla P_i \times \boldsymbol{B}}{neB^2} - \frac{m_i}{eB^2}\frac{d\boldsymbol{v}}{dt} \times \boldsymbol{B} - \frac{\nabla \cdot \bar{\Pi}_i \times \boldsymbol{B}}{neB^2} - \frac{\eta \boldsymbol{J} \times \boldsymbol{B}}{B^2} \\
\boldsymbol{v} &= \boldsymbol{v}_{i,\parallel} \quad\;\; + \boldsymbol{v}_E \qquad\;\; + \boldsymbol{v}_i^* \qquad\quad\; + \boldsymbol{v}_{pol,i} \qquad\; + \boldsymbol{v}_{\Pi_i} \qquad + \boldsymbol{v}_\eta
\end{aligned} \tag{D.6}$$

The gyroviscous cancellation gives:

$$\frac{d\boldsymbol{v}_i^*}{dt} \times \boldsymbol{B} \approx -\nabla \cdot \bar{\Pi}_{i,gv} \times \boldsymbol{B} \tag{D.7}$$

The polarization velocity is usually approximated to its first order:

$$\boldsymbol{v}_{pol,i} = -\frac{m_i}{eB^2}\frac{d\boldsymbol{v}}{dt} \times \boldsymbol{B} = +\frac{m_i}{e}\frac{\boldsymbol{B}}{B^2} \times \frac{d\boldsymbol{v}}{dt} \approx +\frac{m_i}{e}\frac{\boldsymbol{B}}{B^2} \times \frac{d\boldsymbol{v}_E}{dt} \tag{D.8}$$

Thus the total ion velocity is given by:

$$\boldsymbol{v} = \boldsymbol{v}_{i,\|} + \frac{\boldsymbol{E} \times \boldsymbol{B}}{B^2} - \frac{\nabla P_i \times \boldsymbol{B}}{neB^2} + \frac{m_i}{e}\frac{\boldsymbol{B}}{B^2} \times \frac{d\boldsymbol{v}_E}{dt} - \frac{\nabla \cdot \bar{\Pi}_{i,neo} \times \boldsymbol{B}}{neB^2} - \frac{\eta \boldsymbol{J} \times \boldsymbol{B}}{B^2} \tag{D.9}$$

In the density equation, the advection of the last term $(\nabla \cdot (n\boldsymbol{v}_\eta))$ is small as compared to the diffusive terms. Indeed, the ordering of the advection of the resistive velocity $\boldsymbol{v}_\eta$ is:

$$\nabla \cdot \left(n\frac{\eta \boldsymbol{J} \times \boldsymbol{B}}{B^2}\right) = \nabla \cdot \left(n\frac{\eta \nabla P}{B^2}\right) \tag{D.10}$$

Using $\eta = \frac{m_e \nu_{ei}}{ne^2}$ and $\nabla P \approx T\nabla n$, we write this advection term as a diffusive term:

$$\nabla \cdot \left(n\frac{\eta \boldsymbol{J} \times \boldsymbol{B}}{B^2}\right) \approx \nabla \cdot (D_\eta \nabla n) \tag{D.11}$$

with $D_\eta = \frac{m_e \nu_{ei} T}{e^2 B^2} = \nu_{ei}\rho_e^2$, where $\rho_e = \boldsymbol{v}_{th,e}/\Omega_{c,e}$ is the electron Larmor radius. In comparison, the diffusive flux is written:

$$\Gamma_e = -D_e \nabla n \tag{D.12}$$

with $D_e = \nu_e \frac{q^2 \rho_e^2}{\varepsilon^{3/2}}$, $\varepsilon = r/R_0$ being the inverse aspect ratio. So the ratio between D_η and D_e is:

$$\frac{D_\eta}{D_e} = \frac{\varepsilon^{3/2}}{q^2} << 1 \tag{D.13}$$

in tokamaks with a large aspect ratio.

In the MHD ordering, $\boldsymbol{v} = \boldsymbol{v}_{i,\|} + \boldsymbol{v}_E$. In the bi-fluid (drift) ordering used in JOREK, $\boldsymbol{v}_E + \boldsymbol{v}_i^*$ have the same order of magnitude and $\boldsymbol{v} = \boldsymbol{v}_{i,\|} + \boldsymbol{v}_E + \boldsymbol{v}_i^*$. It is furthermore useful to consider in addition the polarization drift (first order compared to $E \times B$ and diamagnetic drifts) if we want to have the electron density and ion density equations consistent / equivalent with each other. Actually, the polarization drifts/currents may be important to provide the ambipolarity $n_e = n_i$. In this study, we therefore keep the ion polarization velocity, as well as the neoclassical term:

$$\boldsymbol{v} = \boldsymbol{v}_{i,\|} + \frac{\boldsymbol{E} \times \boldsymbol{B}}{B^2} - \frac{\nabla P_i \times \boldsymbol{B}}{neB^2} + \frac{m_i}{e}\frac{\boldsymbol{B}}{B^2} \times \frac{d\boldsymbol{v}_E}{dt} - \frac{\nabla \cdot \bar{\Pi}_{i,neo} \times \boldsymbol{B}}{neB^2} \tag{D.14}$$

In the same way as we derived the ion velocity, we calculate the electron velocity from the momentum equation for electrons:

$$m_e n\frac{d\boldsymbol{v}_e}{dt} = en(\boldsymbol{E} + \boldsymbol{v}_e \times \boldsymbol{B}) - \nabla P_e - \nabla \cdot \bar{\Pi}_e + en\eta \boldsymbol{J} \tag{D.15}$$

We neglect the electron inertia, which is of order (m_e/m_i) compared to the ion inertia. Thus the electron velocity is:

$$\boldsymbol{v}_e = \boldsymbol{v}_{e,||} + \frac{\boldsymbol{E} \times \boldsymbol{B}}{B^2} + \frac{\nabla P_e \times \boldsymbol{B}}{neB^2} - \frac{\nabla \cdot \bar{\bar{\Pi}}_{e,neo} \times \boldsymbol{B}}{neB^2} + \frac{\eta \boldsymbol{J} \times \boldsymbol{B}}{B^2} \tag{D.16}$$

For a large aspect ratio, as previously discussed for ions, the velocity associated to the resistive term is neglected. The electron neoclassical term is also neglected as compared to the ion neoclassical term. So the electron velocity writes:

$$\boldsymbol{v}_e = \boldsymbol{v}_{e,||} + \frac{\boldsymbol{E} \times \boldsymbol{B}}{B^2} + \frac{\nabla P_e \times \boldsymbol{B}}{neB^2} \tag{D.17}$$

The electron parallel velocity is expressed using the projection of the plasma current (D.5) along the magnetic field:

$$\boldsymbol{v}_{||,e} = -\frac{\boldsymbol{J}_{||}}{ne} + \boldsymbol{v}_{||,i} \tag{D.18}$$

with $\boldsymbol{v}_{||,s} = (\boldsymbol{v}_s . \boldsymbol{B})\frac{\boldsymbol{B}}{B^2}$ and $\boldsymbol{J}_{||} = (\boldsymbol{J} . \boldsymbol{B})\frac{\boldsymbol{B}}{B^2}$.

Thus with the hypotheses made, the density equation for ions and electrons are respectively:

$$\frac{\partial n}{\partial t} + \nabla \cdot (n\boldsymbol{v}_E) + \nabla \cdot (n\boldsymbol{v}_i^*) + \nabla \cdot (n\boldsymbol{v}_{pol,i}) + \nabla \cdot (nv_{||,i}) + \nabla \cdot (n\boldsymbol{v}_{\Pi_i})$$
$$= D_\perp \nabla_\perp^2 n + S_n \tag{D.19}$$

$$\frac{\partial n}{\partial t} + \nabla \cdot (n\boldsymbol{v}_E) + \nabla \cdot (n\boldsymbol{v}_e^*) - \frac{1}{e}\nabla \cdot \boldsymbol{J}_{||} + \nabla \cdot (nv_{||,i})$$
$$= D_\perp \nabla_\perp^2 n + S_n \tag{D.20}$$

We calculate the divergence of $n\boldsymbol{v}_\perp$ for ions and electrons :

$$\nabla \cdot (n\boldsymbol{v}_E) = \boldsymbol{v}_E \cdot \nabla n + n\nabla \cdot (\frac{\boldsymbol{B} \times \nabla u}{B^2}) = \boldsymbol{v}_E \cdot \nabla n + n\nabla u \cdot \nabla \times \frac{\boldsymbol{B}}{B^2} \tag{D.21}$$

$$\nabla \cdot (n\boldsymbol{v}_s^*) = \frac{1}{e_s}\nabla \cdot (\frac{\boldsymbol{B} \times \nabla P_s}{B^2}) = \frac{1}{e_s}\nabla P_s \cdot \nabla \times \frac{\boldsymbol{B}}{B^2} \tag{D.22}$$

for each species $s = e, i$. And the neoclassical term is:

$$\nabla \cdot (n\boldsymbol{v}_{\Pi_i}) = \nabla \cdot (n\frac{\boldsymbol{B} \times \nabla \cdot \bar{\bar{\Pi}}_{i,neo}}{neB^2}) = \frac{1}{e}\nabla \cdot \left(\frac{\boldsymbol{B}}{B^2} \times \nabla \cdot \bar{\bar{\Pi}}_{i,neo}\right) \tag{D.23}$$

The complete density equations for ions and electrons are thus the following:

$$\frac{\partial n}{\partial t} + \boldsymbol{v}_E \cdot \nabla n + \nabla \cdot (n\boldsymbol{v}_{pol,i}) + \nabla \cdot (n\boldsymbol{v}_{||,i}) + n(\nabla u + \frac{\nabla P_i}{ne}) \cdot \nabla \times \frac{\boldsymbol{B}}{B^2}$$
$$+\frac{1}{e}\nabla \cdot \left(\frac{\boldsymbol{B}}{B^2} \times \nabla \cdot \bar{\bar{\Pi}}_{i,neo}\right) = D_\perp \nabla_\perp^2 n + S_n \tag{D.24}$$

$$\frac{\partial n}{\partial t} + \boldsymbol{v}_E \cdot \nabla n - \frac{1}{e}\nabla \cdot \boldsymbol{J}_{||} + \nabla \cdot (n\boldsymbol{v}_{||,i}) + n(\nabla u - \frac{\nabla P_e}{ne}) \cdot \nabla \times \frac{\boldsymbol{B}}{B^2} = D_\perp \nabla_\perp^2 n + S_n \tag{D.25}$$

Eq. (D.25) shows that the current flowing along the magnetic field lines will transport the electron density (and thus the ion density). If the magnetic field lines are bended by RMPs in the radial direction, the transport of particles will therefore be enhanced, and will be even larger if the magnetic field is stochastic. So this magnetic flutter is likely to induce the density pump-out.

D.3   Equivalence of the equations

The equivalence of these two equations is checked in the following, using the fact that the current is divergence-free. The difference between the 2 equations (Eq. (D.24) − Eq. (D.25)) yields:

$$\nabla \cdot (n\boldsymbol{v}_{pol,i}) + \frac{1}{e}\nabla \cdot \boldsymbol{J}_{||} + \frac{\nabla P}{e} \cdot \nabla \times \frac{\boldsymbol{B}}{B^2} + \frac{1}{e}\nabla \cdot \left(\frac{\boldsymbol{B}}{B^2} \times \nabla \cdot \bar{\bar{\Pi}}_{i,neo}\right) = 0 \tag{D.26}$$

Now with the exact expression of the polarization velocity given in Eq. (D.8):

$$\nabla \cdot \left(\frac{m_i n}{e}\frac{\boldsymbol{B}}{B^2} \times \frac{d\boldsymbol{v}}{dt}\right) + \frac{1}{e}\nabla \cdot \boldsymbol{J}_{||} + \frac{\nabla P}{e} \cdot \nabla \times \frac{\boldsymbol{B}}{B^2} + \frac{1}{e}\nabla \cdot \left(\frac{\boldsymbol{B}}{B^2} \times \nabla \cdot \bar{\bar{\Pi}}_{i,neo}\right) = 0 \tag{D.27}$$

To check the truthfulness of this equation, we need to use the fluid momentum equation (where we neglect the viscous and source terms), on which we apply the operator $(\boldsymbol{B}\times)$ to get the perpendicular component:

$$\boldsymbol{B} \times \left(m_i n \frac{d\boldsymbol{v}}{dt}\right) = \boldsymbol{B} \times \left(\boldsymbol{J} \times \boldsymbol{B} - \nabla P - \nabla \cdot \bar{\bar{\Pi}}_{i,neo}\right) \tag{D.28}$$

Using $\boldsymbol{B} \times (\boldsymbol{J} \times \boldsymbol{B}) = B^2(\boldsymbol{J} - \boldsymbol{J}_{||}) = B^2\boldsymbol{J}_\perp$, we have:

$$m_i n \boldsymbol{B} \times \left(\frac{d\boldsymbol{v}}{dt}\right) = B^2\boldsymbol{J}_\perp - \boldsymbol{B} \times \nabla P - \boldsymbol{B} \times \nabla \cdot \bar{\bar{\Pi}}_{i,neo} \tag{D.29}$$

And the divergence of (*Eq.* (D.29) divided by B^2) yields:

$$\nabla \cdot \left(m_i n \frac{\boldsymbol{B}}{B^2} \times \frac{d\boldsymbol{v}}{dt} \right) = -\nabla \cdot \boldsymbol{J}_{||} - \underbrace{\nabla \cdot \left(\frac{\boldsymbol{B}}{B^2} \times \nabla P \right)}_{\nabla P \cdot \nabla \times (\boldsymbol{B}/B^2)} - \nabla \cdot \left(\frac{\boldsymbol{B}}{B^2} \times \nabla \cdot \bar{\bar{\Pi}}_{i,neo} \right) \quad \text{(D.30)}$$

where we have used the current conservation law: $\nabla \cdot \boldsymbol{J}_\perp = \nabla \cdot \boldsymbol{J} - \nabla \cdot \boldsymbol{J}_{||} = -\nabla \cdot \boldsymbol{J}_{||}$.
We notice that *Eq.* (D.30) is identical to *Eq.* (D.27). Thus the perpendicular momentum
equation provides the equivalence of the two MHD systems of equations including either
the ion or the electron density equation.

D.4 What modifications should be done in JOREK?

The equation currently implemented in JOREK is the density equation for ions, but
without the polarization and neoclassical terms:

$$\frac{\partial n}{\partial t} + \boldsymbol{v}_E \cdot \nabla n + \nabla \cdot (n \boldsymbol{v}_{||,i}) + n(\nabla u + \frac{\nabla P_i}{ne}) \cdot \nabla \times \frac{\boldsymbol{B}}{B^2} = D_\perp \nabla_\perp^2 n + S_n \quad \text{(D.31)}$$

Thus two possibilities enable to add the "magnetic flutter" terms: the first solution is
to add the terms at the next order for the velocity ($\boldsymbol{v}_{pol,i}$ and $\boldsymbol{v}_{\Pi_i}$) into the ion density
equation. Numerically, this solution may be difficult since the polarization drift involves
the time derivative of the velocity.

The other solution, which consists in solving the electron density equation instead of
the ion density equation, seems simpler. Only a new term $-\frac{1}{e}\nabla \cdot \boldsymbol{J}_{||}$ has to be added in
the equation and the ion pressure P_i must be replaced by the opposite of the electron
pressure $-P_e$. We opt for this solution.

The ion and electron pressure are equal in our model ($P_i = P_e = P/2$), so only the
sign must be changed in the diamagnetic term ($\nabla \cdot (\rho \boldsymbol{v}^*)$), and the new term $-\frac{1}{e}\nabla_{||} J_{||}$ is
close to the one that already exists in the vorticity equation so there are very few things
to implement.

D.5 Normalization

The ion density equation (currently implemented, *Eq.* (D.31)) is given in SI units by

$$\frac{\partial \rho}{\partial t} = -\nabla \cdot (\rho \boldsymbol{v}_{||,i}) - \nabla \cdot (\rho \boldsymbol{v}_E) - \nabla \cdot (\rho \boldsymbol{v}_i^*) + D_\perp \nabla_\perp^2 \rho + S_\rho \quad \text{(D.32)}$$

The decomposition of the ion velocity is:

$$\boldsymbol{v}_i = \boldsymbol{v}_{||,i} - R^2 \nabla u \times \nabla \varphi - \frac{R^2 m_i}{\rho e F_0} \nabla P_i \times \nabla \varphi \quad \text{(D.33)}$$

Thus the decomposed form of *Eq.* (D.32) is:

$$\frac{\partial \rho}{\partial t} = -\nabla \cdot (\rho \boldsymbol{v}_{||,i}) + \nabla \cdot (\rho R^2 \nabla u \times \nabla \varphi) + \nabla \cdot (\frac{m_i R^2}{eF_0} \nabla P_i \times \nabla \varphi) + D_\perp \nabla_\perp^2 \rho + S_\rho \text{(D.34)}$$

Similarly, the electron density equation writes in SI units:

$$\frac{\partial \rho}{\partial t} = -\nabla \cdot (\rho \boldsymbol{v}_{||,i}) + \frac{m_i}{e} \nabla \cdot \boldsymbol{J}_{||} + \nabla \cdot (\rho R^2 \nabla u \times \nabla \varphi) - \nabla \cdot (\frac{m_i R^2}{eF_0} \nabla P_e \times \nabla \varphi) + D_\perp \nabla_\perp^2 \rho + S_\rho$$

$$\text{(D.35)}$$

Using the normalizations $\tilde{\rho} = \rho/\rho_0$, $t = \tilde{t}\sqrt{\rho_0 \mu_0}$, $\tilde{v}_\perp = v_\perp \sqrt{\rho_0 \mu_0}$, $\tilde{v}_{||} = v_{||} \sqrt{\rho_0 \mu_0} \boldsymbol{B}$, $\tilde{J} = \mu_0 J$, $\tilde{P} = \mu_0 P$ and $\tilde{D}_\perp = D_\perp \sqrt{\rho_0 \mu_0}$, we obtain the normalized equations for ions and electrons:

$$\frac{\partial \tilde{\rho}}{\partial \tilde{t}} = -\nabla \cdot (\tilde{\rho} \tilde{v}_{||,i} \boldsymbol{B}) + \nabla \cdot (\tilde{\rho} R^2 \nabla \tilde{u} \times \nabla \varphi)$$

$$+ \nabla \cdot (\frac{m_i R^2}{eF_0 \sqrt{\rho_0 \mu_0}} \nabla \tilde{P}_i \times \nabla \varphi) + \tilde{D}_\perp \nabla_\perp^2 \tilde{\rho} + \tilde{S}_\rho \qquad \text{(D.36)}$$

$$\frac{\partial \tilde{\rho}}{\partial \tilde{t}} = -\nabla \cdot (\tilde{\rho} \tilde{v}_{||,i} \boldsymbol{B}) + \frac{m_i}{e \sqrt{\rho_0 \mu_0}} \nabla \cdot \tilde{\boldsymbol{J}}_{||} + \nabla \cdot (\tilde{\rho} R^2 \nabla \tilde{u} \times \nabla \varphi)$$

$$- \nabla \cdot (\frac{m_i R^2}{eF_0 \sqrt{\rho_0 \mu_0}} \nabla \tilde{P}_e \times \nabla \varphi) + \tilde{D}_\perp \nabla_\perp^2 \tilde{\rho} + \tilde{S}_\rho \qquad \text{(D.37)}$$

We define the diamagnetic parameter (inverse of the normalized ion cyclotron frequency) as

$$\tau_{IC} = \frac{m_i}{2F_0 e \sqrt{\rho_0 \mu_0}} \qquad \text{(D.38)}$$

using the definition of τ_{IC} and assuming that $T_e = T_i = T$ and thus $P_e = P_i = P/2$, both equations become:

$$\frac{\partial \tilde{\rho}}{\partial \tilde{t}} = -\nabla \cdot (\tilde{\rho} \tilde{v}_{||,i} \boldsymbol{B}) + \nabla \cdot (\tilde{\rho} R^2 \nabla \tilde{u} \times \nabla \varphi)$$

$$+ \nabla \cdot (\tau_{IC} R^2 \nabla \tilde{P}_i \times \nabla \varphi) + \tilde{D}_\perp \nabla_\perp^2 \tilde{\rho} + \tilde{S}_\rho \qquad \text{(D.39)}$$

$$\frac{\partial \tilde{\rho}}{\partial \tilde{t}} = -\nabla \cdot (\tilde{\rho} \tilde{v}_{||,i} \boldsymbol{B}) + 2F_0 \tau_{IC} \nabla \cdot \tilde{\boldsymbol{J}}_{||} + \nabla \cdot (\tilde{\rho} R^2 \nabla \tilde{u} \times \nabla \varphi)$$

$$- \nabla \cdot (\tau_{IC} R^2 \nabla \tilde{P}_e \times \nabla \varphi) + \tilde{D}_\perp \nabla_\perp^2 \tilde{\rho} + \tilde{S}_\rho \qquad \text{(D.40)}$$

From now, the quantities are normalized in JOREK units yet the tildes are omitted in order to make the equations more readable. The last remaining calculation is the expression of the parallel current $\boldsymbol{J}_{||}$.

$$\boldsymbol{J}_{||} = \frac{\boldsymbol{J} \cdot \boldsymbol{B}}{B^2} \boldsymbol{B} \qquad \text{(D.41)}$$

The magnetic field and the current are expressed in the orthonormed basis $(\nabla R, \nabla Z, R\nabla\varphi)$ as:

$$\boldsymbol{B} = \begin{cases} \frac{1}{R}\frac{\partial\psi}{\partial Z} \\ -\frac{1}{R}\frac{\partial\psi}{\partial R} \\ \frac{F_0}{R} \end{cases}$$

and

$$\boldsymbol{J} = \nabla\times(\nabla\psi\times\nabla\varphi) = \begin{cases} \frac{1}{R^2}\frac{\partial}{\partial\phi}\frac{\partial\psi}{\partial R} \\ \frac{1}{R^2}\frac{\partial}{\partial\phi}\frac{\partial\psi}{\partial Z} \\ -\frac{1}{R}\left(\frac{\partial^2\psi}{\partial R^2}+\frac{\partial^2\psi}{\partial Z^2}\right)+\frac{1}{R}\frac{\partial\psi}{\partial R} = -\frac{\Delta^*\psi}{R} \end{cases}$$

Where

$$\Delta^* = R^2\nabla\cdot\left(\frac{1}{R^2}\nabla_\perp\right) = \left(R\frac{\partial}{\partial R}\left(\frac{1}{R}\frac{\partial}{\partial R}\right)+\frac{\partial^2}{\partial Z^2}\right). \tag{D.42}$$

The definition of the toroidal current in JOREK is $j = +\Delta^*\psi$ so the toroidal component of the current is: $\boldsymbol{J}\cdot\boldsymbol{e}_\varphi = -j/R$

Using the definitions of $\boldsymbol{J}$, $\boldsymbol{B}$ as well as the calculation of $B^2 = \frac{F_0^2+|\nabla\psi|^2}{R^2} \approx \frac{F_0^2}{R^2}$, we obtain the equation:

$$\frac{\boldsymbol{J}\cdot\boldsymbol{B}}{B^2} = \frac{1}{RF_0^2}\left(\frac{\partial^2\psi}{\partial\phi\partial R}\frac{\partial\psi}{\partial Z}-\frac{\partial^2\psi}{\partial\phi\partial Z}\frac{\partial\psi}{\partial R}\right)-\frac{j}{F_0}$$
$$\frac{\boldsymbol{J}\cdot\boldsymbol{B}}{B^2} = \frac{1}{RF_0^2}\left[\frac{\partial\psi}{\partial\varphi},\psi\right]-\frac{j}{F_0} \tag{D.43}$$

Thus

$$\boldsymbol{J}_{||} = \frac{\boldsymbol{J}\cdot\boldsymbol{B}}{B^2}\boldsymbol{B} = \left(\frac{1}{RF_0^2}\left[\frac{\partial\psi}{\partial\varphi},\psi\right]-\frac{j}{F_0}\right)(F_0\nabla\varphi+\nabla\psi\times\nabla\varphi) \tag{D.44}$$

D.6 Weak form of the new term

There are two ways to calculate the weak form of the new term $2F_0\tau_{IC}\nabla\cdot\boldsymbol{J}_{||}$.

D.6.1 First method

First, we directly calculate the divergence of the term:

$$\nabla\cdot\boldsymbol{J}_{||} = \frac{\boldsymbol{J}\cdot\boldsymbol{B}}{B^2}\nabla\cdot\boldsymbol{B}+\boldsymbol{B}\cdot\nabla\left(\frac{\boldsymbol{J}\cdot\boldsymbol{B}}{B^2}\right)$$
$$= (F_0\nabla\varphi+\nabla\psi\times\nabla\varphi)\cdot\nabla\left(-\frac{j}{F_0}+\frac{1}{RF_0^2}\left[\frac{\partial\psi}{\partial\varphi},\psi\right]\right) \tag{D.45}$$
$$= -\frac{1}{R^2}\frac{\partial j}{\partial\varphi}+\frac{1}{F_0R}[\psi,j]+\frac{1}{F_0R^3}\left[\frac{\partial^2\psi}{\partial\varphi^2},\psi\right]+\frac{1}{F_0^2R}\left[\left[\frac{\partial\psi}{\partial\varphi},\psi\right],\psi\right]$$

In the large aspect ratio approximation, we have:

$$\nabla \cdot \boldsymbol{J}_{\parallel} \approx -\frac{1}{R^2}\frac{\partial j}{\partial \varphi} + \frac{1}{F_0 R}[\psi, j] \tag{D.46}$$

Thus the new term in the electron density equation writes in weak form:

$$\int 2\rho^* F_0 \tau_{IC} \nabla \cdot \boldsymbol{J}_{\parallel} dV = \int 2\rho^* F_0 \tau_{IC} \left(-\frac{1}{R^2}\frac{\partial j}{\partial \varphi} + \frac{1}{F_0 R}[\psi, j] \right) dV \tag{D.47}$$

D.6.2 Second method

We directly calculate the weak form integrating by part:

$$\int 2\rho^* F_0 \tau_{IC} \nabla \cdot \boldsymbol{J}_{\parallel} dV = \int -2F_0 \tau_{IC} \nabla \rho^* \cdot \boldsymbol{J}_{\parallel} dV$$

$$= \int -2F_0 \tau_{IC} \nabla \rho^* \cdot \left(\frac{1}{R F_0^2}\left[\frac{\partial \psi}{\partial \varphi}, \psi\right] - \frac{j}{F_0} \right) (F_0 \nabla\varphi + \nabla\psi \times \nabla\varphi) dV$$

$$= \int -2F_0 \tau_{IC} \left(\frac{1}{R F_0^2}\left[\frac{\partial \psi}{\partial \varphi}, \psi\right] - \frac{j}{F_0} \right) \left(\frac{F_0}{R^2}\frac{\partial \rho^*}{\partial \varphi} + \frac{1}{R}[\rho^*, \psi] \right) dV \tag{D.48}$$

As in the first method, we discard the lower order terms:

$$\int 2\rho^* F_0 \tau_{IC} \nabla \cdot \boldsymbol{J}_{\parallel} dV = \int -2F_0 \tau_{IC} \nabla \rho^* \cdot \left(-\frac{j}{F_0} \right) (F_0 \nabla\varphi + \nabla\psi \times \nabla\varphi) dV$$

$$= \int \left(2F_0 \tau_{IC} j \frac{1}{R^2}\frac{\partial \rho^*}{\partial \varphi} + 2\tau_{IC}\frac{j}{R}[\rho^*, \psi] \right) dV \tag{D.49}$$

The density equation for ions that is currently solved is the following (which neglects the ion polarization drifts ; see the complete derivation in appendix B) :

$$\frac{\partial \rho}{\partial t} = R[\rho, u] + 2\rho \partial_Z u + \frac{\rho}{R}[\psi, v_{\parallel}] + \frac{v_{\parallel}}{R}[\psi, \rho] - \frac{F_0}{R^2}v_{\parallel}\partial_\phi \rho - \frac{F_0}{R^2}\rho \partial_\phi v_{\parallel} + 2\tau_{IC}\partial_Z P$$
$$+ \nabla \cdot (D_\perp \nabla_\perp \rho) + S_\rho \tag{D.50}$$

with $\tau_{IC} = \frac{m_i}{F_0 e \sqrt{\rho_0 \mu_0}(1 + T_i/T_e)}$. (The hypothesis $T_i = T_e$ is made, so $P_i = P_e = P/2$).

So if we neglect the lower order components in the parallel current term, the density equation for electrons to be solved is not much different:

$$\frac{\partial \rho}{\partial t} = R[\rho, u] + 2\rho \partial_Z u + \frac{\rho}{R}[\psi, v_{\parallel}] + \frac{v_{\parallel}}{R}[\psi, \rho] - \frac{F_0}{R^2}v_{\parallel}\partial_\phi \rho - \frac{F_0}{R^2}\rho \partial_\phi v_{\parallel} - 2\tau_{IC}\partial_Z P$$
$$+ \frac{m_i}{e \sqrt{\rho_0 \mu_0}}\left(-\frac{1}{R^2}\frac{\partial j}{\partial \phi} + \frac{1}{F_0 R}[\psi, j] \right) + \nabla \cdot (D_\perp \nabla_\perp \rho) + S_\rho \tag{D.51}$$

Now using the τ_{IC} coefficient:

$$
\begin{aligned}
\frac{\partial \rho}{\partial t} =& R[\rho, u] + 2\rho\partial_Z u + \frac{\rho}{R}[\psi, v_\parallel] + \frac{v_\parallel}{R}[\psi, \rho] - \frac{F_0}{R^2}v_\parallel\partial_\phi\rho - \frac{F_0}{R^2}\rho\partial_\phi v_\parallel - 2\tau_{IC}\partial_Z P \\
&+ 2\tau_{IC}F_0\left(-\frac{1}{R^2}\frac{\partial j}{\partial \phi} + \frac{1}{F_0 R}[\psi, j]\right) + \nabla\cdot(D_\perp\nabla_\perp\rho) + S_\rho
\end{aligned}
\tag{D.52}
$$

D.7 Other modifications in JOREK

In momentum and energy equations, the time derivative terms are split into two parts, one of them containing the time derivative of density: $\frac{d(\rho \boldsymbol{v})}{dt} = \rho\frac{d\boldsymbol{v}}{dt} + \boldsymbol{v}\frac{d\rho}{dt}$ and $\frac{d(\rho T)}{dt} = \rho\frac{dT}{dt} + T\frac{d\rho}{dt}$. However the density equation injected in the equation cancels: $\frac{d\rho}{dt} = 0 = \frac{\partial\rho}{\partial t} + \nabla\cdot\rho\boldsymbol{v}$, and the new $\nabla_\parallel J_\parallel$ term is included in the $\nabla\cdot\rho\boldsymbol{v}$ term, so in this respect no additional term is required in the momentum and energy equations. However, as the addition of the parallel current term in the density equation is equivalent to the addition of corrective velocities in the system of equations, the term $P\nabla\cdot\boldsymbol{v}$ should also include a polarization part $P\nabla\cdot\boldsymbol{v}_{pol}$ and a neoclassical part $P\nabla\cdot\boldsymbol{v}_{\Pi_i}$.

D.8 Additional study: coupling between vorticity and density: introduction of new waves in simulation

In this section, all quantities are normalized to unity for simplicity.

We note that the vorticity and density equations have a similar expression, and both equations involve the parallel current gradient:

$$
\frac{dW}{dt} + \nabla_\parallel J_\parallel = \nu\nabla_\perp^2 W
\tag{D.53}
$$

$$
\frac{dn}{dt} + \nabla_\parallel J_\parallel = D_\perp\nabla_\perp^2 n
\tag{D.54}
$$

We also write the induction equation:

$$
\frac{\partial\psi}{\partial t} = -\eta J + \nabla_\parallel u + T\nabla_\parallel n
\tag{D.55}
$$

Where $\nabla_\parallel u = \nabla_{\parallel,eq}u + [\psi, u]$. We use the expressions of current and vorticity $J = -\nabla_\perp^2\psi$ and $W = \nabla_\perp^2 u$, and we assume that $\nu \sim D_\perp$. In this assumption, n can be replaced by W in the induction equation.

If we neglect all dissipative and diffusive terms, we can find the dispersion relation for Alfven waves (first without diamagnetics) :

$$
\frac{dW}{dt} - \nabla_\parallel\nabla_\perp^2\psi = 0
\tag{D.56}
$$

$$
\frac{\partial\psi}{\partial t} = \nabla_\parallel u
\tag{D.57}
$$

The linearization of the system yields:

$$ik_\perp^2 \omega u + ik_{||} k_\perp^2 \psi = 0 \tag{D.58}$$

$$-\omega\psi = k_{||} u \tag{D.59}$$

$$\Rightarrow k_\perp^2 \left(\omega - \frac{k_{||}^2}{\omega^2}\right) = 0 \tag{D.60}$$

We thus find the Alfven equation (without normalization): $\omega^2 = k_{||}^2 V_A^2$

The addition of diamagnetic effects just adds a correction to the expression:

$$\frac{\partial \psi}{\partial t} = \nabla_{||} u + T \nabla_{||} n \tag{D.61}$$

$$\Rightarrow \omega^2 = k_{||}^2 V_A^2 (1 + C k_\perp^2 \rho_s^2) \tag{D.62}$$

Also, in steady state, without neglecting the viscosity or diffusivity, we find the relation between density and potential:

$$\nabla_{||} J_{||} = D_\perp \nabla_\perp^2 n = \nu \nabla_\perp^2 W \tag{D.63}$$

$$\Rightarrow \frac{\delta n}{n_0} = \frac{\nu}{D_\perp} (k_\perp \rho_s)^2 \frac{e\delta u}{T} \tag{D.64}$$

So the addition of polarization current in the electron density equation should introduce new types of waves (sheared Alfven drift waves?) and might introduce turbulence in simulations.

Symbols, variables and acronyms

Symbols and variables

- Q: amplification factor
- τ_E: energy confinement time

- $\boldsymbol{B}$: magnetic field
- $\boldsymbol{E}$: electric field
- ψ: poloidal magnetic flux
- ψ_N or ψ_{norm}: normalized poloidal magnetic flux, label of the flux surfaces
- F_0: toroidal component of the magnetic field multiplied by the major radius R, assumed to be constant
- q: safety factor characterizing the helicity of the flux surfaces
- q_{95}: safety factor at the edge (for $\psi_N = 95\%$)

- R_0: major radius of the tokamak
- a: minor radius of the tokamak
- R: horizontal coordinate along the major radius
- Z: vertical coordinate
- r: coordinate along the minor radius
- θ: angle in the poloidal direction
- φ: angle in the toroidal direction
- m: poloidal mode number (Fourier harmonic)
- n: toroidal mode number (Fourier harmonic)

- t: time
- n: particle density ; n_e: electron density, n_i: ion density
- ρ: mass density
- T: temperature
- P: scalar pressure
- $\bar{\bar{\Pi}}$: pressure tensor
- $\boldsymbol{v}$: fluid velocity
- $\boldsymbol{v}_{||}$: parallel velocity
- $\boldsymbol{v}^*$: diamagnetic velocity
- $\boldsymbol{v}_E$: electric drift
- c_s: sound speed
- $\boldsymbol{J}$: plasma current
- j: toroidal current
- u: electric potential (scalar)
- $\boldsymbol{A}$: vector potential
- W: toroidal vorticity

- τ_{IC}: diamagnetic parameter: inverse of the normalized ion cyclotron frequency
- η: plasma resistivity
- $\mu_{||}, \mu_\perp$: plasma parallel and perpendicular viscosity

- $\kappa_{||}, \kappa_\perp$: parallel and perpendicular heat diffusivity
- $D_{||}, D_\perp$: parallel and perpendicular particle diffusivity
- $\mu_{i,neo}$: neoclassical friction rate
- k_i: ion neoclassical heat diffusivity
- S_ρ: particle source
- S_T: heat source
- $S_{v_{||}}$: source of parallel velocity

- f: probability distribution function
- ν^*: electron collisionality
- $\lambda_{e,e}$: electron-electron collision mean free path
- $v_{th,s}$: thermal velocity
- τ_e: electron collision time
- λ_d: Debye length

- m_e, m_i: electron and ion mass
- q_e, q_i: electron and ion charge
- e: Coulomb charge
- μ_0: magnetic permeability
- ε_0: vacuum permittivity
- c: light speed
- $\gamma = 5/3$: ratio of the specific heats

Acronyms

- **AUG**: Asdex Upgrade: tokamak located in Garching (Germany)
- **DEMO**: Prototype for future fusion reactors (generation after ITER)
- **DIII-D**: Doublet III – D : tokamak in San Diego (USA)
- **DND**: Double Null Divertor
- **EFCC**: Error Field Correction Coils
- **ELM**: Edge Localized Modes
- **ERGOS**: ERGOdic Spectrum: code computing vacuum magnetic perturbations generated by coils, using Biot-Savart law
- **ETB**: External Transport Barrier
- **HFS**: High Field Side
- **ITER**: International Thermonuclear Experimental Reactor, also meaning "the way": tokamak currently in construction in Cadarache, France
- **JET**: Joint European Torus: European tokamak, located in Culham (UK)
- **JOREK**: reduced MHD code in toroidal geometry, named after the bear in Philip Pullman's *His Dark Materials*
- **LFS**: Low Field Side
- **MAST**: Mega Ampere Spherical Tokamak, located in Culham (UK)
- **MHD**: Magnetohydrodynamics
- **NTV**: Neoclassical Toroidal Viscosity
- **RFA**: Resonant Field Amplification
- **RMHD**: Reduced MagnetoHydroDynamic code in cylindrical geometry
- **RMP**: Resonant Magnetic Perturbation
- **SOL**: Scrape-Off Layer

Bibliography

[Andrew 2008] Y. Andrew, N. C. Hawkes, T. Biewer, K. Crombe, D. Keeling, E. De La Luna, C. Giroud, A. Korotkov, A. Meigs, A. Murari, I. Nunes, R. Sartori, T. Tala and JET-EFDA Contributors. *Evolution of the radial electric field in a JET H-mode plasma*. EPL, vol. 83, no. 1, 2008.

[Baylor 2009] L.R. Baylor, S.K. Combs, C.R. Foust, T.C. Jernigan, S.J. Meitner, P.B. Parks, J.B. Caughman, D.T. Fehling, S. Maruyama, A.L. Qualls, D.A. Rasmussen and C.E. Thomas. *Pellet fuelling, ELM pacing and disruption mitigation technology development for ITER*. Nuclear Fusion, vol. 49, no. 8, page 085013, 2009.

[Bécoulet 2003] M Bécoulet, G Huysmans, Y Sarazin, X Garbet, Ph Ghendrih, F Rimini, E Joffrin, X Litaudon, P Monier-Garbet, J-M Ané, P Thomas, A Grosman, V Parail, H Wilson, P Lomas, P deVries, K-D Zastrow, G F Matthews, J Lonnroth, S Gerasimov, S Sharapov, M Gryaznevich, G Counsell, A Kirk, M Valovic, R Buttery, A Loarte, G Saibene, R Sartori, A Leonard, P Snyder, L L Lao, P Gohil, T E Evans, R A Moyer, Y Kamada, A Chankin, N Oyama, T Hatae, N Asakura, O Tudisco, E Giovannozzi, F Crisanti, C P Perez, H R Koslowski, T Eich, A Sips, L Horton, A Hermann, P Lang, J Stober, W Suttrop, P Beyer, S Saarelma and Contributors to JET-EFDA Workprogramme. *Edge localized mode physics and operational aspects in tokamaks*. Plasma Physics and Controlled Fusion, vol. 45, no. 12A, page A93, 2003.

[Bécoulet 2008] M. Bécoulet, E. Nardon, G. Huysmans, W. Zwingmann, P. Thomas, M. Lipa, R. Moyer, T. Evans, V. Chuyanov, Y. Gribov, A. Polevoi, G. Vayakis, G. Federici, G. Saibene, A. Portone, A. Loarte, C. Doebert, C. Gimblett, J. Hastie and V. Parail. *Numerical study of the resonant magnetic perturbations for Type I edge localized modes control in ITER*. Nuclear Fusion, vol. 48, no. 2, page 024003, 2008.

[Becoulet 2009] M. Becoulet, G. Huysmans, X. Garbet, E. Nardon, D. Howell, A. Garofalo, M. Schaffer, T. Evans, K. Shaing, A. Cole, J. K. Park and P. Cahyna. *Physics of penetration of resonant magnetic perturbations used for Type I edge localized modes suppression in tokamaks*. Nuclear Fusion, vol. 49, no. 8, AUG 2009.

[Bécoulet 2012] M. Bécoulet, F. Orain, P. Maget, N. Mellet, X. Garbet, E. Nardon, G. T. A. Huysmans, T. Casper, A. Loarte, P. Cahyna, A. Smolyakov, F. L. Waelbroeck, M. Schaffer, T. Evans, Y. Liang, O. Schmitz, M. Beurskens, V. Rozhansky and E. Kaveeva. *Screening of resonant magnetic perturbations by flows in tokamaks*. Nuc. Fus., vol. 52, no. 5, May 2012. 5th International Workshop on Stochasticity in Fusion Plasmas (SFP), Julich, Germany, Apr 11-14, 2011.

[Biskamp 1997] Dieter Biskamp. *Nonlinear magnetohydrodynamics*, volume 1. Cambridge University Press, 1997.

[Braginskii 1965] S.I. Braginskii. *Transport processes in a plasma.* Reviews of Plasma Physics, vol. 1, page 205, 1965.

[Cahyna 2011] P. Cahyna, E. Nardon and JET EFDA contributors. *Model for screening of resonant magnetic perturbations by plasma in a realistic tokamak geometry and its impact on divertor strike points.* Journal of Nuclear Materials, vol. 415, no. 1, Supplement, pages S927–S931, 2011.

[Cahyna 2013a] P. Cahyna, Y.Q. Liu, E. Nardon, A. Kirk, M. Peterka, J.R. Harrison, A. Thornton, I. Chapman, R. Panek, O. Schmitz and the MAST team. *Modelling of plasma response to resonant magnetic perturbations and its influence on divertor strike points.* In IAEA Fusion Energy Conference 2012 (Proc. 24th IAEA FEC San Diego, 2012), pages TH/P4–27, (Vienna: IAEA), 2013.

[Cahyna 2013b] P. Cahyna, M. Peterka, A. Kirk, A. Thornton, J. Harrison, D. Muir and R. Panek. *Strike point splitting induced by the application of magnetic perturbations on MAST.* Journal of Nuclear Materials, 2013.

[Canik 2010] J.M. Canik, R. Maingi, T.E. Evans, R.E. Bell, S.P. Gerhardt, H.W. Kugel, B.P. LeBlanc, J. Manickam, J.E. Menard, T.H. Osborne, J.-K. Park, S. Paul, P.B. Snyder, S.A. Sabbagh, E.A. Unterberg and the NSTX team. *ELM destabilization by externally applied non-axisymmetric magnetic perturbations in NSTX.* Nuclear Fusion, vol. 50, no. 3, page 034012, 2010.

[CEA] *http://www-fusion-magnetique.cea.fr/gb/.*

[Chang 1992] Z. Chang and J.D. Callen. *Unified fluid/kinetic description of plasma microinstabilities. Part I: Basic equations in a sheared slab geometry.* Physics of Fluids B: Plasma Physics (1989-1993), vol. 4, no. 5, pages 1167–1181, 1992.

[Chapman 2012] I. T. Chapman, A. Kirk, S. Saarelma, J. R. Harrison, R. Scannell and MAST Team. *Towards understanding ELM mitigation: the effect of axisymmetric lobe structures near the X-point on ELM stability.* Nuclear Fusion, vol. 52, no. 12, DEC 2012.

[Classen 2013] I.G.J. Classen, J.E. Boom, A.V. Bogomolov, E. Wolfrum, M. Maraschek, W. Suttrop, P.C. de Vries, A.J.H. Donné, B.J. Tobias, C.W. Domier, N.C. Luhmann and the ASDEX Upgrade Team. *The role of temperature fluctuations in the dynamics of type-I and type-II edge localized modes at ASDEX Upgrade.* Nuclear Fusion, vol. 53, no. 7, page 073005, 2013.

[Cole 2008] A. J. Cole, C. C. Hegna and J. D. Callen. *Neoclassical toroidal viscosity and error-field penetration in tokamaks.* Physics of Plasmas, vol. 15, no. 5, page 056102, 2008.

[Connor 1978] J. W. Connor, R. J. Hastie and J. B. Taylor. *Shear, Periodicity, and Plasma Ballooning Modes.* Phys. Rev. Lett., vol. 40, pages 396–399, Feb 1978.

[Connor 1998] J W Connor. *Edge-localized modes - physics and theory.* Plasma Physics and Controlled Fusion, vol. 40, no. 5, page 531, 1998.

[Czarny 2008] Olivier Czarny and Guido Huysmans. *Bézier surfaces and finite elements for MHD simulations.* Journal of computational physics, vol. 227, no. 16, pages 7423–7445, 2008.

[De la Luna 2009] E. De la Luna. *ELM mitigation studies in JET and implications for ITER.* 51st APS conference, Georgia, Atlanta, 2009.

[Degeling 2003] A W Degeling, Y R Martin, J B Lister, L Villard, V N Dokouka, V E Lukash and R R Khayrutdinov. *Magnetic triggering of ELMs in TCV.* Plasma Physics and Controlled Fusion, vol. 45, no. 9, page 1637, 2003.

[Diamond 1985] P. H. Diamond, P. L. Similon, T. C. Hender and B. A. Carreras. *Kinetic theory of resistive ballooning modes.* Physics of Fluids (1958-1988), vol. 28, no. 4, pages 1116–1125, 1985.

[Drake 1983] J. F. Drake, T. M. Antonsen, A. B. Hassam and N. T. Gladd. *Stabilization of the tearing mode in high-temperature plasma.* Physics of Fluids (1958-1988), vol. 26, no. 9, pages 2509–2528, 1983.

[Dunai 2014] D. Dunai, A. Kirk, S. Saarelma, S. Zoletnik, M. Lampert, A. R. Field, J. C. Hillesheim, C. M. Roach and Y. U. Nam. *Measurements of type I ELM triggering mechanism in MAST and KSTAR.* proceeding of the 41st EPS conference, Berlin, 2014.

[Eich 2003] T. Eich, A. Herrmann and J. Neuhauser. *Nonaxisymmetric Energy Deposition Pattern on ASDEX Upgrade Divertor Target Plates during Type-I Edge-Localized Modes.* Phys. Rev. Lett., vol. 91, page 195003, Nov 2003.

[Evans 2004a] T. E. Evans, R. A. Moyer, P. R. Thomas, J. G. Watkins, T. H. Osborne, J. A. Boedo, E. J. Doyle, M. E. Fenstermacher, K. H. Finken, R. J. Groebner, M. Groth, J. H. Harris, R. J. La Haye, C. J. Lasnier, S. Masuzaki, N. Ohyabu, D. G. Pretty, T. L. Rhodes, H. Reimerdes, D. L. Rudakov, M. J. Schaffer, G. Wang and L. Zeng. *Suppression of Large Edge-Localized Modes in High-Confinement DIII-D Plasmas with a Stochastic Magnetic Boundary.* Phys. Rev. Lett., vol. 92, page 235003, Jun 2004.

[Evans 2004b] T. E. Evans, R. K. W. Roeder, J. A. Carter and B. I. Rapoport. *Homoclinic tangles, bifurcations and edge stochasticity in diverted tokamaks.* Contributions to Plasma Physics, vol. 44, no. 1-3, pages 235–240, 2004.

[Evans 2005] T E Evans, R K W Roeder, J A Carter, B I Rapoport, M E Fenstermacher and C J Lasnier. *Experimental signatures of homoclinic tangles in poloidally diverted tokamaks.* Journal of Physics: Conference Series, vol. 7, pages 174–190, 2005.

[Evans 2007] T.E. Evans, I. Joseph, R.A. Moyer, M.E. Fenstermacher, C.J. Lasnier and L.W. Yan. *Experimental and numerical studies of separatrix splitting and magnetic footprints in DIII-D*. Journal of Nuclear Materials, vol. 363-365, pages 570 – 574, 2007. Plasma-Surface Interactions-17.

[Evans 2008] T.E. Evans, M.E. Fenstermacher, R.A. Moyer, T.H. Osborne, J.G. Watkins, P. Gohil, I. Joseph, M.J. Schaffer, L.R. Baylor, M. Bécoulet, J.A. Boedo, K.H. Burrell, J.S. deGrassie, K.H. Finken, T. Jernigan, M.W. Jakubowski, C.J. Lasnier, M. Lehnen, A.W. Leonard, J. Lonnroth, E. Nardon, V. Parail, O. Schmitz, B. Unterberg and W.P. West. *RMP ELM suppression in DIII-D plasmas with ITER similar shapes and collisionalities*. Nuclear Fusion, vol. 48, no. 2, page 024002, 2008.

[Fenstermacher 2008] M. E. Fenstermacher, T. E. Evans, T. H. Osborne, M. J. Schaffer, M. P. Aldan, J. S. deGrassie, P. Gohil, I. Joseph, R. A. Moyer, P. B. Snyder, R. J. Groebner, M. Jakubowski, A. W. Leonard, O. Schmitz and DIII-D Team. *Effect of island overlap on edge localized mode suppression by resonant magnetic perturbations in DIII-D*. Physics of Plasmas, vol. 15, no. 5, May 2008.

[Fenstermacher 2010] M.E. Fenstermacher, M. Becoulet, P. Cahyna, J. Canik, C.S. Chang, T.E. Evans, A. Kirk, A. Loarte, Y. Liang, R. Maingi, O. Schmitz, W. Suttrop and H. Wilson. *ELM Control by Resonant Magnetic Perturbations: Overview of Research by the ITPA Pedestal and Edge Physics Group*. 23rd IAEA Fusion Energy Conference, Daejeon, Republic of Korea, 2010.

[Ferraro 2012] N. M. Ferraro. *Calculations of two-fluid linear response to non-axisymmetric fields in tokamaks*. Physics of Plasmas, vol. 19, no. 5, page 056105, 2012.

[Fitzpatrick 1998] R Fitzpatrick. *Bifurcated states of a rotating tokamak plasma in the presence of a static error-field*. Physics of Plasmas, vol. 5, no. 9, pages 3325–3341, 1998.

[Frank 2014] E. Frank, M. Hölzl and E. Sonnendrücker. *Theoretical and numerical stability for the reduced MHD models in the JOREK code*. Internal Communication, 2014.

[Freidberg 1982] J P Freidberg. *Ideal magnetohydrodynamic theory of magnetic fusion systems*. Rev. Mod. Phys., vol. 54, pages 801–902, 1982.

[Frerichs 2012] H. Frerichs, D. Reiter, O. Schmitz, P. Cahyna, T. E. Evans, Y. Feng and E. Nardon. *Impact of screening of resonant magnetic perturbations in three dimensional edge plasma transport simulations for DIII-D*. Physics of Plasmas, vol. 19, no. 5, page 052507, 2012.

[Gerhardt 2010] S.P. Gerhardt, J-W. Ahn, J.M. Canik, R. Maingi, R. Bell, D. Gates, R. Goldston, R. Hawryluk, B.P. Le Blanc, J. Menard, A.C. Sontag, S. Sabbagh

and K. Tritz. *First observation of ELM pacing with vertical jogs in a spherical torus.* Nuclear Fusion, vol. 50, no. 6, page 064015, 2010.

[Ghendrih 1996] Ph Ghendrih, A Grosman and H Capes. *Theoretical and experimental investigations of stochastic boundaries in tokamaks.* Plasma Physics and Controlled Fusion, vol. 38, no. 10, page 1653, 1996.

[Gianakon 2002] TA Gianakon, SE Kruger and CC Hegna. *Heuristic closures for numerical simulations of neoclassical tearing modes.* Physics of Plasmas, vol. 9, no. 2, pages 536–547, 2002.

[Goedbloed 2004] Johan Peter Goedbloed and Stefaan Poedts. Principles of magnetohydrodynamics: with applications to laboratory and astrophysical plasmas. Cambridge university press, 2004.

[Gohil 1988] P. Gohil, M. Ali Mahdavi, L. Lao, K. H. Burrell, M. S. Chu, J. C. DeBoo, C. L. Hsieh, N. Ohyabu, R. T. Snider, R. D. Stambaugh and R. E. Stockdale. *Study of Giant Edge-Localized Modes in DIII-D and Comparison with Ballooning Theory.* Phys. Rev. Lett., vol. 61, pages 1603–1606, Oct 1988.

[Grosman 2003] A. Grosman, J.-M. Ané, P. Barabaschi, K.H. Finken, A. Mahdavi, Ph. Ghendrih, G. Huysmans, M. Lipa, P.R. Thomas and E. Tsitrone. *H-mode barrier control with external magnetic perturbations.* Journal of Nuclear Materials, vol. 313–316, no. 0, pages 1314 – 1320, 2003. Plasma-Surface Interactions in Controlled Fusion Devices 15.

[Guckenheimer 1983] John Guckenheimer and Philip Holmes. Nonlinear oscillations, dynamical systems, and bifurcations of vector fields, volume 42. New York Springer Verlag, 1983.

[Halpern 2011] Federico D. Halpern, Hinrich Lütjens and Jean-François Luciani. *Diamagnetic thresholds for sawtooth cycling in tokamak plasmas.* Physics of Plasmas (1994-present), vol. 18, no. 10, pages –, 2011.

[Hawryluk 2009] R.J. Hawryluk, D.J. Campbell, G. Janeschitz, P.R. Thomas, R. Albanese, R. Ambrosino, C. Bachmann, L. Baylor, M. Bécoulet, I. Benfatto, J. Bialek, A. Boozer, A. Brooks, R. Budny, T. Casper, M. Cavinato, J.-J. Cordier, V. Chuyanov, E. Doyle, T. Evans, G. Federici, M. Fenstermacher, H. Fujieda, K. G'al, A. Garofalo, L. Garzotti, D. Gates, Y. Gribov, P. Heitzenroeder, T.C. Hender, N. Holtkamp, D. Humphreys, I. Hutchinson, K. Ioki, J. Johner, G. Johnson, Y. Kamada, A. Kavin, C. Kessel, R. Khayrutdinov, G. Kramer, A. Kukushkin, K. Lackner, I. Landman, P. Lang, Y. Liang, J. Linke, B. Lipschultz, A. Loarte, G.D. Loesser, C. Lowry, T. Luce, V. Lukash, S. Maruyama, M. Mattei, J. Menard, M. Merola, A. Mineev, N. Mitchell, E. Nardon, R. Nazikian, B. Nelson, C. Neumeyer, J.-K. Park, R. Pearce, R.A. Pitts, A. Polevoi, A. Portone, M. Okabayashi, P.H. Rebut, V. Riccardo, J. Roth, S. Sabbagh, G. Saibene,

G. Sannazzaro, M. Schaffer, M. Shimada, A. Sen, A. Sips, C.H. Skinner, P. Snyder, R. Stambaugh, E. Strait, M. Sugihara, E. Tsitrone, J. Urano, M. Valovic, M. Wade, J. Wesley, R. White, D.G. Whyte, S. Wu, M. Wykes and L. Zakharov. *Principal physics developments evaluated in the ITER design review.* Nuclear Fusion, vol. 49, no. 6, page 065012, 2009.

[Hazeltine 1985a] R. D. Hazeltine, M. Kotschenreuther and P. J. Morrison. *A four-field model for tokamak plasma dynamics.* Physics of Fluids, vol. 28, no. 8, pages 2466–2477, 1985.

[Hazeltine 1985b] R.D. Hazeltine and J.D. Meiss. *Shear-Alfvén dynamics of toroidally confined plasmas.* Physics Reports, vol. 121, no. 1, pages 1–164, 1985.

[Hénon 2002] Pascal Hénon, Pierre Ramet and Jean Roman. *PASTIX: a high-performance parallel direct solver for sparse symmetric positive definite systems.* Parallel Computing, vol. 28, no. 2, pages 301–321, 2002.

[Heyn 2008] Martin F. Heyn, Ivan B. Ivanov, Sergei V. Kasilov, Winfried Kernbichler, Ilon Joseph, Richard A. Moyer and Alexey M. Runov. *Kinetic estimate of the shielding of resonant magnetic field perturbations by the plasma in DIII-D.* Nuclear Fusion, vol. 48, no. 2, page 024005, 2008.

[Hölzl 2012] M Hölzl, P Merkel, GTA Huysmans, E Nardon, E Strumberger, R McAdams, I Chapman, S Günter and K Lackner. *Coupling JOREK and STAR-WALL Codes for Non-linear Resistive-wall Simulations.* In Journal of Physics: Conference Series, volume 401, page 012010, 2012.

[Hsu 1986] C.T. Hsu, R.D. Hazeltine and P.J. Morrison. *A generalized reduced fluid model with finite ion-gyroradius effects.* Physics of Fluids (1958-1988), vol. 29, no. 5, pages 1480–1487, 1986.

[Huysmans 2001] G. T. A. Huysmans, S. E. Sharapov, A. B. Mikhailovskii and W. Kerner. *Modeling of diamagnetic stabilization of ideal magnetohydrodynamic instabilities associated with the transport barrier.* Physics of Plasmas (1994-present), vol. 8, no. 10, pages 4292–4305, 2001.

[Huysmans 2007] G.T.A. Huysmans and O. Czarny. *MHD stability in X-point geometry: simulation of ELMs.* Nuclear Fusion, vol. 47, no. 7, page 659, 2007.

[Huysmans 2009] G T A Huysmans, S Pamela, E van der Plas and P Ramet. *Non-linear MHD simulations of edge localized modes (ELMs).* Plasma Physics and Controlled Fusion, vol. 51, no. 12, page 124012, 2009.

[ITER 1999] Physics Basis Editors ITER. *ITER Physics Basis.* Nuclear Fusion, vol. 39, no. 12, page 2137, 1999.

[Izzo 2008] V. A. Izzo and I. Joseph. *RMP enhanced transport and rotational screening in simulations of DIII-D plasmas.* Nuclear Fusion, vol. 48, no. 11, NOV 2008.

[Jakubowski 2009] M.W. Jakubowski, T.E. Evans, M.E. Fenstermacher, M. Groth, C.J. Lasnier, A.W. Leonard, O. Schmitz, J.G. Watkins, T. Eich, W. Fundamenski, R.A. Moyer, R.C. Wolf, L.B. Baylor, J.A. Boedo, K.H. Burrell, H. Frerichs, J.S. deGrassie, P. Gohil, I. Joseph, S. Mordijck, M. Lehnen, C.C. Petty, R.I. Pinsker, D. Reiter, T.L. Rhodes, U. Samm, M.J. Schaffer, P.B. Snyder, H. Stoschus, T. Osborne, B. Unterberg, E. Unterberg and W.P. West. *Overview of the results on divertor heat loads in RMP controlled H-mode plasmas on DIII-D*. Nuclear Fusion, vol. 49, no. 9, page 095013, 2009.

[Jeon 2012] Y. M. Jeon, J.-K. Park, S. W. Yoon, W. H. Ko, S. G. Lee, K. D. Lee, G. S. Yun, Y. U. Nam, W. C. Kim, Jong-Gu Kwak, K. S. Lee, H. K. Kim and H. L. Yang. *Suppression of Edge Localized Modes in High-Confinement KSTAR Plasmas by Nonaxisymmetric Magnetic Perturbations*. Phys. Rev. Lett., vol. 109, page 035004, Jul 2012.

[Joseph 2008] I. Joseph, T.E. Evans, A.M. Runov, M.E. Fenstermacher, M. Groth, S.V. Kasilov, C.J. Lasnier, R.A. Moyer, G.D. Porter, M.J. Schaffer, R. Schneider and J.G. Watkins. *Calculation of stochastic thermal transport due to resonant magnetic perturbations in DIII-D*. Nuclear Fusion, vol. 48, no. 4, page 045009, 2008.

[Kamiya 2007] K Kamiya, N Asakura, J Boedo, T Eich, G Federici, M Fenstermacher, K Finken, A Herrmann, J Terry, A kirk, B Koch, A Loarte, R Maingi, R Maqueda, E Nardon, N Oyama and R Sartori. *Edge localized modes: recent experimental findings and related issues*. Plasma Physics and Controlled Fusion, vol. 49, no. 7, page S43, 2007.

[Keilhacker 1999] M. Keilhacker, A. Gibson, C. Gormezano, P.J. Lomas, P.R. Thomas, M.L. Watkins, P. Andrew, B. Balet, D. Borba, C.D. Challis, I. Coffey, G.A. Cottrell, H.P.L. De Esch, N. Deliyanakis, A. Fasoli, C.W. Gowers, H.Y. Guo, G.T.A. Huysmans, T.T.C. Jones, W. Kerner, R.W.T. König, M.J. Loughlin, A. Maas, F.B. Marcus, M.F.F. Nave, F.G. Rimini, G.J. Sadler, S.E. Sharapov, G. Sips, P. Smeulders, F.X. Söldner, A. Taroni, B.J.D. Tubbing, M.G. von Hellermann, D.J. Ward and JET Team. *High fusion performance from deuterium-tritium plasmas in JET*. Nuclear Fusion, vol. 39, no. 2, page 209, 1999.

[Kessel 1994] C.E. Kessel. *Bootstrap current in a tokamak*. Nuclear Fusion, vol. 34, no. 9, page 1221, 1994.

[Kirk 2004] A. Kirk, H. R. Wilson, G. F. Counsell, R. Akers, E. Arends, S. C. Cowley, J. Dowling, B. Lloyd, M. Price and M. Walsh. *Spatial and Temporal Structure of Edge-Localized Modes*. Phys. Rev. Lett., vol. 92, page 245002, Jun 2004.

[Kirk 2006] A. Kirk, B. Koch, R. Scannell, H. R. Wilson, G. Counsell, J. Dowling, A. Herrmann, R. Martin and M. Walsh. *Evolution of Filament Structures during Edge-Localized Modes in the MAST Tokamak*. Phys. Rev. Lett., vol. 96, page 185001, May 2006.

[Kirk 2010] A. Kirk, E. Nardon, R. Akers, M. Bécoulet, G. De Temmerman, B. Dudson, B. Hnat, Y.Q. Liu, R. Martin, P. Tamain, D. Taylor and the MAST team. *Resonant magnetic perturbation experiments on MAST using external and internal coils for ELM control.* Nuclear Fusion, vol. 50, no. 3, page 034008, 2010.

[Kirk 2011] A. Kirk, Yueqiang Liu, E. Nardon, P. Tamain, P. Cahyna, I. Chapman, P. Denner, H. Meyer, S. Mordijck, D. Temple and MAST Team. *Magnetic perturbation experiments on MAST L-and H-mode plasmas using internal coils.* Plasma Physics and Controlled Fusion, vol. 53, no. 6, JUN 2011.

[Kirk 2012] A. Kirk, J. Harrison, Yueqiang Liu, E. Nardon, I. T. Chapman and P. Denner. *Observation of Lobes near the X Point in Resonant Magnetic Perturbation Experiments on MAST.* Phys. Rev. Lett., vol. 108, page 255003, Jun 2012.

[Kirk 2013a] A. Kirk, I. T. Chapman, J. Harrison, Yueqiang Liu, E. Nardon, S. Saarelma, R. Scannell, A. J. Thornton and MAST Team. *Effect of resonant magnetic perturbations with toroidal mode numbers of 4 and 6 on edge-localized modes in single null H-mode plasmas in MAST.* Plasma Physics and Controlled Fusion, vol. 55, no. 1, page 015006, JAN 2013.

[Kirk 2013b] A Kirk, D Dunai, M Dunne, G Huijsmans, S Pamela, M Becoulet, J R Harrison, J Hillesheim, C Roach and S Saarelma. *Current understanding of the processes underlying the triggering of and energy loss associated with type I ELMs.* no. arXiv:1312.4300, Dec 2013.

[Kirk 2014] A. Kirk. *Effect of resonant magnetic perturbations on low collisionality discharges in MAST and a comparison with ASDEX Upgrade.* 25th IAEA Fusion Energy Conference, St Petersburg, Russia (to be presented), 2014.

[Lang 2007] P.T. Lang, B. Alper, R. Buttery, K. Gal, J. Hobirk, J. Neuhauser, M. Stamp and JET-EFDA contributors. *ELM triggering by local pellet perturbations in type-I ELMy H-mode plasma at JET.* Nuclear Fusion, vol. 47, no. 8, page 754, 2007.

[Liang 2007a] Y. Liang, H. R. Koslowski, P. R. Thomas, E. Nardon, B. Alper, P. Andrew, Y. Andrew, G. Arnoux, Y. Baranov, M. Becoulet, M. Beurskens, T. Biewer, M. Bigi, Kristel Crombé, E. De La Luna, P. de Vries, W. Fundamenski, S. Gerasimov, C. Giroud, M. P. Gryaznevich, N. Hawkes, S. Hotchin, D. Howell, S. Jachmich, V. Kiptily, L. Moreira, V. Parail, S. D. Pinches, E. Rachlew and O. Zimmermann. *Active control of type-I edge-localized modes with n=1 perturbation fields in the JET tokamak.* Phys. Rev. Lett., vol. 98, no. 26, pages 265004–1–265004–5, 2007.

[Liang 2007b] Y Liang, H R Koslowski, P R Thomas, E Nardon, S Jachmich, B Alper, P Andrew, Y Andrew, G Arnoux, Y Baranov, M Bécoulet, M Beurskens, T Biewer, M Bigi, K Crombe, E De La Luna, P de Vries, T Eich, H G Esser, W Fundamenski, S Gerasimov, C Giroud, M P Gryaznevich, D Harting,

N Hawkes, S Hotchin, D Howell, A Huber, M Jakubowski, V Kiptily, A Kreter, L Moreira, V Parail, S D Pinches, E Rachlew, O Schmitz, O Zimmermann and JET-EFDA Contributors. *Active control of type-I edge localized modes on JET.* Plasma Physics and Controlled Fusion, vol. 49, no. 12B, page B581, 2007.

[Liang 2012] Y. Liang, P. Lomas, I. Nunes, M. Gryaznevich, M. N. A. Beurskens, S. Brezinsek, J. Coenen, P. Denner, T. Eich, L. Frassinetti, S. Gerasimov, D. Harting, S. Jachmich, A. Meigs, J. Pearson, M. Rack, S. Saarelma, B. Sieglin, Y. Yang and L. Zeng. *Mitigation of Type–I ELMs with $n = 2$ Fields on JET.* Proceedings of the 24th IAEA Fusion Energy Conference, San Diego, USA, 2012.

[Lieberman 1983] M Lieberman and A Lichtenberg. *Regular and stochastic motion.* Applied Mathematical Sciences, vol. 38, 1983.

[Linke 2007] J. Linke, H. Bolt, R. Duwe, W. Kühnlein, A. Lodato, M. Rödig, K. Schöpflin and B. Wiechers. Proc. of the 13th Int. Conf. on Fusion Reactor Materials, Nice, 2007.

[Liu 2010a] Yueqiang Liu, M. S. Chu, Y. In and M. Okabayashi. *Resonant field amplification with feedback-stabilized regime in Current driven resistive wall mode.* Physics of Plasmas, vol. 17, no. 7, 2010.

[Liu 2010b] Yueqiang Liu, A. Kirk and E. Nardon. *Full toroidal plasma response to externally applied nonaxisymmetric magnetic fields.* Physics of Plasmas, vol. 17, no. 12, page 122502, 2010.

[Liu 2012] Y Q Liu, A Kirk, Y Sun, P Cahyna, I T Chapman, P Denner, G Fishpool, A M Garofalo, J R Harrison, E Nardon and the MAST team. *Toroidal modeling of plasma response and resonant magnetic perturbation field penetration.* Plasma Physics and Controlled Fusion, vol. 54, no. 12, page 124013, 2012.

[Loarte 2002] A Loarte, M Becoulet, G Saibene, R Sartori, D J Campbell, T Eich, A Herrmann, M Laux, W Suttrop, B Alper, P J Lomas, G Matthews, S Jachmich, J Ongena, P Innocente and EFDA-JET Workprogramme Collaborators. *Characteristics and scaling of energy and particle losses during Type I ELMs in JET H-modes.* Plasma Physics and Controlled Fusion, vol. 44, no. 9, page 1815, 2002.

[Loarte 2003] A Loarte, G Saibene, R Sartori, D Campbell, M Becoulet, L Horton, T Eich, A Herrmann, G Matthews, N Asakura, A Chankin, A Leonard, G Porter, G Federici, G Janeschitz, M Shimada and M Sugihara. *Characteristics of type I ELM energy and particle losses in existing devices and their extrapolation to ITER.* Plasma Physics and Controlled Fusion, vol. 45, no. 9, page 1549, 2003.

[Lucas 2000] LL Lucas and MP Unterweger. *Comprehensive review and critical evaluation of the half-life of Tritium.* Journal of research-National institute of standards and technology, vol. 105, no. 4, pages 541–550, 2000.

[Morales 2014] J.A. Morales, M. Bécoulet, F. Orain, X. Garbet, G. Dif-Pradalier, C. Passeron and G.T.A. Huysmans. *Rotation of Edge Localized Modes and their Filaments.* proceeding of the 41st EPS conference, Berlin, 2014.

[Moyer 2005] RA Moyer, TE Evans, TH Osborne, PR Thomas, M Bécoulet, J Harris, KH Finken, JA Boedo, EJ Doyle, ME Fenstermacher, P Gohil, RJ Groebner, M Groth, GL Jackson, RJ La Haye, CJ Lasnier, AW Leonard, GR McKee, H Reimerdes, TL Rhodes, DL Rudakov, MJ Schaffer, PB Snyder, MR Wade, G Wang, JG Watkins, WP West and L Zeng. *Edge localized mode control with an edge resonant magnetic perturbation.* Physics of Plasmas, vol. 12, no. 5, MAY 2005.

[Nardon 2007] E. Nardon. *Edge Localized modes control by resonant magnetic perturbations.* PhD Thesis, Ecole Polytechnique, 2007.

[Nardon 2010] E. Nardon, P. Tamain, M. Bécoulet, G. Huysmans and F.L. Waelbroeck. *Quasi-linear MHD modelling of H-mode plasma response to resonant magnetic perturbations.* Nuclear Fusion, vol. 50, no. 3, page 034002, NOV 2010.

[Nardon 2011] E. Nardon, P. Cahyna, S. Devaux, A. Kirk, A. Alfier, E. De La Luna, G. de Temmerman, P. Denner, T. Eich, T. Gerbaud, D. Harting, S. Jachmich, H.R. Koslowski, Y. Liang and Y. Sun. *Strike-point splitting induced by external magnetic perturbations: observations on JET and MAST and associated modelling.* Journal of Nuclear Materials, vol. 415, no. 1, Supplement, pages S914–S917, 2011.

[Nishimura 2012] S. Nishimura, S. Toda, M. Yagi and Y. Narushima. *Nonlinear stability of magnetic islands in a rotating helical plasma.* Physics of Plasmas, vol. 19, no. 12, DEC 2012.

[Orain 2012] F. Orain, M. Bécoulet, G. T. A. Huysmans, G. Dif-Pradalier, V. Grandgirard, G. Latu, P. Maget, N. Mellet, E. Nardon, C. Passeron and A. Ratnani. *Interaction of Resonant Magnetic Perturbations with flows in toroidal geometry.* 2012. 39th European Physical Society Conference on Plasma Physics and 16th International Congress on Plasma Physics Stockholm, Sweden, 2-6 July 2012.

[Orain 2013] F. Orain, M. Bécoulet, G. Dif-Pradalier, G. Huijsmans, S. Pamela, E. Nardon, C. Passeron, G. Latu, V. Grandgirard, A. Fil, A. Ratnani, I. Chapman, A. Kirk, A. Thornton, M. Hoelzl and P. Cahyna. *Non-linear magnetohydrodynamic modeling of plasma response to resonant magnetic perturbations.* Physics of Plasmas, vol. 20, no. 10, 2013.

[Osborne 2005] T. H. Osborne and et al. Proceedings of the 32nd EPS Conference on Plasma Physics, Mulhouse, vol. 32, page p. 4.012, 2005.

[Pamela 2013] S.J.P. Pamela, G.T.A. Huijsmans, A. Kirk, I.T. Chapman, J.R. Harrison, R. Scannell, A.J. Thornton, M. Becoulet and F. Orain. *Resistive MHD simulation*

of edge-localized-modes for double-null discharges in the MAST device. Plasma Physics and Controlled Fusion, vol. 55, page 095001 (13 pp.), Sept. 2013.

[Park 2009] Jong-kyu Park, Allen H. Boozer and Jonathan E. Menard. *Nonambipolar Transport by Trapped Particles in Tokamaks.* Phys. Rev. Lett., vol. 102, page 065002, Feb 2009.

[Perez von Thun 2004] Christian Pedro Perez von Thun. *MHD analysis of edge instabilities in the JET tokamak.* 2004.

[Pégourié 2007] B Pégourié. *Review: Pellet injection experiments and modelling.* Plasma Physics and Controlled Fusion, vol. 49, no. 8, page R87, 2007.

[Pitts 2007] R.A. Pitts, P. Andrew, G. Arnoux, T. Eich, W. Fundamenski, A. Huber, C. Silva, D. Tskhakaya and JET EFDA Contributors. *ELM transport in the JET scrape-off layer.* Nuclear Fusion, vol. 47, no. 11, page 1437, 2007.

[Rogers 1999] B. N. Rogers and J. F. Drake. *Diamagnetic stabilization of ideal ballooning modes in the edge pedestal.* Physics of Plasmas (1994-present), vol. 6, no. 7, pages 2797–2801, 1999.

[Saad 1986] Y. Saad and M. Schultz. *GMRES: A Generalized Minimal Residual Algorithm for Solving Nonsymmetric Linear Systems.* SIAM Journal on Scientific and Statistical Computing, vol. 7, no. 3, pages 856–869, 1986.

[Sarazin 2010] Y. Sarazin, V. Grandgirard, J. Abiteboul, S. Allfrey, X. Garbet, Ph. Ghendrih, G. Latu, A. Strugarek and G. Dif-Pradalier. *Large scale dynamics in flux driven gyrokinetic turbulence.* Nuclear Fusion, vol. 50, no. 5, SI, MAY 2010. 4th IAEA Technical Meeting on the Theory of Plasma Instabilities, Kyoto, JAPAN, MAY 18-20, 2009.

[Sartori 2004] R Sartori, G Saibene, L D Horton, M Becoulet, R Budny, D Borba, A Chankin, G D Conway, G Cordey, D McDonald, K Guenther, M G von Hellermann, Yu Igithkanov, A Loarte, P J Lomas, O Pogutse and J Rapp. *Study of Type III ELMs in JET.* Plasma Physics and Controlled Fusion, vol. 46, no. 5, page 723, 2004.

[Schaffer 2008] M.J. Schaffer, J.E. Menard, M.P. Aldan, J.M. Bialek, T.E. Evans and R.A. Moyer. *Study of in-vessel nonaxisymmetric ELM suppression coil concepts for ITER.* Nuclear Fusion, vol. 48, no. 2, page 024004, 2008.

[Schmitz 2008] O Schmitz, T E Evans, M E Fenstermacher, H Frerichs, M W Jakubowski, M J Schaffer, A Wingen, W P West, N H Brooks, K H Burrell, J S deGrassie, Y Feng, K H Finken, P Gohil, M Groth, I Joseph, C J Lasnier, M Lehnen, A W Leonard, S Mordijck, R A Moyer, A Nicolai, T H Osborne, D Reiter, U Samm, K H Spatschek, H Stoschus, B Unterberg, E A Unterberg, J G Watkins, R Wolf and the DIII-D and TEXTOR Teams. *Aspects of three dimensional transport for*

ELM control experiments in ITER-similar shape plasmas at low collisionality in DIII-D. Plasma Physics and Controlled Fusion, vol. 50, no. 12, page 124029, 2008.

[Schmitz 2013] O. Schmitz, M. Becoulet, P. Cahyna, T.E. Evans, Y. Feng, H. Frerichs, A. Kischner, A. Kukushkin, R. Laengner, T. Lunt, A. Loarte, R. Pitts, D. Reiser, D. Reiter, G. Saibene and U. Samm. *Modeling of divertor particle and heat loads during application of resonant magnetic perturbation fields for {ELM} control in {ITER}.* Journal of Nuclear Materials, no. 0, pages –, 2013.

[Schnack 2006] D.D. Schnack, D.C. Barnes, D.P. Brennan, C.C. Hegna, E. Held, C.C. Kim, S.E. Kruger, A.Y. Pankin and C.R. Sovinec. *Computational modeling of fully ionized magnetized plasmas using the fluid approximation.* Physics of Plasmas, vol. 13, no. 5, page 058103, 2006.

[Shimada 2007] M. Shimada, D.J. Campbell, V. Mukhovatov, M. Fujiwara, N. Kirneva, K. Lackner, M. Nagami, V.D. Pustovitov, N. Uckan, J. Wesley, N. Asakura, A.E. Costley, A.J.H. Donné, E.J. Doyle, A. Fasoli, C. Gormezano, Y. Gribov, O. Gruber, T.C. Hender, W. Houlberg, S. Ide, Y. Kamada, A. Leonard, B. Lipschultz, A. Loarte, K. Miyamoto, V. Mukhovatov, T.H. Osborne, A. Polevoi and A.C.C. Sips. *Chapter 1: Overview and summary.* Nuclear Fusion, vol. 47, no. 6, page S1, 2007.

[Snyder 2004] P B Snyder, H R Wilson, T H Osborne and A W Leonard. *Characterization of peeling–ballooning stability limits on the pedestal.* Plasma Physics and Controlled Fusion, vol. 46, no. 5A, page A131, 2004.

[Strauss 1997] HR Strauss. *Reduced MHD in nearly potential magnetic fields.* Journal of Plasma Physics, vol. 57, no. Part 1, pages 83–87, JAN 1997.

[Strauss 2009] H.R. Strauss, L. Sugiyama, G.Y. Park, C.S. Chang, S. Ku and I. Joseph. *Extended MHD simulation of resonant magnetic perturbations.* Nuclear Fusion, vol. 49, no. 5, page 055025, 2009.

[Sun 2010] Y. Sun, Y. Liang, K. C. Shaing, H. R. Koslowski, C. Wiegmann and T. Zhang. *Neoclassical Toroidal Plasma Viscosity Torque in Collisionless Regimes in Tokamaks.* Phys. Rev. Lett., vol. 105, page 145002, Oct 2010.

[Suttrop 2000] W Suttrop. *The physics of large and small edge localized modes.* Plasma Physics and Controlled Fusion, vol. 42, no. 5A, page A1, 2000.

[Suttrop 2011] W. Suttrop, T. Eich, J. C. Fuchs, S. Günter, A. Janzer, A. Herrmann, A. Kallenbach, P. T. Lang, T. Lunt, M. Maraschek, R. M. McDermott, A. Mlynek, T. Pütterich, M. Rott, T. Vierle, E. Wolfrum, Q. Yu, I. Zammuto and H. Zohm. *First Observation of Edge Localized Modes Mitigation with Resonant and Nonresonant Magnetic Perturbations in ASDEX Upgrade.* Phys. Rev. Lett., vol. 106, page 225004, Jun 2011.

[Suttrop 2014] W. Suttrop. 25th IAEA Fusion Energy Conference, St Petersburg, Russia (to be presented), 2014.

[Tokar 2008] M. Z. Tokar, T. E. Evans, R. Singh and B. Unterberg. *Particle transfer in edge transport barrier with stochastic magnetic field.* Physics of Plasmas (1994-present), vol. 15, no. 7, pages –, 2008.

[Waelbroeck 2012] F.L. Waelbroeck, I. Joseph, E. Nardon, M. Bécoulet and R. Fitzpatrick. *Role of singular layers in the plasma response to resonant magnetic perturbations.* Nuclear Fusion, vol. 52, no. 7, page 074004, 2012.

[Wagner 1982] F. Wagner, G. Becker, K. Behringer, D. Campbell, A. Eberhagen, W. Engelhardt, G. Fussmann, O. Gehre, J. Gernhardt, G. v. Gierke, G. Haas, M. Huang, F. Karger, M. Keilhacker, O. Klüber, M. Kornherr, K. Lackner, G. Lisitano, G. G. Lister, H. M. Mayer, D. Meisel, E. R. Müller, H. Murmann, H. Niedermeyer, W. Poschenrieder, H. Rapp, H. Röhr, F. Schneider, G. Siller, E. Speth, A. Stäbler, K. H. Steuer, G. Venus, O. Vollmer and Z. Yü. *Regime of Improved Confinement and High Beta in Neutral-Beam-Heated Divertor Discharges of the ASDEX Tokamak.* Phys. Rev. Lett., vol. 49, pages 1408–1412, Nov 1982.

[Wesson 2011] J Wesson. *Tokamaks.* Oxford University Press, 2011.

[Yu 2008] J. H. Yu, J. A. Boedo, E. M. Hollmann, R. A. Moyer, D. L. Rudakov and P. B. Snyder. *Fast imaging of edge localized mode structure and dynamics in DIII-D.* Physics of Plasmas, vol. 15, no. 3, 2008.

[Yu 2011] Q. Yu and S. Guenter. *Plasma response to externally applied resonant magnetic perturbations.* Nuclear Fusion, vol. 51, no. 7, JUL 2011.

[Yun 2011] G. S. Yun, W. Lee, M. J. Choi, J. Lee, H. K. Park, B. Tobias, C. W. Domier, N. C. Luhmann, A. J. H. Donné and J. H. Lee. *Two-Dimensional Visualization of Growth and Burst of the Edge-Localized Filaments in KSTAR H-Mode Plasmas.* Phys. Rev. Lett., vol. 107, page 045004, Jul 2011.

[Zohm 1996] H Zohm. *Edge localized modes (ELMs).* Plasma Physics and Controlled Fusion, vol. 38, no. 2, page 105, 1996.